Hughes Hall
College

UNIVERSITY OF CAMBRIDGE

MRC Mitochondrial Biology Unit

Identification and characterisation of new factors and mechanisms regulating human cytochrome c oxidase biogenesis

Alba Signes Marrahi

Dissertation submitted for the degree of Doctor of Philosophy

November 2018

Declaration

This dissertation describes the results of my own work, except for the experiments performed by collaborators, which are specified in the figure legends. All the work was carried out under the supervision of Prof. Massimo Zeviani assisted by Dr. Erika Fernandez-Vizarra (Senior Investigator Scientist) at the Medical Research Council (MRC) Mitochondrial Biology Unit, between January 2015 and November 2018. This thesis has not been submitted, in whole or in part, for a degree at this or any other institution and the length of it does not exceed the prescribed word limit.

Part of the text in Chapter 1 has been published in a review article: Assembly of mammalian oxidative phosphorylation complexes I–V and supercomplexes (2018) (Signes & Fernandez-Vizarra, *Essays in Biochemistry*, 62(3): 255–270).

The results described in Chapter 3 led to a publication: MR-1S Interacts with PET100 and PET117 in Module-Based Assembly of Human Cytochrome c Oxidase (2017) (Vidoni et al., *Cell reports*, 18 (7), 1727-1738).

The results described in Chapter 4 and 5 led to a publication: APOPT1/COA8 assists COX assembly and is oppositely regulated by UPS and ROS (2019) (Signes et al., *EMBO Molecular Medicine*, 11(1), e9582).

Alba Signes Marrahi,

Cambridge (UK), November 2018.

Acknowledgements

Firstly, I would like to thank my supervisor, Prof. Massimo Zeviani, for giving me the opportunity to carry out my work in his laboratory. I also want to give a huge thank you to Dr. Erika Fernandez-Vizarra for her guidance, enthusiasm and support during the past four years. Her passion for science is inspiring.

A big thank you to every single member of the Mitochondrial Medicine group, including those that already left, because no matter how busy they were, they always gave me their invaluable guidance and help (as scientists and as friends). Thanks also to all the many colleagues in the unit who were always kind and supportive with me. Special thanks to Massimo and Erika for proofreading my thesis and giving me constructive feedback. I must also thank Dr. Carlo Viscomi, Raffaele Cerutti, Prof. Mike Murphy, Dr. Liz Hinchy, Prof. James Nathan and Anna Dickson, who greatly contributed to this project.

I must also acknowledge the team from the Phenomics Laboratory, Forvie Site (Cambridge Biomedical Campus, Cambridge CB2 0PY) for their fantastic work and help with animal models.

A special thank you to Penny, Janet, Irina, Jennifer, Dave, Steve, Merlin, Ash, and Andrew for their help with student, administrative, technical and IT matters. And a big thanks to the Medical Research Council for funding my research experience.

I have been very lucky to meet wonderful people in Cambridge, many of whom have become very close friends. A very special thank you is reserved to Nicole, who gave me her kind support and advice and was always there when needed.

Lastly, I want to thank my family for their love and support and for giving me the strength and motivation that I, sometimes, lack.

Summary

Assembly of the mitochondrial complex IV (CIV) or cytochrome *c* oxidase (COX) is an intricate and highly regulated process in which the three-core mitochondrial DNA (mtDNA) encoded subunits assemble in a coordinated way with the remaining eleven supernumerary nuclear DNA (nDNA) encoded subunits. This process requires a large number of additional factors, which are necessary for the correct maturation of the complex but are not part of the fully assembled enzyme. Studies in mutant strains of the yeast *Saccharomyces cerevisiae* have been very useful to find many assembly factors and their human orthologs. However, it has become evident that there are animal-specific factors not present in yeast, which need to be identified using other techniques. In this work, two of these COX assembly factors, identified through two different approaches, have been characterised.

First, quantitative proteomic analysis of the subassemblies accumulated in a *MT-CO3* deficient cell line allowed the identification of MR-1S, conserved only in vertebrates. The downregulation of this protein produced a COX assembly and enzymatic defect. In addition, it was found to interact with the highly conserved *bona fide* COX assembly factors PET100 and PET117.

Secondly, genomic screening of patients displaying mitochondrial encephalopathy and COX deficiency, revealed the presence of pathogenic variants in *APOPT1.* An *Apopt1* knockout (KO) mouse model was generated by CRISPR/Cas9 to study the role of the APOPT1 protein in relation with COX biogenesis. Phenotypic characterisation showed COX deficiency in all tissues, associated with neuromuscular impairment, similar to the features found in human individuals carrying mutations in *APOPT1*, for which two immortalised skin fibroblast cell lines were studied. All the analysed mouse tissues and human cells showed decreased levels of fully assembled COX and subassembly accumulation. Interestingly, APOPT1 was found to be tightly regulated at the post-translational level, being its turnover controlled by the cytoplasmic ubiquitin-proteasome system (UPS), while increased oxidative stress had stabilising effects on the mature intramitochondrial form, which was shown to protect COX subunits from oxidatively-induced degradation.

Abbreviations

AAVs	adeno-associated virus
ACO2	mitochondrial aconitase
ADP	adenosine diphosphate
AIF	apoptosis inducing factor
ALS	amyotrophic lateral sclerosis
ANT	adenine nucleotide translocator
AOX	alternative oxidase
ATP	adenosine triphosphate
bp	base pairs
BN-PAGE	Blue Native Polyacrylamide Gel Electrophoresis
BSA	bovine serum albumin
CI	complex I
CII	complex II
CIII	complex III
CIV	complex IV
CV	complex V
CLAMS	comprehensive laboratory animal monitoring system
CNS	central nervous system
COX	cytochrome *c* oxidase
CT	computed tomography
CS	citrate synthase
D-loop	displacement loop
DDM	n-dodecyl-β-D-maltoside
DMEM	dulbecco's modified eagle's medium
DNA	deoxyribonucleic acid
DUBs	deubiquitinating enzymes
EM	electron microscopy
ER	endoplasmic reticulum
ERAD	ER–associated protein degradation
ETC	electron transport chain
EV	empty vector
FAD	flavin adenine dinucleotide
FBS	foetal bovine serum
FMN	flavin mononucleotide
FVB	friend virus B
g	gram
GSH	glutathione (reduced)
GSSG	glutathione (oxidised)
HA	hemagglutinin
HEK	human embryonic kidney
HIF-1α	hypoxia-inducible factor-1α

HS	heavy strand
IGA	in gel activity
IHC	immunohistochemistry
IMM	inner mitochondrial membrane
IMS	inter-membrane space
ISC	iron-sulphur cluster
kDa	kilodalton
KGDH	α-ketoglutarate dehydrogenase
KO	knockout
LACE1	ATPase lactation elevated 1
l	litre
LS	light strand; leigh syndrome
M	molar
mM	millimolar
MAD	mitochondrial-associated degradation
MAVS	mitochondrial antiviral signalling
MCIA	mitochondrial complex I assembly
MCU	mitochondrial calcium uniporter
MEFs	mouse embryo fibroblasts
MELAS	mitochondrial myopathy, encephalopathy, lactic acidosis and stroke-like episodes
MIA	mitochondrial intermembrane space assembly machinery
MitoPQ	mitoparaquat
MITRAC	mitochondrial translation regulation assembly intermediate of cytochrome c oxidase
ml	millilitre
MOMP	mitochondrial outer membrane permeabilisation
MPT	mitochondrial permeability transition
MR-1S/M/L	myofibrillary-related protein 1 short/medium/long isoform
MRI	magnetic resonance imaging
MRS	MR-spectroscopy
MS	mass spectrometry
Mt	mitochondria
mtDNA	mitochondrial DNA
MTS	mitochondrial targeting signal
MW	molecular weight
NAD	nicotinamide adenine dinucleotide
NBF	neutral buffered formalin
nDNA	nuclear DNA
NGS	next-generation sequencing
NMD	nonsense-mediated mRNA decay
OAA	oxaloacetic acid
O_H	origin of the heavy strand

OMM	outer mitochondrial membrane
OXPHOS	oxidative phosphorylation
PBS	phosphate buffered saline
PCR	polymerase chain reaction
PDHC	pyruvate dehydrogenase complex
PET	positron emission tomography
Pi	inorganic phosphate
PLS	pump loading site
PMF	proton-motive force
PNKD	paroxysmal non-kinesigenic dyskinesia
Q, CoQ	ubiquinone or coenzyme Q
RNA	ribonucleic acid
rRNA	ribosomal RNA
RET	reverse electron transfer
SDH	succinate dehydrogenase
SDS-PAGE	sodium dodecyl sulphate-polyacrylamide polyacrylamide gel electrophoresis
shRNA	small hairpin RNA
SILAC	stable isotope-labelled amino acids in cell culture
SOD2/MnSOD	superoxide dismutase 2
TCA	tricarboxylic acid cycle
TIM	transporter of the inner membrane
TOM	translocase of the outer membrane
Tm	melting temperature
tRNAs	transfer RNAs
UPR	unfolded protein response
UPS	ubiquitin-proteasome system
WB	Western blot
WT	Wild-type
µg	microgram
µl	microlitre
µM	micromolar

Table of contents

Preface

Chapter 1: Introduction

Chapter 2: Materials and methods

Chapter 3: Identification and characterisation of MR-1S, a vertebrate-specific COX assembly factor

Chapter 4: Generation and characterisation of an Apopt1 KO mouse model

Chapter 5: Characterisation of the APOPT1 protein in cellular models

Chapter 6: Discussion and future aims

CHAPTER 1

Introduction

1.1 General introduction to mitochondrial biology

1.1.1 Mitochondrial origin

Mitochondria are subcellular organelles, found in nearly all eukaryotic cells, that supply the cell with energy in form of ATP (adenosine triphosphate) generated by aerobic respiration. Mitochondria are thought to have evolved 2.4 billion years ago, when oxygen (O_2) started to build up in the Earth's atmosphere (Cavalier-Smith, 2006). The endosymbiotic theory proposes that mitochondria were originally independent oxygen-utilising alpha-protobacteria that were engulfed by a host cell, most likely related to modern archaea (Embley and Martin, 2006; Martijn and Ettema, 2013). This event led to an evolutionary transition in which the transfer of the majority of the mitochondrial genes to the nucleus of the host cell, allowed the expansion and restructuration of the nuclear genome, a key factor for the development of more complex organisms (Lane and Martin, 2010). After the endosymbiotic event, mitochondria became semi-autonomous organelles, being their function and biogenesis heavily dependent on the nucleus (Cavalier-Smith, 2006). However, by retaining a small genome, mitochondria possess the ability to synthesise key proteins of the mitochondrial respiratory chain in a flexible way that is able to adapt to the influx of nuclear-encoded subunits (Richter-Dennerlein *et al.*, 2016).

1.1.2 Mitochondrial architecture and dynamics

The term "mitochondrion" was coined in 1898 by microbiologist Carl Benda, who identified these organelles with a light microscope by the "threads dotted with grains" that appear to run across them, giving origin to the name "mitochondrion", derived from the Greek "mitos", meaning thread, and "chondrion" meaning grain (Ernster and Schatz, 1981). The first high resolution images of the mitochondrial internal structure were provided in the 1950s (Palade, 1953; Sjöstrand, 1953), thanks to the development of electron microscopy (EM) techniques (**Figure 1.1**). Mitochondria appeared to have two

membranes, evidence of the endosymbiotic theory: the outer mitochondrial membrane (OMM), similar to eukaryotic cell membranes, and the inner mitochondrial membrane (IMM), that shares many characteristics with the bacterial cell membrane, such as the presence of cardiolipin (Cavalier-Smith, 2006). This double membrane architecture results in the formation of four morphologically and functionally distinct compartments: the outer mitochondrial membrane (OMM), the intermembrane space (IMS), the inner mitochondrial membrane (IMM) and the matrix (**Figure 1.1**). The OMM, which forms the boundary with the cytoplasm, is a relatively simple phospholipid bilayer with a protein:phospholipid ratio similar to the eukaryotic plasma membrane (Ernster and Schatz, 1981). It contains large numbers of integral membrane proteins, called porins, that allow free traffic of ions and small molecules (< 5 kDa) (Young *et al.*, 2007). Bigger proteins need to be imported through the translocase of the outer membrane (TOM complex) (Ferramosca and Zara, 2013). In contrast, the IMM is more complex and protein-dense than the OMM (Flescher, Klouwen and Brierley, 1961) and presents many invaginations, called cristae, that protrude into the matrix space and harbour the oxidative phosphorylation (OXPHOS) system (Ernster and Schatz, 1981). The high folding of the IMM increases its surface, maximising the area available for energy production (Nunnari, 2014). This membrane is permeable only to O_2, carbon dioxide (CO_2), and water (H_2O), and therefore sophisticated mitochondrial carriers are necessary to transport proteins and other molecules through this membrane. For instance, the adenine nucleotide translocator (ANT) exchanges ATP with ADP across the membrane (Klingenberg, 2008) and the translocase of the inner membrane (TIM complex) imports proteins into the IMM and the matrix (Rehling *et al.*, 2003; Dolezal *et al.*, 2006). The tight control of the IMM permeability allows the generation and maintenance of an electrochemical gradient across the membrane that is essential not only for the synthesis of ATP (Nicholls, 1974), but also for other mitochondrial functions such as Ca^{2+} uptake through the mitochondrial calcium uniporter (MCU) (Baughman *et al.*, 2008; De Stefani *et al.*, 2014). On the other hand, the IMS is crucial for several mitochondrial functions, such as the exchange of proteins, lipids and metal ions between the matrix and the cytosol (Wiedemann, Frazier and Pfanner, 2004) or the activation of apoptosis (Tait and Green, 2013). It also contains the mitochondrial intermembrane space assembly (MIA)

machinery that mediates oxidative protein transport and folding (Stojanovski *et al.*, 2008). Finally, the mitochondrial matrix harbours multiple copies of the mtDNA, the mitochondrial ribosomes and pools of ions and proteins involved in many different processes, such as the tricarboxylic acid cycle (TCA) (Martínez-reyes *et al.*, 2017), the biosynthesis of haem moieties (Ajioka, Phillips and Kushner, 2006) and iron-sulphur (Fe-S) clusters (Rouault and Maio, 2017), the synthesis and degradation of several amino acids (Guda, Guda and Subramaniam, 2007), etc.

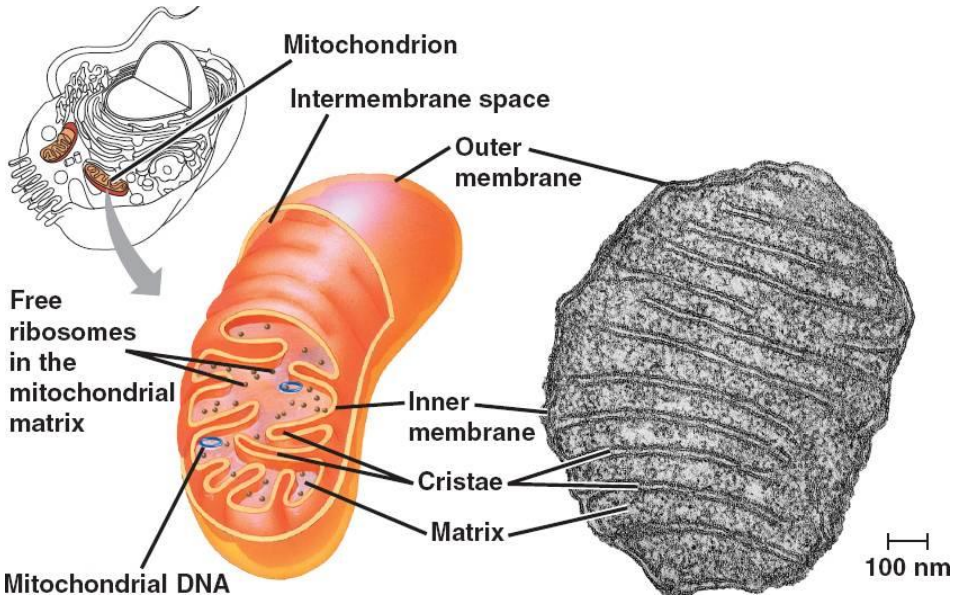

Figure 1.1 Architecture of the mitochondrion. Left to right: Subcellular location of mitochondria. Cartoon of a typically rod-shaped mitochondrion depicting its different compartments. Electron micrograph of a mitochondrion. Image extracted from (Lejay *et al.*, 2007).

Mitochondria have usually been described as individual rod-shaped structures (**Figure 1.1**) (Palade, 1953; Ernster and Schatz, 1981). However, it is now well established that they are dynamic organelles forming a network of tube-like structures (Tilokani *et al.*, 2018). The shape of this network is controlled by two opposing processes, fission and fusion (Twig, Hyde and Shirihai, 2008; Zamponi *et al.*, 2018). Fusion maximises mitochondrial function by allowing the spreading of metabolites, protein and DNA throughout the network, while fission allows segregation of damaged components of a mitochondrion and isolation of dysfunctional mitochondria (Youle, Pickles and Vigi, 2018). Mitochondria can

adapt to different cellular metabolic demands not only by changing the shape of their network, but also by increasing/decreasing the number of mitochondria per cell and their intracellular location (Robin and Wong, 1988; Anesti and Scorrano, 2006; Frazier *et al.*, 2006; Campello and Scorrano, 2010). Normally, mitochondria concentrate in areas where high amounts of energy are required, like for example in skeletal muscle, where mitochondria are aligned in rows parallel to the contractile fibrils (Anesti and Scorrano, 2006; Frangini *et al.*, 2013). Thus, mitochondrial dynamics, which includes fission/fusion, movements through the cytoskeleton and turnover (balance between mitochondrial biogenesis and mitophagy), are crucial for the regulation of mitochondrial function and quality (Campello and Scorrano, 2010; Suárez-Rivero *et al.*, 2016; Tilokani *et al.*, 2018).

1.1.3 Mitochondrial metabolic pathways

Mitochondria are commonly known as the 'powerhouses of the cell' because their main function is the generation of ATP via the mechanism called OXPHOS (Cavalier-Smith, 2006). The chemiosmotic theory, developed in 1960 by the British biochemist Peter Mitchell, is the basis for understanding this process (Peter, 1961; Ernster and Schatz, 1981). The catabolism of carbohydrates, fatty acids and proteins converge in the formation of acetyl-CoA, which enters the TCA cycle to completely oxidise its acetyl group to CO_2. During this process, the reducing equivalents are transferred to NAD+ (nicotinamide adenine dinucleotide) and FAD (flavin adenine dinucleotide), generating NADH and $FADH_2$, respectively (Martínez-reyes *et al.*, 2017). These cofactors donate electrons to the electron transport chain (ETC), composed of four enzymes (complexes I to IV; CI-IV). Two mobile electron carriers mediate the electronic transfer between these complexes: the lipophilic ubiquinone or coenzyme Q (CoQ, Q) embedded in the IMM, and the hydrophilic heme protein cytochrome *c* (cyt *c*), located in the IMS. The sequential redox reactions through the complexes are exergonic and provide energy for complexes I, III and IV to pump protons (H^+) from the matrix to the IMS (**Figure 1.2**), making the latter more positive and acidic than the matrix (Watt *et al.*, 2010). This creates an electrochemical gradient between the two sides of the IMM, which is called proton-motive force (PMF),

defined by two components: an electrical membrane potential (ΔΨ) and a chemical pH gradient (ΔpH) (Nicholls, 1974). The PMF drives H^+ back across the IMM through the last of the OXPHOS enzymes, complex V (CV) or ATP synthase, generating a rotation movement that powers the synthesis of ATP from adenosine diphosphate (ADP) and inorganic phosphate (Pi) (see section **1.2.5 Complex V** for more details) (Abrahams *et al.*, 1994; Stock *et al.*, 2000; Watt *et al.*, 2010; He, Carroll, *et al.*, 2017).

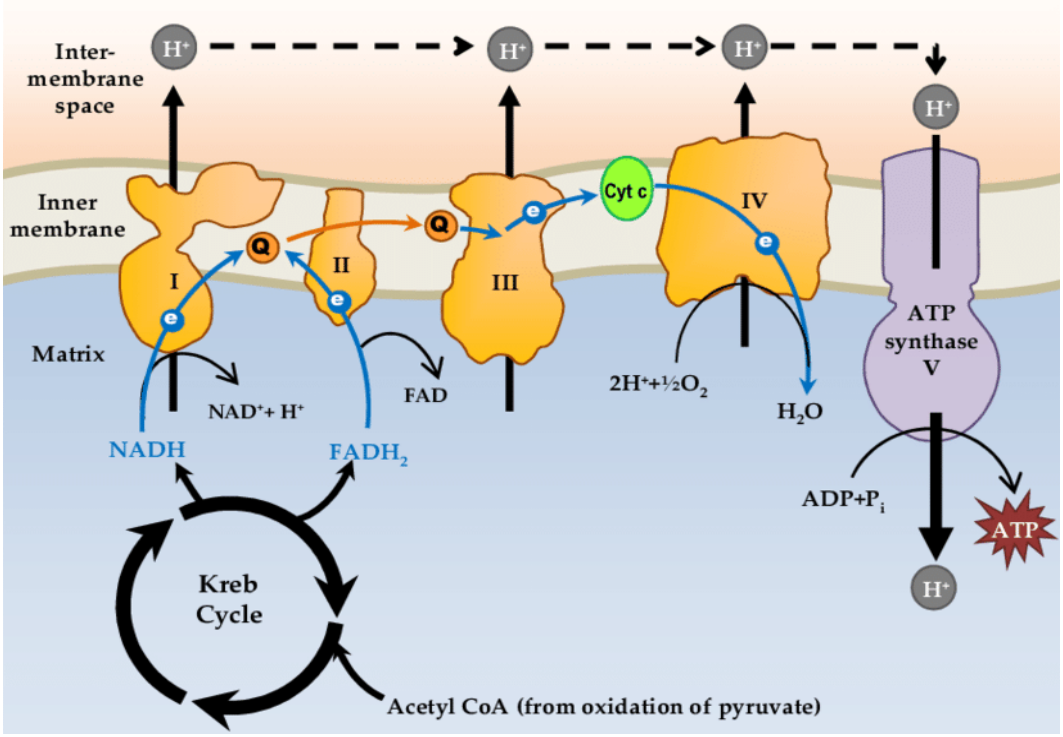

Figure 1.2 Cartoon of the OXPHOS system. The NADH and $FADH_2$ produced by the TCA cycle are oxidised by CI and CII, respectively. The electrons then flow to CIII and CIV, with the help of Q and cyt *c*, and are used to reduce O_2 to H_2O at CIV. The PMF created through the IMM powers the generation of ATP at the matrix side of CV. Image extracted from (Yusoff *et al.*, 2015).

In addition to OXPHOS, mitochondria are involved in many other metabolic processes. For instance, the incorporation of iron into haems and Fe-S clusters occurs inside this organelle (Richardson *et al.*, 2010; Kim *et al.*, 2013; Lane *et al.*, 2015). Although most of the intermediate steps of haem synthesis are cytosolic, the first and last reactions are catalysed in the mitochondrial matrix. Once haems are formed, they are incorporated into haem-containing proteins, such as haemoglobin and cytochromes (Ajioka, Phillips and Kushner, 2006; Richardson

et al., 2010; Kim *et al.*, 2013). On the other hand, the mitochondrial matrix Fe-S cluster assembly (ISC) machinery coordinates the biosynthesis of Fe-S centres and their incorporation into apoproteins, some of which are components of complexes I, II and III of the ETC (Brzóska, Męczyńska and Kruszewski, 2006; Braymer and Lill, 2017; Rouault and Maio, 2017).

Moreover, all the 20 amino acids, both 'essential' (need to be taken from food) and 'non-essential' (can be synthesised in humans) have metabolic pathways associated with mitochondria (catabolic and anabolic for the 'non-essential' and only catabolic for the 'essential' ones) (Guda, Guda and Subramaniam, 2007). For instance, glutamine is deaminated to glutamate in the mitochondrial matrix and after a series of transamination reactions is used for the synthesis of proline, alanine and aspartate (Guda, Guda and Subramaniam, 2007). Additionally, some steps of the synthesis and degradation of nucleotides also occur inside mitochondria. For instance, glutamate can be converted to α-ketoglutarate, enter the TCA cycle and be oxidised to oxaloacetate (OAA), which can then be transaminated to aspartate and transported to the cytosol where it is used for nucleotide biosynthesis (Wang, 2016). Many other metabolic pathways have also some steps taking place inside the mitochondria, such as cardiolipin synthesis (Houtkooper and Vaz, 2008; Paradies *et al.*, 2014) and quinone and steroid biosynthesis (Miller, 2013),

As previously mentioned, mitochondria also have a role in Ca^{2+} uptake through the MCU (Baughman *et al.*, 2008; Stefani *et al.*, 2014), which acts as a channel opening when the cytosolic free calcium concentration is higher than 0.5 µM (Chem *et al.*, 2015). Once in the matrix, where it can be stored temporarily, Ca^{2+} stimulates three dehydrogenases of the TCA cycle (pyruvate, NAD-isocitrate, and 2-oxoglutarate dehydrogenases), increasing the production of NADH and therefore, the synthesis of ATP, which is particularly important during skeletal muscle contraction (Denton and Martin, 1972; Denton, 2009; Christoph Maack, 2013).

Finally, mitochondria are also crucial in the regulation of cell fate, as they can activate cell death via apoptosis or via necrosis. Apoptosis, or programmed cell death, occurs in response to various stresses, such as DNA damage, growth factor withdrawal and oxidative stress, and is characterised by the permeabilisation of the OMM, called MOMP (mitochondrial outer membrane

permeabilisation), which leads to the release of several IMS proapoptotic proteins, such as cyt *c* (Tait and Green, 2013; Chen, Kang and Fu, 2018; Galluzzi *et al.*, 2018). Necrosis is activated by more severe stresses, such as very high levels of oxidative stress and cytosolic Ca_2^+ overload, and is characterised by permeabilisation of the IMM, called MPT (mitochondrial permeability transition), which leads to the dissipation of the IMM potential, ion deregulation, mitochondrial and cellular swelling, activation of degradative enzymes, failure of the plasmatic membrane and cell lysis (Halestrap, 2009; Chen, Kang and Fu, 2018; Galluzzi *et al.*, 2018).

1.1.4 The mitochondrial genome

Throughout evolution mitochondria have retained a small amount of genetic material, known as mtDNA, which in humans is a circular double stranded DNA molecule of 16.6 kilobases (kb) composed of a heavy strand (purine-rich; HS) and a light strand (pyrimidine-rich; LS). It is a very compact genome with contiguous genes and no introns, and it has only one small non-coding region, called the displacement loop (D-loop), which contains the replication origin of the HS (O_H) and the transcription promoters for both strands (HSP and LSP) (Bogenhagen, 2012; Gray *et al.*, 2012; Chinnery and Hudson, 2013). The coding region harbours 37 genes: 22 tRNAs (transfer RNAs), 2 rRNAs (ribosomal RNAs) and 13 proteins (all structural subunits of the OXPHOS system) (**Figure 1.3**) (Chinnery and Hudson, 2013). All the other structural subunits of complexes I-V plus all the proteins required for the normal mitochondrial physiology (assembly of the respiratory chain complexes, maintenance and expression of mtDNA, etc.), which compose the mitochondrial proteome of around 1500 proteins, are encoded in the nDNA (Ruiz-Pesini *et al.*, 2007; Gray *et al.*, 2012). This means that their expression has to be somehow coordinated with the mitochondrial genome (Couvillion *et al.*, 2016; Richter-Dennerlein *et al.*, 2016) and that they have to be translated in the cytosol and imported into the organelle through specific sorting, translocation and folding machineries (Wasilewski, Chojnacka and Chacinska, 2017).

Each human cell has hundreds to several thousands of mitochondria and every mitochondrion can carry as many as ten copies of mtDNA, which associate with histone-like proteins to form densely packed nucleoprotein particles, called nucleoids, that attach to the IMM (Robin and Wong, 1988; Kukat *et al.*, 2011; Bogenhagen, 2012). The mitochondrial genome replicates independently from the nuclear DNA and the cell cycle (Chinnery and Hudson, 2013) and by mitochondria-specific factors different from those used for nuclear replication (Falkenberg, 2018). The replication mechanism is also different from the one in the nucleus. It follows a strand-displacement mechanism, in which the synthesis of the HS initiates at the O_H and proceeds continuously and unidirectionally without simultaneous replication of the opposite strand, which starts from a distinct position, called O_L, from where it also proceeds continuously and unidirectionally (Falkenberg, 2018). The entire mitochondrial genome is transcribed, also using a distinct machinery, from the HSP and LSP as polycistronic transcripts. According to the ‘tRNA punctuation model’, these long transcripts undergo several processing steps. First the different RNA species are cleaved, then multiple chemical modifications allow the tRNAs and mRNAs to be functional and the rRNAs to assemble into the mitoribosome, where the translation of the mtDNA-encoded OXPHOS subunits occurs (D’Souza and Minczuk, 2018).

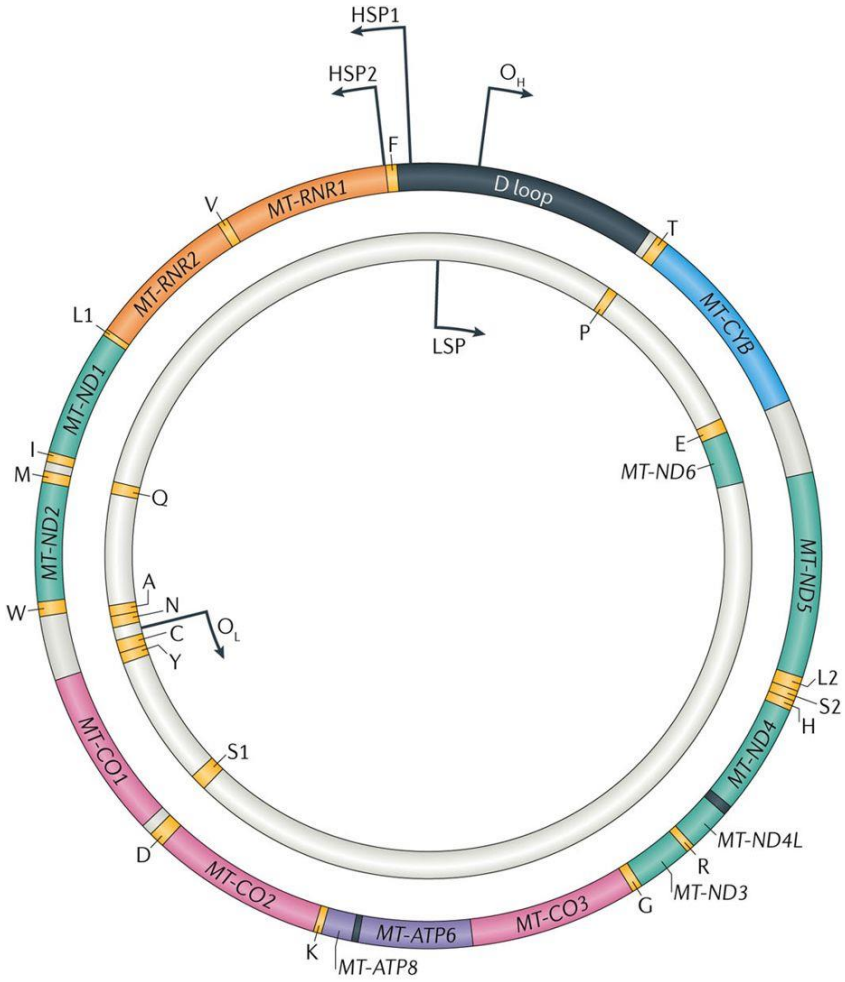

Figure 1.3 The human mitochondrial genome. Both rRNAs (depicted orange) and the genes encoding proteins are located on the HS, except the ND6 gene, which is located on the LS. CI subunits are depicted in green, CIII in blue, CIV in pink and CV in purple. tRNA genes, located both in the HS and the LS, are depicted in yellow with single letters, such as 'Q' and 'L'. O_H and O_L indicate the origins of replication and HSP and LSP indicate the transcription promoters. The D-loop is depicted in black. Image extracted from (Gorman *et al.*, 2016).

1.2 Function and biogenesis of the mammalian OXPHOS system

In mammals, all the components of the OXPHOS system are multimeric and, except for CII, composed of subunits encoded both in the mtDNA and the nDNA, which makes the OXPHOS system unique (Fernández-Vizarra, Tiranti and Zeviani, 2009; Signes and Fernandez-vizarra, 2018). Along with structural subunits, many other factors necessary for the correct biogenesis of OXPHOS

are encoded in the nDNA (Chinnery and Hudson, 2013; Richter-Dennerlein *et al.*, 2016). Many of these nuclear-encoded proteins are 'assembly factors', which are complex-specific proteins that assist the assembly of nascent complexes but do not form part of the final structure. These assembly factors, which in some cases outnumber the structural subunits, can be involved in a variety of functions, such as the incorporation and stabilisation of specific subunits and/or assembly intermediates or the synthesis and incorporation of prosthetic groups (Fernández-Vizarra, Tiranti and Zeviani, 2009; Ghezzi and Zeviani, 2018; Signes and Fernandez-vizarra, 2018). The assembly pathways and the known factors involved for each of the five OXPHOS complexes are described below. Due to the focus of this thesis on COX (CIV), the function and biogenesis of this complex will be described in greater detail.

1.2.1 Complex I

Complex I (EC 1.6.5.3) or NADH:ubiquinone reductase (H+ translocating) is composed of forty-five subunits and is the largest OXPHOS complex. It is an L-shaped enzyme composed of a hydrophilic arm protruding into the matrix, where the electron transfer from NADH to Q occurs, and of a proton-translocating hydrophobic arm. The Q binding site is at the interphase of both arms (Efremov, Baradaran and Sazanov, 2010; Baradaran *et al.*, 2013). The catalytic core, conserved from bacteria to humans, is composed of 14 subunits: 7 are mtDNA-encoded (ND1, ND2, ND3, ND4, ND4L, ND5, and ND6), located in the hydrophobic arm and involved in proton translocation (Vinothkumar, Zhu and Hirst, 2014); and the other 7 are nDNA-encoded (NDUFV1, NDUFV2, NDUFS1, NDUFS2, NDUFS3, NDUFS7, and NDUFS8), located in the hydrophilic arm and containing the redox active centres (one non-covalently bound flavin mononucleotide, FMN, and seven Fe-S clusters) (Hirst and Roessler, 2016). The remaining thirty subunits are 'supernumerary' but important for assembly and stability (Vinothkumar, Zhu and Hirst, 2014; Stroud *et al.*, 2016; Zhu, Vinothkumar and Hirst, 2017).

Exhaustive research has been carried out concerning human CI assembly (Antonicka, Ogilvie, *et al.*, 2003; Ugalde, Janssen, *et al.*, 2004; Ugalde, Vogel, *et al.*, 2004; Lazarou *et al.*, 2007; Vogel, Dieteren, *et al.*, 2007; Vogel, Smeitink and Nijtmans, 2007; Mimaki *et al.*, 2012; Sánchez-Caballero, Guerrero-Castillo and Nijtmans, 2016). However, several recent breakthroughs have granted a much deeper understanding about this process. Thus, we now know the complete mammalian CI structure (Vinothkumar, Zhu and Hirst, 2014; Zhu, Vinothkumar and Hirst, 2016) and how the subunits are organised in six modules (N, Q, ND1, ND2, ND4 and ND5) that, with the help of specific assembly factors, are brought together through five distinct subassemblies (Stroud *et al.*, 2016; Guerrero-Castillo *et al.*, 2017) (**Figure 1.4**).

The **N-module**, which is the tip of the hydrophilic arm and the last one to be incorporated (Lazarou *et al.*, 2007; Vogel, van den Brand, *et al.*, 2007), results from the assembly of NDUFV1, NDUFV2, NDUFS1 and NDUFA2 (Guerrero-Castillo *et al.*, 2017) to which NDUFA6, NDUFA7, NDUFA12, NDUFS4, NDUFS6 and NDUFV3 must be further associated to complete the module (Stroud *et al.*, 2016).

The **Q-module** is built through the association of NDUFA5, NDUFS2 and NDUFS3 plus NDUFS7 and NDUFS8. The chaperones NDUFAF3/C3ORF60 and NDUFAF4/C6ORF66 (Saada *et al.*, 2008, 2009) remain bound to this module until the final assembly steps (Guerrero-Castillo *et al.*, 2017). NDUFAF6/C8ORF38 (Pagliarini *et al.*, 2008) also seems to participate in the assembly of the Q-module (Bianciardi *et al.*, 2016; Stroud *et al.*, 2016). NDUFAF3, 4 and 6, are necessary to maintain normal MT-ND1 synthesis (McKenzie *et al.*, 2011; Zurita Rendón and Shoubridge, 2012). NDUFAF5 adds a hydroxyl group to Arg-73 of NDUFS7 (Rhein *et al.*, 2016) and NDUFAF7 dimethylates NDUFS2 in Arg-85 (Rhein *et al.*, 2013), an essential modification for CI assembly (Zurita Rendón *et al.*, 2014). NUBPL/IND1 delivers [4Fe-4S] clusters specifically to the N- and Q-module subunits (Sheftel *et al.*, 2009; Calvo *et al.*, 2010).

The **ND1-module** builds around the Q-module with the help of TIMMDC1/C3ORF1 (Andrews *et al.*, 2013; Guarani *et al.*, 2014), which remains bound to the Q/ND1 subassembly until the last maturation steps. MT-ND1 joins

first and then NDUFA3, NDUFA8 and NDUFA13 are added (Guerrero-Castillo *et al.*, 2017).

The **ND2-module** is formed by an initial intermediate that contains MT-ND2, NDUFC1 and NDUFC2 bound to NDUFAF1/CIA30 (Vogel *et al.*, 2005; Dunning *et al.*, 2007), ECSIT (Vogel, Janssen, *et al.*, 2007) and ACAD9 (Haack *et al.*, 2010; Nouws *et al.*, 2010). Then, MT-ND3 is added together with TMEM126B (Heide *et al.*, 2012), forming a larger intermediate to which subunits MT-ND6 and MT-ND4L bind. The latest assembly stages involve the incorporation of subunits NDUFA1, NDUFA10 and NDUFS5 (Stroud *et al.*, 2016; Guerrero-Castillo *et al.*, 2017). The stable association of the assembly factors NDUFAF1+ECSIT+ACAD9+TMEM126 was denominated Mitochondrial Complex I Assembly (MCIA) complex (Heide *et al.*, 2012; Guarani *et al.*, 2014). Two other chaperones were found interacting with this module: TMEM186 and COA1 (Guerrero-Castillo *et al.*, 2017), the latter being a well-known CIV assembly factor (Mick *et al.*, 2012; Szklarczyk *et al.*, 2012).

The main **ND4-module** intermediate binds NDUFB1, NDUFB4, NDUFB5, NDUFB6, NDUFB10, NDUFB11 and MT-ND4 together with FOXRED1 (Calvo *et al.*, 2010; Fassone *et al.*, 2010; Formosa *et al.*, 2015; Zurita Rendón *et al.*, 2016), ATP5SL (Ugalde, Vogel, *et al.*, 2004; Stroud *et al.*, 2016) and also TMEM70, described as a CV assembly factor (Čížková *et al.*, 2008; Hejzlarová *et al.*, 2014; Guerrero-Castillo *et al.*, 2017).

The **ND5-module** corresponds to the distal part of the membrane arm and it is composed of MT-ND5, NDUFB2, NDUFB3, NDUFB7, NDUFB8, NDUFB9 and NDUFAB1 (Stroud *et al.*, 2016; Guerrero-Castillo *et al.*, 2017). DMAC1/TMEM261 is implicated in its stabilisation and/or assembly (Stroud *et al.*, 2016).

The ND2- and the ND4-modules get together first, with still all the chaperones bound to them. Later on, the Q/ND1 and the ND5-modules join the nascent complex. This intermediate only lacking the N-module is stabilised by NDUFAF2/NDUFA12L/B17.2L (Ogilvie, Kennaway and Shoubridge, 2005; Vogel, van den Brand, *et al.*, 2007; Stroud *et al.*, 2016). In the last step, the pre-assembled N-module becomes attached and the chaperones released (Guerrero-Castillo *et al.*, 2017).

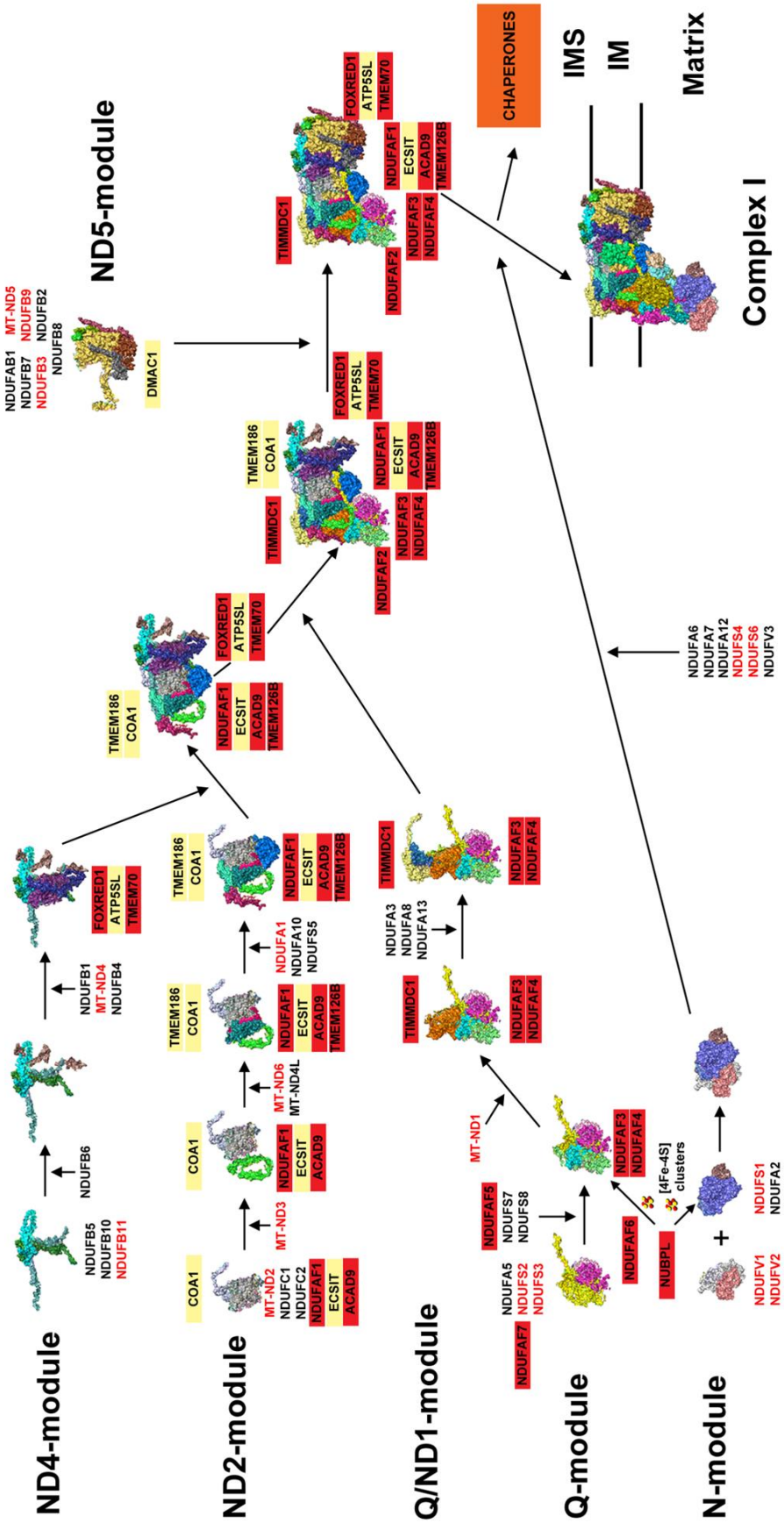
ND4-module
NDUFB5
NDUFB10
NDUFB11
NDUFB6
NDUFB1
MT-ND4
NDUFB4
FOXRED1
ATP5SL
TMEM70
ND2-module
COA1
MT-ND2
NDUFC1
NDUFC2
NDUFAF1
ECSIT
ACAD9
MT-ND3
COA1
NDUFAF1
ECSIT
ACAD9
MT-ND6
MT-ND4L
TMEM186
COA1
NDUFAF1
ECSIT
ACAD9
TMEM126B
NDUFA1
NDUFA10
NDUFS5
TMEM186
COA1
NDUFAF1
ECSIT
ACAD9
TMEM126B
FOXRED1
ATP5SL
TMEM70
Q/ND1-module
TIMMDC1
NDUFAF3
NDUFAF4
NDUFA3
NDUFA8
NDUFA13
TIMMDC1
NDUFAF3
NDUFAF4
MT-ND1
NDUFAF5
NDUFS7
NDUFS8
NDUFA5
NDUFS2
NDUFS3
NDUFAF7
Q-module
NDUFAF3
NDUFAF4
NDUFAF6
[4Fe-4S]
clusters
NUBPL
N-module
NDUFS1
NDUFA2
NDUFV1
NDUFV2
ND5-module
NDUFAB1
NDUFB7
NDUFB3
MT-ND5
NDUFB9
NDUFB2
NDUFB8
DMAC1
TIMMDC1
FOXRED1
ATP5SL
TMEM70
NDUFAF2
NDUFAF3
NDUFAF4
NDUFAF1
ECSIT
ACAD9
TMEM126B
CHAPERONES
IMS
IM
Matrix
Complex I
NDUFA6
NDUFA7
NDUFA12
NDUFS4
NDUFS6
NDUFV3

Figure 1.4

Figure 1.4 Complex I assembly model based on the bovine CI cryo-EM structure with Protein Data Bank (PDB) ID: 5LC5 (Zhu, Vinothkumar and Hirst, 2017) and the models proposed in references (Sánchez-Caballero, Guerrero-Castillo and Nijtmans, 2016; Formosa *et al.*, 2017; Guerrero-Castillo *et al.*, 2017). Red colour indicates proteins with described pathological mutations. See main text for details. Image extracted from (Signes and Fernandez-Vizarra, 2018).

1.2.2 Complex II

Complex II (EC 1.3.5.1) or succinate dehydrogenase (quinone) couples the oxidation of succinate to fumarate (step 6 of the TCA) in the matrix, with the reduction of Q to QH_2 (ubiquinol) in the membrane. It is composed of four nDNA-encoded subunits: SDHA/SDH1 and SDHB/SDH2, the bigger and hydrophilic subunits, form the catalytic domain and contain the redox active centres (one covalently-bound FAD cofactor, in SDHA, and three Fe-S clusters, in SDHB); SDHC/SDH3 and SDHD/SDH4, the smaller and hydrophobic subunits, anchor the enzyme to the IMM and harbour two Q binding sites and a haem *b* group (Oyedotun and Lemire, 2001; Sun *et al.*, 2005). Although two H^+ are generated from the oxidation of succinate, two H^+ are needed for the reduction of Q to QH_2, therefore there is no net proton pumping into the IMS (Sun *et al.*, 2005; Oyedotun, Sit and Lemire, 2007).

CII assembly (**Figure 1.5**) takes place through the independent maturation of SDHA, SDHB and SDHC+SDHD mediated by subunit-specific chaperones (Van Vranken *et al.*, 2015). **SDHA** is flavinylated before assembly into CII, and SDHAF2/Sdh5 mediates this step (Hao *et al.*, 2009; Kim *et al.*, 2012). Following FAD incorporation, SDHA binds to SDHAF4/Sdh8, which keeps the subunit stable and competent for assembly with SDHB, while protecting it from auto-oxidation (Van Vranken *et al.*, 2014).

SDHB also incorporates its Fe-S clusters before joining the rest of the subunits. Fe-S clusters are synthesised in the mitochondrial matrix (Braymer and Lill, 2017; Rouault and Maio, 2017) and then transferred to the apoprotein. This step is mediated by SDHAF1, necessary also for SDHB stability (Ghezzi, Goffrini, *et al.*, 2009; Maio *et al.*, 2014, 2016). SDHAF3/ACN9/LYRM10 is another protein involved in SDHB stability and oxidative damage protection after insertion of the Fe-S clusters (Na *et al.*, 2014; Van Vranken *et al.*, 2015; Dwight *et al.*, 2017).

When both SDHA and SDHB acquire their respective prosthetic groups, they join together, liberating SDHAF4 but keeping the binding with SDHAF1 and SDHAF3 (Na *et al.*, 2014; Van Vranken *et al.*, 2015).

SDHC and **SDHD** are assembled together in the inner membrane by a yet unknown mechanism. The heme *b* group, coordinated in the interphase of both subunits, does not play any catalytic role but is required for their stability (Lemarie and Grimm, 2009; Kim *et al.*, 2013). Another factor that influences the dimerization of SDHC and SDHD, as well as their stability, is the presence of both hydrophilic subunits (Kim *et al.*, 2012; Na *et al.*, 2014).

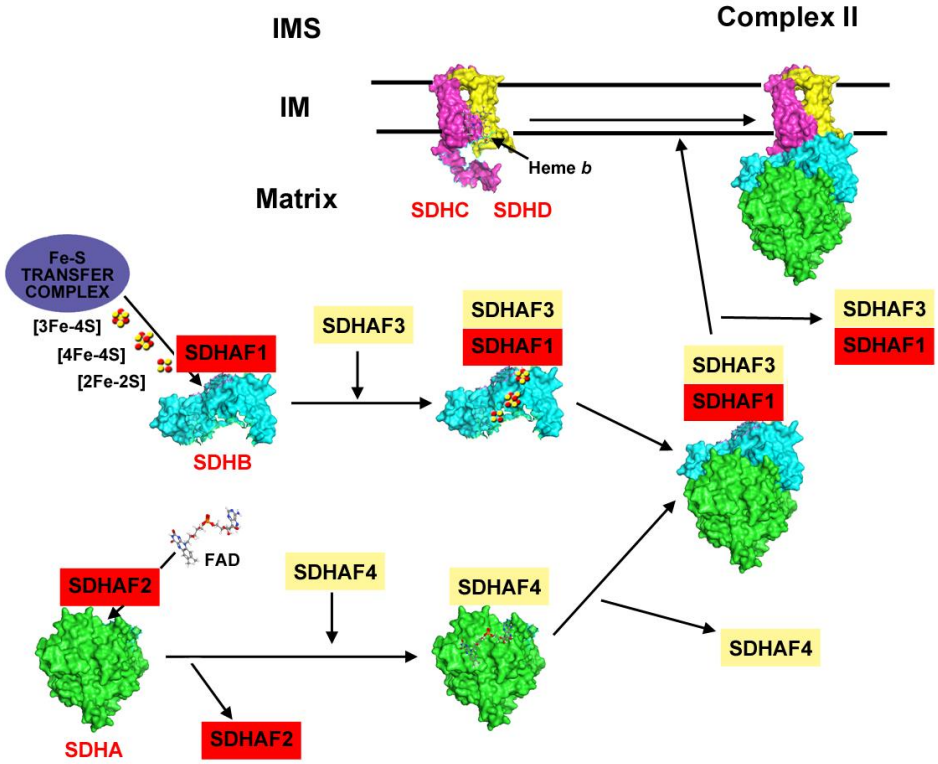

Figure 1.5 Complex II assembly model based on the porcine CII crystal structure with PDB ID: 1ZOY (Sun *et al.*, 2005) and the model proposed in reference (Van Vranken *et al.*, 2015). Red colour indicates proteins with described pathological mutations. See main text for details. Image extracted from (Signes and Fernandez-vizarra, 2018).

1.2.3 Complex III

Complex III (EC 1.10.2.2) or quinol- cytochrome-c reductase performs the electron transfer from QH_2 to cyt *c* coupled to proton pumping using the 'Q-cycle'

mechanism (Trumpower, 1990; Crofts *et al.*, 2008). Structurally, it is a tightly bound symmetrical dimer ($CIII_2$), being each 'monomer' composed of three catalytic core subunits (MT-CYB, CYC1 and UQCRFS1) and seven supernumerary subunits (Iwata *et al.*, 1998), which are not involved in the catalysis but are important for correct assembly and/or stability of the enzyme (Haut *et al.*, 2003; Barel *et al.*, 2008). The 78-amino acid mitochondrial targeting sequence (MTS) cleaved off from UQCRFS1 was considered an extra subunit (Brandt *et al.*, 1993; Iwata *et al.*, 1998), but it needs to be cleared out to maintain $CIII_2$ structural and functional fitness (Bottani *et al.*, 2017; Fernandez-Vizarra *et al.*, 2018). MT-CYB contains two b-type hemes with different redox potential as well as two Q binding sites. There is one [2Fe-2S] cluster inserted in the C-terminal of UQCRFS1, and CYC1 binds a heme c1 group that transfers the electrons to cyt *c*.

Yeast CIII assembly (**Figure 1.6**) starts with the synthesis of **cytochrome b** (MT-CYB in human nomenclature) by mitochondrial ribosomes and its insertion into the inner membrane, mediated by Cbp3/UQCC1 and Cbp6/UQCC2 that remain bound to MT-CYB once it is completely synthesised. Cbp4/UQCC3 joins after the first heme-*b* (b_L) but before the second one (b_H) is incorporated (Gruschke *et al.*, 2011, 2012; Hildenbeutel *et al.*, 2014). Once the first structural subunits (UQCRB and UQCRQ) are incorporated, UQCC1-UQCC2 detach and go back to act as translational activators (Gruschke *et al.*, 2011, 2012). These first steps in CIII assembly (Figure 3) are supposedly conserved, because the three factors are present in humans and mutations in *UQCC2* impair MT-CYB synthesis (Tucker *et al.*, 2013; Wanschers *et al.*, 2014).

Maturation of CIII occurs, both in yeast and humans, with the addition of the **Rieske Fe-S protein** (Rip1/UQCRFS1) and of the smallest subunit (Qcr10/UQCR11) to an already dimeric pre-complex III (pre-$CIII_2$) (Cruciat *et al.*, 1999; Fernandez-Vizarra *et al.*, 2007; Conte *et al.*, 2015). After import into mitochondria, UQCRFS1 is bound and stabilised in the matrix by MZM1L/LYRM7 (Atkinson *et al.*, 2011; Cui *et al.*, 2012; Sánchez *et al.*, 2013) that also mediates binding to the Fe-S cluster transfer complex (Maio *et al.*, 2017). Incorporation of UQCRFS1 to pre-$CIII_2$ is mediated by Bcs1/BCS1L (Cruciat *et al.*, 1999; De Lonlay *et al.*, 2001; Fernandez-Vizarra *et al.*, 2007; Wagener *et al.*, 2011). In human and mouse mitochondria, TTC19 (Ghezzi *et al.*, 2011) binds fully

assembled $CIII_2$ and favours the elimination of UQCRFS1 N-terminal fragments to maintain normal activity levels (Bottani *et al.*, 2017). The intermediate steps of $CIII_2$ assembly are not known in humans. However, being that the initial and the final stages are the same and the assembly factors involved are orthologous proteins, it is assumed that they will share very many similarities (Fernández-Vizarra and Zeviani, 2015). The order of incorporation in *S. cerevisiae* was determined by creating yeast strains missing one structural subunit at a time and studying the stability of the remaining CIII components (Zara, Conte and Trumpower, 2007, 2009b, 2009a). Up to now, there are no described assembly factors involved in the incorporation or stabilisation of $CIII_2$ intermediate subunits and transitional subcomplexes.

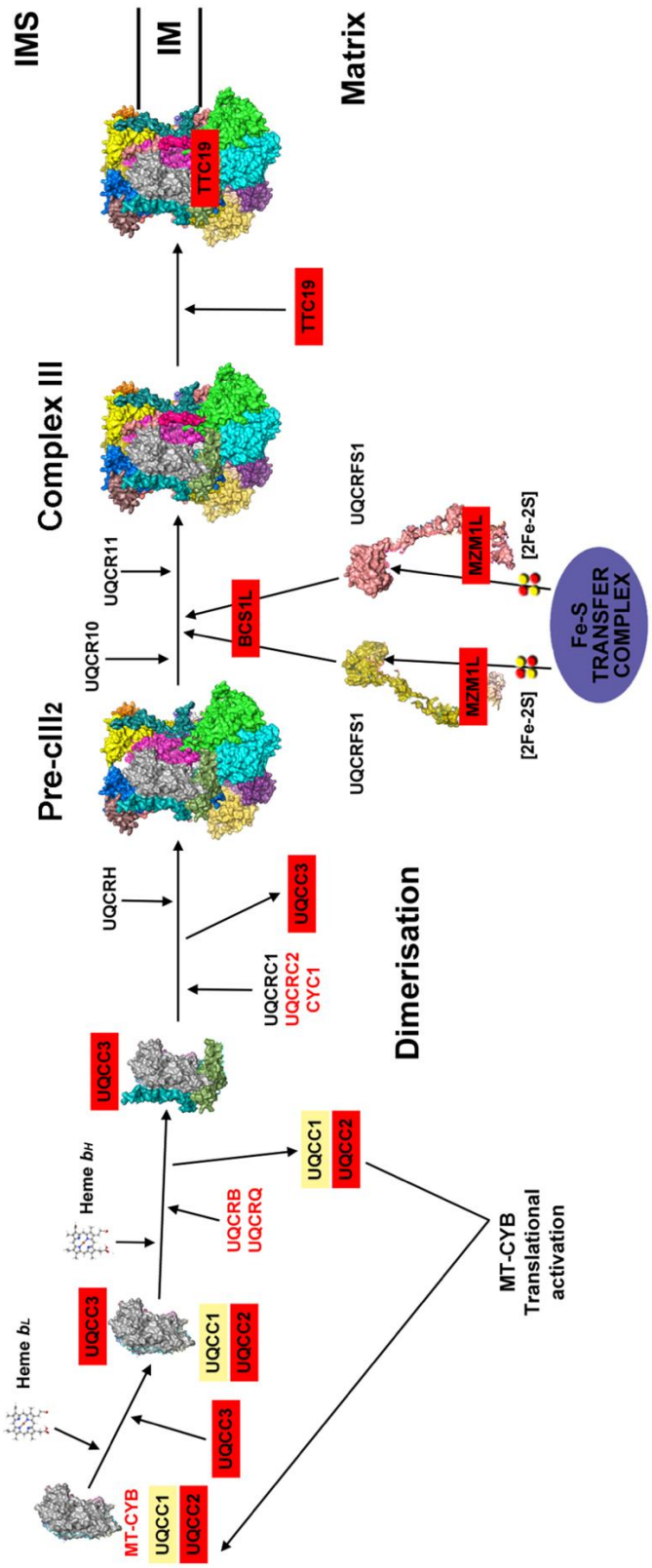

Figure 1.6 Complex III assembly model based on the bovine $CIII_2$ crystal structure with PDB ID: 1BGY (Iwata *et al.*, 1998) and the models proposed in references (Fernández-Vizarra and Zeviani, 2015; Fernandez-Vizarra *et al.*, 2018). Red colour indicates proteins with described pathological mutations. See main text for details. Image extracted from (Signes and Fernandez-Vizarra, 2018).

1.2.4 Complex IV

1.2.4.1 Complex IV function and regulation

Complex IV (EC 1.9.31) or COX catalyses the oxidation of cyt *c* and the reduction of O_2 to H_2O coupled to proton pumping across the IMM. Mammalian CIV from bovine heart was crystallised as a 13-subunit enzyme (Tsukihara T, Aoyama H, Yamashita E, Tomizaki T, Yamaguchi H, Shinzawa-Itoh K, Nakashima R, Yaono R, 1996; Yoshikawa, Shinzawa-Itoh and Tsukihara, 1998). However, recent studies have demonstrated that it contains another less tightly bound subunit, NDUFA4 (COXFA4), which was previously thought to be part of complex I (Balsa *et al.*, 2012; Pitceathly *et al.*, 2013; Pitceathly and Taanman, 2018). The three largest and highly hydrophobic subunits (MT-CO1, MT-CO2 and MT-CO3), encoded in the mtDNA, form the core of the enzyme. MT-CO1 harbours a haem *a* group and a binuclear haem a_3-Cu_B centre buried within the IMM, while MT-CO2 contains a Cu_A centre located in its globular domain facing the IMS (Fontanesi, Soto and Barrientos, 2008; Soto *et al.*, 2012; Dennerlein and Rehling, 2015). MT-CO3, although a structural part of the core, has no prosthetic groups and plays no direct catalytic role (Wikström, Krab and Sharma, 2018). The eleven 'supernumerary' subunits (COX4, COX5A, COX5B, COX6A, COX6B, COX6C, COX7A, COX7B, COX7C, COX8 and NDUFA4), encoded in the nDNA, are thought to be important for the stabilisation of the catalytic core and regulation of its activity (Arnold and Kadenbach, 1997; Arnold, Goglia and Kadenbach, 1998; Kadenbach and Arnold, 1999; Massa *et al.*, 2008; Daniela Fornuskova, Lukas Stiburek, Laszlo Wenchich, Kamila Vinsova, Hana Hansikova, 2010; Pitceathly *et al.*, 2013; Kadenbach, 2017). All these subunits contain hydrophobic transmembrane regions, except COX5A and COX5B that are on the matrix side and COX6B that is facing the IMS (Nijtmans *et al.*, 1998; Fontanesi, Soto and Barrientos, 2008). Electrons from reduced cyt *c* are transferred to the Cu_A, then to the haem *a* group and finally to the haem a_3-Cu_B. In the last step, O_2 is bound to haem a_3 and reduced to H_2O (Soto *et al.*, 2012). The free energy from each electron transfer is used to pump one H^+ across the IMM (called "pumped protons") and one H^+ from the matrix to the binuclear centre (called "substrate protons"). Four electrons are required for the reduction of one molecule of O_2,

which means that four “substrate protons” are taken from the matrix to synthesise two molecules of H_2O; and four “pumped protons” are translocated from the matrix to the IMS, contributing to the PMF (Michel, 1998; Lu and Gunner, 2014; Wikström, Krab and Sharma, 2018). Two channels are well known for the proton uptake from the mitochondrial matrix to the catalytic core, channel D and channel K, named after the conserved aspartate and lysine residues located at the beginning of the channel, at the matrix side (Lu and Gunner, 2014). However, the proton exit pathway from the binuclear centre to the IMS is not well understood yet.

Being the rate-limiting enzyme of the ETC, CIV is an OXPHOS key regulatory site, which is why its biogenesis and activity are subjected to a high level of regulation (Kadenbach, 2018). Indeed, CIV is the only OXPHOS complex in which several tissue-specific and oxygen-regulated isoforms have been found (Hüttemann, Kadenbach and Grossman, 2001; Sinkler *et al.*, 2017). In mammals, there are six subunits with tissue-specific isoforms: COX6A1/COX6A2, COX7A2/COX7A1, and COX8A(2)/COX8B(1) liver/heart-specific, COX4I2 is the main isoform in the lung (while COX4I1 is ubiquitously expressed) and COX6B2 and COX8C(3) are testis-specific. The heart-type isoforms are expressed in the heart and skeletal muscle, which are tissues with high energy demands. The liver-type subunits are expressed in brain, liver, kidney and other tissues (Sinkler *et al.*, 2017). Moreover, the hypoxia-inducible factor 1-alpha (HIF-1α), which senses and coordinates the cellular adaptive response to hypoxia by transcriptionally activating the expression of key genes, has been shown to also regulate the catalytic activity of COX in cultured cells under hypoxic conditions by inducing the expression of COX subunit isoforms COX4I2 and COX7A1 (Fukuda *et al.*, 2007; Hwang *et al.*, 2015).

In addition, COX activity seems to be also regulated by several allosteric inhibitors. Intramitochondrial ATP and ADP can bind COX4I1 subunit and change the hyperbolic COX kinetics into sigmoidal, i.e. inhibit CIV activity, at high ATP/ADP-ratios (Follman *et al.*, 1998; Arnold and Kadenbach, 1999). The thyroid hormone 3,5 diiodothyronine (T2) has been shown to directly bind to subunit COX5A and abrogate ATP mediated allosteric inhibition, activating CIV activity in response to hormonal stimulation (Arnold, Goglia and Kadenbach, 1998). On the other hand, calcium can bind a special cation binding site located in MT-CO1,

and inhibit CIV activity by 50–80%, which has been proposed to modulate Ca^{2+} mitochondrial uptake (Gellerich *et al.*, 2010; Vygodina *et al.*, 2017). Additionally, four different gases, nitric oxide (NO), carbon monoxide (CO), hydrogen sulphide (H_2S) and hydrogen cyanide (HCN) have been found able to bind CIV and inhibit its activity. The physiological significance of this regulation has been reviewed somewhere else (Cooper and Brown, 2008).

Finally, the activity of CIV can be regulated by chemical modifications via phosphorylation and/or acetylation of nuclear-encoded subunits (Bender and Kadenbach, 2000; Liko *et al.*, 2016; Potthast *et al.*, 2017)**.** Between 14 and 18 phosphorylation sites have been identified so far in CIV, although only a few have been characterised functionally (Klement *et al.*, 1995; Fang *et al.*, 2007; Hüttemann *et al.*, 2007; Zhao *et al.*, 2011; Mahapatra *et al.*, 2017). For example, the allosteric ATP-inhibition of COX4I1 seems to be reversibly switched on and off by phosphorylation (Bender and Kadenbach, 2000). In addition, MS analysis identified acetylation modifications in subunits COX5B and COX4I1 (Choudhary *et al.*, 2009). However, the physiological significance of these modifications remains unknown.

1.2.4.2 Assembly of complex IV

The first model for human COX assembly was proposed by studying the incorporation dynamics of the different CIV subunits after inhibition of mitochondrial translation in cultured cells (Nijtmans *et al.*, 1998). This model proposed a linear process starting with MT-CO1 as the ‘seed’ around which the rest of the subunits build up, being COX4 and COX5A the first ones to join. The stable subassemblies created during the process were named S1 to S4, being S4 the fully assembled COX (Fernández-Vizarra, Tiranti and Zeviani, 2009). This view of the process basically still stands but more recent data have allowed to refine the model (Stiburek *et al.*, 2005, 2006; Massa *et al.*, 2008; Timón-Gómez *et al.*, 2017; Vidoni *et al.*, 2017). In particular, the proteomic identification of the subassemblies accumulated in a *MT-CO3* mutant cybrid cell line helped to complete the view about COX subunit incorporation in humans, which takes place

in groups or “modules” that are defined by each of the three core subunits (**Figure 1.7**) (Vidoni *et al.*, 2017).

COX biogenesis has also been extensively studied in respiratory-deficient mutants of the yeast *S. cerevisiae*, which has been fundamental for the understanding of COX biogenesis both in yeast and in mammals, including the synthesis and incorporation of prosthetic groups and the function of many of the assembly factors involved (Tzagoloff and Dieckmann, 1990; Barrientos, 2003; Fontanesi *et al.*, 2006). However, it has become evident that there are some differences among species, such as the existence of assembly factors in higher animals that are not present in yeast (Mootha *et al.*, 2003; Weraarpachai *et al.*, 2009; Melchionda *et al.*, 2014; Vidoni *et al.*, 2017). The study of COX assembly defects in mouse disease models and in patient-derived cell lines is helping to identify mammal-specific assembly factors (Fernández-Vizarra, Tiranti and Zeviani, 2009). In particular, in Chapter 3 I will describe the analyses that led to the identification of a new COX assembly factor, MR-1S, which is only present in vertebrates, and in Chapter 4 and 5 I will present the characterisation of APOPT1, a COX assembly factor, conserved only in animals.

1.2.4.2.1 Initial assembly

According to the modified COX assembly pathway (**Figure 1.7**), the initial COX subunits to assemble appear to be COX4I1+COX5A (Vidoni *et al.*, 2017). HIGD1A, one of the human homologues of yeast Rcf1 (Hayashi *et al.*, 2015; Lundin *et al.*, 2016) is also part of this early group of proteins (Vidoni *et al.*, 2017).

1.2.4.2.2 Assembly of the MT-CO1 module

The MT-CO1 module contains the many chaperones and assembly factors involved in its maturation and stabilisation. It has also been denominated “MITRAC” for mitochondrial translation regulation assembly intermediate of cytochrome c oxidase (Mick *et al.*, 2012; Dennerlein *et al.*, 2015). COX14/C12ORF62 (Szklarczyk *et al.*, 2012; Weraarpachai *et al.*, 2012) and

COA3/CCDC56/MITRAC12 (Mick *et al.*, 2012; Richter-Dennerlein *et al.*, 2016) bind nascent MT-CO1 and probably mediate its insertion into the IMM. It has been suggested that they are implicated in assembly regulation either by translational (Richter-Dennerlein *et al.*, 2016) or post-translational mechanisms (Bourens and Barrientos, 2017a). In human mitochondria, MT-CO1 expression is especially sensitive to defects in the mitochondrial RNA-binding protein LRPPRC (Mootha *et al.*, 2003; XU *et al.*, 2004; Ruzzenente *et al.*, 2012) and requires the specific translational activator TACO1 (Weraarpachai *et al.*, 2009; Richman *et al.*, 2016). Later on, CMC1, a twin CX_9C protein, interacts and stabilises the early MT-CO1+COA3+COX14 complex (before or during addition of the prosthetic groups) (Bourens and Barrientos, 2017a). Once in the membrane, heme *a* can be added, which is synthesized in the mitochondria in two steps: heme *b* conversion to heme *o* and heme *o* conversion to heme *a*, catalysed by the IMM enzymes COX10 (Antonicka, Leary, *et al.*, 2003; Diaz *et al.*, 2005) and COX15 (Antonicka, Mattman, *et al.*, 2003), respectively. However, the mechanism of heme *a* delivery to MT-CO1 is not clear yet. It has been suggested that COX15 could directly transfer it to MT-CO1 with the help of PET117, which has been shown to interact with COX15 in yeast and may promote its oligomerisation (Taylor *et al.*, 2017). Another protein, SURF1 (Tiranti *et al.*, 1998; Zhu *et al.*, 1998), has also been proposed to be involved in heme *a* delivery (Timón-Gómez *et al.*, 2017), although its exact molecular function is still not clear. Cu_B assembly requires the metallochaperone COX11 (Hiser *et al.*, 2000; Banci *et al.*, 2004), which is bound to the IMM and has a domain facing the IMS which contains two cysteines involved in copper binding and a third involved in copper delivery to MT-CO1. The assembly of Cu_B is assumed to be similar in yeast and humans due to the highly conserved proteins involved. COX19 (Bode *et al.*, 2015), an IMS copper-binding protein with a twin CX_9C motif, keeps the third cysteine of COX11 reduced, but it does not participate in copper delivery to COX11, which is done by COX17 (Glerum, Shtanko and Tzagoloff, 1996; Cobine, Pierrel and Winge, 2006), another IMS with a twin CX_9C motif that overlaps with a CCXC copper-binding motif. However, it is still not totally clear how copper enters the mitochondria and reaches COX17 (Zischka and Einer, 2018). CMC1 is released prior to the addition of COA1/C7ORF44/MITRAC15 (Pierrel *et al.*, 2007; Mick *et al.*, 2012; Szklarczyk *et al.*, 2012) and SURF1. MITRAC7/SMIM20 was proposed to stabilise MT-CO1

bound to COX4I1+COX5A before addition of any other subunits (Dennerlein *et al.*, 2015).

1.2.4.2.3 MT-CO2 module

The intermediate step in COX assembly is the joining of COX4I1+COX5A, MT-CO1 with the **MT-CO2 module** (MT-CO2+COX5B+COX6C+COX7C+COX8A and, most probably COX7B), corresponding to the 'S3' intermediary (Nijtmans *et al.*, 1998) without MT-CO3 (Vidoni *et al.*, 2017). MT-CO2 requires COX18 for membrane translocation of its globular domain (Bourens and Barrientos, 2017b) and COX20/FAM36A (Szklarczyk *et al.*, 2013; Bourens *et al.*, 2014) for stabilisation. Copper-binding proteins COX17, SCO1 and SCO2 (Leary *et al.*, 2004, 2007, 2009) together with COA6 (Pacheu-Grau *et al.*, 2015; Stroud *et al.*, 2015; Ghosh *et al.*, 2016) and COX16 (Abhishek Aich, Cong Wang, Arpita Chowdhury, Christin Ronsör, Pacheu-Grau1, Ricarda Richter-Dennerlein and Rehling, 1978; Carlson *et al.*, 2003; Cerqua *et al.*, 2018), are involved in the assembly of the Cu_A centre, which occurs in the IMS. COX18 is released during or after SCO1 joins the complex, but definitely before SCO2 and COA6 are bound (Bourens and Barrientos, 2017b). The assembly of Cu_A must happen before binding to the MT-CO1 module, as MT-CO2 and MT-CO1 are tightly and strongly bound, impeding the accessibility to the Cu_A site (Soto *et al.*, 2012). The IMS COX17 protein transfers copper to both SCO1 and SCO2, which are bound to the IMM and have a globular domain in the IMS where the CX_3C motif involved in copper binding and delivery is located (Glerum, Shtanko and Tzagoloff, 1996; Leary *et al.*, 2004). Then, both SCO proteins physically interact with COA6, an IMS soluble protein with a CX_9C-$CX_{10}C$ domain, and form a metallochaperone module that binds to the COX20-MT-CO2 complex to assemble the Cu_A site (Bourens and Barrientos, 2017b). COX16, also seems to interact with MT-CO2, the SCO proteins and COA6. However, it was also found interacting with the MT-CO1 module, suggesting that it could be involved in the joining of the MT-CO1 and MT-CO2 modules (Aich *et al.*, 2018). MR-1S has been found to interact with the highly conserved factors PET100 (Church *et al.*, 2005; Lim *et al.*, 2014; Oláhová *et al.*, 2015) and PET117

(McEwen *et al.*, 1993; Renkema *et al.*, 2017) during the assembly of the MT-CO2 module (Vidoni *et al.*, 2017).

1.2.4.2.4 MT-CO3 module

The incorporation of the **MT-CO3 module** (MT-CO3+COX6A1+COX6B1+COX7A2) completes the assembly of the thirteen canonical COX subunits (Vidoni *et al.*, 2017). No specific assembly factors for this module are currently known.

The **last subunit** to be incorporated is NDUFA4, previously thought to be part of complex I (Carroll *et al.*, 2006) but recently assigned to complex IV (Balsa *et al.*, 2012; Pitceathly *et al.*, 2013).

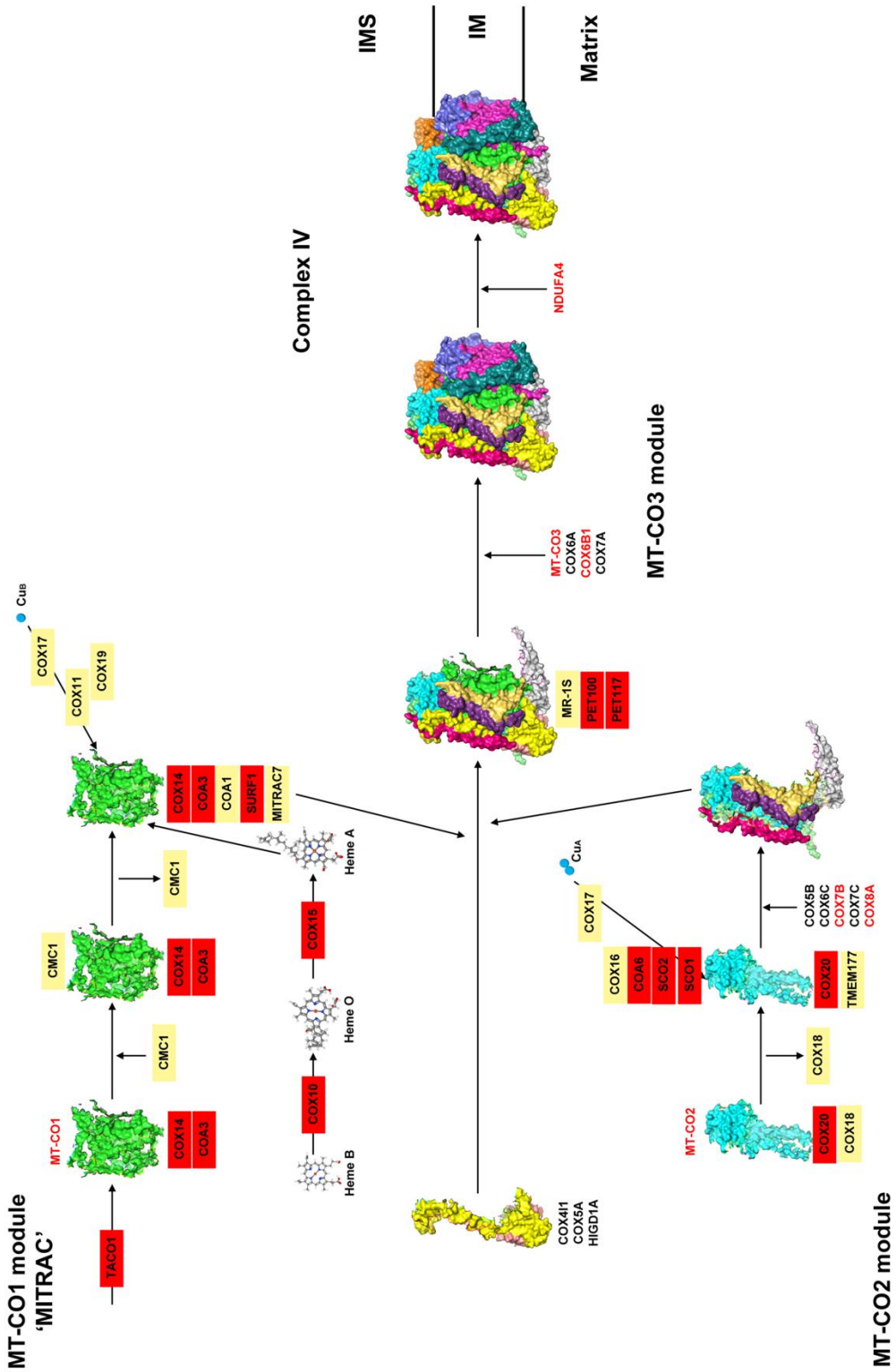

Figure 1.7 Complex IV assembly model based on the bovine CIV crystal structure with PDB ID: 2OCC (Yoshikawa, Shinzawa-Itoh and Tsukihara, 1998) and the model proposed in reference (Vidoni *et al.*, 2017). Red colour indicates proteins with described pathological mutations. See main text for details. Image extracted from (Signes and Fernandez-Vizarra, 2018).

1.2.5 Complex V

Complex V (EC 3.6.14), H^+-transporting two-sector ATPase or F_oF_1-ATPase, is the enzyme that synthesises ATP using the proton-motive force generated by CI, III and IV. It is composed of two topological and functional distinct domains: membrane-extrinsic and matrix-facing F_1 plus membrane-intrinsic F_o, with a central axis and a peripheral stalk connecting them (Carroll *et al.*, 2006). Subunits a (MT-ATP6) and A6L (MT-ATP8) of the F_o domain are encoded in the mtDNA and seem to be crucial for the stabilization of CV di- and oligomers, whereas all the rest of CV components are nDNA-encoded (Walker, 2013). When H^+ from the IMS pass through the F_0 region driven by the PMF, it undergoes conformational changes that cause the rotation of the central axis causing the catalytic sites at the F1 portion to switch cooperatively through conformations in which ADP and Pi bind and ATP is formed (Stock *et al.*, 2000).

Assembly of CV has been studied using subunit incorporation dynamics (Watt *et al.*, 2010), analysis of mtDNA-deficient cell lines (Nijtmans *et al.*, 1995; Carrozzo *et al.*, 2006) and more recently by creating KO cell lines for specific CV subunits (Wittig *et al.*, 2010; Fujikawa *et al.*, 2015; He, Carroll, *et al.*, 2017; He, Ford, *et al.*, 2017). As depicted in **Figure 1.8**, this complex is also put together by assembling three pre-formed modules corresponding to: F_1 particle, c_8-ring (a ring composed by eight copies of the c-subunit) and peripheral stalk (Walker, 2013).

The **F_1 subcomplex**, composed of three copies of the α subunit/ATP5A1, three β subunits/ATP5B together with the central stalk subunits γ/ATP5C1, δ/ATP5D and ε/ATP5E, is assembled with the assistance of chaperones ATPAF1/ATP11 and ATPAF2/ATP12, which bind ATP5B and ATP5A1, respectively (Ackerman and Tzagoloff, 1990; Wang and Ackerman, 2000; Wang *et al.*, 2000; Wang, White and Ackerman, 2001; He *et al.*, 2018). The **c_8-ring**, encoded by *ATPG1*, *ATPG2* and *ATPG3*, is assembled in the membrane by still unknown mechanisms (Walker, 2013). A subcomplex containing subunits of the **peripheral stalk** is also pre-formed (Wittig *et al.*, 2010; Fujikawa *et al.*, 2015; He, Carroll, *et al.*, 2017; He, Ford, *et al.*, 2017).

After the c_8-ring and the F_1 subcomplex come together, the peripheral stalk is incorporated in two steps: first subunits b/ATP5F1, d/ATPH, F_6/ATP5J and

OSCP/ATP5O and then e/ATP5I, g/ATP5L and f/ATPJ2 (Walker, 2013; He, Ford, *et al.*, 2017). The peripheral stalk can also join the F_1 subcomplex in absence of the c_8-ring (He, Carroll, *et al.*, 2017; He, Ford, *et al.*, 2017). During these initial steps, the inhibitor protein IF_1 is bound to the intermediates, being liberated with the insertion of the two mtDNA-encoded subunits (Fujikawa *et al.*, 2015; He, Carroll, *et al.*, 2017; He, Ford, *et al.*, 2017). In the cases in which a/MT-ATP6 and A6L/MT-ATP8 are missing, the previous assembly intermediate is readily accumulated (Carrozzo *et al.*, 2006; Watt *et al.*, 2010; He, Carroll, *et al.*, 2017). The interaction of the last subunits is stabilised by 6.8L/MLQ/C14ORF2 and the peripheral subunit DAPIT/USMG5 is incorporated to finish CV assembly (He, Ford, *et al.*, 2017).

One of the few proteins known to be involved in CV biogenesis is TMEM70 and although its exact function is still not known, mutations in the gene encoding this factor have consistently been associated to ATP synthase deficiency (De Meirleir *et al.*, 2004; Magner *et al.*, 2015).

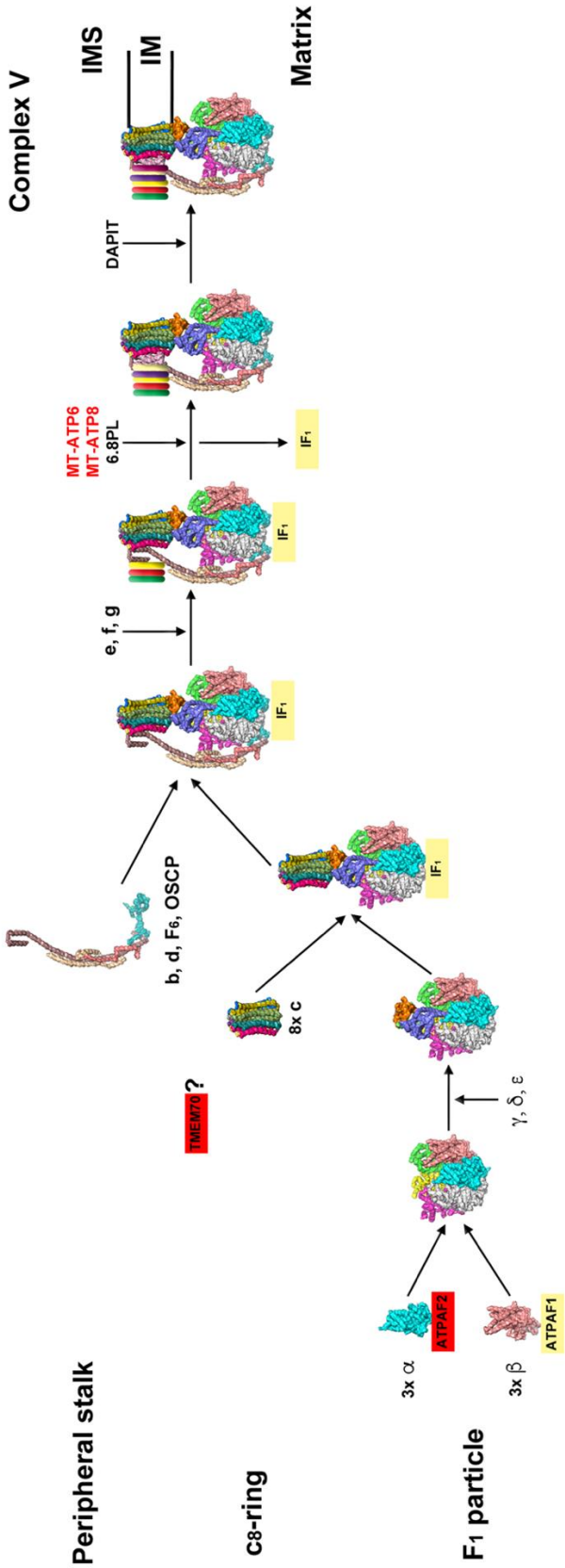

Figure 1.8 Complex V assembly model based on the bovine CV cryo-EM structure with PDB ID: 5ARA (Zhou *et al.*, 2015) and the model proposed in references (Jonckheere, Smeitink and Rodenburg, 2012; He *et al.*, 2018). Red colour indicates proteins with described pathological mutations. See main text for details. Image extracted from (Signes and Fernandez-vizarra, 2018).

1.2.6 Supercomplexes

The development of the BN-PAGE techniques, i.e. mitochondrial extracts solubilised with the mild detergent digitonin and separated through native electrophoresis (Schägger, 2002; Acín-Pérez *et al.*, 2008), granted a better understanding of the mitochondrial respiratory chain organisation by allowing the separation and detection of both the individual complexes and the supercomplexes (associations of complexes I, III and IV). According to their molecular size and subunit composition, the main supercomplexes have been assigned the following stoichiometries: III_2IV_1, I_1III_2, $I_1III_2IV_1$ defined as the "respirasome", and $I_2III_2IV_1$ named as "respiratory megacomplex" (Mourier *et al.*, 2014). Additionally, complexes IV and V can form dimers and oligomers (Schägger, 2002; Wittig and Schägger, 2008; Mourier *et al.*, 2014). The interactions between the complexes have been extensively validated (Dudkina *et al.*, 2005; Acín-Pérez *et al.*, 2008; Davies, Blum and Kühlbrandt, 2018) and high-resolution Cryo-EM structures of the respirasome of several mammalian species, including human, have already been resolved (Mourier *et al.*, 2014; Gu *et al.*, 2016; Letts, Fiedorczuk and Sazanov, 2016; Wu *et al.*, 2016; Guo *et al.*, 2017). The functional relevance of CV associations seems to be related with enzyme stabilisation and cristae morphology definition (Strauss *et al.*, 2008; Davies *et al.*, 2011). However, the functional implications of the existence of the supercomplexes remain unclear and several alternative views have been proposed to explain it. The first possibility is that they are necessary for 'substrate channelling', i.e. their association allows the formation of enclosed pools of Q and cyt *c* leading to an increased electron transfer efficiency (Acín-Pérez *et al.*, 2008; Lapuente-Brun *et al.*, 2013). In addition, the "plasticity model" proposes that the complexes associate and disassociate constantly to adapt to varying energy demands, which implies the complete formation of each of the individual complexes before they associate into the supercomplexes (Acín-Pérez *et al.*, 2008; Lapuente-Brun *et al.*, 2013). However, substrate channelling is not supported by kinetic data (Trouillard, Meunier and Rappaport, 2011; Blaza *et al.*, 2014; Fedor and Hirst, 2018) and some evidence in the literature point out to subunits from different complexes co-assembling before completion of the single enzymes (Fernández-Vizarra, Tiranti and Zeviani, 2009). Maturation of CI has

been proposed to happen after $CIII_2$ and CIV are bound to a 'pre-CI' scaffold (Moreno-Lastres et al., 2012), although recent assembly kinetic studies using complexome profiling with BN-PAGE suggest that CI is fully assembled independently of the supercomplex scaffold (Guerrero-Castillo *et al.*, 2017). Interestingly, the same report describes how COA1, a well characterised CIV chaperone is bound to CI assembly intermediates (Guerrero-Castillo *et al.*, 2017), which could reflect co-assembly of at least CI and CIV. Another hypothesis that has been proposed to explain the existence of the supercomplexes is that they could minimise ROS (reactive oxygen species) production, as measurements in bovine heart showed that disruption of the I_1III_2 supercomplex leads to increased superoxide formation from CI (Maranzana *et al.*, 2013). Moreover, studies in neurons and astrocytes showed a correlation between ROS production and the levels of CI associated into supercomplexes (Lopez-Fabuel *et al.*, 2016). Lastly, it has been suggested that supercomplexes could prevent aggregations among the individual complexes, which are likely to happen due to the high protein density of the IMM (Flescher, Klouwen and Brierley, 1961). This theory suggests that some of the supernumerary subunits may exist to protect the core of the enzymes from deleterious interactions and that those promoting the formation of supercomplexes may have been selected to this scope (Milenkovic *et al.*, 2017). More studies are clearly necessary to fully understand the physiological role of supercomplexes.

Regarding assembly factors that regulate the formation of these associations, the factors 1, 2 and 3 (Rcf1, Rcf2 and Rcf3) were proposed as supercomplex assembly factors in yeast (Chen *et al.*, 2012; Strogolova *et al.*, 2012; Vukotic *et al.*, 2012). However, they are also needed for CIV assembly (Vukotic *et al.*, 2012) and knocking down their expression led to a decrease of CIV activity (Lundin *et al.*, 2016), suggesting that their effect on supercomplex formation might be indirect. HIGD1A and HIGD2A are the mammalian orthologs of Rcf1. HIGD1A has been found to interact with early assembly intermediates of CIV (Vidoni *et al.*, 2017) and knocking down its expression did not affect supercomplex formation (Hayashi *et al.*, 2015). HIGD2A knock down actually led to a depletion of III_2IV_1, suggesting a true and direct role in supercomplex stabilisation (Chen *et al.*, 2012). On the other hand, COX7A2L or SCAFI (supercomplex assembly factor 1), an orthologue of the CIV structural subunit

COX7A, was described as a supercomplex assembly factor in mammals because was deemed to be necessary for the incorporation of CIV into supercomplex structures (Sousa *et al.*, 2016). However, more recent evidence has demonstrated a role for this protein in the formation of III_2IV_1 but not in the incorporation of CIV into the respirasomes (Mourier *et al.*, 2014; Pérez-Pérez *et al.*, 2016; Williams *et al.*, 2016). The dynamic interchange between the three isoforms of COX7A proteins (COX7A2L/SCAFI, COX7A1 and COX7A2) could potentially determine whether CIV stays as a monomer, oligomerises or forms the III_2IV_1 supercomplex, as well as the mode of binding to CI (Cogliati *et al.*, 2016). In any case, the recently resolved structures of the supercomplexes did not reveal the presence of any of these proteins bound to the supercomplexes (Gu *et al.*, 2016; Letts, Fiedorczuk and Sazanov, 2016; Wu *et al.*, 2016).

1.3 Mitochondrial diseases

Mitochondrial diseases are a group of genetic disorders caused by dysfunctional OXPHOS. Although they are considered rare diseases, as a whole these disorders are the most frequent inborn errors of metabolism, affecting at least 1 in 5,000 live births (Schiff *et al.*, 2012; Chinnery and Hudson, 2013). The pathophysiology of mitochondrial diseases is very complex as these disorders are highly heterogenous, both genetically and clinically (Gorman *et al.*, 2016).

From the genetic point of view, the origin can be due to mutations in either nuclear genes, showing mendelian inheritance, or in the mitochodrial genome, and therefore inherited maternally (Craven *et al.*, 2017). Some rare cases of diseases caused by *de novo* mutations in either mtDNA or nDNA genes have also been found (Gorman *et al.*, 2016). In patients with mutations in the mitochondrial genome, the inheritance and clinical phenotype is further complicated by the existance of many mtDNA copies in the same cell (Stewart and Chinnery, 2015). All these copies are usually identical, a situation referred to as homoplasmy. However, errors occurring during mtDNA replication or repair, can generate mutated mtDNA molecules, which can clonally expand and coexist with WT copies. This condition is known as heteroplasmy and the proportion

between mutated and WT mtDNA molecules can be variable. Cells can tolerate mutations in the mitochondrial genome up to a critical threshold, which is typically ≈70%, although this depends on the type of cell and mutation. Percentages of heteroplasmy above the threshold result in respiratory deficiency and manifestation of the mitochondrial disease phenotype (Stewart and Chinnery, 2015; Gorman *et al.*, 2016). Moreover, different levels of heteroplasmy of the same mtDNA mutation result in different phenotypes. Currently, more than 250 pathogenic mtDNA mutations have been identified (Mito-MAP database, www.mitomap.org) and can be classified as: large-scale rearrangements (i.e. partial deletions or duplications), that are usually sporadic; and point mutations, that are usually maternally inherited (Gorman *et al.*, 2016; Viscomi and Zeviani, 2017).

Mitochondrial disorders can also be caused by mutations in any of the more than 1500 nuclear genes encoding the mitochondrial proteome (Calvo and Mootha, 2010), which can be classified as: genes encoding structural subunits or assembly factors of complexes I-V (Smeitink, Heuvel and Dimauro, 2001; Ghezzi and Zeviani, 2018), proteins responsible for mtDNA maintenance (Viscomi and Zeviani, 2017), factors involved in mitochondrial protein synthesis (Jacobs, 2003; Rötig, 2011) or mitochondrial proteins involved in other processes, such as mitochondrial dynamics (Suárez-Rivero *et al.*, 2016), biosynthesis of lipids and cofactors (Aufschnaiter, Kohler, Diessl and Peselj, 2017), etc. In the last decades, genetic testing by using Sanger's sequencing technology only allowed to test a few candidate genes, providing limited success and leaving many patients without genetic diagnosis (Carroll *et al.*, 2014). Sanger sequencing is still used in laboratories to determine the sequence of short DNA fragments, however, sequencing the whole genome of a person by this method would take years. The development of next-generation sequencing (NGS) technlogies has revolutionised the diagnosis of genetic disorders by allowing high-throughput DNA sequencing and analysis of huge amounts of data, while reducing the costs (Henson, Tischler and Ning, 2014). This method is now frequently used in healthcare and research increasing the diagnostic yield in mitochondrial disorders and the identification of new disease genes (Craven *et al.*, 2017; Stenton and Prokisch, 2018). Whole exome sequencing, which analyses only the exons (around 1.6 % of the total genome) allows the identification of pathogenic

variants in the protein-coding region of any gene, which is the most common case (85%). On the other hand, whole genome sequencing, which extends the analysis to the whole genome, is helpful to detect variations outside the exons that the whole exome sequencing would miss (Craven *et al.*, 2017).

From the clinical point of view, mitochondrial diseases are characterised by a wide range of symptoms, severity, age of onset and outcome (Koopman *et al.*, 2012; Gorman *et al.*, 2016). This high heterogenity makes the diagnosis very difficult, relying on the identification of common clinical, biochemical and morphological features (Craven *et al.*, 2017). Although any organ or tissue may be affected, typically those with a high metabolic demand, such as the central nervous system (CNS) and the skeletal and cardiac muscle, are the most affected (Gorman *et al.*, 2016). Common clinical presentations in these patients are encephalopathy and myopathy, although ophthalmoplegia, blindness, deafness and diabetes are also very usual. Patients with late-onset mitochondrial disease usually display myopathy associated with variable involment of the CNS, while in early childhood the most common presentation is Leigh syndrome (LS) characterised by severe phsychomotor delay, cerebellar and pyramidal signs, dystonia, seizures, respiratory abnormalities, incoordination of ocular movements and recurrent vomiting (Gorman *et al.*, 2016). Imaging studies, such as computed tomography (CT), magnetic resonance imaging (MRI), proton and phosphorus MR-spectroscopy (MRS) and positron emission tomography (PET), of the most common affected tissues are very useful for the diagnosis (Finsterer and Zarrouk-Mahjoub, 2018). Regarding classic biochemical features, deficiency in one or more OXPHOS complexes is commonly found in mitochondrial disease patients. These enzymatic deficiencies can be detected histo- and biochemically in tissue biopsies or in patient-derived cultured cells. Then, molecular analyses, such as Western blot and BN-PAGE, help to determine the abundance and assembly of each of the OXPHOS complexes and of the supercomplexes. However, these biochemical and molecular hallmarks may not be found when other errors of metabolism, such as heme synthesis or TCA cycle, or the accumulation of toxic substances (Di Meo, Lamperti and Tiranti, 2015) are causing the disease. Another common biochemical feature is the increase in lactic acid levels in blood and/or cerebrospinal fluid, caused by the block of pyruvate aerobic oxidation, and, as a consequence, reduction of pyruvate to lactate by utilising the reduced NADH

formed during glycolysis. Lactate is released into body fluids, and may determine severe metabolic acidosis (Gorman *et al.*, 2016; Finsterer and Zarrouk-Mahjoub, 2018). Regarding morphological alterations, the “ragged-red” transformation of scattered muscle segments (ragged-red fibers, RRF) due to the accumulation of abnormal mitochondria under the sarcolemmal membrane, is very common in adult mitochondrial disease patients (Finsterer and Zarrouk-Mahjoub, 2018).

1.3.1 Disease models and therapies

The conservation of many mitochondrial pathways in higher organisms, such as the fruit fly (*Drosophila melanogaster*), worm (*Caenorhabditis elegans*), zebrafish (*Danio rerio*) and mouse (M*us musculus*), makes recombinant organisms, generated by genetic manipulation, important tools to study the molecular basis of mitochondrial disorders (Nightingale *et al.*, 2016). The clinical phenotypes shown by the deficient animal models do not always phenocopy the human disease, although they tend to be less heterogeneous than those found in humans with mitochondrial disorders (Huttemann, Kadenbach and Grossman, 2001; Spinazzola et al., 2006; Dell’Agnello et al., 2007). The use of clonally-selected animals, which eliminates the impact of the genetic background, and the genetic modification of only one or a few targeted organs/tissues, which eliminates the implication of other organs of the body, may explain this phenomenon (Smeitink, Heuvel and Dimauro, 2001; El-khoury *et al.*, 2010).

1.3.1.1 Generation of KO mouse models using the CRISPR/Cas system

The CRISPR/Cas system is an RNA-based immunological defense mechanism present in bacteria that recognises and degrades foreign DNA from invading viruses and plasmids (Garneau *et al.*, 2010). The bacterial CRISPR locus contains clustered, regularly interspaced, short, palindromic repeats (hence the name), or spacers, each of which derives from nucleic acid of different viruses and plasmids that attacked the cell in the past. When bacteria need to defend, the Cas protein is expressed and the spacer matching with the invading virus or

plasmids is transcribed from the CRISPR locus. The spacer then guides the Cas protein to the invading nucleic acid, which is cleaved and degraded. Feng Zhang et al established the protocol to make this system function in mammalian cells in order to modify specific genomic regions (Cong *et al.*, 2013). The system requires two elements to be injected in the cell, a CRISPR-associated endonuclease (Cas protein) and a short synthetic RNA (guide RNA, gRNA). The gRNA contains a scaffold sequence, necessary for Cas binding, and a spacer, which is a user-defined 20-nucleotide sequence that determines the target genomic region where the Cas protein will cut. In addition to the gRNA, the Cas protein also requires the presence of a 3-nucleotide sequence, called PAM, immediately at the 3′ end of the targeted DNA site (but must not be included in the synthetic gRNA construct) (Rath *et al.*, 2015). The PAM sequence depends on the type of Cas protein used (reviewed in (Rath *et al.*, 2015). When both elements (gRNA and Cas) are injected as RNAs in a cell, the Cas RNA is translated into a protein and interacts with the scaffold of the gRNA to form a ribonucleoprotein (cas9:gRNA complex), which produces a conformational change on the Cas9 allowing the spacer to start binding to the target DNA. Upon target binding and PAM recognition, the Cas enzyme undergoes a second structural change that allows its nuclease domain to make a double-strand break in the target DNA, ~3-4 nucleotides upstream of the PAM sequence. The gaps can then be repaired by the less efficient but high-fidelity homology directed repair (HDR) pathway or, much more commonly, by the efficient but error-prone non-homologous end joining (NHEJ) pathway. The last one, frequently causes small nucleotide insertions or deletions (indel) that result in amino acid deletions, insertions or frameshift mutations, many of them likely to be loss-of-function mutations (Rath *et al.*, 2015). This strategy was used to generate an *Apopt1* knock out mouse model (see Chapter 4).

1.3.1.2 Mitochondrial treatments and therapies

Despite the great advances made by using genetically modified models, a universal and effective therapy has not yet been found. However, some interesting and promising strategies, have been developed, aiming to compensate the alterations that play major roles in the pathogenesis of these

disorders, such as decreased levels of ATP or increased ROS (Garone and Viscomi, 2018):

- Increasing autophagy: rapamycin is an inhibitor of mTOR, a protein with a central role in many cellular processes, such as protein translation, glucose metabolism, autophagy, etc (Saxton and Sabatini, 2018). Administration of rapamycin has been successful in the treatment of mitochondrial diseases in fly and mice (Johnson *et al.*, 2013; Wang *et al.*, 2016; Felici *et al.*, 2017; Civiletto *et al.*, 2018), most likely by inhibiting translation, which would reduce the energy demand, and by activating autophagy, which would eliminate dysfunctional mitochondria (Peng *et al.*, 2015; Civiletto *et al.*, 2018).

- Decreasing ROS: antioxidants are routinely used in the therapy of mitochondrial diseases with the aim of decreasing the potentially damaging high levels of ROS consequence of respiratory chain dysfunction (Enns, 2014). Recently, a new clinical-stage drug, named KH176, has been shown to effectively reduce increased cellular ROS levels and protect OXPHOS-deficient human cells against redox perturbation by targeting the thioredoxin/peroxiredoxin system (Beyrath *et al.*, 2018). However, the use of antioxidants should be carefully considered in patients as ROS may act as signalling compounds sustaining mitochondrial biogenesis (Moreno-Loshuertos *et al.*, 2006; Dogan *et al.*, 2018).

- Increasing mitochondrial biogenesis: increasing mitochondrial mass and/or activity aiming to compensate the bioenergetic defect and increase ATP production is the most promising therapy for mitochondrial diseases (Nightingale *et al.*, 2016; Viscomi, 2016). AICAR, an AMPK agonist that activates PGC-1α, which is a key co-activator of the mitochondrial biogenesis programme (Wu *et al.*, 1999; Vega, Huss and Kelly, 2000; Gleyzer, Vercauteren and Scarpulla, 2005), has been shown to successfully recover OXPHOS activity in a mouse model (Viscomi *et al.*, 2011). On the other hand, NR (a NAD+ precursor) (Cerutti *et al.*, 2014; Khan *et al.*, 2014) and PARP1 (an inhibitor of NAD+ consuming enzymes) (Cerutti *et al.*, 2014) have been found to activate Sirt1 and other sirtuins, which are deacetylases that activate PGC-1α, which then stimulates mitochondrial biogenesis (Wu *et al.*, 1999; Vega, Huss and Kelly, 2000; Gleyzer, Vercauteren and Scarpulla, 2005).

- Shifting heteroplasmy: culture of a cybrid cell line with a large deletion in the mtDNA in ketogenic media deprived of glucose (ketogenic diet) led to a shift in

its heteroplasmy levels below the critical threshold, allowing a recovery of mitochondrial functions (Santra *et al.*, 2004). The mechanism behind this recovery remains unclear, although a favoured selection of cells containing healthier mitochondria was proposed. This approach has been successful used also in mouse models (Sofia *et al.*, 2010). Another strategy to modify heteroplasmy levels is by selectively cleaving mutated mtDNA. Mitochondrially targeted TALENs (transcription activator-like effector nucleases) and ZNFs (zinc-fingers nucleases) have been shown to selectively eliminate pathogenic DNA, decreasing the heteroplasmy percentage in mouse models (Gammage *et al.*, 2018; Bacman *et al.*, 2014 and 2018; Yahata *et al.*, 2017).

- Restoring the deoxynucleotide triphosphate (dNTP) pool: supplementation of dNTPs has been shown to be successful in several models with disorders characterised by defects in mtDNA synthesis or in dNTP metabolism, which causes a decrease in the mtDNA copy number and/or the generation of mutations in this genome (Camara *et al.*, 2014; Garone *et al.*, 2014; Barca and Garcia-diaz, 2018).

- Shaping mitochondria: overexpression of some proteins such as Opa1, a GTPase of the IMM involved in the regulation of mitochondrial fusion and mitochondrial cristae structure (Varanita *et al.*, 2015), has been shown to correct mitochondrial ultrastructure and to ameliorate the phenotype of mice with defective mitochondrial bioenergetics (Civiletto *et al.*, 2015).

- Scavenging toxic compounds: pharmacological compounds such as N-acetylcysteine and metronidazole (Viscomi *et al.*, 2010) partially corrected the effects of increased concentration of hydrogen sulphide (H_2S) in a *Ethe1* KO mouse model and in patients with ethylmalonic encephalopathy, a fatal infant disease due to mutations in *ETHE1* (Tiranti *et al.*, 2009 and 2004). This gene encodes a mitochondrial sulphur dioxygenase involved in the removal of H_2S, a toxic compound produced by the colonic bacterial flora (Tiranti et al., 2009).

- Gene therapy: delivery of therapeutic genes, as well as replacement of mutated genes with their WT form, by using adeno-associated viral vectors (AAVs) targeted to specific tissues (the whole body is unrealistic) is a very promising strategy for some diseases (Garone and Viscomi, 2018). Although the achievement of therapeutic titters in tissues and safety concerns are major challenges, several successes have already been reported both in preclinical

models and in some clinical trials on patients with neurodegenerative conditions, for instance spinal muscular atrophy type 1 (Mendell *et al.*, 2017; Di Meo *et al.*, 2017).

- Preventing mtDNA transmission: given the complexity to find a cure for mitochondrial disorders, preventing the transfer of mutated mtDNA from mother to offspring seems a promising alternative for this kind of defects (Rai *et al.*, 2018). Several reproductive techniques have been developed with this aim, but mitochondrial replacement or 'donation' is the most recent and promising one. This strategy, which replaces all the mitochondria contained in the mother's oocyte with those collected from a healthy donor's oocyte, has already been approved for use in selected patients in the UK (Herbert and Turnbull, 2018).

1.3.2 Mitochondrial COX deficiency

COX deficiency is a mitochondrial disorder characterised by biochemical and/or assembly defects in the complex IV of the ETC (Rak *et al.*, 2016). There are several types of COX deficiency with different symptoms and age of onset (https://rarediseases.org/rare-diseases/cytochrome-c-oxidase-deficiency/).
However, four syndromes are probably the most prevalent among children. The first type is called benign infantile mitochondrial myopathy, affects mainly the skeletal muscles and patients tend to spontaneously recover within the first few years of life (OMIM # 500009). The second is known as infantile mitochondrial myopathy, affects the skeletal muscles and other tissues such as kidney, liver, brain and heart and the symptoms appear within the first few weeks after birth (OMIM # 551000). The third form is systemic, referred to as Leigh's disease (clinical presentation previously described) and usually begins between three months and two years of age (OMIM # 256000). The fourth is called French-Canadian type of Leigh-like syndrome, the organs affected are skeletal muscles, brain and liver (kidney activity is normal) and it also has an early-onset (OMIM # 220111). The range and severity of the symptoms varies greatly among the affected individuals (even within the same family), although is usually fatal in childhood. Mildly affected individuals can survive into adolescence or adulthood (Diaz, 2010).

Isolated COX deficiency is normally caused by mutations in any of its structural subunits or in the assembly factors involved in its biogenesis. Mutations in the mtDNA-encoded subunits (MT-CO1, MT-CO2 and MT-CO3) (Manfredi *et al.*, 1995; Bruno *et al.*, 1999; Horvath *et al.*, 2005) are associated with more than twenty different phenotypes, the most common being: myopathy, anaemia, ALS-like syndrome, encephalomyopathy and MELAS (Rak *et al.*, 2016). Mutations in the nDNA-encoded subunits are uncommon and until the first mutation in *COX6B1* (Massa *et al.*, 2008) was found, they were thought to be embryonic lethal. Pathological mutations in *COX4I2*, *COX6A1*, *COX6B1*, *COX7B*, *COX8A* and *NDUFA4* have been found later on (Massa *et al.*, 2008; Indrieri *et al.*, 2012; Pitceathly *et al.*, 2013; Tamiy *et al.*, 2014; Hallmann *et al.*, 2016). However, the majority of isolated COX deficiencies are due to mutations in genes encoding ancillary proteins necessary for COX assembly and for the biogenesis of the prosthetic groups (Ghezzi and Zeviani, 2018). Although many of these assembly factors have already been described (see section 1.2.4.2), the exact role of several of them is still unknown. The next table summarises all those COX deficiencies caused by pathological mutations in genes encoding COX assembly factors.

Table 1.2 COX assembly factors and syndromes associated to mutations in their genes. A brief description of their roles is also included.

Assembly factor	Role	Clinical presentation and OMIM entry
RNA stability and translation		
LRPPRC	Mitochondrial RNA-binding protein that plays a role in translation or stability of mtDNA-encoded COX subunits	French Canadian Leigh syndrome (OMIM # 607544)
TACO1	MT-CO1 mRNA specific translational activator	Leigh syndrome (OMIM # 612958)
Membrane insertion/transport		
COX20	Required for MT-CO2 stabilisation in the IMM	Ataxia and muscle hypotonia, dystonia-ataxia (OMIM # 614698)
Heme a byosynthesis and insertion		
COX10	Farnesylation of heme *b*	Leigh syndrome, proximal renal tubulopathy, hypertrophic cardiomyopathy, sensorineural deafness, metabolic acidosis (OMIM # 602125)
COX15	Hydroxylation of heme *o* to form heme *a*	Infantile cardiomyopathy, Leigh syndrome (OMIM # 603646)
SURF1	Involved in the assembly of the MT-CO1 module; proposed to participate in heme *a* delivery	Leigh Syndrome, CMT (OMIM # 185620)
Copper trafficking and insertion		
SCO1	CX_3C proteins involved in copper binding and delivery to the Cu_A site on MT-CO2; non-overlapping functions	Infantile encephalopathy, neonatal hepatopathy, ketoacidotic comas (OMIM # 603644)
SCO2		Infantile cardioencephalomyopathy, myopia, CMT (OMIM # 604272)
COA6	CX_9C-$CX_{10}C$ protein involved in Cu_A formation on MT-CO2	Fatal infantile cardioencephalomyopathy (OMIM # 614772)
COX assembly		
COX14 (C12orf62)	Interacts with MT-CO1; involved in its stability and assembly	Respiratory and neurologic distress, metabolic acidosis and neonatal death (OMIM # 614478)
COA3 / MITRAC12	Interacts with MT-CO1; involved in its stability and assembly	Exercise intolerance and neuropathy (OMIM # 614775)
PET100	Involved in the MT-CO2 module assembly	Psychomotor delay, seizures, hypotonia, and Leigh syndrome. Also can cause fatal infantile lactic acidosis (OMIM # 614770)
PET117	Couples heme *a* synthase activity with COX assembly. Interacts with PET100	Neurodevelopmental regression (Renkema *et al.*, 2017)
COA5	Involved in the MT-CO1 module assembly	Fatal neonatal cardiomyopathy (OMIM # 613920)
Other		
COA7	Unknown function	Ataxia and neuropathy with cavitating leukodystrophy (OMIM # 615623)
APOPT1	Unknown function	Leukoencephalopathy (see section 1.3.2.1) (OMIM # 616003)

1.3.2.1 APOPT1

Several pathogenic mutations in the *APOPT1* human gene (**Table 1.3**) have been associated with infantile- or childhood-onset mitochondrial disease (Melchionda *et al.*, 2014; Sharma *et al.*, 2018). The clinical features were very variable, even among siblings, ranging from acute neuroregression in early infancy to subtle neurologic signs in adolescence. The acute presentations were: loss of milestones, seizures, and pyramidal signs rapidly evolving into spastic tetraparesis. All subjects presented profound isolated COX deficiency in skeletal muscle and a very peculiar brain MRI pattern, characterised by cavitating leukodystrophy (Melchionda *et al.*, 2014; Sharma *et al.*, 2018) . Interestingly, of the 7 reported patients, 3 had an onset of the disease after a febrile illness or infection.

Table 1.3 *APOPT1* mutations. All the subjects found to date with mutations in *APOPT1* are listed in this table. The position of the mutation in the cDNA and the predicted effect in the protein sequence are specified. [a]Nomenclature according to HGVS; reference cDNA sequence: RefSeq NM_032374.3. [b] S1 and S2 are sisters.

Subject	Country of origin	Mutations[a]		
		DNA	Protein	State
S1[b]	Italy	c.235C>T	p.Arg79*	Homozygous
S2[b]	Italy	c.235C>T	p.Arg79*	Homozygous
S3	Turkey	c.163-1G>A	Exon 2 skipping; p.Val55_Lys120del	Homozygous
S4	Morocco	Exon 3 del	Ex3 del; p.Glu121 Valfs*6	Homozygous
S5	Oman	c.353T>C	p.Phe118Ser	Homozygous
S6	Italy	c.235C>T c.370_372del	p.Arg79* p.Glu124del	Hoterozygous compound
S7	India	Exon 3 del	Ex3 del; p.Glu121 Valfs*6	Homozygous

APOPT1 is evolutionarily conserved only in Animalia (multicellular eukaryotic organisms), including fish (*Danio rerio*), arthropoda (*Drosophila melanogaster*) and warm (*Caenorhabditis elegans*) (http://www.ensembl.org/index.html). The APOPT1 amino acid sequence alignment for the human and mouse APOPT1 is shown in **Figure 1.9**.

```
CLUSTAL O(1.2.4) multiple sequence alignment


sp|Q96IL0|APOP1_HUMAN      MLPCAAGARGRGAMVVLRAGKKTFLPPLCRAFACR-GCQLAPERGAERRDTAPSGVSRFC 59
Apopt1-201                 -------------MAALRPGSRALRRLLCRSFSGGGGVRLARERPTDHRDAASSRVSRFC 47
                                        *..** *.:::   ***:*:   * :** ** :::**:* * *****

sp|Q96IL0|APOP1_HUMAN      PPRKSCHDWIGPPDKYSNLRPVHFYIPENESPLEQKLRKLRQETQEWNQQFWANQNLTFS 119
Apopt1-201                 PPRQSCHDWIGPPDKCSNLRPVHFHIPENESPLEQRLRELRQETQEWNQQFWAKQNLSFN 107
                           ***:*********** ********:**********:**:**************:***:*.

sp|Q96IL0|APOP1_HUMAN      KEKEEFIHSRLKTKGLGLRTESGQKATLNAEEMADFYKEFLSKNFQKHMYYNRDWYKRNF 179
Apopt1-201                 KEKEEFIYSRLQAKGAGLRTESGQRATLDAEEMADFYKDFLSKNFQKHMRYNRDWYKRNF 167
                           *******:***::** ********:***:*********:********** **********

sp|Q96IL0|APOP1_HUMAN      AITFFMGKVALERIWNKLKQKQKKRSN  206
Apopt1-201                 AITFFMGKVVLERMWSKLRQKKTSS--  192
                           *********.***:*.**:**:..
```

Figure 1.9 Mouse Apopt1 and human APOPT1 sequence alignment. The alignment was obtained using the CLUSTALW multiple sequence alignment program (https://www.genome.jp/tools-bin/clustalw). The cleavage site of the human APOPT1 MTS is indicated with a red arrow. * (asterisk) means identical amino acids, : (colon) means amino acids with strongly similar properties, . (period) means amino acids with weakly similar properties, no symbol means very different properties. Each residue in the alignment is assigned a color if the amino acid profile of the alignment at that position meets some minimum criteria specific for the residue type. Color legend: blue = hydrophobic, red = positive charge, magenta = negative charge, green = polar, pink = cysteines, orange = glycines, yellow = prolines, cyan = aromatic.

Regarding secondary structure, the protein modelling softwares PsiPred (http://bioinf.cs.ucl.ac.uk/psipred/) and Phyre[2] ((http://www.sbg.bio.ic.ac.uk/phyre2/html/page.cgi?id=index) predict with high confidence two main conserved blocks of 60 and 50 amino acids forming a non-transmembrane alpha-helix each. No conserved domains were found and the protein is predicted to be rather hydrophilic.

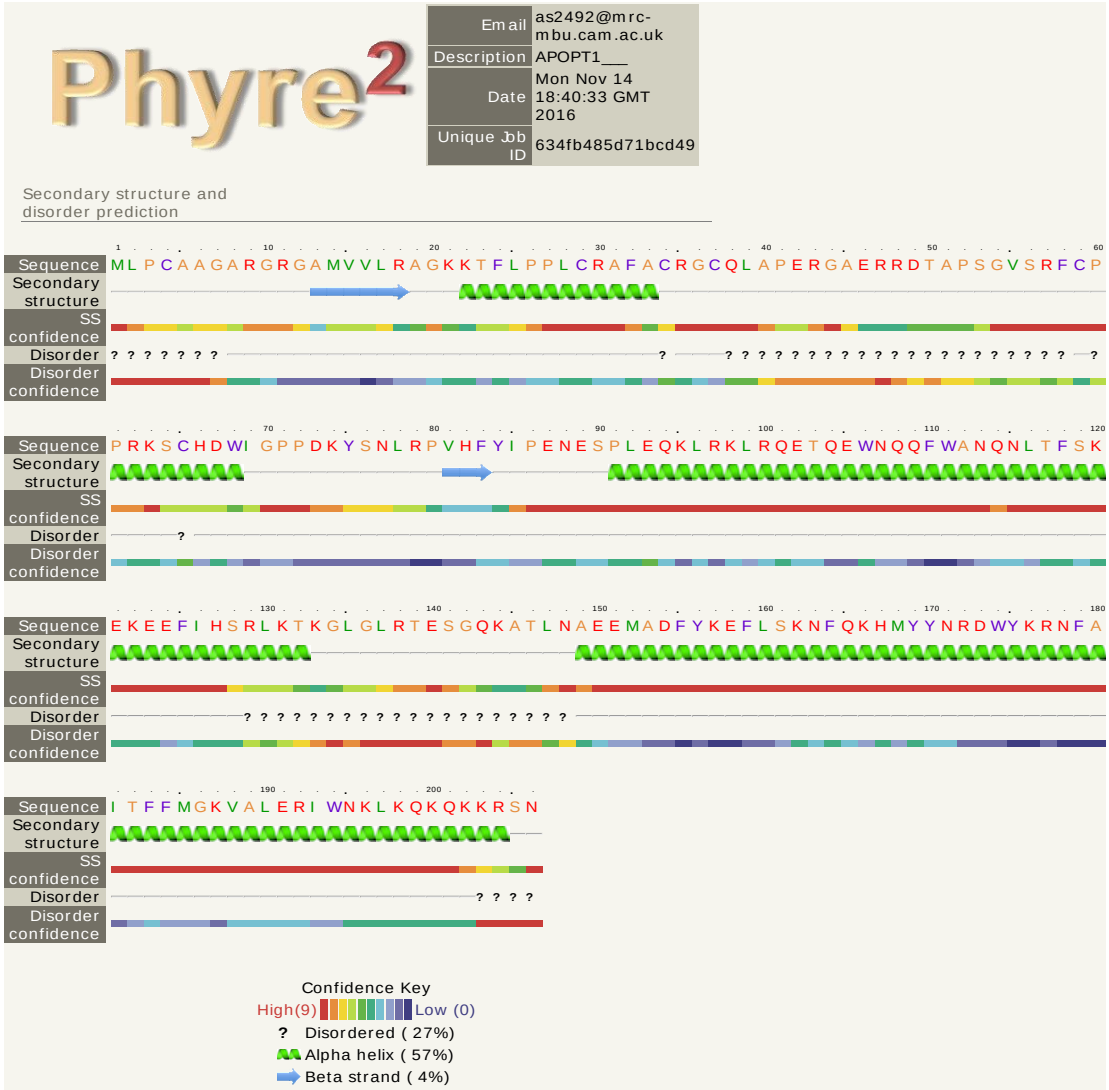

Figure 1.10 APOPT1 secondary structure predicted by the protein modelling software Phyre2. Note that the two first small alpha-helix are predicted with low confidence. Two small beta strands are also predicted with low confidence. Instead, two large blocks are predicted to form alpha-helix structures with high confidence.

At the transcript level, APOPT1 is ubiquitously expressed in humans, the highest levels being in skeletal muscle, thyroid gland and testis (http://www.proteinatlas.org/ENSG00000256053-APOPT1/tissue). Moreover, different transcripts, i.e. alternative splicing isoforms, exist, several of which are protein coding (https://www.ensembl.org/index.html). At the level of the protein, of the 14 tissues screened, it was detected only in large intestine and placenta in the mitochondrial proteome compendium "Mitocarta" (http://archive.broadinstitute.org/pubs/MitoCarta/index.html). The first N-terminal

39 amino acids of the protein coding sequence constitute the MTS in humans, but it is poorly conserved in other organisms. Proteins with an MTS are normally targeted to the mitochondrial matrix and imported through the TIM23 complex (Chacinska *et al.*, 2009). The MTS, rich in positive charged amino acids, aids protein translocation across the IMM (more negative in its matrix side) and is cleaved upon import to the matrix. Thus, APOPT1 206 amino acid precursor gives rise to a 167-amino acid mature intra-mitochondrial protein upon MTS cleavage (Melchionda *et al.*, 2014) (see Chapter 5 for more details).

Although the association of mutations in *APOPT1* with mitochondrial COX deficiency is well established, the role of the protein remained unknown. Thus, one of the aims of this project was to characterise the involvement of the APOPT1 protein in COX biogenesis in both mouse and human cellular models. The post-translational mechanisms that regulate the protein, i.e. degradation by the UPS in the cytosol and stabilisation by ROS, were also investigated. The results are presented in Chapters 4 and 5.

1.4 Mitochondrial regulation by the UPS system

The proteasome is a multi-component and dynamic system of ATP-dependent proteases recognising and degrading ubiquitinated proteins, while recycling the ubiquitin tag, which is a small protein of 76 amino acids highly conserved in eukaryotes (Pickart and Eddins, 2004). The catalytic core of the proteasome is a barrel-shaped 20S particle, which can bind to the 19S regulatory particles to form the 2.5 MDa 26S proteasome. The 19S particles provide specificity to the degradation process by recognising specific ubiquitinated proteins, which are then transported inside the 20S structure (Finley, 2009). Three enzymes are required to attach the ubiquitin tag to the target protein: the ubiquitin-activating E1, the ubiquitin-conjugating E2 and the ubiquitin-ligase E3. In humans, there are around 600-1000 genes encoding different E3 enzymes recognising different substrates (Bragoszewski, Turek and Chacinska, 2017). The high specificity of this process means that the UPS can regulate cellular functions, like cell growth and apoptosis, by degrading key proteins (Kubbutat,

Jones and Vousden, 1997; Yang *et al.*, 2000; Benard *et al.*, 2010). The UPS can also regulate mitochondrial function at several levels as described below.

First, some of the mitochondrial precursor proteins synthesised in the cytosol are ubiquitinated and degraded by the UPS, both to prevent their accumulation in the cytosol when import fails and under normal physiological conditions (Margineantu *et al.*, 2007; Radke *et al.*, 2008; Bragoszewski *et al.*, 2013; Wrobel *et al.*, 2015; Itakura *et al.*, 2016; Bragoszewski, Turek and Chacinska, 2017). In particular, a fraction of some IMS precursors were shown to be continuously degraded in the cytosol by the UPS, even when import was fully functional (Bragoszewski *et al.*, 2013; Kowalski *et al.*, 2018; Zöller, Todd Alexander and Herrmann, 2018), which means that the UPS can directly control the availability of these proteins. Although all IMS proteins have structural similarities, a common cytosolic factor responsible for the degradation of all these proteins was not found, and instead different factors were shown to be involved in the removal of each IMS protein (Kowalski *et al.*, 2018). In the same study it was found that ubiquitinated precursor proteins cannot be imported into mitochondria, suggesting that mitochondrial import competes with the ubiquitination process under normal conditions.

On the other hand, several studies have shown that a variety of mitochondrial processes can be regulated by proteasomal degradation of key proteins (Matsushima and Kaguni, 2012; Bezawork-Geleta *et al.*, 2015). For instance, mitochondrial dynamics can be modulated by ubiquitination and degradation of OMM proteins involved in mitochondrial fusion and fission (Nakamura *et al.*, 2006; Karbowski, Neutzner and Youle, 2007; Braschi, Zunino and McBride, 2009). Energy metabolism can also be regulated by degradation of specific OXPHOS subunits, such as SDHA, and metabolic enzymes (Lavie *et al.*, 2018). The UPS seems to also play a role in the metabolic adaptation to hypoxia by ubiquitination and degradation of α-ketoglutarate dehydrogenase (KGDH) (Sun and Denko, 2014).

However, how mitochondrial proteins located in the IMS, IMM and matrix, i.e. not directly available to the cytosolic UPS, are retro-translocated to the cytosol is a process not completely understood yet (Bragoszewski, Turek and Chacinska, 2017). IMS proteins can exit mitochondria through the TOM complex, as it has already been demonstrated (Bragoszewski *et al.*, 2015), but IMM proteins would

need specific factors that extract them from the membrane. The AAA-ATPase P97 has already been shown to remove proteins from the outer mitochondrial membrane (mitochondrial-associated degradation, MAD) (Xu *et al.*, 2011) and could also be involved in the extraction of proteins from the IMM.

Interestingly, the UPS is also involved in the modulation of mitophagy, both dependent and independent of Parkin. The E3 ligase Parkin, together with PINK1 (PTEN-induced kinase 1), both encoded by Parkinson's disease-associated genes, are responsible for marking mitochondria for mitophagy. In normal conditions, PINK1 is imported into the IMM, where its catalytic domain is cleaved, translocated to the cytosol and rapidly degraded by the UPS (Poole *et al.*, 2008). If the import fails, due to different mitochondrial stresses, PINK1 cannot be imported and it accumulates in the OMM, where it phosphorylates ubiquitin groups conjugated to OMM proteins (such as VDAC, TOM proteins, mitofusins etc.) (Sarraf *et al.*, 2013) and to Parkin, activating its ubiquitin ligase function (Aguileta *et al.*, 2015). Once activated, Parkin adds more ubiquitins to the OMM proteins, which are then phosphorylated by PINK1. This cycle continues, resulting in the formation of polyubiquitin chains in some OMM proteins, which are signals for mitophagy. Moreover, some of the Parkin-ubiquitinated OMM proteins (e.g. mitofusins) are specifically degraded by the proteasome (Tanaka *et al.*, 2010), which prevents mitochondrial fusion, isolating dysfunctional mitochondria and facilitating their engulfment by autophagosomes (Sarraf *et al.*, 2013; Kocaturk and Gozuacik, 2018). On the other hand, several deubiquitinating enzymes (DUBs), such as USP15, USP8 and the mitochondrial USP30, can remove the ubiquitin tag of OMM proteins, thus counteracting Parkin activity and preventing excessive mitophagy (Bingol *et al.*, 2014; Cornelissen *et al.*, 2014; Durcan *et al.*, 2014). Alternative E3 ligases, such as Mulan (MUL1) (Ambivero *et al.*, 2014; Yun *et al.*, 2014) and MITOL (MARCH5) (Nakamura *et al.*, 2006; Yonashiro *et al.*, 2006), which are located on the OMM, are involved in Parkin-independent mitophagy.

Finally, the mitochondrial unfolded protein response (UPR^{mt}), which activates the degradation of misfolded proteins accumulated in the mitochondria (Jovaisaite, Mouchiroud and Auwerx, 2014; Qureshi, Haynes and Pellegrino, 2017), may also involve the UPS, since several studies showed that UPR^{mt}

activation increases the expression of UPS-related proteins, such as UBL5 (Haynes *et al.*, 2007) and PINK1 (Thomas *et al.*, 2014).

1.5 Mitochondrial ROS production

1.5.1 Mitochondrial ROS production sites

Although the ETC is a highly efficient system, there is a constant leakage of electrons escaping the system that can partially reduce oxygen forming reactive oxygen species (ROS) (Turrens, 2003). Indeed, approximately 90% of cellular ROS are generated in the mitochondria during respiration (Turrens, 2003; Andreyev, Kushnareva and Starkov, 2005; Nissanka and Moraes, 2018). Superoxide radicals ($O_2^{\cdot-}$), generated by the one electron reduction of O_2, are the major form of ROS and are rapidly converted to hydrogen peroxide (H_2O_2), either spontaneously or enzymatically by superoxide dismutase 2 (SOD2/MnSOD) (Murphy, 2009). H_2O_2 is much less reactive and can be reduced to water by the peroxiredoxin/thioredoxin and mitochondrial glutathione systems (Cox, Winterbourn and Hampton, 2010). However, superoxide can also react with nitric oxide (NO•), which can diffuse into mitochondria, and generate peroxynitrite (ONOO−), a highly reactive and damaging radical (Murphy, 2009). In addition, H_2O_2 can be reduced by divalent metal ions (Fenton reaction) or superoxide (Haber-Weiss reaction) resulting in the formation of hydroxyl radicals (OH•), which are extremely reactive and damaging species (Pryor, 1986; Mahaseth and Kuzminov, 2018). Superoxide radicals are mostly released from complex I, II and III (Murphy, 2009; Quinlan *et al.*, 2012). CI generates ROS mainly through reverse electron transfer (RET), that occurs when an over-reduced Q pool forces electrons back from QH_2 into CI, reducing NAD^+ to NADH at the FMN site (Murphy, 2009; Pryde and Hirst, 2011; Chouchani *et al.*, 2016). Low levels of succinate in the presence of Q-site inhibitors have been shown to generate superoxide and H_2O_2 at the flavin site of complex II independently of the redox state of the Q pool and the activity of other respiratory chain complexes (Quinlan *et al.*, 2012; Siebels and Dröse, 2013; Grivennikova, Kozlovsky and Vinogradov,

2017). On the other hand, complex III generates superoxide at the Q_o site, most likely as a result of the autoxidation of ubisemiquinone, an intermediate produced during the Q-cycle of complex III (Boveris, Cadenas and Stoppani, 1976; Turrens, Alexandre and Lehninger, 1985; Trumpower, 1990). Generation of ROS from complex IV, a major oxygen-consuming enzyme, seems to be prevented due to the rapid kinetics of electron transfer to oxygen (Bourens *et al.*, 2013). However, defects in its biogenesis can lead to a decrease in its activity and an accumulation of subcomplexes, some of which can be pro-oxidant, generating peroxide sensitivity in yeast cells (Khalimonchuk, Bird and Winge, 2007). Apart from the ETC, there are other ROS production sites in the mitochondria. For instance, the OMM enzyme monoamine oxidase catalyses the oxidative deamination of dietary monoamines, producing aldehydes and H_2O_2. The rate limiting TCA cycle enzyme α-ketoglutarate dehydrogenase complex (KGDH) and the pyruvate dehydrogenase complex (PDHC) in the mitochondrial matrix can also generate ROS (Pizzinat *et al.*, 1999; Starkov *et al.*, 2004). Interestingly, all mitochondrial ROS production sites release ROS into the matrix, whereas complex III can release ROS into either the IMS or the matrix (Boveris, Cadenas and Stoppani, 1976; Muller, Liu and Van Remmen, 2004).

1.5.2 ROS-mediated mitochondrial physiopathology

The majority of ROS have a short life and are rapidly degraded by antioxidant and detoxification systems. However, if the antioxidant defences are overwhelmed or not functioning properly, ROS can accumulate and oxidise critical mitochondrial components, playing a role in many diseases and in aging (Kirkinezos and Moraes, 2001; Brieger *et al.*, 2012). The main components that can be damaged by ROS in the mitochondria are fatty acids of the IMM, proteins and the mtDNA (Kirkinezos and Moraes, 2001). The IMM is rich in unsaturated fatty acids, which can be attacked by ROS through a chain of reactions generating lipid peroxidation products, mainly reactive aldehydes, that then damage other mitochondrial components (Pizzimenti *et al.*, 2013; Ayala, Muñoz and Argüelles, 2014). The modification of lipid composition in the IMM can lead to cell death and has been associated to neurodegeneration (Ademowo *et al.*,

2017; Aufschnaiter, Kohler, Diessl, Peselj, *et al.*, 2017). For instance, in Alzheimer's Disease, lipid peroxidation is increased in many regions of the brain (Yaoa and Brinton, 2011). On the other hand, reactions between protein amino acid residues, most commonly tyrosine and cysteine, and reactive oxygen or nitrogen species can generate protein oxidative modifications, such as protein carbonyl formation, loss of protein thiols, and nitrotyrosine and dityrosine formation, which are mostly irreversible. Several mechanisms take place for the removal of oxidatively modified proteins such as proteolytic degradation by LonP1, one of the major ATP-dependent mitochondrial proteases (Bulteau, Szweda and Friguet, 2006; Hamon, Bulteau and Friguet, 2015; Bulteau *et al.*, 2017) and proteasomal degradation (Davies, 2001; Hemion, Flammer and Neutzner, 2014). Specifically, LonP1 protease plays a critical role in the removal of oxidised aconitase, a TCA enzyme very sensitive to oxidative inactivation in the mitochondria matrix (Bota and Davies, 2002; Bulteau, Ikeda-Saito and Szweda, 2003). Failure in the elimination of oxidised proteins seems to be a critical component of the aging process (Nilanjana *et al.*, 2001; Bulteau, Szweda and Friguet, 2006). On the other hand, superoxide can inactivate Fe-S proteins by oxidising their iron-sulphur clusters, which are then quickly degraded (Popović-Bijelić *et al.*, 2016). Finally, the mtDNA is also a target of ROS because of its vicinity to superoxide production sites and because, unlike the nDNA, lacks protective histones (Bogenhagen, 2012). Indeed, the free radical theory of aging proposed that oxidative damage accumulated in the mtDNA is the main cause of aging (Harman, 1956; Sohal, 1996). However, although mtDNA damage increases in an age-related manner and an increase of ROS has been found in aged tissues, the link between ROS and age-related mtDNA mutations remains controversial (Gladyshev, 2014; Nissanka and Moraes, 2018)

Interestingly, mitochondrial ROS have recently been shown to serve as messenger molecules that regulate many biological and physiological processes, suggesting a more important role for ROS in signalling than in oxidative damage (Schieber and Chandel, 2014). The levels of ROS produced by the ETC depend on the rate constants of the enzymatic reactions of the respiratory complexes and the mitochondrial membrane potential, which in turn depend on many other factors such as the concentration of oxygen or ADP availability (Murphy, 2009).

This means that ROS from the ETC could potentially be the major signal that links mitochondrial metabolism with other cellular processes. Indeed, RET has already been reported to contribute to the metabolic adaptation of immune cells during inflammation (Mills *et al.*, 2016), the immune response to viral infection (Buskiewicz *et al.*, 2016) and lifespan extension in fruit flies (Scialò *et al.*, 2016). Moreover, perturbation of ROS signalling from mitochondria has been shown to contribute to the worsening of a disease phenotype in mice (Dogan *et al.*, 2018). The transfer of mitochondrial redox signals from mitochondria to the cytosol implies that H_2O_2 can diffuse through the membrane (unlikely for oxygen radicals) and modify target proteins in the cytosol, either directly by redox modification of cysteine residues, or indirectly by facilitating redox-relay interactions with other redox-sensitive proteins (Herrmann and Riemer, 2012; Sobotta *et al.*, 2015a). However, another option is that within the mitochondria ROS modify/activate key proteins that then transfer the signal outside the organelle through redox-relay reactions with other proteins. Changes in the redox state of thiol groups, located in cysteine residues, can regulate the activity, binding interactions, turnover and localisation of a protein (Holmström and Finkel, 2014). The oxidation of thiol groups by H_2O_2, resulting in the formation of disulphide bonds, S-acetylation and S-glutathionylation among other redox modifications (Paulsen and Carroll, 2013), can be either reversible, like in the inactivation of tyrosine phosphatases (Meng, Fukada and Tonks, 2002), or irreversible, such as the thiol alkylation of KEAP-1 (Kelch-like ECH-associated protein 1) that induces nuclear translocation of NRF-2 (nuclear factor erythroid 2-related factor 2) (Kobayashi and Yamamoto, 2006).

1.6 Project aims

The order of incorporation of the structural subunits in the human cytochrome c oxidase assembly pathway is nowadays a well-defined process (Nijtmans *et al.*, 1998; Stiburek *et al.*, 2006; Vidoni *et al.*, 2017). More than 30 assembly factors are known to be involved in the different steps of COX biogenesis (Timón-Gómez *et al.*, 2017; Signes and Fernandez-Vizarra, 2018). Most of these ancillary proteins were identified in studies using mutant strains of

the yeast *Saccharomyces cerevisiae* (Tzagoloff and Dieckmann, 1990; Barrientos, 2003; Fontanesi *et al.*, 2006). However, it has become evident that there are mammal-specific factors (Mootha *et al.*, 2003; Weraarpachai *et al.*, 2009; Melchionda *et al.*, 2014; Vidoni *et al.*, 2017) that need to be studied specifically in mammalian systems, such as mouse disease models and human cell lines with COX assembly defects (Fernández-Vizarra, Tiranti and Zeviani, 2009).

The first aim of this project was to perform quantitative proteomic analysis of the assembly intermediates accumulated in a cybrid cell line with a nearly homoplasmic frameshift mutation in *MT-CO3*, in order to characterise the composition of these subassemblies and identify potential novel COX assembly factors bound to them. **Chapter 3** describes the identification and characterisation of MR-1S, a vertebrate-specific novel COX assembly factor that interacts with the highly conserved PET100 and PET117 proteins.

The second aim of this project was to characterise the function and regulatory mechanisms of APOPT1 in relation to COX biogenesis. Pathogenic mutations in *APOPT1*, a gene exclusively found in animals, have been determined to cause isolated mitochondrial COX deficiency and encephalopathy with a very characteristic MRI pattern (Melchionda *et al.*, 2014; Sharma *et al.*, 2018). However, the biochemical link between APOPT1 function and COX remained elusive for some time. In **Chapter 4** I will describe how we generated an *Apopt1* knockout mouse model which recapitulates the biochemical hallmarks found in human patients, making it an optimal model to study the role of APOPT1 in COX assembly and function in differentiated tissues. An extensive phenotypical and biochemical characterisation will be presented in that chapter. In addition, **Chapter 5** describes the generation of stable human cell lines expressing several APOPT1 tagged isoforms used to investigate APOPT1 localisation, turnover regulated by the UPS and stabilisation promoted by oxidants. To further investigate the biochemical and physiological consequences of APOPT1 ablation, patient-derived immortalised fibroblasts, in which COX content and activity is reduced by half compared to the controls, were extensively characterised. Complementation assays were performed in order to confirm that

loss-of-function mutations in *APOPT1* were actually the cause of the observed isolated COX deficiency in these cells. Molecular analyses, i.e. Western blot of SDS- and BN-PAGE, were used to determine the abundance and assembly of COX, which helped to underpin the role of this factor in COX assembly. Finally, the stability of the mtDNA-encoded COX subunits and the effect of oxidative stress were also investigated in the APOPT1-null human cells.

CHAPTER 2

Materials and Methods

2.1 Mouse model

An *Apopt1* KO mouse model in the FVB/NJ background (Jackson laboratories), was generated using CRISPR/Cas9 genome editing technology (see section 2.1.1) in order to study the effects of *Apopt1* ablation in mouse development and physiology. All procedures were conducted under the UK Animals (Scientific Procedures) Act, 1986, approved by Home Office license (PPL: 70/7538) and local ethical review. The animals were maintained in a temperature- and humidity-controlled animal-care facility (Phenomics Laboratory, Forvie Site, Cambridge Biomedical Campus, Cambridge CB2 0PY) with a 12-hr light/dark cycle and free access to water and food.

2.1.1 Generation of an *Apopt1* KO mouse model

The CRISPR/Cas9 technology was used to edit the genome of mouse zygotes in order to generate an *Apopt1* KO mouse model (Rath *et al.*, 2015) (**Figure 2.2**). The gRNA spacer sequences, targeted to exon 2 of the mouse *Apopt1* gene (GenBank ID: 68020), were designed using the online CRISPR tool (http://crispr.mit.edu/). Exon 2 was chosen in order to mutate the gene from the beginning of its sequence, but after the MTS (located in exon1). The spacer sequence with the highest quality score, which is based on features such as minimal homology with other genes and presence of the PAM sequence in the 3' genomic end, was 5'- CTGGGGGGCCTATCCAATCA -3'. A customised forward primer carrying the T3 promotor sequence plus the selected spacer sequence and the first 20 nucleotides of the scaffold sequence (**Table 2.5**), as well as a reverse primer (**Table 2.5**) carrying the last 20 nucleotides of the scaffold sequence, were used to amplify by PCR (see section 2.3.3) the entire scaffold sequence from the template in the pX330-U6-Chimeric_BB-CBh-hSpCas9 plasmid, gift from the Feng Zhang team (Addgene plasmid # 42230, https://www.addgene.org/). The amplified product, i.e. the complete gRNA sequence (spacer + scaffold) under the T3 promotor, was then cloned into the pCR2.1 vector using a TOPO TA cloning kit (Invitrogen) (see section 2.3.7). Then,

the insert was liberated from the vector by digestion with the restriction enzyme EcoRI (see section 2.3.6), run on a 1 % agarose gel and purified from the gel (see section 2.3.6). On the other hand, the commercial plasmid encoding the SpCas9 nuclease (Addgene plasmid # 48625, https://www.addgene.org/) (**Figure 2.1**), which has been shown successful in the literature for the genetic modification of mouse embryos (Fujii *et al.*, 2013), was linearised by digestion with SphI (see section 2.3.6) and purified using the QIAquick PCR Purification kit (Qiagen) (see section 2.3.5).

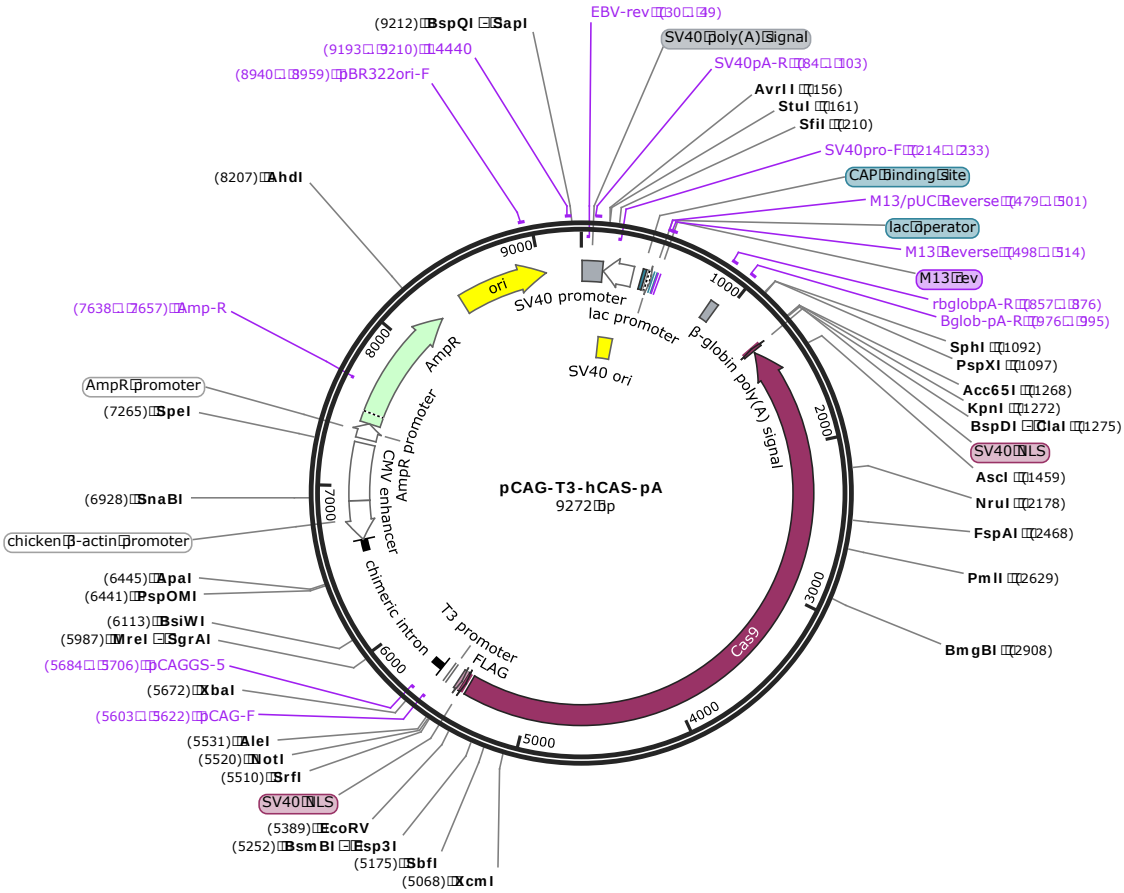

Figure 2.1 Vector encoding the SpCas9 nuclease (Addgene plasmid # 48625). This vector was successfully used to genetically modify mouse embryos (Fujii *et al.*, 2013).

Both purified DNAs (gRNA fragment and linearised SpCas9), together with a positive control template (pGEM® Express Positive Control Template, Promega), were transcribed *in vitro* (Riboprobe® in vitro Transcription System, Promega). The reaction mix described in **Table 2.1** was incubated at 37 °C for 2

hours. After 1 hour of incubation, 2 additional µL of T3 RNA Polymerase and 2.5 additional µL of rNTP mix were added to the Cas9 mix to increase RNA yield.

Table 2.1 In vitro transcription reaction set-up.

Reagent	gRNA	Cas9	Control
Transcription optimised buffer (5X)*	20 µL	10 µL	5 µL
DTT (100 mM)*	10 µL	5 µL	2.5 µL
Recombinant RNasin® Ribonuclease (40 U/µL)*	2.5 µL	1.2 µL	0.6 µL
Unlabeled rNTP mix (10mM each)*	20 µL	5 µL	5 µL
Ribo m^7G Cap Analog (5mM)*	-	5 µL	-
5 µg of linearised DNA template	20 µL	23 µL	0.5 µL
T3 RNA Polymerase (17 U/µL)*	3.5 µL	2.5 µL	1 µL
Nuclease-Free Water	24 µL	-	10.4 µL
Total volume	100 µL	50 µL	25 µL

* Reagents provided in the Riboprobe® in vitro Transcription System (Promega).

The resulting RNAs were purified using PureLink™ RNA Mini Kit Spin Cartridge (Invitrogen-ThermoFisher Scientific) (see section 2.3.1). The eluted RNA was treated with DNase (Turbo DNA-free, Life technologies) and run in a denaturing 7M urea 5 % polyacrylamide gel to check RNA quality. Concentration and purity were estimated using a NanoDrop spectrophotometer (ND-8000, Labtech, UK). Aliquots of 50 ng/µL gRNA + 100 ng/ µL Cas9 were prepared and sent to the ‘Core Facility for Conditional Mutagenesis’ at the IRCCS Ospedale San Raffaele, (Milan, Italy) for microinjection into fertilised mouse one-cell zygotes. FVB/NJ was the mouse strain of choice because the large size of the pronuclei in the fertilised oocytes facilitates the injection procedure.

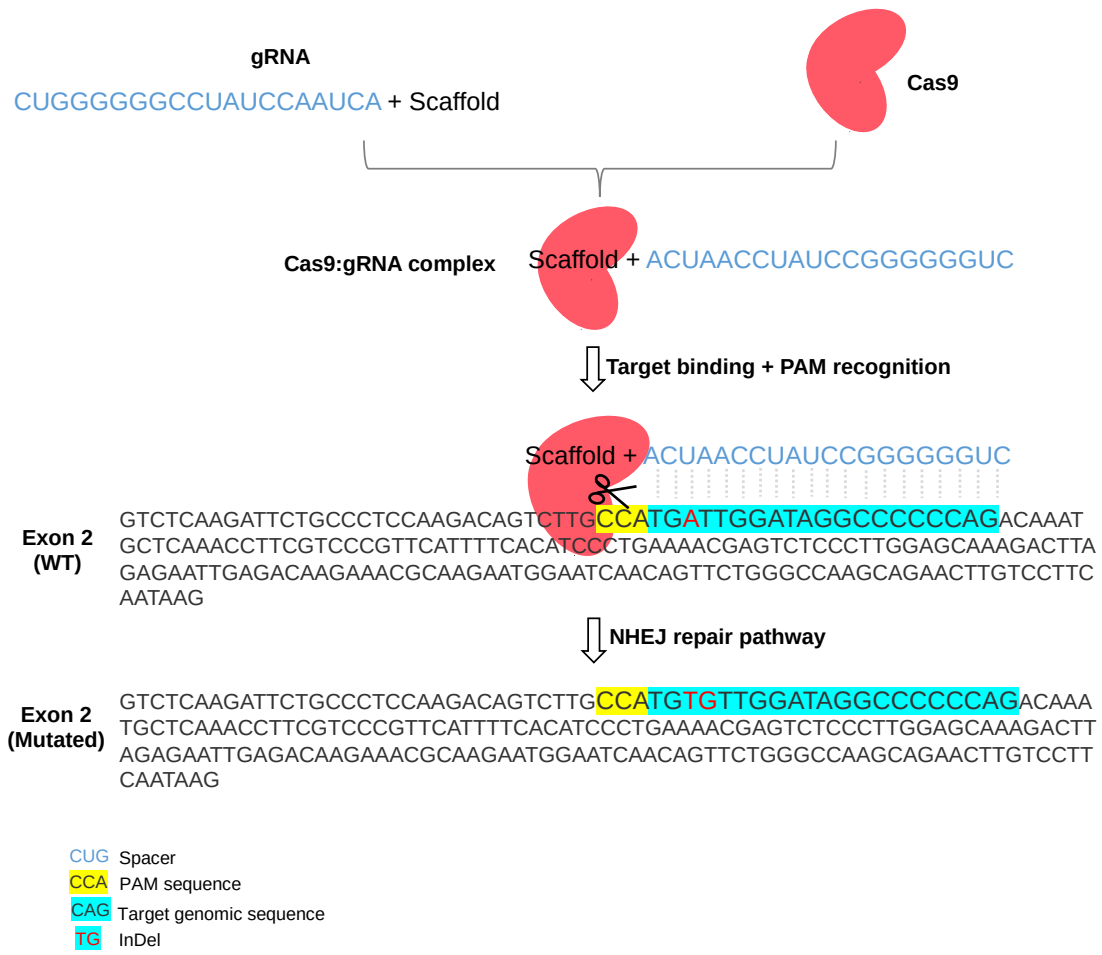

Figure 2.2 Schematic representation of the CRISPR/Cas9 technology. First the Cas9 protein (transcribed from the Cas9 RNA injected in the cell) interacts with the scaffold sequence of the gRNA to form the Cas9:gRNA ribonucleoprotein complex. Then, the spacer sequence of the gRNA guides the Cas9 to the target genomic sequence where the Cas9 will cleave the double strand DNA after recognition of the protospacer adjacent motif (PAM). The non-homologous end joining NHEJ pathway usually introduces indels during the DNA repair process.

2.1.2 Metabolic and behavioural analysis

Mice were monitored weekly to examine body condition and general health. The metabolic, neurological and motor phenotype was evaluated with a set of different tests described below. All apparatus and surfaces used were cleaned and disinfected after each session.

2.1.2.1 Energy metabolism

The CLAMS system (Columbus Instruments, Columbus, Ohio) allows simultaneous, automated and non-invasive measurement of numerous metabolic parameters. *Apopt1*$^{-/-}$ mice and control littermates were individually placed in CLAMS cages and monitored over a 36-hour period. Data were collected every 10-minutes. The following parameters were recorded: VO_2 (volume of oxygen consumed, ml/Kg/hr), VCO_2 (volume of carbon dioxide produced, ml/Kg/hr), locomotor activity in the xyz axis (measured as infrared beam interruptions, termed 'counts') and food and water consumption (measured as accumulated data in g and ml, respectively).

2.1.2.2 Hindlimb clasping

Hindlimb clasping is a marker of disease progression in many mouse models of neurodegeneration. Mice were grasp from the base of the tail, lift clear of all surrounding objects and their hindlimb position observed for 10 seconds. Normal position was defined as hindlimbs splayed outward, away from the abdomen, and abnormal as one or both hindlimbs retracted towards the abdomen.

2.1.2.3 Gait

Evaluation of mouse gait, i.e. walking movement, was used to monitor mice coordination and muscle function. Animals were placed in a flat surface with their head facing away from the investigator, allowing to observe the mouse from behind while it walks. Normal movement was defined as body weight being supported on all limbs, abdomen not touching the surface and both hindlimbs participating evenly. Abnormal gait was defined as tremors, limp while walking, lowered pelvis, etc.

2.1.2.4 Treadmill

A treadmill apparatus (Columbus Instruments, Columbus, Ohio) was used to evaluate exercise capacity and endurance. Mice were forced to run to exhaustion over a conveyor belt with gradually increasing speed. The number of falls was the parameter recorded to determine exhaustion, defined as > 10 falls/min. One trial for two consecutive days was conducted prior to testing to allow the mice enough time to acclimatize. The trial consisted on 10 minutes at a fixed speed of 13 m/min. On the test day, the treadmill was set to an angle of inclination of 10 °. The speed was initially set at 11 m/min for 3 minutes. Then it was increased 0.3 m/min up to a maximum speed of 75 m/min. Time and distance were recorded at the exhaustion point of each mouse.

2.1.2.5 Rotarod

A rotarod apparatus (Ugo Basile, Varese, Italy) was used to assess motor performance and coordination. During the test, mice had to maintain themselves on a rod turning at accelerating speeds. The latency to fall was recorded. One trial for two consecutive days was conducted prior to testing to allow the mice enough time to acclimatize. The adaptation trial consisted in 4 minutes static plus 5 minutes at a fixed speed of 10 rpm/min. On the test day, three trials were completed setting the apparatus to accelerate from 2 to 40 rpm in 300 seconds. Mice were returned to their home cage during the inter-trial interval of 15 minutes.

2.1.2.6 Y maze spontaneous alternation

The Y maze test was used to assess exploratory behaviour and cognitive function (memory and learning) in mice. The test was conducted in a large Y-shaped maze with three opaque, plastic and equal arms of 40 cm length, 8 cm width, and 15 cm height, attached at 120° angle from each other. Mice were placed in the centre of the maze and allowed to freely explore the three arms for

5 minutes (**Figure 2.3**). No acclimatization was required as this test evaluates the willingness of mice to explore new environments.

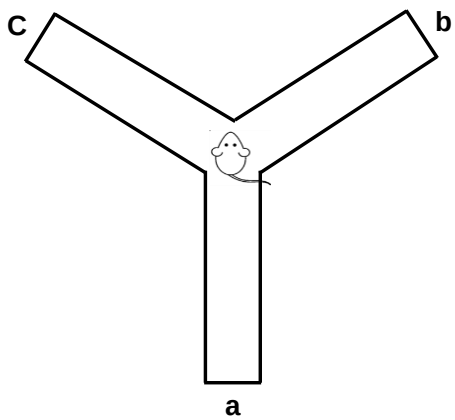

Figure 2.3 A schematic representation of the Y maze test described in the text. Mice are placed in the centre and let explore the arms freely for 5 minutes. Each arm was labelled a, b or c.

Healthy mice prefer to investigate a new arm of the maze (spontaneous alternation) rather than returning to one that was already visited. Many parts of the brain, including the hippocampus, septum, basal forebrain, and prefrontal cortex are involved in this task. The sequence of arm entries was manually recorded, the arms being labelled a, b or c. An actual alternation was defined as entry into all three arms consecutively. For example, in this sequence of arm entries: ABBABCABCABACBB, the total number of entries is 15, the maximum alternation is 13 (total number of entries minus two) and the number of actual alternations is 8 (only correct alternations are accounted: ~~ABB~~, ~~BBA~~, ~~BAB~~, ABC, BCA, CAB, ABC, BCA, CAB, ~~ABA~~, BAC, ACB, ~~CBB)~~. The percentage of alternation in this example is 61,5 %, calculated as:

$$\%\ alternation = \left(\frac{actual\ alternation}{maximum\ alternation}\right) x\ 100$$

2.1.2.7 Pole test

The pole test was used to assess general proprioception. Mice were placed head-upward on the top of a vertical rough-surfaced pole (diameter 5 mm; height 50 cm) and the time to descend it was recorded (with a maximum duration of 60 seconds). The base of the pole was placed in the home cage. Healthy mice quickly orientate themselves downwards and descend the pole back into their home cage. Three trials for two consecutive days were conducted prior to testing to allow the mice enough time to acclimatise.

2.1.2.8 Activity cage

An activity cage (Ugo Basile, Varese, Italy) was used to record spontaneous activity in mice. Animal movements, detected as infrared beams interruptions, were counted and recorded by the electronic unit's internal memory. Mice were individually placed in the centre of the cage and horizontal and vertical movements were recorded in intervals of 1 minute for 30 minutes. Movements/minute and total movements (as accumulated data) were plotted and analysed.

2.1.3 Immunohistochemistry (IHC) in mice tissues

<u>From frozen tissues</u>

This method is commonly used to preserve enzymes and antigen expression but is not recommended for histopathology analysis because the formation of ice crystals can negatively affect tissue structure and cellular morphology.

Mice were sacrificed, and organs were quickly dissected and cryopreserved by immersion in isopentane cooled with liquid nitrogen. Samples were placed in cryovials, stored at -80 °C and analysed as soon as possible to prevent them from drying. Frozen tissues were sectioned in a cryostat, placed in slides, fixed with alcohol and washed with deionised water. The slides were

stained as described in (Sciacco and Bonilla, 1996). Briefly, to allow the use of biotinylated horseradish peroxidase H (HRP) conjugated secondary antibodies, the endogenous peroxidase was blocked by incubating the slides with 0.3 % H_2O_2 in tris-buffered saline buffer (TBS) for 30 minutes at RT. Then, the slides were washed with deionised water and incubated in blocking solution: 10 % foetal bovine serum (FBS, Gibco) with 1 % bovine serum albumin (BSA) in TBS for 2 hours at RT. After washing, the slides were incubated with the correspondent primary antibody diluted in TBS with 1 % BSA overnight at 4 °C. The slides were then washed, incubated for 1 hour at RT with the correspondent biotinylated secondary antibody diluted in TBS with 1 % BSA, washed again and incubated with ABC revelation reagent. After washing, the slides were incubated in peroxidase substrate solution until the desired stain intensity was developed. The slides were then dehydrated, cleared and mounted.

<u>From fixed tissues</u>

Fixation of tissues with formaldehyde is recommended for histopathological analysis in order to better preserve tissue and cell morphology, to harden the samples for posterior processing, to inactivate proteolytic enzymes and to protect the samples against contamination and decomposition.

Mice were anesthetised with pentobarbital, perfused with phosphate-buffered saline (PBS) for exsanguination and then perfused with a methanol-stabilised formaldehyde solution, NBF, which is a crosslinking fixative agent that creates covalent chemical bonds between proteins. In this case, the perfusion was performed directly through the heart, allowing a rapid and uniform fixation of entire organs via the vascular system. Organs were dissected and immersed in 10 % (v/v) NBF (to ensure thorough fixation throughout the tissue), dehydrated in alcohol, cleared in xylene (an intermedium that can be equally well mixed with both alcohol and NBF) and then embedded in paraffin, which helps to harden the samples in order to be then sectioned in a microtome (6 µm-thick). Slides were deparaffinised with ethanol (paraffin can interfere with the posterior staining) and rehydrated. Antigen retrieval was then performed in order to expose the antigenic sites and allow the antibodies to bind. For that, samples were incubated with retrieval solution and heated in a microwave (conditions were optimised for each

antibody). After washing, IHC was continued as described for frozen tissues (from the step of blocking the endogenous peroxidase).

2.1.4 Isolation of MEFs

MEFs were derived from female mice 12.5 to 13.5 days after the appearance of the copulation plug. The pregnant female was sacrificed, the abdominal wall and uterus were cut through and embryos retrieved and placed in a covered 100 mm Petri dish (Corning®, Falcon®) filled with ice-cold PBS without Ca^{2+} and Mg^{2+} (Life Technologies, Gibco®). The Petri dish was then transferred to a tissue culture hood and only sterilised surgical instruments were used from that moment. Each embryo was separated and transferred to one well of a 6-well culture plate (Corning® Costar®) filled with PBS, where it was pulled out of the yolk sac, cleaning out all the uterine tissue. Holding the embryo with forceps, all the red tissue (heart and liver), limbs and tail were removed, while the head was cut and kept in an Eppendorf tube for posterior DNA extraction and genotyping. The rest of the embryo was transferred to a well of a 24-well culture plate (Corning® Costar®) filled with PBS, minced with scissors into 1–2 mm pieces and pipetted up and down several times with a 10-ml serological pipette (Starstedt). The homogenate was then transferred to a 15-ml centrifuge tube (Sarstedt) and centrifuged 5 minutes at 200 x g and room temperature (RT). A second wash with PBS was done and the final pellet was resuspended in 1 ml of digestion solution: 40 mg of collagenase dissolved in 20 ml of culture medium: DMEM containing 4.5 g/L D-glucose, sodium pyruvate and GlutaMAX™, supplemented with 10 % foetal bovine serum and 100 units/ml penicillin, 0.1 mg/ml streptomycin and 25 µg/ml amphotericin B (Fungizone) (all from Life Technologies, Gibco®). Tubes were put at 37 °C in the water bath (Grant instruments, UK) for 30-90 minutes and the embryo pieces pipetted up and down with a P1000 micropipette every 15-20 minutes. When the tissue was completely disaggregated, it was washed with PBS and centrifuged for 5 minutes at 200 x g and RT to pellet the cells. The solution was then resuspended in 12-14 ml of culture medium and left 10 minutes to let undigested pieces sediment at the

bottom. The clean solution was plated in a 100 mm Petri dish (Corning®, Falcon®) and cultured under 5 % (vol/vol) CO_2 and 37 ºC.

2.2 Human cell models

2.2.1 Cell lines

Cultured fibroblasts derived from skin biopsies taken from two unrelated patients, S2 and S6, carrying pathological mutations in *APOPT1* (Melchionda *et al.*, 2014) were used in this project. S6 and S2 primary fibroblasts were kindly provided by Dr. Enrico Bertini (Ospedale "Bambino Gesu", Rome, Italy) and Dr. Daniele Ghezzi (Neurological Institute "Carlo Besta", Milan, Italy), respectively. S2 carries a homozygous variant in *APOPT1*, c.235C>T (RefSeq accession number NM_032374.3) that is predicted to introduce a stop codon causing the synthesis of a truncated protein (p.Arg79∗; RefSeq NP_115750.2). S6 has two heterozygous mutations, the same present in individual S2 and a three-nucleotide deletion (c.370_372delGAA) causing the elimination of a highly conserved amino acid residue (p.Glu124del) (Melchionda *et al.*, 2014). Four other human skin fibroblasts lines (C1, C2, C3 and C4) were used as controls. Primary cultures were immortalised by lentiviral transduction with the pLOX-Ttag-iresTK, obtained from Didier Trono (Addgene plasmid # 12246) (see section 2.2.3).

In addition, two cancer cell lines were used for overexpression of different isoforms of APOPT1 tagged with either GFP or HA: HeLa (human cervical cancer cells) and 143B (human bone osteosarcoma cells).

2.2.2 Cell culture conditions

The different human cell lines were grown in DMEM containing 4.5 g/L D-glucose, sodium pyruvate and GlutaMAX™, supplemented with 10 % FBS, 100 units/ml penicillin and 0.1 mg/ml streptomycin (all from Life Technologies, Gibco®). The medium used to grow human skin fibroblasts with defects in

complex IV of the respiratory chain was supplemented with 50 µg/ml uridine (Sigma-Aldrich) to compensate the reduced synthesis of pyrimidine derivatives due to a decrease in the activity of the dihydroorotate dehydrogenase, which is an ETC-dependent enzyme that mediates the fourth step of *de novo* pyrimidine biosynthesis. After transduction with expression plasmids containing antibiotic selection cassettes, selective medium was prepared adding 1 µg/ml puromycin or 100 µg/ml hygromycin (both from Invitrogen). Cells were grown in humidified atmosphere at 37 °C and 5 % CO_2.

2.2.3 Lentiviral 2nd generation expression system

Both gene silencing and protein overexpression were performed using a second-generation lentiviral expression system, which allows for stable and heritable integration of a specific nucleic acid sequence into the target cell genome. Gene silencing was achieved by inserting a short hairpin RNA (shRNA) sequence in the expression plasmid. Once transcribed, the shRNA produces an artificial double stranded RNA molecule that silences target gene expression by RNA interference, a biological mechanism that degrades mRNAs (Moore *et al.*, 2010). Different shRNA, already cloned into the pLKO.1 vector (MISSION® shRNA Library, Sigma-Aldrich), were used for silencing each specific target gene. Overexpression of tagged proteins was achieved by inserting a specific cDNA sequence, cloned in the pWPXLd-based expression plasmid, for each protein. The components required for lentiviral particle generation are:

1. <u>Transfer/expression plasmid</u>: it encodes the insert of interest flanked by long terminal repeat (LTR) sequences which facilitate integration of the construct into the host genome and the promotors for expression in mammalian cells. For shRNA expression, the pLKO.1 plasmid (Addgene plasmid # 10878) was used, while for protein overexpression, pWPXLd-based vectors were employed (**Figure 2.4**).
2. <u>Packaging plasmid</u>: it encodes the proteins Gag, Pol, Rev, and Tat, essential for transcription and packaging of an RNA copy of the insert into

recombinant pseudoviral particles. The pSPAX2 (Addgene plasmid # 12260) vector was used (**Figure 2.4**).

3. Envelope plasmid: it encodes the envelope surface glycoproteins, which can be modified to change the cell type to be infected. In this case the vesicular stomatitis virus GP (VSV-G) glycoproteins were used, which have been shown to give lentiviral vectors a broad host-cell range (Cronin, Zhang and Reiser, 2005). Specifically, the pMD2.G (Addgene plasmid # 12259) vector was used (**Figure 2.4**).
4. Pseudoviral particle producer cell line: HEK 293T cells (a variant of the HEK 293 cells), which contain the SV40 T-antigen that allows episomal replication of transfected plasmids containing the SV40 origin of replication, leading to greater plasmid amplification and expression of the gene product.

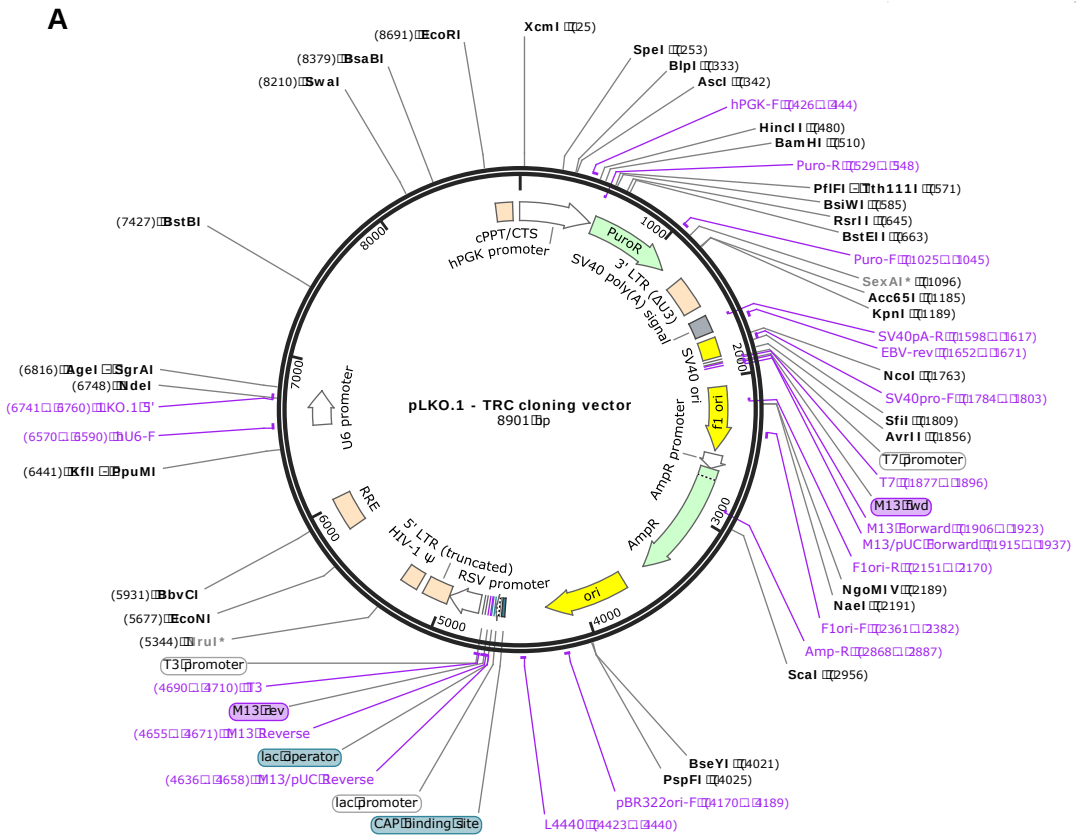

B

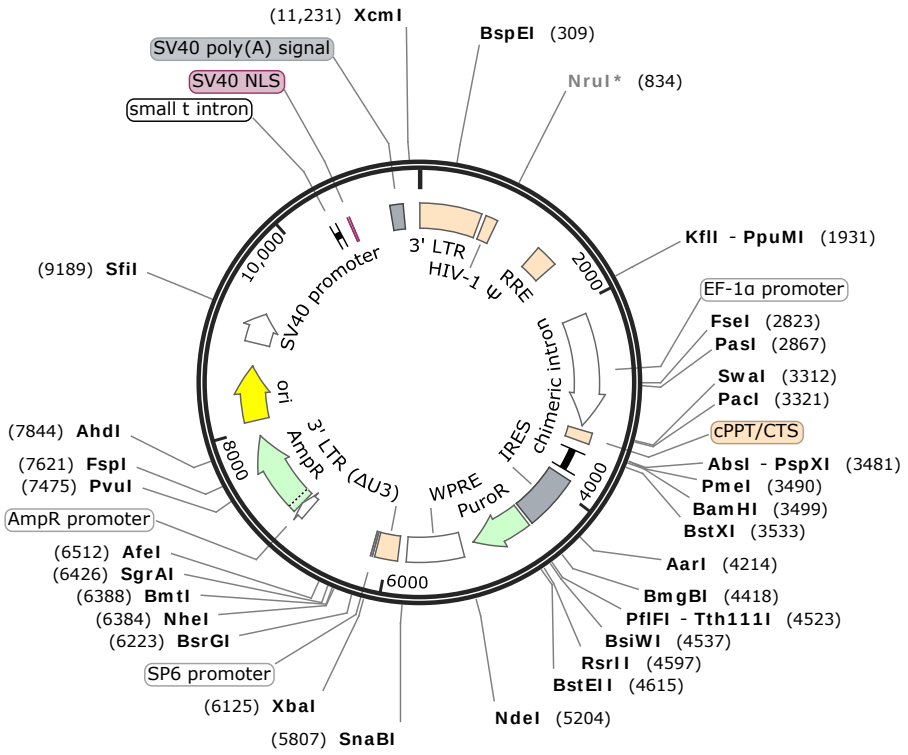
(11,231) XcmI
BspEI (309)
SV40 poly(A) signal
SV40 NLS
small t intron
NruI* (834)
KflI - PpuMI (1931)
(9189) SfiI
EF-1α promoter
FseI (2823)
PasI (2867)
SwaI (3312)
PacI (3321)
cPPT/CTS
AbsI - PspXI (3481)
PmeI (3490)
BamHI (3499)
BstXI (3533)
AarI (4214)
BmgBI (4418)
PflFI - Tth111I (4523)
BsiWI (4537)
RsrII (4597)
BstEII (4615)
NdeI (5204)
(5807) SnaBI
(6125) XbaI
SP6 promoter
(6384) NheI
(6223) BsrGI
(6388) BmtI
(6426) SgrAI
(6512) AfeI
AmpR promoter
(7621) FspI
(7475) PvuI
(7844) AhdI
10,000
2000
4000
6000
8000
SV40 promoter
3' LTR HIV-1
Ψ
RRE
chimeric intron
IRES
WPRE
PuroR
3' LTR (ΔU3)
AmpR
ori
pWPXLd-ires-PuroR
11,326 bp

C

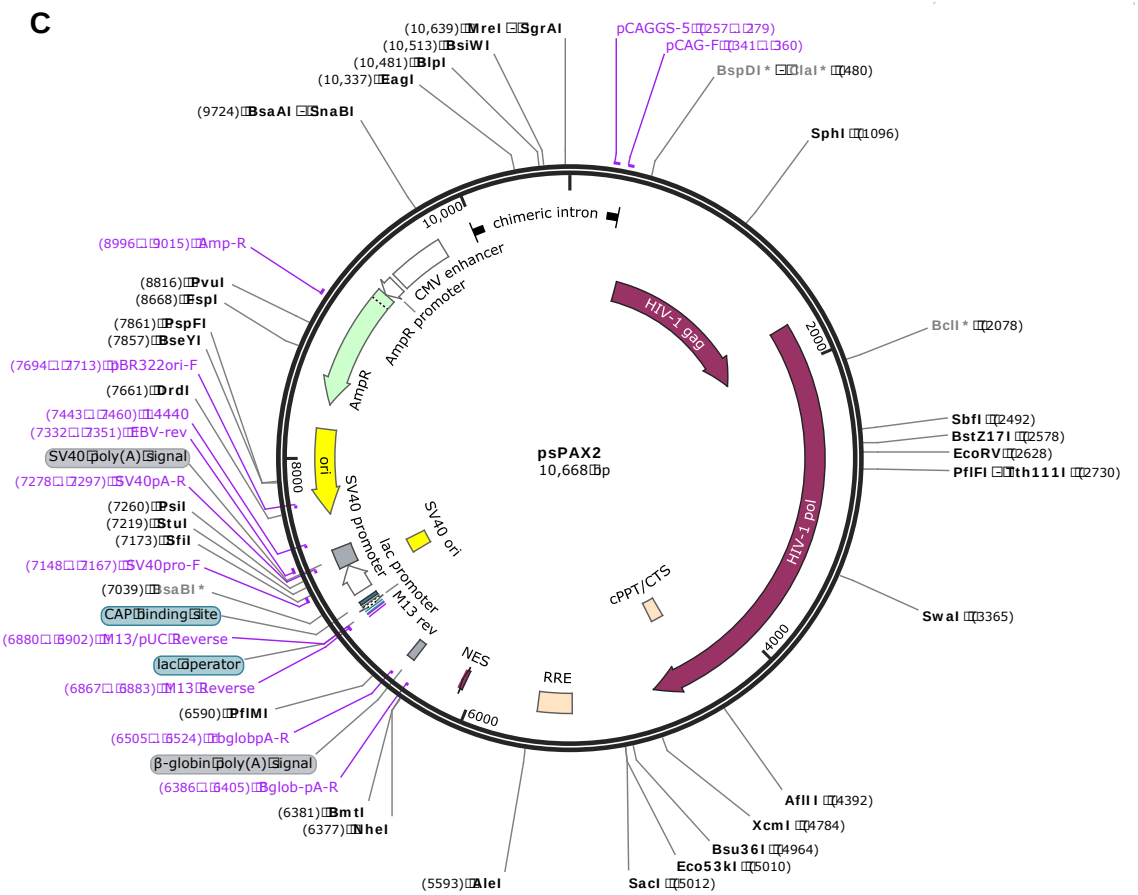
(10,639) MreI - SgrAI
(10,513) BsiWI
(10,481) BlpI
(10,337) EagI
(9724) BsaAI - SnaBI
pCAGGS-5 (257-279)
pCAG-F (341-360)
BspDI* - ClaI* (480)
SphI (1096)
(8996-9015) Amp-R
(8816) PvuI
(8668) BspI
(7861) PspFI
(7857) BseYI
(7694-7713) pBR322ori-F
(7661) DrdI
(7443-7460) 4440
(7332-7351) EBV-rev
SV40 poly(A) signal
(7278-7297) SV40pA-R
(7260) PsiI
(7219) StuI
(7173) SfiI
(7148-7167) SV40pro-F
(7039) BsaBI*
CAP binding site
(6880-6902) M13/pUC Reverse
lac operator
(6867-6883) M13 Reverse
(6590) PflMI
(6505-6524) bglobpA-R
β-globin poly(A) signal
(6386-6405) Bglob-pA-R
(6381) BmtI
(6377) NheI
(5593) AleI
SacI (5012)
Eco53kI (5010)
Bsu36I (4964)
XcmI (4784)
AflII (4392)
SwaI (3365)
4000
6000
RRE
cPPT/CTS
HIV-1 pol
NES
M13 rev
lac promoter
SV40 ori
SV40 promoter
ori
8000
AmpR
AmpR promoter
CMV enhancer
chimeric intron
10,000
2000
HIV-1 gag
BclI* (2078)
SbfI (2492)
BstZ17I (2578)
EcoRV (2628)
PflFI - Tth111I (2730)
psPAX2
10,668 bp

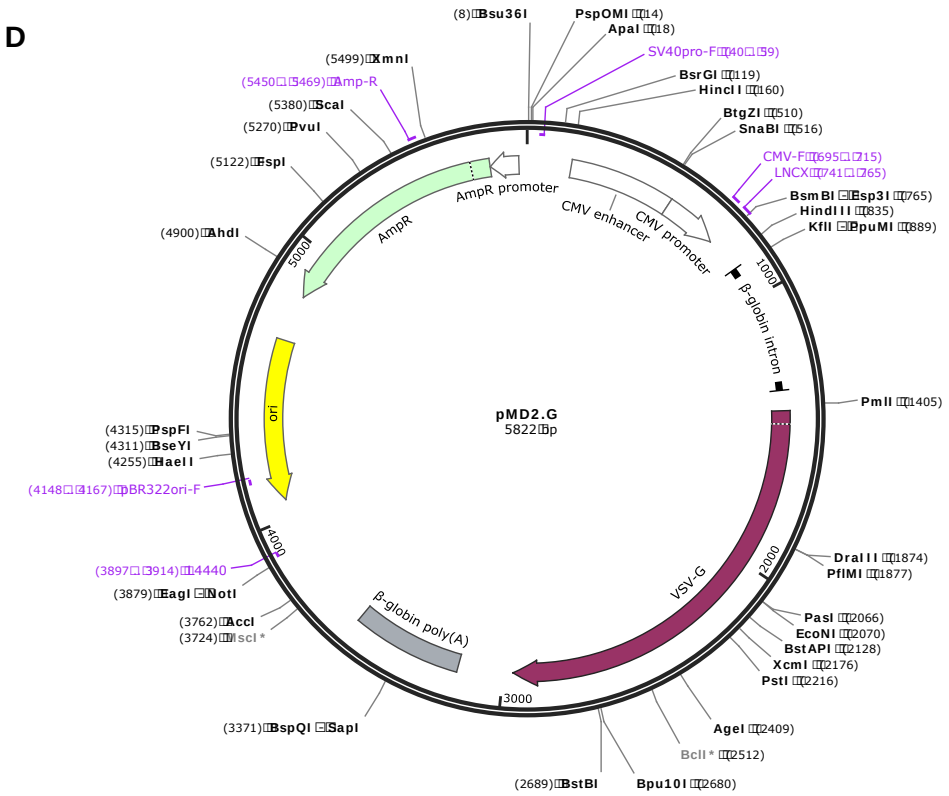

Figure 2.4 Vectors used for the lentiviral expression system. (**A**) pLKO.1: for shRNA expression, (**B**) pWPXLd: for protein overexpression. In this work, the pWPXLd-Ires-Puro^R and the pWPXLd-Ires-Hygro^R, which have puromycin and hygromycin, respectively, as a selectable marker, were used (**B**) psPAX2: plasmid encoding the polymerase and proteins for the viral capsid. (**C**) pMD2.G: plasmid encoding the proteins for the viral envelope.

The day prior to the transfection 2x10^6 HEK 293T cells were seeded on a 10-cm petri dish. The transfer, packaging and envelop plasmid mixture was prepared as described in **Table 2.2**.

Table 2.2 Mixture of reagents for transfection of HEK 293T cells.

Reagent	Volume
Transfer plasmid	Corresponding to 10µg
Packaging plasmid	Corresponding to 6.55µg
Envelope plasmid	Corresponding to 3.5µg
FUGENE	FUGENE:DNA ratio 3:1 → 60 µl
DMEM	Adjust to 1 ml

The mixture was incubated for 30 minutes at RT and then added to the medium of the producer HEK 293T cells. After 6-8 hours the transfection medium was replaced with fresh culture medium. During the following 48 hours, the expression constructs packaged in pseudoviral particles were secreted in the medium, which was then collected, centrifuged at 3,000 rpm, filtered through 0.45 µm pore size PVDF filters, mixed with 8µg/µL polybrene (to increase transduction efficiency) and added directly to the target cells, of which 2 x 10^6 cells per cm of dish were plated the previous day. 24 hours after the transfection, the medium was replaced with fresh culture medium and antibiotic, puromycin (1 µg/ml) or hygromycin (100 µg/ml), was added to select for the positively transduced cells.

2.2.4 Live cell imaging

Cell viability and growth were assessed using an IncuCyte HD instrument (Essen Bioscience,UK) and an algorithm to calculate cell confluency based on phase contrast microscope imaging of the plates. Images were taken every 2 hours for a total period of 7 days.

An IncuCyte ZOOM instrument (Essen Bioscience, UK) was used to monitor protein expression by detection of green fluorescence. Images were taken every hour for a total period of 4 days.

2.2.5 Immunofluorescence on fixed cells

Immunofluorescence labelling was used to demonstrate the presence and the subcellular localisation of different antigens. Cells were seeded on a collagen-coated 2cm-diameter coverslip in a multiwell plate (Corning® Costar®). For visualisation of the mitochondrial network, MitoTracker®RedCMXRos (Invitrogen) was added to the culture medium at a final concentration of 50 nM and incubated during 20-30 minutes at 37 ºC. Cells were then washed with PBS, fixed with 4 % (wt/vol) paraformaldehyde (PFA) for 15 minutes at 37 ºC, washed again and permeabilised for 5 minutes at RT with 0.3 % (vol/vol) Triton X-100 (Fisher Bioreagents) dissolved in 5 % FBS in PBS. After washing the coverslips,

one hour of blocking at RT was performed with 5 % FBS in PBS followed by incubation with the different primary antibodies, either for 2 hours at RT or overnight at 4 ºC. After washing, the coverslips were incubated with fluorescently labelled secondary antibodies for 1 hour at RT, washed again and let dry while protected from light. Slides were mounted using ProLong Gold antifade with 4',6-diamidino-2-phenylindole dihydrochloride (DAPI, Invitrogen). The fluorescence was detected in a confocal laser microscope (A1/A1R Confocal Microscope System, Nikon, UK).

2.3 General DNA-based methods

2.3.1 Retrotranscription of RNA

Total RNA was extracted from mice tissues or cultured cells using the TRIzol Plus RNA Purification System (Invitrogen-ThermoFisher Scientific). Briefly, the TRIzol® reagent was used to lyse the cells, chloroform was then added to the homogenate and samples were centrifuged. The RNA, contained in the upper aqueous phase, was then bound to the clear silica-based membrane in the PureLink™ RNA Mini Kit Spin Cartridge. Contaminants were washed, and RNA was eluted in RNase-Free water. Purified RNA was then treated with DNase (Turbo DNA-free, Life technologies) to remove any DNA traces and retrotranscribed with the Omniscript® Reverse Transcription kit (Qiagen) to obtain complementary DNA (cDNA) (**Table 2.3**).

Table 2.3 In vitro transcription reaction set-up.

Reagent	Volume/reaction	Final concentration
Transcription buffer (10X)*	2 µL	1 X
dNTP mix (5mM each)*	2 µL	0.5 mM each
Oligo-dT primer (10 µM)*[2]	2 µL	1 µM
Random hexamer*[3]	0.2 µL	0.6 µM
RNase inhibitor (10 U/µL)*[4]	1 µL	10 U
RNA template	variable	Up to 2 µg
Omniscript Reverse Transcriptase (4 U/µL)*	1 µL	4 U
RNase-Free Water to	20 µL	-

* Reagents included the Omniscript® Reverse Transcription kit (Qiagen).
*[2] Oligo ordered from Sigma-Aldrich.
*[3] Reagent from Thermo Fisher Scientific.
*[4] RNasin® from Promega.

2.3.2 Real-time reverse transcription PCR

To perform a relative quantification of gene expression levels, real-time reverse transcription-PCR, using pre-tested and validated specific Gene Expression TaqMan assays (Thermo Fisher Scientific) for each of the transcripts of interest (**Table 2.5**), was used. Reaction volumes were typically 20 µL, containing 1X TaqMan® Gene Expression Assay, 1X TaqMan® Gene Expression Master Mix, cDNA template (40 to 100 ng), and adjusted with RNase-free water. Each 20 µL amplification reaction mix was transferred into one well of a 96-well reaction plate, which was sealed and load in a Real-Time PCR System (Applied Biosystems 7900HT, Thermo Fisher Scientific, USA) for the amplification reaction following the cycling conditions described in **Table 2.4**. For each cDNA sample, three technical replicates were added to the plate. The reactions are set for the target and for the reference sequences, usually a house-keeping gene such as GAPDH, used as an internal standard for expression level normalisation.

Table 2.4 Real time PCR thermocycling conditions.

Step	Temperature	Time	Cycle
Initial denaturation	95 ºC	10 minutes	1
Denaturation	95 ºC	15 seconds	40
Annealing/Elongation	60 ºC	1 minute	

Table 2.5 Gene expression TaqMan assays used in this project.

Gene	Target species	TaqMan Assay ID
APOPT1	Mouse	Mm00509619_m1
COX4	Human	Hs00971639_m1
COX6b	Human	HS01086739_g1
Gapdh	Mouse	Mm9999915_g1
GAPDH	Human	Hs02758991_g1
Mt-Co1	Mouse	Mm04225243_g1
MT-CO1	Human	Hs02596864_g1
MT-CO2	Human	Hs02596865_g1
Nd1	Mouse	Mm04225274_s1
PET100	Human	Hs00418278_g1
PET117	Human	Hs01550880_g1

TaqMan probes contain a 6-carboxyfluorescein (FAM) fluorophore covalently attached to the 5’-end and a tetramethylrhodamine (TAMRA) quencher at the 3’-end. As long as the fluorophore and the quencher are close enough, the fluorescence is quenched. However, when the probe binds the specific DNA region, the Taq polymerase synthesise the new strand and degrades the probe, liberating the fluorophore and allowing fluorescence. The amplification cycle at which the fluorescence becomes measurable, i.e. crosses the background threshold, is called the threshold cycle (CT) or crossing point (**Figure 2.5**). The CT value is then used to calculate relative gene expression in target and reference samples using the Double Delta Ct analysis, detailed in (Livak and Schmittgen, 2001).

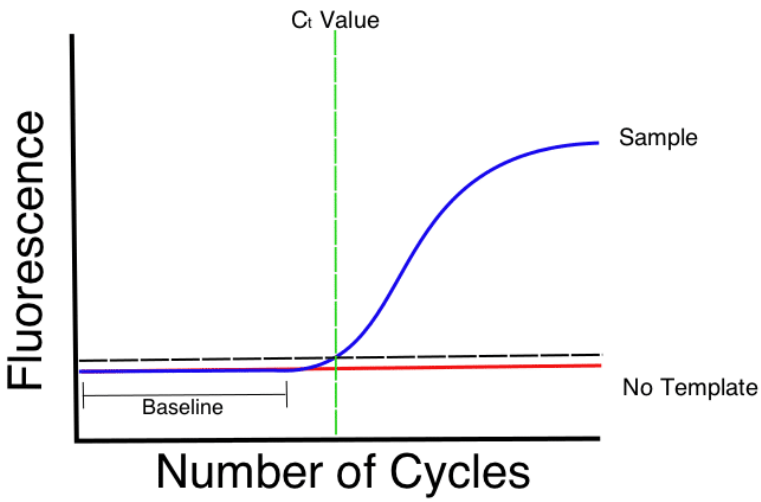

Figure 2.5 Graphical representation of real-time PCR data. Fluorescence is plotted against PCR number of cycles. The point in which fluorescence increases above the threshold (black dashed line) is called CT (green line). Image extracted from https://bitesizebio.com/.

2.3.3 PCR

PCR was used to generate multiple copies of the sequence of interest through three steps: 1) denaturation, in which the template DNA is denatured to single stranded molecules; 2) annealing, in which the designed oligonucleotide primers anneal to the complementary DNA sequences; and 3) extension, in which the DNA is extended from the primers, by the DNA polymerase enzyme.

All PCR reactions were performed using a thermocycler (TRIO Thermocycler, Biometra, Germany) and the amplification products were analysed by agarose gel electrophoresis (see section 2.3.4).

2.3.3.1 PCR primer design

PCR primers were designed manually (**Table 2.6**). Good primer design is essential for a successful PCR reaction. The most important factors considered were:

-Length: ideally between 19 and 21 bp, long enough to provide good specificity but short enough so it can easily bind the target DNA at the annealing temperature.

-Melting temperature (T_m): ideally between 55 and 80 ºC. T_m is defined as the temperature at which one half of the DNA dissociates to single strands. Both primers (forward and reverse) should have a very similar T_m. The formula used to calculate it was:

$$T_m = 4 \times (G + C) + 2 \times (A + T)$$

Where

G + C is the sum of guanine and cytosine bases

A + T is the sum of adenine and tymine bases

-GC content: the number of G's and C's in the primer as percentage of the total bases should be around 50 %.

-GC clamp: the presence of G or C bases in the 5' and 3' end of the primer helps specific binding due to the stronger bonding of G and C bases.

-Secondary structures, hairpins and cross dimers: should be avoided because they affect primer-template annealing and thus, amplification yield.

-Cross homology: primers designed for a sequence must not amplify other genes in the mixture. Homology of the primer to other genomic regions was checked using the BLAST software available in the NCBI website (https://blast.ncbi.nlm.nih.gov/Blast.cgi).

Table 2.6 List of primers used in this project.

Name	Sequence (5' -> 3')
APOPT1 cDNA Fw	AATGCTGCCGTGCGCCGC
APOPT1 cDNA Rv	TGCTTCCTGTGGAAACCTGG
APOPT1-M1-PmeI-Fw	GTTTAAACCATGCTGCCGTGCGCCGCG
APOPT1-M14-PmeI-Fw	GTTTAAACCATGGTGGTCTTGCGGGCGG
APOPT1-201-HA-Rv	TCAAGCGTAATCTGGAACATCGTATGGGTAGTT GCTCCTCTTCTTTTGTTTC
APOPT1-203-HA-Rv	TCAAGCGTAATCTGGAACATCGTATGGGTAATG TTGCTTTCTGACCTTAC
APOPT1-201-GFP-pCR-NdeI-Rv	CATATGGTTGCTCCTCTTCTTTTGTTTC
APOPT1-203-GFP-pCR-NdeI-Rv	CATATGATGTTGCTTTCTGACCTTAC
Apopt1_Ms_Exon2_Fw	CATAGAGTAAGGTGATGAGG
Apopt1_Ms_Exon2_Rv	CCAAAACCCGCATCAGAAAG
CRISPR_T3_gRNA-scaffold_Fw	AATTAACCCTCACTAAAGGTGTGAAAATGAACG GGACGAGTTTTAGAGCTAGAAATAGC
CRISPR_scaffold_Rv	AGCACCGACTCGGTGCCACT
MR1S-PmeI-Fw	GTTTAAACACCATGGCGGCGGTGGTAG
MR1S-HA-Rv	GGTCAAGCGTAATCTGGAAC
PET100-Fw	GAACTGGCTTTGTTGACCGG
PET100-FLAG-Rv	TCACTTGTCGTCATCGTCTTTGTAGTCGGAGTT CTGCTGGGCGTCGC
PET117-Fw	CAGCGTGGGGATGTCTAGG
PET117-FLAG-Rv	TCACTTGTCGTCATCGTCTTTGTAGTCTGATTTT TGAGATCCTTTTG

2.3.3.2 PCR for mouse genotyping

Mouse genomic DNA was extracted from ear punch samples using The Maxwell® RSC Tissue DNA Kit in combination with the Maxwell® RSC Instrument (Promega). The extracted DNA was then used for PCR amplification of *Apopt1* exon 2 (primers in **Table 2.6**). The reactions were performed using the GoTaq® DNA Polymerase kit (Promega). The 5X Green GoTaq® Reaction Buffer contains two dyes (blue and yellow) that separate during electrophoresis to monitor migration progress. It also contains $MgCl_2$ at a concentration of 7.5 mM. PCR reaction set-up and thermocycling conditions are detailed in the next table.

Table 2.7 PCR amplification using the GoTaq® DNA Polymerase kit.

(a) PCR amplification reaction set-up

Reagent	Final volume	Final concentration
Green GoTaq® Reaction Buffer (5X)*	5 µL	1X (1.5 mM $MgCl_2$)
PCR nucleotide Mix, 10 mM each	0.5 µL	0.2 mM each dNTP
Apopt1_Fw_MouseExon2 (100 µM)	1 µL	2 µM
Apopt1_Rv_MouseExon2 (100 µM)	1 µL	2 µM
DNA template (25 ng/µL)	2	1ng/µL
GoTaq® DNA polymerase (5 u/µL)*	0.25 µL	1.25 U
Nuclease-Free Water to	25 µL	

* Reagents included in the GoTaq® DNA Polymerase kit (Promega).

(b) Thermocycling conditions

Step	Temperature	Time	Cycle
Initial denaturation	95 ºC	10 minutes	1
Denaturation	95 ºC	30 seconds	30
Annealing	56 ºC	45 seconds	
Elongation	72 ºC	1 minute	
Final elongation	72 ºC	5 minutes	1
Hold	4 ºC	∞	1

The presence or absence of the *Apopt1* mutation in the mouse biopsies was detected by Sanger sequencing of the purified PCR products (see sections 2.3.5 and 2.3.10).

2.3.3.3 PCR for cloning

PCR amplifications for cloning purposes were performed using the BIOTAQ™ DNA Polymerase kit (Bioline). PCR reactions were set up as detailed in **Table 2.8** and the thermocycling conditions (annealing temperature and extension times) were optimised for each specific reaction (**Table 2.8**).

Table 2.8 PCR amplification using the BIOTAQ™ DNA Polymerase kit.

(a) PCR amplification reaction set-up

Reagent	Volume/reaction	Final concentration
BIOTAQ™ Reaction Buffer (10X)*	5 µL	1X
$MgCl_2$ 50mM*	2.5 µL	2.5 mM
PCR nucleotide Mix, 10 mM each	1 µL	0.2 mM each dNTP
Forward primer (10 µM)	2 µL	0.4 µM
Reverse primer (10 µM)	2 µL	0.4 µM
Template gDNA (50 ng/µL) or cDNA template	1 µL (4 µL)	1ng/µL
BIOTAQ™ DNA polymerase (5 u/µL)*	0.25 µL	1.25 U
Nuclease-Free Water to	50 µL	

* Reagents included in the BIOTAQ™ DNA Polymerase kit (Bioline).

(b) Thermocycling conditions

Step	Temperature	Time	Cycle
Initial denaturation	95 ºC	3 minutes	1
Denaturation	95 ºC	30 seconds	30
Annealing	50-60 ºC	30 seconds-2 minutes	
Elongation	72 ºC	1 minute/kb	
Final elongation	72 ºC	5 minutes	1
Hold	4 ºC	∞	1

2.3.4 Agarose gel electrophoresis

Agarose gel electrophoresis was used for the separation of DNA fragments of varying sizes. 1 % agarose gels were used for general applications, 0.7-0.8 % when resolving plasmids (>5 kb) and 1.5 % for smaller fragments (<0.5 kb). Gels were cast with the appropriated percentage [w/v] of agarose (Thermo

Scientific) dissolved in 50 ml Tris/Borate/EDTA (TBE) buffer (89 mM Tris-borate, 100 mM boric acid, 2 mM ethylenediaminetetraacetic acid (EDTA) and 5 µL of SYBR Safe dye (10,000X, Invitrogen). TBE buffer was also used as the running buffer. DNA samples were mixed with loading dye (6X) at a 5:1 volume ratio and were always run alongside the 1kb Plus DNA ladder (Invitrogen). Gel electrophoresis was performed at voltage of 100 V (EM100, Mini Gel Unit, Engineering & Design Plastics, UK). An ultraviolet (UV) light transilluminator (Gel Doc™ Imaging System, Bio-Rad, UK) was then used to visualise the separated DNA fragments.

2.3.5 PCR-amplified DNA purification

PCR-amplified DNA was purified from reaction mixtures using the QIAquick PCR Purification kit (Qiagen). Briefly, a high-salt binding buffer is added to the PCR sample. The mixture is then applied to the QIAquick spin column, where DNA binds to the membrane. Impurities are then washed, and the DNA is eluted using a low-salt buffer.

2.3.6 DNA digestion

DNA plasmids were digested at 37 ºC for 2-4 hours with the restriction enzymes: *Pme*I, *Bam*HI, *Eco*RI, *Sph*I or *Bbs*I, (New England Biolabs) according to manufacturer's instructions. Reaction volumes were either 10 or 20 µL. After digestion, all vectors were dephosphorylated (to avoid self-ligation) by adding 1 µL of phosphatase for each 10 µL of reaction volume and incubating at 37 ºC for 30 minutes. DNA fragments were then separated on 1 % (w/v) agarose gels. The band corresponding to the fragment of interest (either the linearised vector or the insert) was excised from the gel and purified using the QIAquick Gel extraction kit (Qiagen). Briefly, gel slices are dissolved at 50 ºC in a high-salt binding buffer. The mixture is then applied to the QIAquick spin column, where DNA binds to the membrane. Impurities are then washed, and the DNA is eluted using a low-salt buffer.

2.3.7 DNA ligation

PCR products were cloned directly into the pCR2.1 vector using the TOPO TA cloning kit (Invitrogen), which has a linearised and Topoisomerise I-activated pCR2.1 vector with 3´-T overhangs that allow quick ligation (10 minutes at RT) with the A overhangs added by the Taq polymerase at the 3' ends of the PCR products.

The restriction enzyme digested (see section 2.3.6) inserts and vectors, were ligated using T4 DNA ligase (New England Biolabs). Ligation reactions of 10 µL containing 1X reaction buffer and 6 U/µL of ligase were set up at a 1:3 vector:insert ratio and incubated at 16 °C overnight. 50 ng of linearised vector were used and the amount of insert required was determined using the following equation:

$$ng\ of\ insert = \frac{3}{1}\ x\ \frac{length\ of\ insert\ in\ kb}{lenght\ of\ vector\ in\ kb}\ x\ 50\ ng\ vector$$

T4 DNA ligase was then heat inactivated at 65°C for 5 minutes. Ligation products were kept at -20°C until used for transformation into DH5-alpha chemically competent *E. coli* cells (see section 2.3.8).

2.3.8 Plasmid preparation

2.3.8.1 Transformation of *E. coli* chemically competent cells

2 µL of the ligation reactions (section 2.3.7) were added to a 100 µl aliquot of Subcloning Efficiency™ DH5α™ Competent Cells (Invitrogen). A heat shock of 45 seconds was performed in a thermoblock (AccuBlock Digital Dry Baths, Labnet, UK) at 42 ºC. Cells were recovered by adding 300 µl of SOC medium (2 % tryptone, 0.5 % yeast extract, 10 mM NaCl, 2.5 mM KCl, 10 mM MgCl2, 10 mM MgSO4, and 20 mM glucose) and incubation at 37 ºC for 1 hour with shaking at 225 rpm. 150 µL of the transformed cells were plated onto a LB (10 g/L

tryptone, 5 g/L yeast Extract, 5 g/L NaCl) agar plate with 100 µg/ml ampicillin and incubated at 37 ºC overnight.

2.3.8.2 Colony replication and plasmid DNA isolation

Single white positive colonies, i.e. with the sequence of interest inserted in the vector interrupting the coding region of the lacZ enzyme and therefore lacking the ability to metabolise X-gal substrate that produces an insoluble blue dye (negative blue colonies), were picked and grown overnight in 5 ml LB-medium supplemented with 100 µg/ml ampicillin at 37 ºC with shaking at 225 rpm. DNA plasmids from the overnight cultures were isolated using the QIAprep Spin Miniprep kit (Qiagen). Briefly, bacterial cultures were lysed and the cellular debris was separated by centrifugation. Cleared lysates were then applied to the QIAprep 2.0 column, where DNA binds to the membrane. Impurities were washed and pure DNA was eluted in elution buffer.

2.3.9 Long-term storage of *E. coli* transformed cells

Microbank™ vials (Pro-Lab Diagnostics), containing porous beads and cryopreservative fluid, were used for the long-term storage of *E. coli* transformed cells. A young colonial growth (18-24 hours) picked from a pure culture was used to inoculate the beads and fluid of the vial which was then stored at -80 °C.

2.3.10 DNA sequencing

PCR products and cloned plasmids were always verified by DNA Sanger sequencing (Source Bioscience UK Ltd., Cambridge, UK) and analysed by sequence alignment using Basic Local Alignment Search Tool (BLAST) online (accessible at https://blast.ncbi.nlm.nih.gov/Blast.cgi). Sequencing primers are listed in **Table 2.5**.

2.3.11 Cloning of MR-1S, PET100, PET117 and APOPT1 cDNA

For the amplification of MR-1S, PET100, PET117 and APOPT1 cDNA, total RNA was extracted and retrotranscribed (see section 2.3.1) from HeLa and HEK293T cells. Approximately 200 ng of cDNA were used as templates for the PCR amplification (see section 2.3.3.3) of MR-1S, PET100, PET117 and APOPT1 using specific primers (see section 2.3.3.1). C-terminal hemagglutinin (HA) tags were added to APOPT1 and MR-1S as well as FLAG tags were added to PET100 and PET117 by PCR amplification. The GFP tag was added to APOPT1 by cloning a stop codon-less APOPT1 cDNA in frame with EGFP already inserted into pCR2.1. The PCR generated fragments, cloned into the pCR2.1 TA-cloning vector (Invitrogen) (see section 2.3.7), were checked for mutations by Sanger sequencing (see section 2.3.10). Then, the cDNA encoding the tagged version of each gene was excised by restriction enzyme digestion with PmeI and BamHI (see section 2.3.6), purified (see section 2.3.6) and ligated into pWPXLd-ires-PuroR and pWPXLd-ires-HygroR lentiviral expression vectors (see section 2.2.5), modified versions of the pWPXLd lentiviral expression vector (Addgene #12258), using T4 DNA ligase (see section 2.3.7).

2.4 Protein-based methods

2.4.1 SDS-PAGE

Cells were harvested by trypsinisation (Trypsin-EDTA 0.5 %), washed twice with PBS and lysed with 2 % n-dodecyl-β-D-maltoside (DDM) in PBS with the addition of protease inhibitors (Complete™ Mini EDTA-free Protease Inhibitor Cocktail, Roche). Lysates were mixed for 15 minutes and 4 ºC in a mini lab rotator (PTR-35, Grant Bio™, UK) and then centrifuged for 20 minutes at 20,000 x g and 4 ºC. Cleared supernatants were collected and protein concentration was determined (see section 2.4.2).

Small pieces of around 50 mg of frozen mice tissue were homogenised in 10 volumes of 50 mM Tris-HCl, 1 % Triton X-100, 1mM DTT pH 7.6 with protease

inhibitors (Complete™ Mini EDTA-free Protease Inhibitor Cocktail, Roche) in a Dounce-type glass homogeniser using a manually-driven glass pestle (10-15 strokes, depending on the tissue). The homogenate was left on ice for 15 minutes and then centrifuged at 16,900 x g for 10 minutes at 4 °C. Cleared supernatants were collected and protein concentration was determined (see section 2.4.2).

Between 5 and 50 µg of protein were mixed with 2X Laemmli sample buffer (126 mM Tris-HCl pH 6.8, 20 % glycerol, 4 % sodium dodecyl sulfate (SDS) and 0.02 % bromophenol blue) and run through a polyacrylamide 4-12 %, 10 % or 12 % SDS-PAGE gel (NuPAGE® Novex® Bis-Tris gels, Thermo Fisher Scientific) at a fixed voltage of 130 V for 90 minutes. The running buffer used for optimal separation of medium- to large-sized proteins was NuPAGE® MOPS SDS Running Buffer (1X: 50 mM MOPS, 50 mM Tris Base, 0.1 % SDS, 1 mM EDTA, pH 7.7). For the best separation of small proteins, the buffer of choice was NuPAGE® MES SDS Running Buffer (1X: 50 mM MES, 50 mM Tris Base, 0.1 % SDS, 1 mM EDTA, pH 7.3.

2.4.2 Protein concentration determination

Protein concentration was determined using a modified version of the Lowry protein assay (DC™ Protein Assay, detergent compatible, Bio-Rad). In this biochemical assay, a change in the colour of the sample solution (chemistry of the assay detailed in (Lowry *et al.*, 1951), which is proportional to the total protein concentration, is measured using a spectrophotometer. The absorbance of the protein sample with unknown concentration and of six BSA standards in a concentration range from 0 to 2 mg/ml were measured at λ=750 nm on a SpectraMax Plus384 plate reader (Molecular Devices, Sunnyvale, CA, USA). The absorbance vs. concentration of the known standards was plotted and the resulting calibration curve was used to determine the concentration of the protein sample of interest by interpolation of its absorbance value.

2.4.3 Blue-Native-Gel Electrophoresis (BN-PAGE)

BN-PAGE was used for the separation of mitochondrial complexes in non-denaturing conditions, i.e. solubilisation of the mitochondrial membranes using a neutral mild detergent such as DDM or digitonin (Schägger and Von Jagow, 1991).

Cells were permeabilised with 8 mg/ml digitonin and then washed twice with PBS by centrifugation at 10,000 x g for 5 minutes at 4 ºC. The pellet, enriched in mitochondria, was resuspended in 1.5 M aminocaproic acid, 50 mM Bis-Tris/HCl pH 7 and 1 % DDM or 2 % digitonin), incubated for 5 minutes on ice and centrifuged at 18,000 x g for 30 minutes at 4 ºC (Klement *et al.*, 1995; Nijtmans, Henderson and Holt, 2002).

Small pieces of around 50 mg of frozen mice tissue were homogenised in 10 volumes of Medium A (320 mM sucrose, 1mM EDTA, 10mM Tris-Hcl, pH 7.4) in a Dounce-type glass homogeniser using a manually-driven glass pestle, 5-15 strokes. The homogenate was centrifuged at 800 x g for 5 minutes at 4 ºC to remove nuclei and debris. The supernatant was collected and centrifuged at 9,000 x g for 10 minutes at 4 ºC to obtain an enriched mitochondrial fraction. The obtained pellet was then resuspended in Medium A. Protein concentration was determined and the samples were centrifuged again at 9,000 x g for 5 minutes at 4 ºC. The pellet was resuspended in the appropriated amount of 1.5 M aminocaproic acid, 50 mM Bis-Tris/HCl pH 7 to obtain a protein concentration of 10 mg/ml. Samples were solubilised with 1.6 mg DDM/mg protein, incubated in ice for 5 minutes and centrifuged at 18,000 x g for 30 minutes at 4 ºC.

Cleared supernatants from the high-speed centrifugations were mixed with sample buffer (750 mM aminocaproic acid, 50 mM Bis-Tris, 0,5 mM EDTA and 5 % Serva Blue G-250) and run through a 3-12 % Native-PAGE gel (NativePAGE™ Novex™ Bis-Tris Gels, Thermo Fisher Scientific) at 10 mA. The cathode buffer was 50 mM Tricine, 15 mM Bis-Tris, 0.02 % Serva blue G-250, pH 7.4 and the anode buffer 50 mM Bis-Tris, pH 7.4. The cathode buffer requires a constant supply of negative charges (from the Serva blue G-250) to keep the proteins negatively charged, which ensures their electrophoretic mobility and their separation in the gel according to molecular weight differences.

After first dimension (1D), run in native conditions, a denaturing second dimension (2D) can be performed to separate the different subunits from the native complexes. For that, each lane was cut, denatured with 1 % SDS and 1 % β-mercaptoethanol for 1 hour at RT and then run through a 4-12 % SDS-PAGE gel (NuPAGE® Novex® Bis-Tris Protein Gels, 1.0 mm, 2D-well, Thermo Fisher Scientific).

2.4.4 Western blot (WB)

Proteins separated both through SDS-PAGE and BN-PAGE gels were electroblotted to methanol activated PVDF membranes (Immobilon-P Membrane, Merck Millipore) using a wet transfer system (Mini-PROTEAN® Tetra Cell, Mini Trans-Blot® Module, Bio-Rad, UK). Transfer of SDS-PAGE was performed at 4 ºC and 100 V for one hour in transfer buffer (25 mM Tris-HCl, 192 mM Glycine, 20 % methanol (v/v) and 0.025 % SDS). Blotting of BN-PAGE was done at 4 ºC and 300 mA for one hour in bicarbonate transfer buffer (10 mM $NaHCO_3$, 3 mM $NaCO_3$).

2.4.5 Immunodetection

PVDF membranes, with immobilised proteins, were blocked with 5 % milk in PBS with 0.1 % Tween 20 (PBS-T) either for one hour at room temperature or overnight at 4 ºC, washed three times for 10 minutes with PBS-T and immunodecorated by incubation with different specific antibodies diluted at the appropriate concentrations in 3 % BSA in PBS-T (**Table 2.9**).

Table 2.9 List of antibodies used in this project.

Antigen	Type	Incubation conditions	Company	Catalog number
ACO2	Mouse monoclonal	1:10,000 o/n, 4 ºC	Abcam	6F12BD9
APOPT1	Rabbit polyclonal	1:1,000 o/n, 4 ºC	Proteintech	27300-1-AP
APOPT1	Rabbit polyclonal	1:1,000 o/n, 4 ºC	ProteoGenix	8992-A01
APOPT1	Chicken	1:1,000 o/n, 4 ºC	Agrisera	2218
APOPT1	Rabbit polyclonal	1:1,000 o/n, 4 ºC	Antibodies Online	ABIN1492361
AIF	Mouse monoclonal	1:1,000 o/n, 4 ºC	Santa Cruz	sc-13116
AK2	Rabbit monoclonal	1:3,000, o/n, 4 ºC	Abcam	ab166901
COX4	Mouse monoclonal	1:3,000 o/n, 4 ºC	Abcam	ab14744
COX5A	Mouse monoclonal	1:1,000 o/n, 4 ºC	Abcam	ab110262
COX5B	Mouse monoclonal	1:1,000 o/n, 4 ºC	Abcam	ab110263
COX6B	Mouse monoclonal	1:1,000 o/n, 4 ºC	Abcam	ab110266
GAPDH	Mouse monoclonal	1:5,000 o/n, 4 ºC	Abcam	ab8245
GFP	Mouse monoclonal	1:10,000 o/n, 4 ºC	Abcam	ab1218
HA	Rat monoclonal	1:1,000 o/n, 4 ºC	Roche	11 867 431 001
HIF-1α	Mouse monoclonal	1:500 o/n, 4 ºC	BD Science	BD 610959
HSP70	Mouse monoclonal	1:1,000 o/n, 4 ºC	Abcam	ab2787
MTCO1	Mouse monoclonal	1:3,000 o/n, 4 ºC	Abcam	ab14705
MTCO2	Mouse monoclonal	1:10,000 o/n, 4 ºC	Abcam	ab110258
MTCO2	Rabbit polyclonal	1:2,000 o/n, 4 ºC	Abcam	ab91317
MTCO3	Mouse monoclonal	1:5,000 o/n, 4 ºC	Abcam	ab110259
NDUFS1	Rabbit polyclonal	1:1,000 o/n, 4 ºC	Abcam	ab102552
PNKD (MR-1S)	Rabbit polyclonal	1:1,000 o/n, 4 ºC	Atlas Antibodies	HPA010134
SDHB	Mouse monoclonal	1:10,000 o/n, 4 ºC	Abcam	ab14714
SOD2	Mouse monoclonal	1:2,000 o/n, 4 ºC	Abcam	ab16956
BETA-TUBULIN	Mouse monoclonal	1:10,000 o/n, 4 ºC	Sigma	T5201
TOM20	Rabbit monoclonal	1:10,000 o/n, 4 ºC	Abcam	ab186734
UBIQUITIN	Mouse monoclonal	1:2,000 o/n, 4 ºC	Invitrogen	13-1600
UQCRC2	Mouse monoclonal	1:2,000 o/n, 4 ºC	Abcam	ab14745

After the incubation with the primary antibodies, the membranes were washed three times at room temperature. For the detection, either anti-mouse, anti-rabbit, anti-chicken (all from Promega) or anti-rat (Santacruz) secondary antibodies conjugated to the enzyme horseradish peroxidase (HRP) and diluted 1:1,000 to 1:10,000 in 5 % milk were incubated for one hour at room temperature. The membranes were incubated with ECL Western Blotting Detection Reagent (GE Healthcare, Chalfont St Giles, UK) according to manufacturer's instructions. Protein bands were then visualised on X-ray films (Fujifilm, Tokyo, Japan) at different exposure times, and developed using an X-ray film processor (ECOMAX, Protec, Germany).

2.4.5.1 Development of an antibody against APOPT1

Four different antibodies were tested against the human APOPT1 protein (see results in Chapter 5). Two were commercially available: one raised against the C-terminal of the human APOPT1 protein: KEFLSKNFQKHMYYNRDWYKRNFAITFFMGKVALERIWNKLKQKQKKRSN (ABIN1492361, Antibodies Online); and one raised against the full-length human APOPT1 protein (anti-C14orf153) by Proteintech (27300-1-AP). The other two were custom-made antibodies. In the first case, the antibody was produced by Agrisera (228) in hens immunised against the human APOPT1 peptide: LRTESGQKATLNAEEMAD. In the second case, the antibody was produced by ProteoGenix (8992-A01) in rabbits immunised against the full-length human APOPT1 protein (anti-C14orf153). The purified antibodies were then tested.

2.4.6 Mitochondria isolation for localisation studies

Mitochondrial isolation was performed as described in Fernandez-Vizarra et al. (Fernández-vizarra *et al.*, 2010) by differential centrifugation. About $4x10^8$ cells were harvested and washed with cold PBS. The pellet was resuspended in hypotonic homogenisation buffer (IB 0.1X: 3.5 mM Tris-HCl, pH 7.8, 2.5 mM NaCl, 0.5 mM $MgCl_2$) to facilitate the breakage of the cells by homogenisation

with a motor-driven Teflon pestle. Immediately after this, 1/10 of the initial volume of cells of hypertonic buffer (IB 10X) was added to make the medium isotonic. The homogenate was transferred to a 15-ml Falcon tube and centrifuged at 1,000 x g for 5 minutes at 4 °C in order to pellet unbroken cells, debris and nuclei. The supernatant was transferred to a clean tube and the remaining pellet was homogenised again. The second supernatant obtained was added to the first supernatant and these were centrifuged again in the same conditions to remove any remaining debris. The supernantant was transferred to four 1.5 ml Eppendorf tubes and mitochondria were then isolated by centrifugation at 13,000 rpm in a refrigerated microfuge for 2 minutes at 4 °C ('mitochondrial fraction'). The pellets were washed several times, transferring the material into a single tube, using homogenisation medium (0.32 M sucrose, 1 mM EDTA, and 10 mM Tris-HCl, pH 7.4). The supernatant obtained after the first high-speed centrifugation ('post-mitochondrial fraction') was kept for posterior analysis.

2.4.6.1 Mitochondrial subfractionation and carbonate extraction

Soluble and membrane mitochondrial fractions were separated by resuspending the mitochondrial pellet in PK buffer (20 mM Potassium Phosphate pH 7.8; 150 mM KCl), followed by sonication (3 pulses of 10 seconds at 10 % amplitude) and centrifugation at 100,000 x g at 4°C for 30 minutes to separate the supernatant containing the soluble proteins ('mitochondrial soluble fraction') and the membrane-associated proteins in the pellet (mitochondrial membrane fraction'). To split the peripherally bound from the integral membrane proteins, the pellets obtained in the previous centrifugation step were resuspended in a buffer containing 0.1 M Na_2CO_3, pH 10.5, 0.25 M sucrose and 0.2 mM EDTA; incubated for 30 min on ice and then centrifuged at 100,000 x g for 30 minutes at 4 °C to separate the pellet ('Na_2CO_3 pellet fraction) from the supernatant containing the loosely-bound membrane proteins ('Na_2CO_3 soluble fraction'). The presence or absence of the proteins of interest was analysed by SDS-PAGE, WB and immunodetection in the total homogenates and in each of the fractions.

2.4.6.2 Sub-mitochondrial localisation

For sub-mitochondrial localisation, mitochondria were isolated as described in section 2.4.6 and split in aliquots of 0.5 mg of protein.

Digitonin treatment: Mitochondria were treated with increasing amounts of the detergent digitonin (from 0 to 1200 µg), which disrupts the OMM, for 10 minutes at 4 °C followed by incubation with 50 µg/ml trypsin for 30 minutes at RT. Samples were centrifuged at 9,000 x g for 10 minutes at 4 °C and only the pellet was kept for SDS-PAGE, WB and immunodetection analysis.

Hypotonic shock: Mitochondria were then incubated with a hypotonic buffer solution (5 mM sucrose, 10 mM Tris-HCl, pH 7.4, 1 mM EDTA), which produces osmotic swelling in the mitochondrial space, for 5 and 15 minutes on ice. Since the IMM has a larger surface area than the OMM, upon osmotic swelling of the matrix, the IMM can expand until it physically breaks the OMM. Samples were then incubated with 50 µg/ml trypsin for 30 minutes at RT. Samples were centrifuged at 9,000 x g for 10 minutes at 4 °C and both the pellet and the supernatant were kept for SDS-PAGE, WB and immunodetection analysis.

Both treatments disrupt the OMM, generating ‘mitoplasts’, which contain only the IMM and the matrix. Thus, proteins in the IMS or IMM facing the IMS become more and more accessible to proteolysis after treatment with increasing concentrations of digitonin or hypotonic shock. Instead, IMM proteins facing the matrix and matrix proteins should remain undigested during all treatments. A positive control for proteolysis was done treating with trypsin and 1 % Triton X-100 for maximum solubilisation of membranes.

2.4.7 Oxidative stress treatment in cell cultures

H_2O_2 was added once (‘bolus’) to the culture medium at a concentration of 100 µM. The exact concentration of the H_2O_2 solution stock was determined by measuring the absorbance at λ = 240 nm in an UV-visible spectrophotometer and a quartz cuvette. The molar extinction coefficient was considered to be ε = 43.6

$M^{-1}cm^{-1}$. Cells were harvested 5 and 10 minutes and 3, 6, 10 and 20 hours after the addition of H_2O_2 to the medium.

On the other hand, to generate ROS continuously and selectively within mitochondria, Mitoparaquat (MitoPQ) was used (Robb *et al.*, 2015). 143B cells overexpressing APOPT1^{HA} or APOPT1^{GFP} plus WT, mutated and APOPT1^{GFP} complemented fibroblasts were treated with 5 µM MitoPQ. Cells were harvested 10 and 30 minutes and 3, 6 and 20 hours after the addition of MitoPQ.

The effect of oxidative stress in the proteins of interest at different time points was analysed by SDS-PAGE, WB and immunodetection.

2.4.8 Proteasome inhibitor treatment in cell cultures

To investigate APOPT1 degradation by the UPS, 143B cells transduced with the 'empty vector' or APOPT1^{HA} were treated with 10 µM MG132, a potent proteasome inhibitor, for 2 and 6 hours. The effect of proteasomal inhibition in the precursor and mature forms of APOPT1 was analysed by SDS-PAGE, WB and immunodetection.

2.4.9 Immunoprecipitation assay to assess protein ubiquitination

For isolation of APOPT1^{HA}, an immunoprecipitation assay using an anti-HA antibody was performed. $1x10^7$ 143B cells transduced with the 'empty vector' or APOPT1^{HA} were incubated with 10 µM MG132 for 2 hours and then lysed in RIPA buffer (50 mM Tris pH 7.4, 0.1 % SDS, 1 % NP40, 0.5 % Na deoxycholate, 150 mM NaCl) with the addition of protease inhibitors (Complete™ Mini EDTA-free Protease Inhibitor Cocktail, 100 mM NEM and 100 mM IAA). Untreated cells, from the same two cell lines, were used as controls. Lysates were centrifuged at 16,900 x g for 10 min. The clear supernatant was centrifuged at 50,000 rpm for 1 hour, before samples were pre-cleared using sepharose CL4B for (1 hour, 4 °C). Samples were then incubated with 10 µL EZviewTM Red Anti-HA beads (Sigma-Aldrich) overnight at 4 °C. Resins were washed 5 times with RIPA buffer and the bound proteins were eluted using 40 µL 100 µg/ml HA peptide (Sigma-Aldrich)

(in 0.5 % NP40 with protease inhibitors) for 1 hr at 4 °C. Protein samples in loading buffer were heated at 75°C for 10 minutes. The presence or absence of ubiquitinated APOPT^{HA} in the eluate was analysed by SDS-PAGE, WB and immunodetection with an anti-ubiquitin antibody.

2.4.10 FLAG immunoprecipitation

For isolation of PET100^{FLAG} and PET117^{FLAG}, immunopurification using an anti-FLAG antibody was performed. 1x10^{7} PET100^{G48*} fibroblasts transduced with the 'empty vector', PET100^{FLAG} or PET117^{FLAG} were resuspended in lysis-buffer: PBS with 10 % (w/v) glycerol, protease inhibitor (Complete™ Mini EDTA-free Protease Inhibitor Cocktail), 1X lipid stock (10X stock: 0.9 mg/ml 1-palmitoyl-2-oleoyl-glycero-3-phosphocholine (POPC), 0.3 mg/ml 1-hexadecanoyl-2-(9Z-octadecenoyl)-sn-glycero-3-phosphoethanolamine (POPE), 0.3 mg/ml 1-palmitoyl-2-oleoyl-sn-glycero-3-phospho-(1'-rac-glycerol) (POPG), Avanti Polar Lipids) and 1.5 % (w/v) DDM, and incubated for 30 minutes at 4°C. Lysates were centrifuged at 16,900 x g for 15 min. Clear supernatants were filtered using spin-X-columns (Costar). The samples were incubated with anti-FLAG-M2-agarose (Sigma-Aldrich) overnight at 4°C in rotation. The unbound material was collected and affinity resins were washed 8-10 times with buffer containing 0.05 % DDM. Bound material was eluted using 5 mg/ml FLAG peptide (Sigma-Aldrich). The presence or absence of FLAG-tagged and other proteins in the eluate was analysed by SDS-PAGE, WB and immunodetection.

2.4.11 Quantitative SILAC mass spectrometry (MS)

The two cell lines to be compared by SILAC MS were grown in 'heavy' DMEM containing ^{15}N- and ^{13}C- labelled arginine and lysine and in 'light' DMEM containing ^{14}N and ^{12}C arginine and lysine (Sigma-Aldrich). Equal portions of the differentially labelled H and L cells were mixed and solubilised with 4 mg/ml digitonin and then washed twice with PBS by centrifugation at 10,000 x g for 5 minutes at 4 ºC. The pellet, enriched in mitochondria, was then treated with 4

mg/ml digitonin to break the mitochondria. Insoluble material was removed by centrifugation at 16,900 x g for 10 min and the clear supernatant was filtered using spin-X-columns (Costar). Affinity purifications were performed using anti-HA-agarose (Cell Signalling), anti-FLAG-agarose (Sigma-Aldrich) or CIV immunocapture kit (Abcam) beads incubated overnight at 4 °C in rotation. The unbound material was collected and affinity resins were washed 8-10 times with buffer containing 0.05 % DDM. Bound material was eluted depending on the affinity resin used: proteins bound to HA were eluted with Laemmly sample buffer, CIV immunocaptured proteins were eluted with 0.1 M glycine pH 2.8, and proteins isolated by anti-FLAG agarose were eluted with 5 mg/ml FLAG peptide (Sigma-Aldrich). Eluted samples were prepared for MS by reducing and alkylating the cysteine residues. Reduction was done by adding tris(2-carboxyethyl)phosphine (TCEP) (5 mM final concentration, Sigma-Aldrich) dissolved in gel sample buffer (GSB): 40 % (w/v) glycerol, 200 mM Tris pH 9, 4 mM EDTA pH 8, 4 % (w/v) SDS, and incubating at 37 °C for 30 min. Samples were brought to RT and alkylation was performed by adding iodoacetamide (15 mM final concentration) and incubating in dark at RT for 30 minutes. Then dithiothreitol (DTT) (25 mM final concentration, Melford Stores) was added to quench the excess of iodoacetamide. Proteins were then resolved by SDS-PAGE electrophoresis and the gel was cut in slices, which were then digested with trypsin. After peptides were extracted from the gel matrix, salts and detergents were removed and the tryptic peptides were analysed by liquid chromatography mass spectrometry (LC-MS) employing an LTQ XL-Orbitrap system (Thermo Fisher Scientific) essentially as described in (Rhein *et al.*, 2013, 2014). Proteins were identified by Andromeda and quantification of heavy to light (H/L) ratio was calculated with MaxQuant (Cox and Mann, 2008). Ratio was based on reciprocal labelling duplicate SILAC experiments. The median peptide ratio was taken to be the protein ratio, using at least two ratio counts for each peptide. The ratios from each experiment were plotted on horizontal and vertical axes, respectively, of a ‘scatter plot’ as the log base 2 value, where each protein is represented by a point. Proteins unaffected by experimental conditions cluster around the origin as a ratio of 1 corresponds to two raised to the power of zero. Those proteins with a consistent increase or decrease in abundance occur in the top right or bottom left quadrants, respectively. Points in the two other quadrants represent proteins where the

differences are irreproducible in the replicate experiments. Those in the top left quadrant contain exogenous contaminants. A diagonal line from the top right to bottom left represents a perfect correlation between the two experiments. Statistically significant proteins ($P < 0.05$) in one or both orientations of labelling were identified with Perseus (Wagner *et al.*, 2011; Tyanova, Temu and Cox, 2016). The significance of the enriched proteins was calculated based on significance B with permutation-based False Discovery Rate (FDR) control (Benjamini and Hochberg, 1995), considering a Benjamin-Hochberg FDR < 5 %.

2.4.12 In vivo [^{35}S]-L-methionine labelling of mitochondrial translation products

Pulse-labelling was performed as described in (Chomyn, 1996). Briefly, cytosolic translation was irreversibly inhibited with 100 µg/ml emetine (Sigma-Aldrich) and labelling of mitochondrial proteins was performed for 1 hour using [^{35}S]-L-methionine (L-Methionine, [^{35}S]-Cell Labelling Grade, PerkinElmer) in fibroblasts non-transduced or transduced with the GFP protein alone or APOPT1^{GFP}.

For the pulse-chase experiments, cells were incubated overnight with 40 µg/ml chloramphenicol to reversibly inhibit mitochondrial translation, which was washed out before starting the experiment the next morning. In this case, the specific labelling of the mitochondrial peptides with [^{35}S]-L-methionine was performed for two hours in the presence of 100 µg/ml anisomycin (Sigma-Aldrich), a reversible inhibitor of cytosolic translation. Labelled medium was then replaced with fresh culture medium containing non-radioactive methionine. Cells were harvested 0, 1.5, 3, 6.5 and 20 hours after the addition of fresh medium. Samples were lysed and centrifuged (see section 2.4.1) and the clear supernatants were run through a 18 % Tris-Glycine gel (Novex™ 18 % Tris-Glycine Protein Gels, Thermo Fisher Scientific). The gel was fixed with 20 % methanol, 10 % acetic acid solution and dried for 2 h at 80 °C. Phosphor screens (GE Healthcare's Life Sciences) were exposed to the radioactive gels for several

days at room temperature. The signal was detected using a laser scanner (Amersham Typhoon, GE Healthcare's Life Sciences, UK).

2.5 Respiratory chain functional assays

2.5.1 Mitochondrial respiratory chain (MRC) complex enzymatic activity

Harvested cells were solubilised in Buffer A (20mM MOPS, 250mM sucrose, pH 7.4) and 0.2 mg/ml of digitonin. The homogenate was kept on ice for 5 minutes and centrifuged at 5,000 x g at 4°C for 3 minutes. The supernatant (cytosolic fraction) was discarded and the pellet (enriched in mitochondria) was resuspended in Buffer B (Buffer A + 1mM EDTA), kept in ice for 5 minutes and centrifuged at 10,000 x g at 4 °C for 3 minutes. The pellet was frozen at −80 °C until use. Once thawed, pellets were resuspended in 10 mM potassium phosphate buffer pH 7.4 and the suspensions were frozen in liquid nitrogen and thawed at 37°C three times, for appropriate disruption of the mitochondrial membranes. Protein concentration was determined as described in section 2.4.2

Small pieces of around 50 mg of frozen mice tissue were homogenised in 15 volumes of medium A in a Dounce-type glass homogeniser using a manually-driven glass pestle, 10-15 strokes. The homogenate was centrifuged at 800 x g for 5 min at 4 °C and the supernatant was frozen in liquid nitrogen and thawed at 37°C three times. Protein concentration was determined as described in section 2.4.2.

Kinetic spectrophotometric measurement of complex I was performed in mouse homogenates or cell suspensions incubated in a final volume of 200 µL of the mixture described in **Table 2.10** in 96-well plates at 30 °C by following the NADH oxidation (disappearance) as the change in the absorbance at λ= 340 nm, for 2 minutes. $\varepsilon_{NADH340nm}$ = 6.81 ml/nmol*cm.

Table 2.10 Complex I mixture.

Compound	Final concentration
PK buffer pH 8	20 mM
NADH	0.2 mM
Sodium azide (NaN_3)	1 mM
BSA (in EDTA 10 mM pH 7.4)	1 mg/ml
CoQ	50 μM
Rotenone	5 μM

Kinetic spectrophotometric measurement of complex II was performed in mouse homogenates or cell suspensions incubated in a final volume of 200 µL of the mixture described in **Table 2.11** in 96-well plates at 30 °C by following the DCPIP (electron acceptor) reduction as the change in the absorbance at λ= 600 nm, for 2 minutes. $\varepsilon_{DCPIP600nm}$ = 19 ml/nmol*cm.

Table 2.11 Complex II mixture.

Compound	Final concentration
PK buffer pH 7	50 mM
Potassium cyanide (KCN)	1.5 mM
2,6-Dichlorophenolindophenol (DCPIP)	0.1 mM
Succinate	16 μM
CoQ	50 μM

Kinetic spectrophotometric measurement of complex III was performed in mouse homogenates or cell suspensions incubated in a final volume of 200 µL of the mixture described in **Table 2.12** in 96-well plates at 30 °C by following the cytochrome c (electron acceptor) reduction as the change in the absorbance at λ= 550 nm, for 2 minutes. $\varepsilon_{NADH340nm}$ = 21 ml/nmol*cm.

Table 2.12 Complex III mixture.

Compound	Final concentration
PK buffer pH 7.4	50 mM
NaN_3	2 mM
BSA (in EDTA 10 mM pH 7.4)	1 mg/ml
Cytochrome c	50 μM
Decylubiquinone (DBH_2)	50 μM

Kinetic spectrophotometric measurement of complex IV was performed in mouse homogenates or cell suspensions incubated in a final volume of 200 µL of the mixture described in **Table 2.13** in 96-well plates at 37 °C by following the cytochrome c (electron donor) oxidation as the change in the absorbance at λ= 550 nm, for 2 minutes. $\varepsilon_{Cytc550nm}$ = 18.5 ml/nmol*cm.

Table 2.13 Complex IV mixture.

Compound	Final concentration
90-95 % reduced cytochrome c in 50 mM KP buffer pH 7	50 mM

Kinetic spectrophotometric measurement of the Krebs cycle enzyme citrate synthase (CS) was performed in mouse homogenates or cell suspensions incubated in a final volume of 200 µL of the mixture described in **Table 2.14** in 96-well plates at 30 °C by following the appearance of TNB, proportional to the amount of liberated CoA, as the change in the absorbance at λ= 412 nm, during 2 minutes. $\varepsilon_{TNB412nm}$ = 13.8 ml/nmol*cm.

Table 2.14 CS mixture.

Compound	Final concentration
Tris-HCl buffer pH 8	75 mM
5,5-dithio-bis-(2-nitrobenzoic acid (DTNB)	0.1 mM
Triton X-100	0.1 %
Acetyl-CoA	0.4 mM
Oxalacetate	0.5 mM

The specific activity, that is the units (µmoles of substrate consumed per minute) normalised by protein amounts, of each enzyme was calculated using the Lambert–Beer law:

$$\text{Specific activity} = \frac{\Delta Abs * Total\ Volume\ (ml)}{\varepsilon * \text{Sample volume(ml)} * [\text{prot}]\left(\frac{\text{mg}}{\text{ml}}\right) * \ell(\text{cm})}$$

The specific activity of each of the respiratory chain enzymes was normalised to that of the CS, the standard marker of mitochondrial volume.

2.5.2 COX and SDH enzymatic activity in mouse frozen tissues

The histochemical method for the microscopic demonstration of SDH activity was performed on 8-mm-thick cryostat sections from mouse frozen tissues incubated for 20 minutes at 37 °C with 10 ml of the mixture described in **Table 2.15**.

Table 2.15 SDH mixture.

Compound	Final concentration
Phosphate buffer pH 7.4	5 mM
EDTA	5 mM
KCN	1 mM
Phenazine methosulfate (PMS)	0.2 mM
Succinic acid	50 mM
Nitro blue tetrazolium chloride (NBT)	1.5 mM

The histochemical method for the microscopic demonstration of COX activity was performed on 8-mm-thick cryostat sections from mouse frozen tissues incubated for 1 hour at 37 °C with 10 ml of the mixture described in **Table 2.16**.

Table 2.16 SDH mixture.

Compound	Final concentration
Phosphate buffer pH 7.4	5 mM
3'-Diaminobenzidine (DAB)	0.1 %
Cytochrome c	0.1 %

2.5.3 In-gel activity assays

The in-gel activity assays followed the principles described by Zerbetto 1996 (Zerbetto, Vergani and Dabbeni-Sala, 1997). Samples were run through 1D BN-PAGE (see section 2.4.3). The gel was then washed and incubated for 2 hours at RT with 10 ml of the complex I assay: 0.1 M Tris-HCl pH 7.4, 0.14 mM NADH, 1 mg/ml Nitro blue tetrazolium (NBT, Sigma-Aldrich), or the complex IV assay: 50 mM PK buffer pH 7.4, 1 mg/ml DAB (Sigma-Aldrich), 24 U/ml catalase (Sigmal-Aldrich), 1 mg/ml cytochrome c (Sigma-Aldrich), 75 mg/ml sucrose (Acros Organics). Gels were then washed with water and scanned using a professional scanner (EPSON Expression 1680 Pro, EPSON, UK).

2.5.4 H_2O_2 production in mice isolated mitochondria

Mitochondria were isolated from brain and heart as described (Fernández-vizarra *et al.*, 2010). Briefly, mice were sacrificed, and the brain and heart were extirpated. The heart was placed in medium AT (0.075 M sucrose, 0.225 M sorbitol, 1 mM Ethylene Glycol Tetraacetic Acid (EGTA, Sigma-Aldrich), 0.1 % fatty acid-free BSA, and 10 mM Tris–HCl, pH 7.4), cut in small pieces and homogenised in 10 ml medium AT per g of heart in a glass Elvehjem potter using a motor-driven Teflon pestle with 10 up and down strokes at 600 rpm. The brain was also placed in AT medium and cut in small pieces but was homogenised in 5 ml medium AT per g of brain in a Dounce-type glass homogeniser using a manually-driven glass pestle with 10-15 strokes. Both homogenates were then centrifuged at 1,000 x g for 5 min at 4 °C to pellet unbroken debris and the resulting supernatants were transferred to a clean tube and centrifuged again at 9,000 x g for 10 min at 4 °C. The supernatant from each organ homogenate was

then transferred to eight 1.5 ml-Eppendorf tubes, which were centrifuged at 15,000 x g for 2 min at 4 °C. The supernatant of each tube was removed, carefully eliminating all the fat that can be seen on the top of the darker pellet containing the mitochondria. The contents of two Eppendorf tubes were combined into a single one and resuspended together in 1.5 ml of medium AT. Samples were then centrifuged, washed and combined again until only one Eppendorf tube containing all mitochondria from one organ is left.

H_2O_2 production rate was measured at 37°C using 130 µg of mitochondrial protein diluted in 2 ml of mitochondrial respiration buffer (120 mM sucrose, 50 mM KCl, 20 mM Tris–HCl, 4 mM KH2PO4, 2 mM MgCl2, 1 mM EGTA, 1 mg/ml fatty-acid-free BSA, pH 7.2) in an Oxygraph-2k using O2k-Fluo LED2-Module (Oroboros instruments, Innsbruck, Austria). The oxidation of the fluorogenic indicator Amplex Red Reagent (Life Technologies, A12222) was monitored in the presence of horseradish peroxidase (Sigma-Aldrich, P8250). The final concentrations of Amplex Red and horseradish peroxidase in the incubation medium were 10 µM and 4 U/ml, respectively. H_2O_2 production was initiated by the complex II substrate succinate (final concentration 10 mM). 1 mM ADP was then added to the Oxygraph-2k chambers followed by 1 µM of antimycin to inhibit complex III. In a separate experiment, a standard curve was obtained by adding amounts of H_2O_2 with known concentration to the assay medium in the presence of all the reactants. The H_2O_2 production rate was determined from the slope of a plot of the fluorogenic indicator versus time.

2.6 Statistical analysis

Data analysis was performed with GraphPad Prism 5.0. All numerical data are expressed as mean ± standard error (SEM). Results ($n \geqslant 3$) were analysed by unpaired, one-tailed t-tests (2 groups) or two-way analysis of variance (ANOVA) (> 2 groups), typically with Sidak's multiple comparison post-hoc test. P-values <0.05 were considered statistically significant.

CHAPTER 3

Identification and characterisation of MR-1S, a vertebrate-specific COX assembly factor

3.1 Introduction

A m.9536_9537insC frameshift mutation in *MT-CO3*, predicted to produce a prematurely truncated protein (p.Gln111Profs∗113), was identified in an 11-year-old girl affected by a progressive neurological disorder characterised by symmetric necrotic lesions of putamina, similar to those observed in LS (Tiranti *et al.*, 2000). The mutation was homoplasmic in both muscle and skin fibroblasts and was associated with a profound isolated COX deficiency. A cybrid cell line, generated by fusing the patient's cytoplasts with mtDNA-less (rho-zero, ρ^0) derivatives of 143B.206 human osteosarcoma cells (143B.206-ρ^0) (Lqj *et al.*, 1989) was used to study the biochemical consequences of this mutation. Although *MT-CO3* transcript levels were normal compared to control cells, the protein was absent when *in vivo* mitochondrial translation assays were performed. Fully assembled COX was not detectable by BN-PAGE (**Figure 3.1A**) and many accumulated MT-CO1-containing assembly intermediates were shown by Western-blot analysis (Tiranti *et al.*, 2000). We hypothesised that COX assembly factors must remain associated to these accumulated intermediates.

In this chapter, I describe how we used the aforementioned *MT-CO3* mutated cybrid cell line for MS studies, in order to characterise the composition of the accumulated COX subassemblies. The identification of MR-1S, which was bound to these subassemblies, and the confirmation of its involvement in COX assembly demonstrated the success of this strategy.

3.2 Results

3.2.1 Identification of MR-1S, a potential novel COX assembly factor

The numerous subassembly species accumulated in the *MT-CO3* mutant cybrid cell line (MT-CO3mut) were detected by WB analysis of DDM-treated mitochondrial fractions run through 1D BN-PAGE (**Figure 3.1A**).

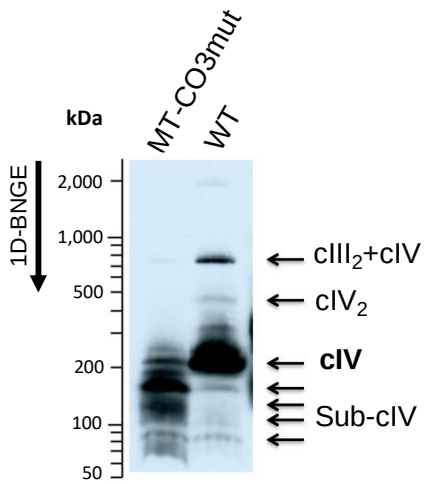

Figure 3.1 COX assembly intermediates in cybrids carrying a MT-CO3 mutation. Mitoplasts isolated from WT and MT-CO3 mutant cybrids analysed by 1D BN-PAGE and WB using an anti-MT-CO1 antibody. Arrows indicate MT-CO1 in mature COX (cIV), subassembly intermediates (Sub-cIV), COX dimer (cIV_2), and the $cIII_2$ + cIV supercomplex. Sara Vidoni performed this experiment.

A comparison of COX immunopurified from mitoplasts of WT and mutant cybrid cell lines was then carried out by quantitative SILAC MS in order to identify proteins associated with the assembly species in greater abundance in the MT-$CO3^{mut}$ cells relative to the WT cybrid line. This experiment was performed in duplicate with reciprocal isotopic labelling between mutant and WT cell lines. After analysing the MS results, we found a cluster of proteins with mutant/WT log2 ratios of ~0.75–1 (i.e. 1.5–2 times more abundant in the mutant line than in the WT cells), in which four already known COX assembly factors were identified: COA3 (CCDC56 or MITRAC12) (Clemente *et al.*, 2013), PET100 (Lim *et al.*, 2014; Oláhová *et al.*, 2015) and the human orthologs of the yeast Pet117 (McEwen *et al.*, 1993; Szklarczyk *et al.*, 2012) and Cmc2 (Horn *et al.*, 2010) (**Figure 3.2**). Within this group there was a protein named myofibrillary-related protein 1 short isoform (MR-1S; also known as PNKD isoform 3; Uniprot: Q8N490-2) (Ghezzi, Viscomi, *et al.*, 2009), which we decided to further investigate as a putative COX assembly factor (**Figure 3.2**). All the other entries in the cluster were non-mitochondrial proteins according to two mitochondrial specific proteome databases: Mitocarta (http://archive.broadinstitute.org/pubs/MitoCarta/index.html) and Mitominer (http://mitominer.mrc-mbu.cam.ac.uk/release-4.0/begin.do). These non-

mitochondrial proteins were not considered relevant for this study. A number of COX structural subunits was found significantly less abundant in the mutant line than in the WT cells and are therefore clustered in the bottom left quadrant of the graph (**Figure 3.2**).

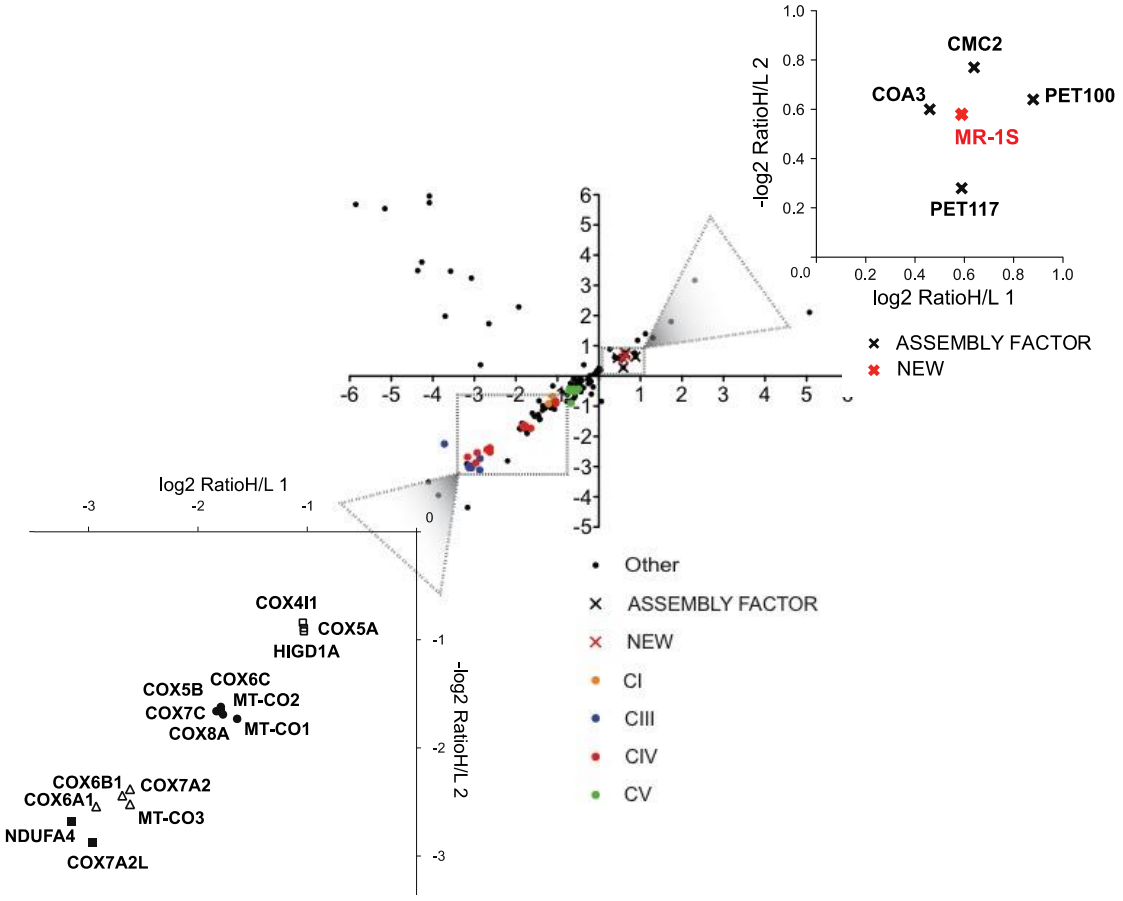

Figure 3.2 Quantitative SILAC MS analysis. Bi-directional Heavy (H) and Light (L) mitoplasts from both cybrid cell lines were isolated, mixed, and subjected to COX immunocapture. Each data point represents a specific protein. All of the identified COX subunits were located in the bottom left quadrant. A group of proteins known to be involved in COX assembly, in which MR-1S was found, is also shown in detail in the top right quadrant. The values in the x axis correspond to the $\log_2$ heavy-to-light (H/L) ratio of the peptides detected in experiment 1, where the heavy (H)-labelled MT-CO3 mutant and unlabelled (L) WT cells were mixed. The values in the y axis correspond to the inverted $\log_2$ H/L ratio ($-\log_2$ H/L) of the peptides detected in experiment 2, where the unlabelled (L) MT-CO3 mutant and the labelled (H) WT cells were mixed. Erika Fernandez-Vizarra, Sara Vidoni and Sujing Ding performed and analysed these experiments.

3.2.2 Confirming the role of MR-1S in COX assembly

The paroxysmal non-kinesigenic dyskinesia (*PNKD*) gene, only found in vertebrates, encodes three different proteins, MR-1L, MR-1M and MR-1S (L for long, M for medium and S for short) formed by alternative splicing (**Figure 3.3A**). MR-1S, composed of 142 amino acids (**Figure 3.3B**), is encoded by the *PNKD-201* transcript, which has 3 coding exons and 2 introns. MR-1L (transcript *PNKD-203*) and MR-1S contain the same exon 1, which encodes a MTS and are therefore located in the mitochondria, whereas MR-1M (transcript *PNKD-202*) shares the same C-terminal functional domain as MR-1L but is targeted to the

A

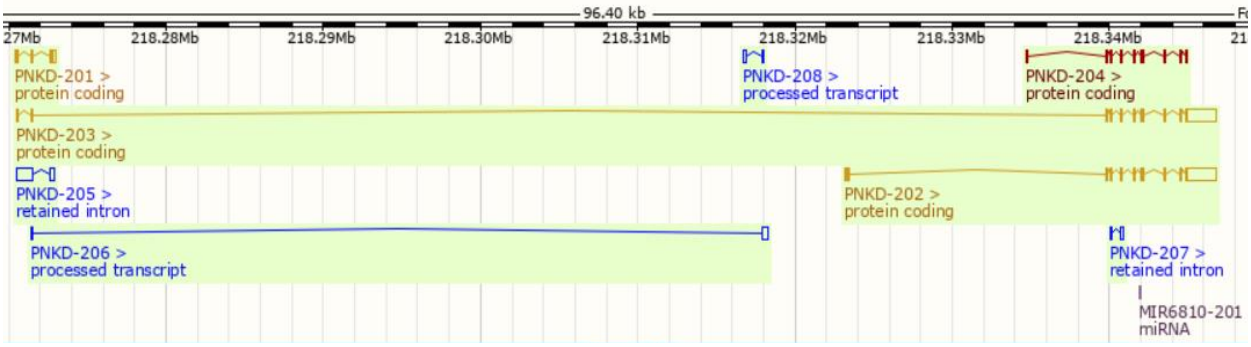

Golgi apparatus (Ghezzi, Viscomi, *et al.*, 2009).

B

```
        10         20         30         40         50
MAAVVAATAL KGRGARNARV LRGILAGATA NKASHNRTRA LQSHSSPEGK
        60         70         80         90        100
EEPEPLSPEL EYIPRKRGKN PMKAVGLAWA IGFPCGILLF ILTKREVDKD
       110        120        130        140
RVKQMKARQN MRLSNTGEYE SQRFRASSQS APSPDVGSGV QT
```

Figure 3.3 (**A**) *PNKD* gene annotation. Image taken from www.ensembl.org. The gene is predicted to encode four protein coding transcripts but only three have been experimentally confirmed (depicted in yellow). *PNKD-203* transcript encodes the MR-1L protein composed of 385 amino acids, PNKD-202 transcript encodes the MR-1M protein composed of 361 amino acids and PNKD-201 transcript encodes the MR-1S protein composed of 142 amino acids. (**B**) Amino acid sequence of MR-1S. Uniprot code: Q8N490-2. Image taken from www.uniprot.org.

To confirm the role of MR-1S in COX assembly, RNA interference (RNAi) was performed through lentiviral transduction of three small hairpin RNAs (shRNAs) specific for *PNKD-201* (shMR-1S^{RNA1,2,3}). From WT cybrids treated

with shMR-1S^{RNA1}, two clones (shMR-1S^{RNA1-7} and shMR-1S$^{RNA1-11}$), which showed the virtual absence of MR-1S (**Figure 3.4A**), were selected for further analysis. Both cell lines displayed 30% reduction in COX enzyme activity (**Figure 3.4B**) compared with cells transduced with the 'empty vector', i.e. with no open reading frame cloned in it, or with an shMR-1S^{RNA1-3} clone, which showed MR-1S levels similar to the control (**Figure 3.4A**).

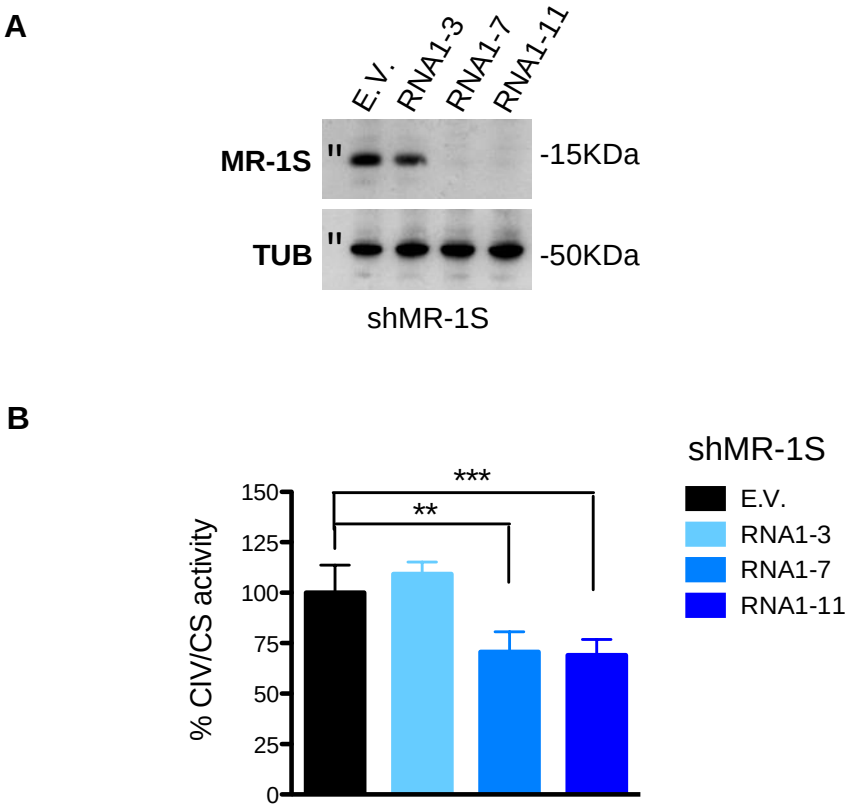

Figure 3.4 COX functional defect after MR-1S knockdown. (**A**) SDS-PAGE and WB analysis showing MR-1S steady-state levels in three different clones (clones shMR-1S$^{RNA1-3, 7, and 11}$), isolated after lentiviral transduction of WT cybrids with pLKO.1 containing a shRNA sequence specifically targeting the MR-1S isoform, in comparison with cells transduced with the pLKO.1 empty vector (E.V.). Tubulin (TUB) was used as the loading control. (**B**) COX enzyme activity normalised to citrate synthase (CS) activity of the shMR-1S$^{RNA1-3, 7, and 11}$ clones and of the WT cells transduced with the empty vector (E.V.). Data are presented as mean ± SD (n = 4). *** $p < 0.0005$, ** $p < 0.005$ (unpaired Student's t-test). Sara Vidoni and Erika Fernandez-Vizarra performed these experiments.

Furthermore, the shRNA cells displayed a reduction in the amount of MT-CO1 incorporated into mature COX and into the advanced intermediates ('S3') when analysed by 1D BN-PAGE (**Figure 3.5**). Taken together these results demonstrate the involvement of MR-1S in COX biogenesis and activity.

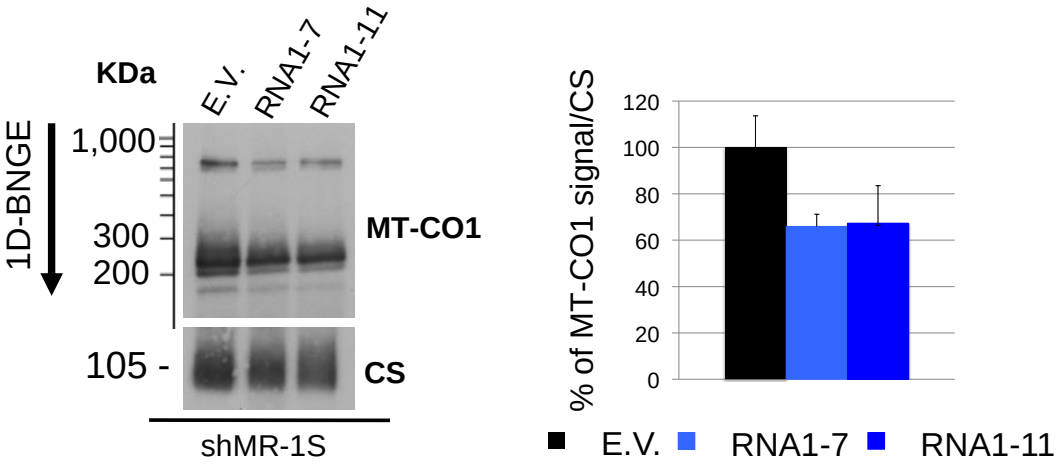

Figure 3.5 COX assembly defect after MR-1S knockdown. 1D BN-PAGE and WB analysis of the shMR-1S$^{RNA1-7 \text{ and } 11}$ clones and of the WT cells transduced with the empty vector using an anti-MT-CO1 antibody. CS was used as a normalization and molecular weight (MW) standard signal. The densitometric quantification of the MT-CO1 signal, normalised to the CS signal and expressed as the percentage of the normalised control signals, is shown on the right. Data are presented as mean ± SD (n = 3). Sara Vidoni and Erika Fernandez-Vizarra performed these experiments.

3.2.3 MR-1S Interacts with PET100 and PET117

To further define the role of MR-1S in COX assembly, WT and MT-CO3^{mut} cybrid cell lines were transduced with a C-terminal HA-tagged recombinant MR-1S cDNA (MR-1S^{HA}) and with the pWPXLd-ires-Hygro^{R} 'empty vector'. The protein interactions of HA-tagged MR-1S were then investigated by quantitative MS of SILAC-labelled anti-HA immunoprecipitates from both WT and MT-CO3^{mut} cybrids. The specific interactors consistently detected by these analyses included several COX structural subunits, belonging to the early (COX5A, COX4I1) and intermediate (MT-CO2, COX5B, COX6C) assembly groups, and two COX assembly factors, i.e., PET100 (Church *et al.*, 2005; Lim *et al.*, 2014; Oláhová *et al.*, 2015) and PET117 (McEwen *et al.*, 1993; Soto *et al.*, 2012; Szklarczyk *et al.*, 2012) (**Figure 3.6**).

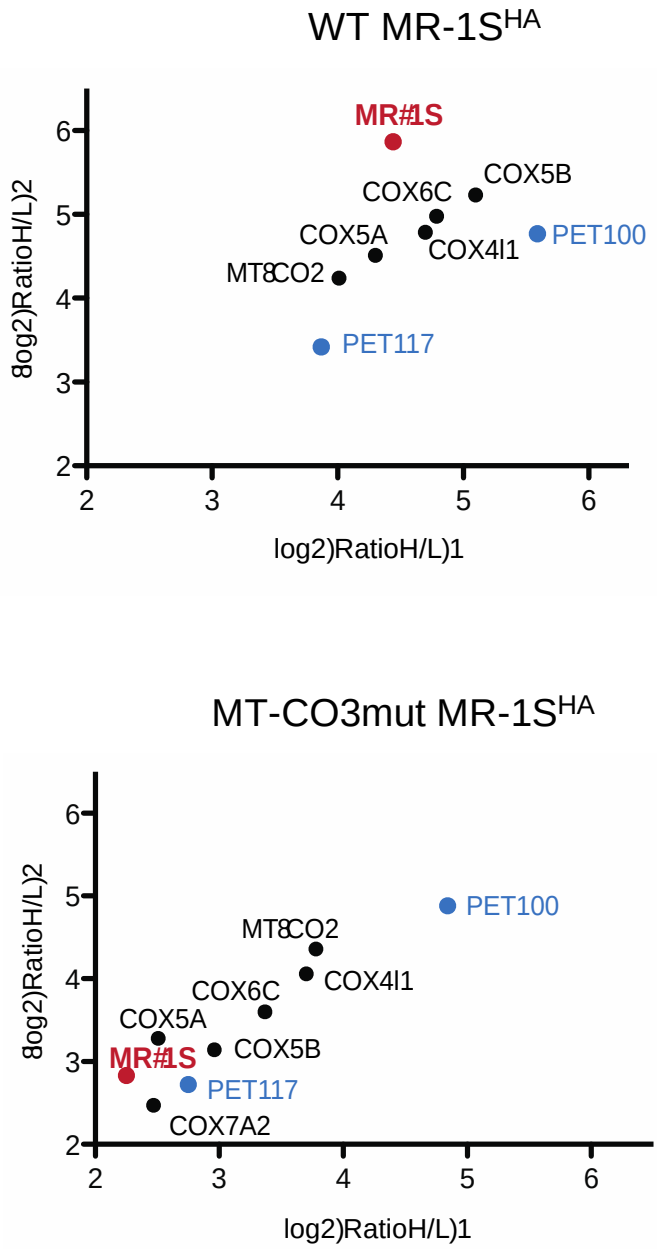

Figure 3.6 MR-1S binds COX structural subunits and assembly factors. Scatterplots showing the log2 and −log2 H/L ratios obtained after mass spectrometry analysis of anti-HA co-immunoprecipitation fractions of bi-directional SILAC of WT (upper graph) or MT-CO3 mutant (lower graph) cybrid cells expressing MR-1S^{HA}, combined with material from cybrid cells transduced with the empty vector. Only the upper right quadrants of the plots, showing the statistically significant interactions (based on significance B, Perseus analysis platform; Cox and Mann, 2008, Tyanova et al., 2016), are displayed. Sara Vidoni and Sujing Ding performed these experiments.

3.2.4 MR-1S interaction with COX assembly intermediates is affected by the absence of PET100

In order to further investigate the interaction of MR-1S with PET100, we used primary fibroblasts carrying a truncating homozygous p.Gly48* mutation in PET100 ($PET100^{G48*}$) (Oláhová *et al.*, 2015). Neither fully assembled COX nor subassembly intermediates were found in this cell line when analysed by 1D BN-PAGE (**Figure 3.7**). Interestingly, the MR-1S-containing supramolecular structures observed in WT cells were also absent in the PET100 mutant fibroblasts (**Figure 3.7**), suggesting that the stability and interaction of MR-1S with COX assembly intermediates is disrupted in the absence of PET100.

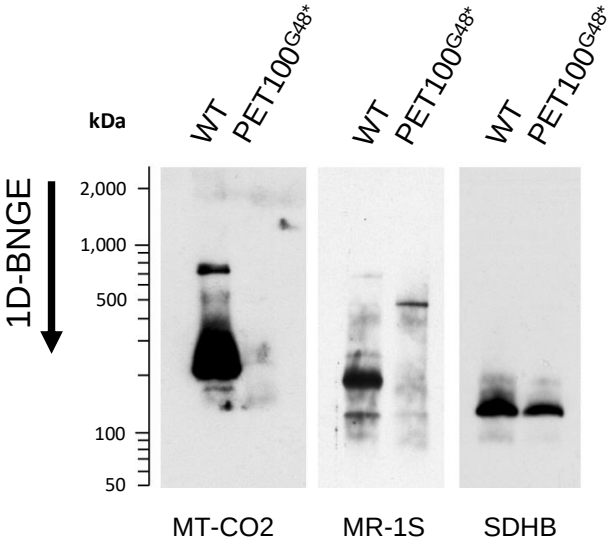

Figure 3.7. COX assembly defect in $PET100^{G48*}$ mutant cells. (**A**) 1D BN-PAGE, WB, and immunodetection analysis showing the absence of fully assembled COX, detected with anti-MT-CO2, and of the MR-1S supramolecular complexes, detected with anti-MR-1S, in the $PET100^{G48*}$ primary fibroblasts, kindly donated by R.W. Taylor from Newcastle University, UK. SDHB was used as a normalization and MW standard signal. Erika Fernandez-Vizarra performed these experiments.

To confirm that these defects were specifically due to the absence of PET100 and also to explore its possible interaction with PET117, both WT and $PET100^{G48*}$ immortalised fibroblasts were transduced with FLAG-tagged versions of either PET100 or PET117 and with the pWPXLd-ires-$Hygro^{R}$ 'empty

vector'. Very high expression of recombinant PET117^{FLAG} was found in both lines, whereas the amounts of PET100^{FLAG} were much lower (**Figure 3.8**).

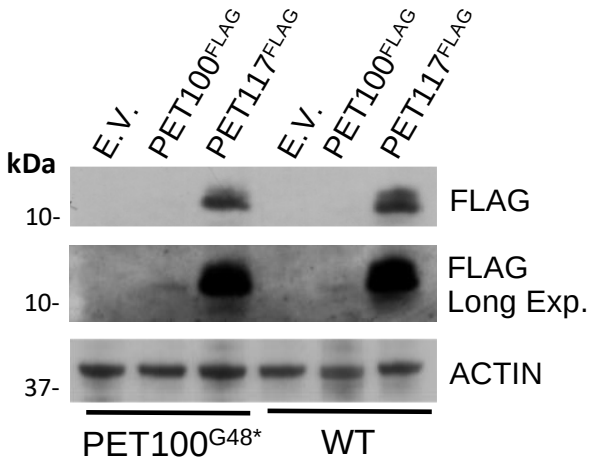

Figure 3.8 Overexpression of PET100^{FLAG} and PET117^{FLAG}. SDS-PAGE, WB, and immunodetection using anti-FLAG of PET100^{FLAG} and PET117^{FLAG} in the WT and PET100^{G48*} immortalised fibroblasts transduced with the empty vector (E.V.), PET100^{FLAG} or PET117^{FLAG}. Actin was used as a loading standard. Longer exposures than usual were necessary to visualise the PET100^{FLAG} band. Experiment performed by myself.

However, despite the very low protein levels of PET100^{FLAG}, its mRNA levels were clearly overexpressed according to analysis by quantitative PCR (**Figure 3.9**). Interestingly, the levels of PET100 transcripts were also increased when PET117 was overexpressed both in WT and PET100^{G48*} immortalised fibroblasts (**Figure 3.9)**, suggesting that PET117 requires the presence of PET100.

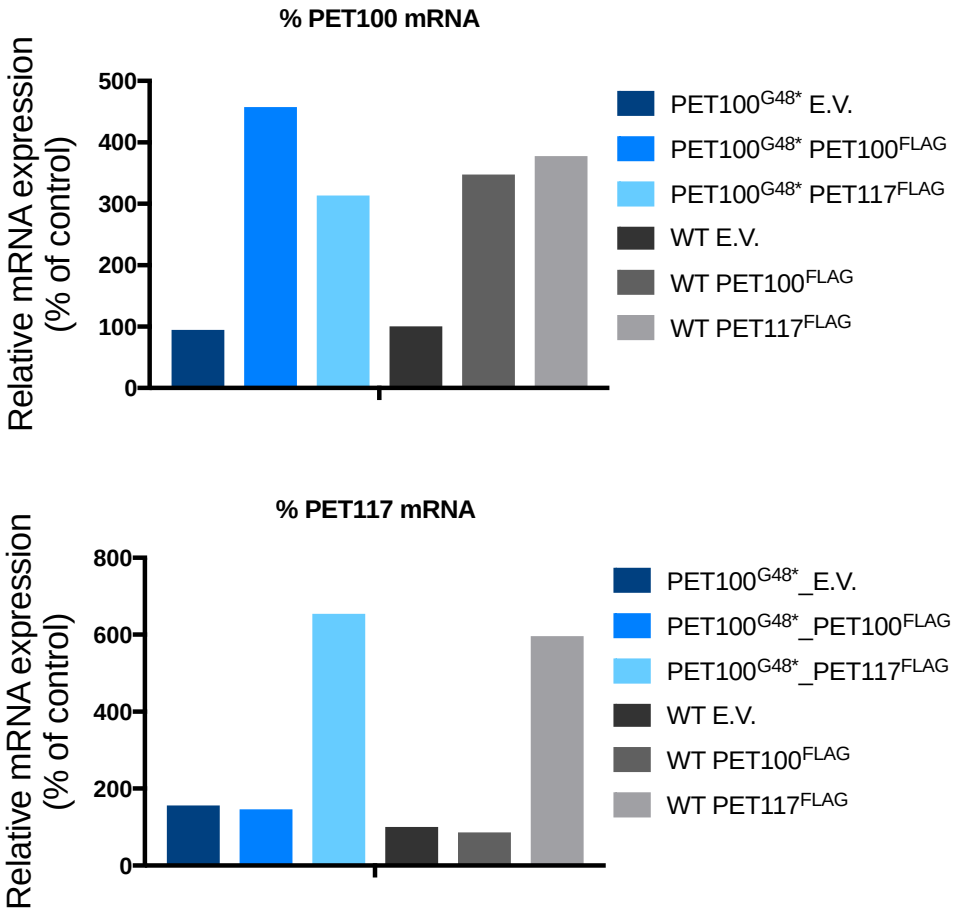

Figure 3.9 Transcript levels of PET100 and PET117. Relative mRNA expression of PET100 and PET117, normalised to the expression of GAPDH and expressed as percentage of the control, in the WT and PET100^{G48*} patient immortalised fibroblasts transduced with either the empty vector (E.V.), PET100^{FLAG} or PET117^{FLAG}. N = 1. Experiments performed by myself.

The low protein levels of PET100^{FLAG} were sufficient to rescue the phenotype as COX activity levels, measured by in-gel activity, were found normal in the mutant fibroblasts transduced with PET100^{FLAG}, whereas no recovery was observed in mutant cells transduced with the 'empty vector' or the PET117^{FLAG} (**Figure 3.10B**). Complex I activity was unchanged in all the analysed cell lines (**Figure 3.10A**).

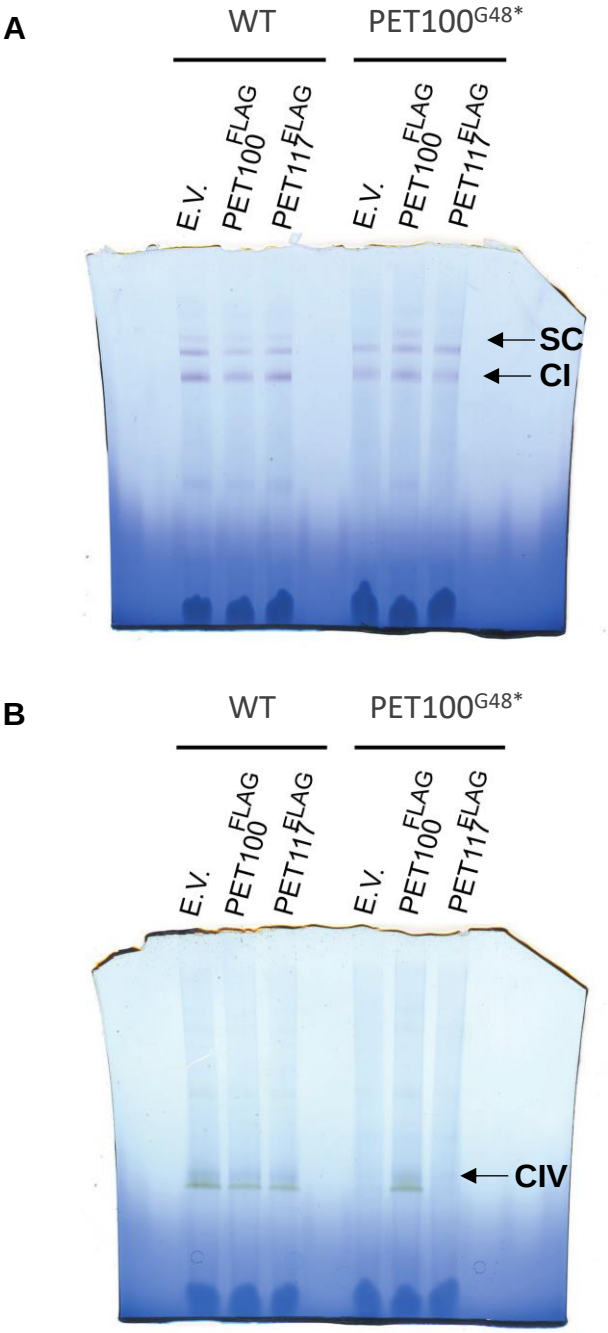

Figure 3.10 COX activity is rescued by overexpression of PET100^{FLAG}. 1D BN-PAGE and in-gel activity of complex I (**A**) and complex IV (**B**) in the control fibroblasts (WT) or the PET100 mutated fibroblasts (PET100^{G48*}) transduced either with the empty lentiviral expression vector (E.V.), PET100^{FLAG} or PET117^{FLAG}. The arrows indicate the in-gel activity of complex IV (IV), free complex I (CI) and complex CI in the supercomplexes (SC). Experiments performed by myself.

The steady-state levels of the COX subunits, which were found markedly reduced in the PET100^{G48*} mutant cells transduced with the 'empty vector', were

recovered to normal WT-levels when transduced with PET100^{FLAG} (**Figure 3.11**). The same was found for MR-1S protein levels, confirming that this protein is affected by the absence/presence of PET100.

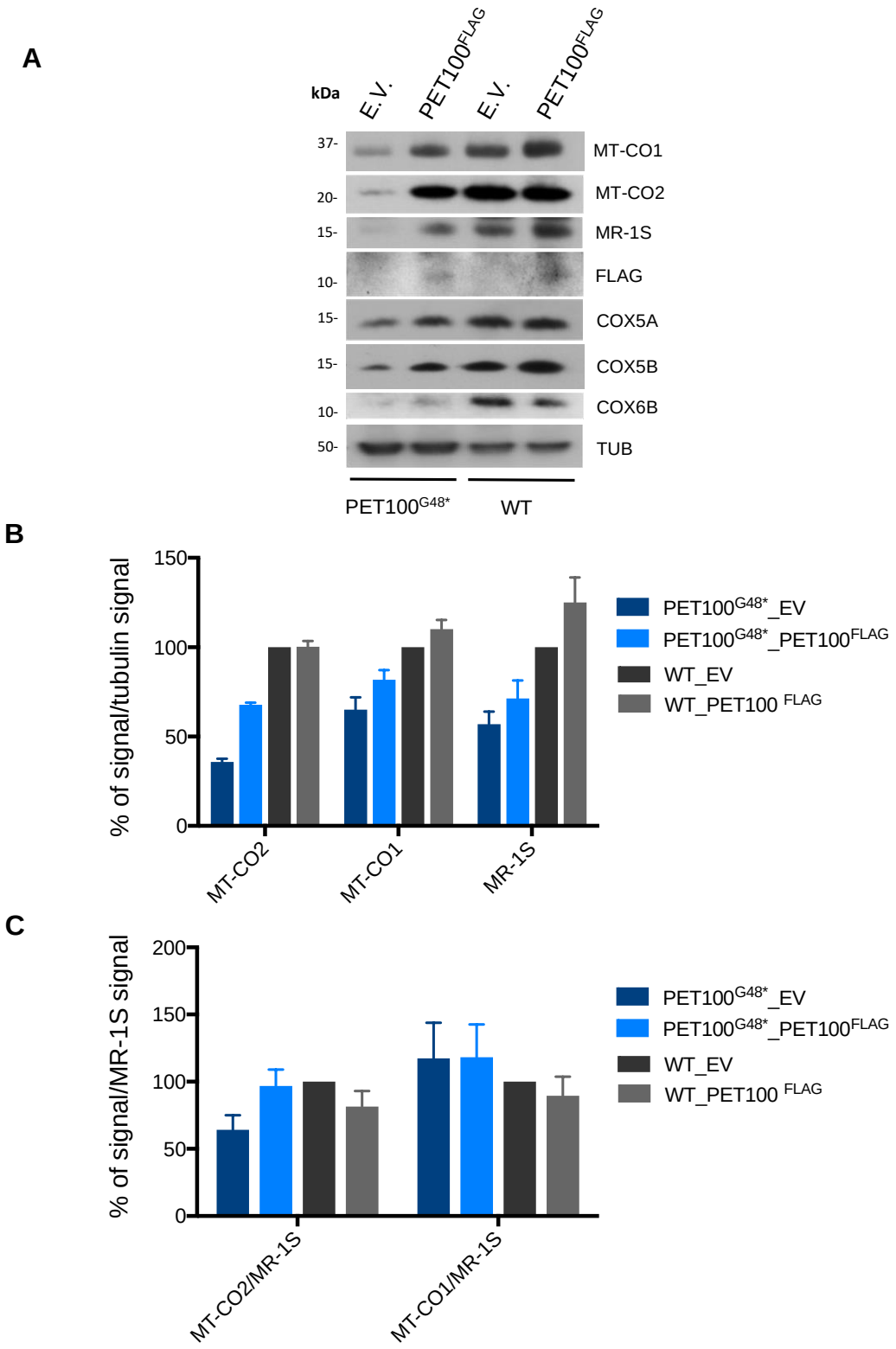

Figure 3. 11

Figure 3.11 COX and MR-1S protein levels rescued by overexpression of PET100^{FLAG}. (**A**) Steady-state levels of proteins visualised by SDS-PAGE, WB, and immunodetection in the PET100^{G48*} patient and in the WT immortalised fibroblasts transduced with either the empty vector (E.V.) or PET100^{FLAG}. (**B**) Densitometric quantification of the immunodetection signals. The signal intensities expressed as percentage of the control (WT_E.V.) of MT-CO2, MT-CO1, and MR-1S normalised to tubulin are plotted in the graph (mean ± SD; n = 2). (**C**) Signal intensities expressed as percentage of the control (WT_E.V.) of MT-CO2 and MT-CO1 normalised to the MR-1S signal (mean ± SD; n = 2). Experiments performed by myself.

3.2.5 PET100 also mediates the interaction of PET117 with MR-1S and COX subunits

To confirm that PET117 interacts with MR-1S, the reciprocal experiment was performed. WT cybrid cells were transduced with PET117^{FLAG} and with the pWPXLd-ires-Hygro^{R} 'empty vector'. Then, PET117 interactors were investigated by quantitative MS of SILAC-labelled anti-FLAG co-immunoprecipitates from the cybrids transduced with PET117^{FLAG} and with the 'empty vector' as the control. The same COX structural subunits that co-immunoprecipitated with MR-1S (COX5A, COX4I1, MT-CO2, COX5B and COX6C), were also found to interact with PET117 (**Figure 3.12)**. MR-1S and COX11, another human ortholog of a yeast COX assembly factor (Carr, George and Winge, 2002), also co-immunoprecipitated with PET117^{FLAG} (**Figure 3.12)**. Yeast Cox11 is a Cu(I)-binding protein essential for cytochrome c oxidase assembly (Carr, George and Winge, 2002).

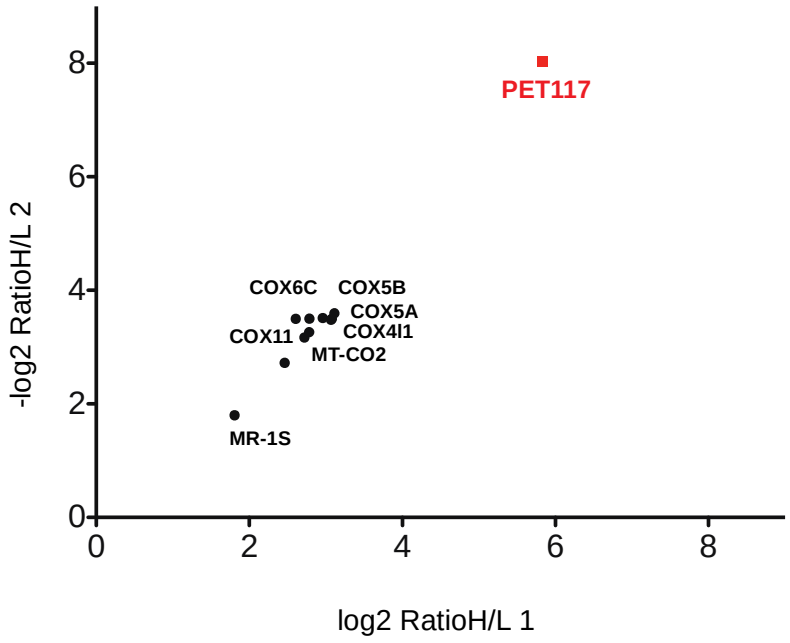

Figure 3.12 PET117 interacts with COX subunits, MR-1S and COX11. Scatterplots and heavy-to-light (H/L) ratio table obtained after MS analysis of anti-FLAG co-immunoprecipitation fractions of bi-directional SILAC labelling of cybrid cells transduced with PET117^{FLAG}, combined with material from cybrid cells transduced with the empty vector. Only the top right quadrant of the plot and the statistically significant interactions are shown (significance B, Perseus analysis platform; (Cox and Mann, 2008; Tyanova, Temu and Cox, 2016). Sara Vidoni and Sujing Ding performed these experiments.

To further analyse the role of the interactions among MR-1S, PET100 and PET117, anti-FLAG immunopurification of PET100^{G48*} fibroblasts transduced with the 'empty vector', PET100^{FLAG} or PET117^{FLAG} was carried out in non-labelled cells. MR-1S, together with MT-CO1, MT-CO2, COX5A, and COX5B were contained in the immunopurified eluted fraction of the mutant cells transduced with PET100^{FLAG} (**Figure 3.13**). However, no co-immunoprecipitation of any of these proteins was obtained in the same cell line transduced with the 'empty vector' or PET117^{FLAG} (**Figure 3.13**). These results demonstrate that PET117 interaction with MR-1S and COX structural elements requires the presence of PET100.

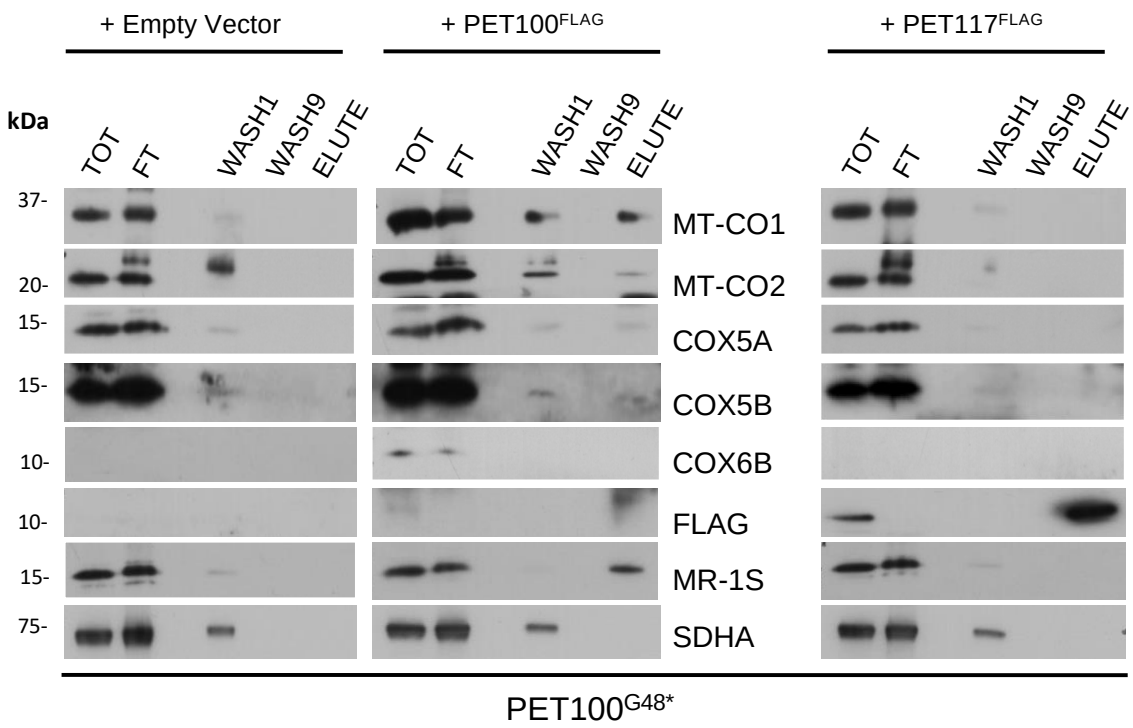

Figure 3.13 PET117 interaction with MR-1S and COX subunits is mediated by PET100. SDS-PAGE, WB analysis and immunodetection of the co-immunoprecipitation fractions using anti-FLAG in PET100^{G48*} immortalised fibroblasts transduced with the empty vector (E.V), PET100^{FLAG} or PET117^{FLAG}. TOT: total mitoplast lysate before immunoprecipitation. FT: flow-through fraction with the unbound proteins. WASH1 and WASH9: fractions obtained after the first and ninth washes of the anti-FLAG-M2-agarose resin. ELUTE: eluted fractions of the material bound to the resin after treatment with the specific FLAG peptide. Experiments performed by myself.

3.3 Conclusions

- MS studies of mutated cell lines with accumulated COX subassemblies can be useful to identify new COX assembly factors. By using this strategy, we found MR-1S bound to the COX subassemblies accumulated in a *MT-CO3* (Tiranti *et al.*, 2000) cybrid cell line.

- Knockdown of *MR-1S* expression had functional consequences on COX activity and assembly, confirming its involvement in COX biogenesis.

- MR-1S interacts with COX structural subunits belonging to the early (COX5A, COX4I1) and intermediate (MT-CO2, COX5B, COX6C) assembly groups.

- MR-1S interacts with the highly conserved PET100 (Church *et al.*, 2005; Lim *et al.*, 2014; Oláhová *et al.*, 2015) and PET117 (McEwen *et al.*, 1993; Soto *et al.*, 2012; Szklarczyk *et al.*, 2012) COX assembly factors.

- Human skin fibroblasts with a truncating homozygous p.Gly48* mutation in PET100 ($PET100^{G48*}$) (Oláhová *et al.*, 2015) showed absence of fully assembled COX and profoundly reduced steady-state levels of COX structural subunits and MR-1S.

- Overexpression of $PET100^{FLAG}$ rescued COX assembly and activity as well as MR-1S protein levels, confirming that the interaction of MR-1S with COX assembly intermediates requires the presence of PET100.

- $PET117^{FLAG}$, expressed in wild-type (WT) cells, co-immunoprecipitated with MR-1S and several COX structural subunits belonging to the early (COX5A, COX4I1) and intermediate (MT-CO2, COX5B, COX6C) assembly groups.

- $PET100^{FLAG}$ co-immunoprecipitated with MR-1S and several COX structural subunits belonging to the early (COX5A) and intermediate (MT-CO1, MT-CO2, COX5B) assembly groups.

- Neither MR-1S nor COX subunits co-immunoprecipitated with $PET117^{FLAG}$ overexpressed in fibroblasts carrying mutations in PET100, indicating that the interaction of PET117 with MR-1S and COX structural subunits is mediated by PET100.

CHAPTER 4

Generation and characterisation of an *Apopt1* KO mouse model

4.1 Introduction

As described in previous chapters, loss-of-function mutations in the human *APOPT1* gene have been associated with mitochondrial encephalopathy, characterised by cavitating leukodystrophy with a very distinctive MRI pattern (Melchionda *et al.*, 2014; Sharma *et al.*, 2018). Biochemically, these mutations were also associated with isolated COX deficiency in skin and muscle biopsies (Melchionda *et al.*, 2014). However, although the genetic association of *APOPT1* pathogenic variants with COX deficiency was well established, the link with CIV biogenesis and function remained unclear. In an attempt to validate this association, *APOPT1* expression was knocked down by RNAi in different human cells (Melchionda *et al.*, 2014). Although *APOPT1* mRNA levels were significantly reduced in the interfered cell lines, COX activity and assembly were unaffected, possibly due to residual normal *APOPT1* transcripts still being translated. In addition, acute shRNA treatment in control immortalised fibroblasts induced cell death, an unexpected phenomenon since APOPT1-null patient fibroblasts showed normal growth in standard culture conditions (Melchionda *et al.*, 2014).

In this chapter, I describe how a KO mouse model with a targeted disruption of the *Apopt1* gene was generated. This model was used to clearly validate the role of this protein in COX biogenesis and to study the physiological effects of the ablation of *Apopt1* at the whole-organism level and the biochemical consequences in post-mitotic tissues.

4.2 Results

4.2.1 Generation of the *Apopt1* KO mouse model

CRISPR/Cas9 was used for genome editing in order to generate an *Apopt1* KO mouse model. To this end, RNA encoding the SpCas9 plus a customised gRNA targeting *Apopt1* exon 2 (see Chapter 2 for more details) were injected into FVB/NJ one-day zygotes (Core Facility for Conditional Mutagenesis at the IRCCS Ospedale San Raffaele, Milan, Italy). The edited embryos were

then transferred into pseudo-pregnant females. Genotyping of the resulting pups allowed the identification of four founder mice (F0), each one of them carrying several indel modifications. This chimerism could be attributed to gene editing taking place in some nuclei after the first embryonic mitotic division (Li *et al.*, 2017). To ensure germline transmission and allow allele segregation, one F0 male mouse was bred with a WT FVB/NJ female mouse. Genetic analyses of the resulting pups (F1) confirmed the presence of different heterozygous mutations in four individuals. Of these different mutations, we selected two: Mutation #1 and Mutation #4, and established two different *Apopt1* KO mouse lineages, each carrying one of the mutations. Mutation #1 was a substitution of one A for TG in *Apopt1* exon 2 (c.188delAinsTG, considering the reference mRNA sequence GenBank NM_026511). This indel predicts a frameshift and the appearance of a stop codon leading to a truncated protein of only 75 amino acids (p.Asp55Valfs*20) (**Figure 4.1**), whereas the WT protein is composed of 192 amino acids. Mutation #4 was a deletion of 11 nucleotides in *Apopt1* exon 2 (c.184_195delCATGATTGGAT, considering the reference mRNA sequence GenBank NM_026511). This deletion also predicts the translation of a truncated protein of only 84 amino acids (p.His54Glnfs*30) (**Figure 4.1**). Both selected mutations were considered for the creation of the KO mouse model as they would lead to the complete absence of the Apopt1 protein. The other two mutations (Mutation #2 and Mutation #3) were predicted to not change the reading frame and were therefore not appropriated for the generation of a KO mouse model.

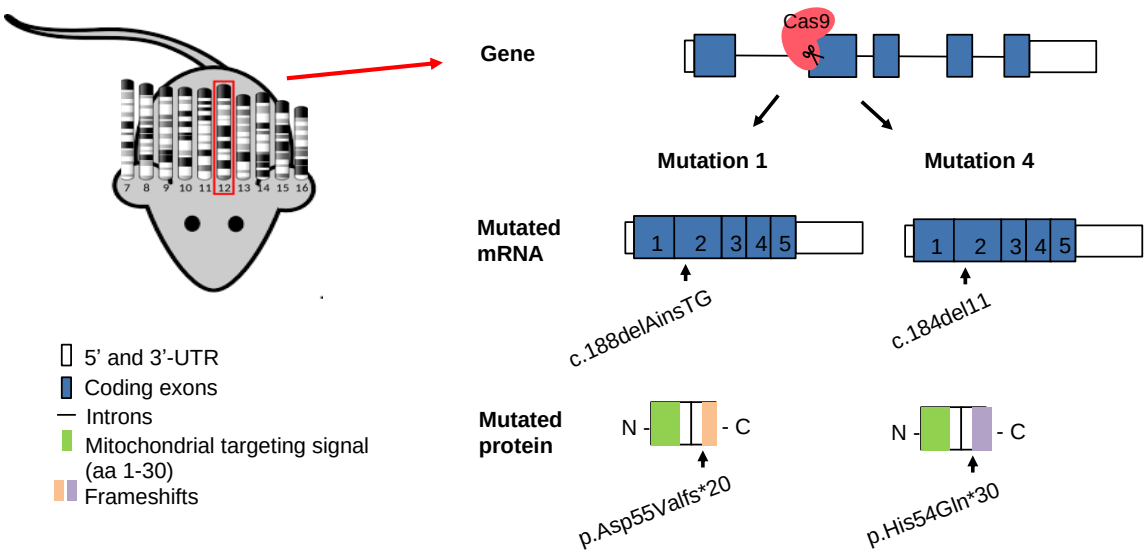

Figure 4.1 Generation of the *Apopt1* KO mouse model. CRISPR/Cas9 was employed for the targeted disruption of mouse chromosome 12 *Apopt1* coding exon 2. The *Apopt1* gene, mRNA and mutated protein products are displayed.

Skeletal muscle extracted from homozygous individuals from both mutated mouse lines (carrying mutation #1 or mutation #4) showed exactly the same level of COX deficiency (**Figure 4.2**). Thus, in order to minimise the number of animals used in this project (following the principles of the 3Rs: replace, reduce and refine the use of animals in research and testing), the subsequent analyses were carried out using only the KO mouse lineage carrying mutation #1.

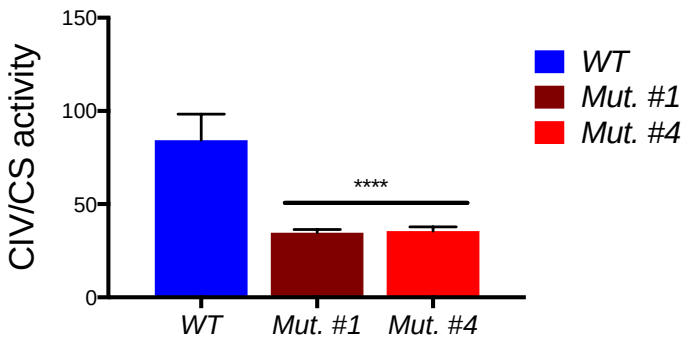

Figure 4.2 COX activity in skeletal muscle. COX (CIV) enzymatic activity normalised to the activity of citrate synthase (CS) measured in skeletal muscle from three-month-old mice. Data are presented as mean ± SEM (n = 5 mice per genotype). **** $p < 0.0001$ (two-way ANOVA Sidak's multiple comparisons test). WT: homozygous wild type mice. Mut 1: homozygous *Apopt1* KO mice carrying mutation #1. Mut 4: homozygous *Apopt1* KO mice carrying mutation #4.

To determine the effects of Mutation #1 on *Apopt1* expression, total RNA from skeletal muscle and liver was extracted. Direct sequencing of the cDNA confirmed that the mutation was present in the transcripts of heterozygous and KO animals. No traces of the WT sequence were detected in the KO cDNA sample, demonstrating that all the mRNA was carrying the indel change (**Figure 4.3A**), whereas a mix of the mutated and WT sequences was detected in the cDNA sample from heterozygous mice (not shown). Quantitative PCR was used to determine the relative abundance of the *Apopt1* mRNA, which was strongly reduced in both skeletal muscle and liver from *Apopt1*$^{-/-}$ animals compared with WT *Apopt1*$^{+/+}$ mice (**Figure 4.3B**). The amount of *Apopt1* mRNA in the heterozygous mice (*Apopt1*$^{+/-}$) was between those of the +/+ and -/- genotypes (**Figure 4.3B**). This decrease of *Apopt1* mRNA transcripts carrying a premature stop codon is a phenomenon known as nonsense-mediated mRNA decay (NMD) (Brogna and Wen, 2009). NMD serves as a surveillance mechanism that reduces the expression of genes carrying nonsense mutations by eliminating the aberrant mRNAs and avoiding the translation of a shorter and mutated protein, which may lead to a loss, switch or gain of protein function (Brogna and Wen, 2009).

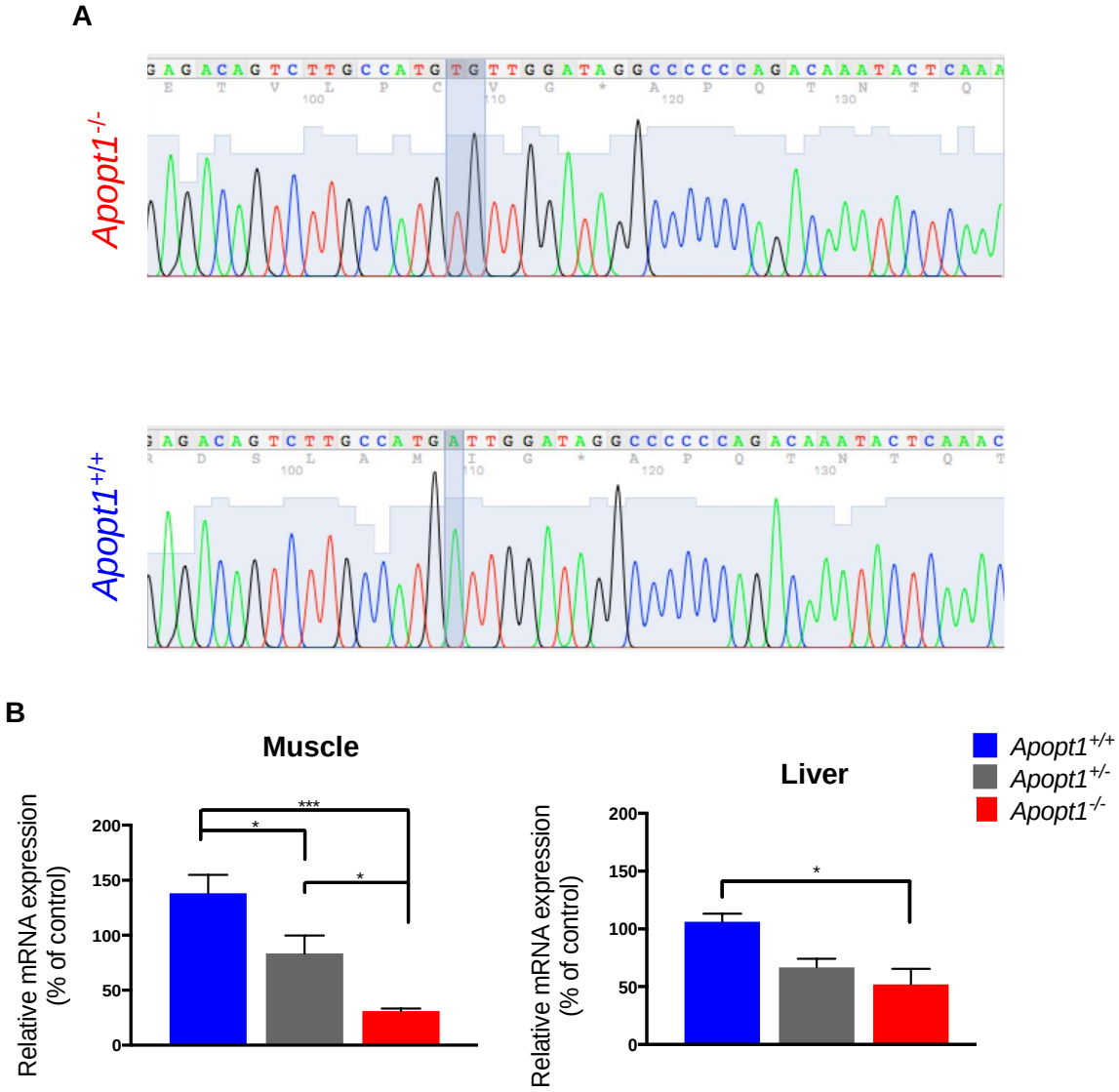

Figure 4.3 *Apopt1* mutation at the transcriptional level. (**A**) Chromatograms generated by Sanger sequencing of *Apopt1*$^{-/-}$ (homozygous KO) and *Apopt1*$^{+/+}$ (homozygous WT) cDNA from skeletal muscle highlighting the mutated position in comparison with the WT sequence. (**B**) Relative *Apopt1* mRNA expression in skeletal muscle and liver from three-month-old animals normalised to the expression of GAPDH and expressed as percentage of the WT. Data are presented as mean ± SEM (n = 5 mice per genotype; measurement repeated 3 times). *** $p < 0.0005$, ** $p < 0.005$, * $p < 0.05$ (two-way ANOVA Sidak's multiple comparisons test). *Apopt1*$^{+/+}$: homozygous WT mice, *Apopt1*$^{+/-}$: heterozygous mice, *Apopt1*$^{-/-}$: homozygous *Apopt1* KO mice.

We then attempted to confirm the absence of the Apopt1 protein in the KO mice tissues by Western blot and immunodetection using two antibodies raised against the full-length human APOPT1 (see Chapter 2 for more details), which shows 75% identity (calculated as: amino acids that match exactly between the

two sequences divided by the total number of amino acids and multiplied by 100) and 86% homology (calculated as: amino acids that match exactly plus those with similar characteristics divided by the total number of amino acids and multiplied by 100) to the mouse Apopt1 protein. The predicted MW of the WT mouse Apopt1 precursor is 22.7 kDa and of the mature protein 19.5 kDa. As shown in **Figure 4.4**, no specific signal corresponding to the predicted size for Apopt1, which should be present in the WT and absent in the KO samples, was detected in the mouse tissue and cell lysates.

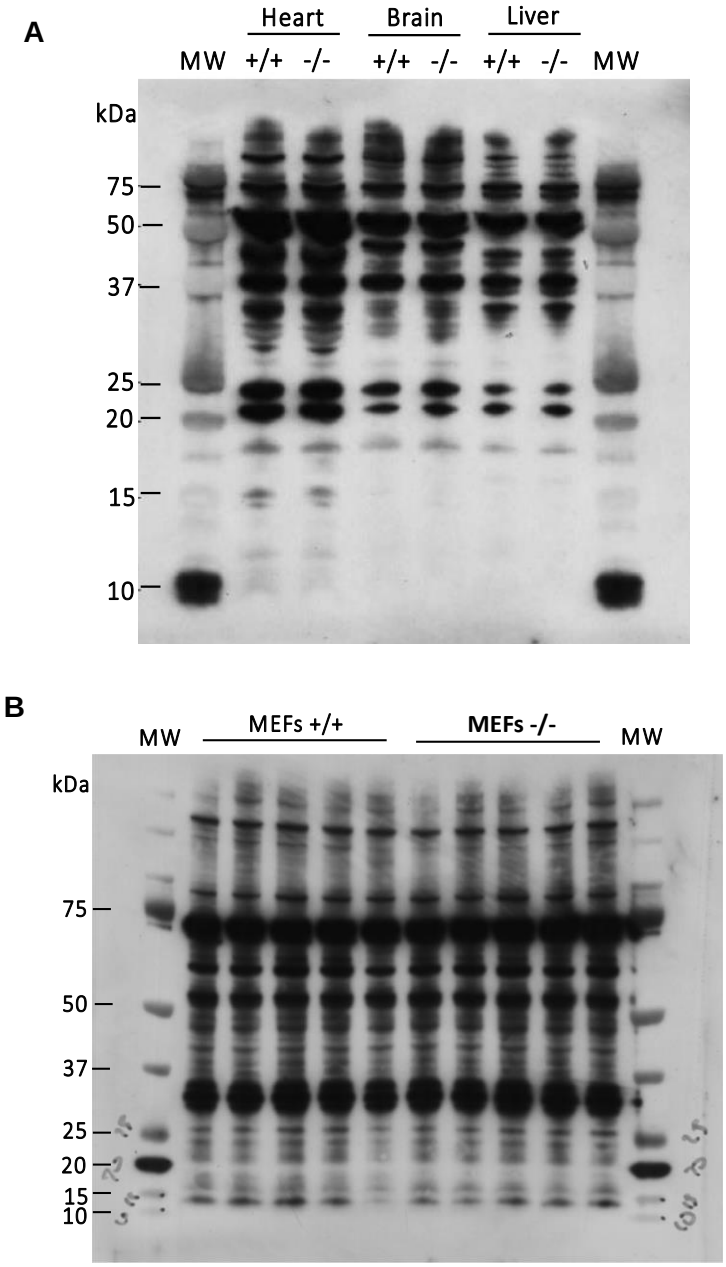

Figure 4.4

Figure 4.4 Apopt1 immunodetection trials. (**A**) SDS-PAGE (12% NuPAGE Bis-Tris, Thermo Fisher Scientific) and WB analysis of homozygous WT (+/+) and homozygous KO (-/-) mouse isolated mitochondria from heart, brain and liver, using an anti-APOPT1 primary antibody (Proteintech 27300-1-AP). 30 µg of total protein lysates were loaded. (**B**) SDS-PAGE (4-12 % NuPAGE Bis-Tris, Thermo Fisher Scientific) and WB analysis of homozygous WT (+/+) and homozygous KO (-/-) MEFs, using a custom-made anti-APOPT1 primary antibody (ProteoGenix 8992-01). 30 µg of protein were loaded.

To propagate the mutated mouse lineage, heterozygous individuals were crossed. The litters (F2) showed Mendelian ratios of homozygous WT (+/+), heterozygous (+/-) and homozygous *Apopt1* KO (-/-) (**Table 4.1**). These groups of animals were subsequently used for phenotypic and biochemical characterisation.

Table 4.1 Mendelian ratios of pups (N=50) born from *Apopt1*$^{+/-}$ mice interbreeding.

Genotype	Expected	Observed
+/+	25 %	20 %
+/-	50 %	56 %
-/-	25 %	24 %

All animals carrying at least one WT allele presented the same phenotypic characteristics. Therefore, animals from both genotypes were used as controls (termed as *Apopt1*^{WT}) for many of the behavioural and biochemical analyses shown in the following sections.

4.2.2 *Apopt1*$^{-/-}$ mice did not show major alterations on energy metabolism

To determine the impact of *Apopt1* ablation on energy metabolism we used a CLAMS^{TM} system, that measures several metabolic parameters including food and water intake, oxygen consumption and carbon dioxide production. In addition, the mice were weighted every 30 days. Oxygen consumption and carbon dioxide production (**Figure 4.6A and 4.6B**) are used as variables by the

CLAMS™ software for the indirect calorimetry or respirometry calculations of heat production, which is directly related to energy expenditure and was unchanged in *Apopt1*$^{-/-}$ compared with *Apopt1*^{WT} mice (**Figure 4.6D**). The respiratory exchange ratio (RER) is the ratio between the amount of carbon dioxide produced and oxygen consumed and is directly related to the type of substrates metabolised to produce energy, which can switch from glucose to fat in the case of metabolic alterations. Therefore, a RER of 0.7 indicates that the main fuel used is fat, a RER of around 0.85 means that both fat and carbohydrates are being used and a RER of 1.0 or above means that the source of energy is mainly carbohydrates. Mice in both experimental groups showed normal RER of around 0.85 (**Figure 4.6C**).

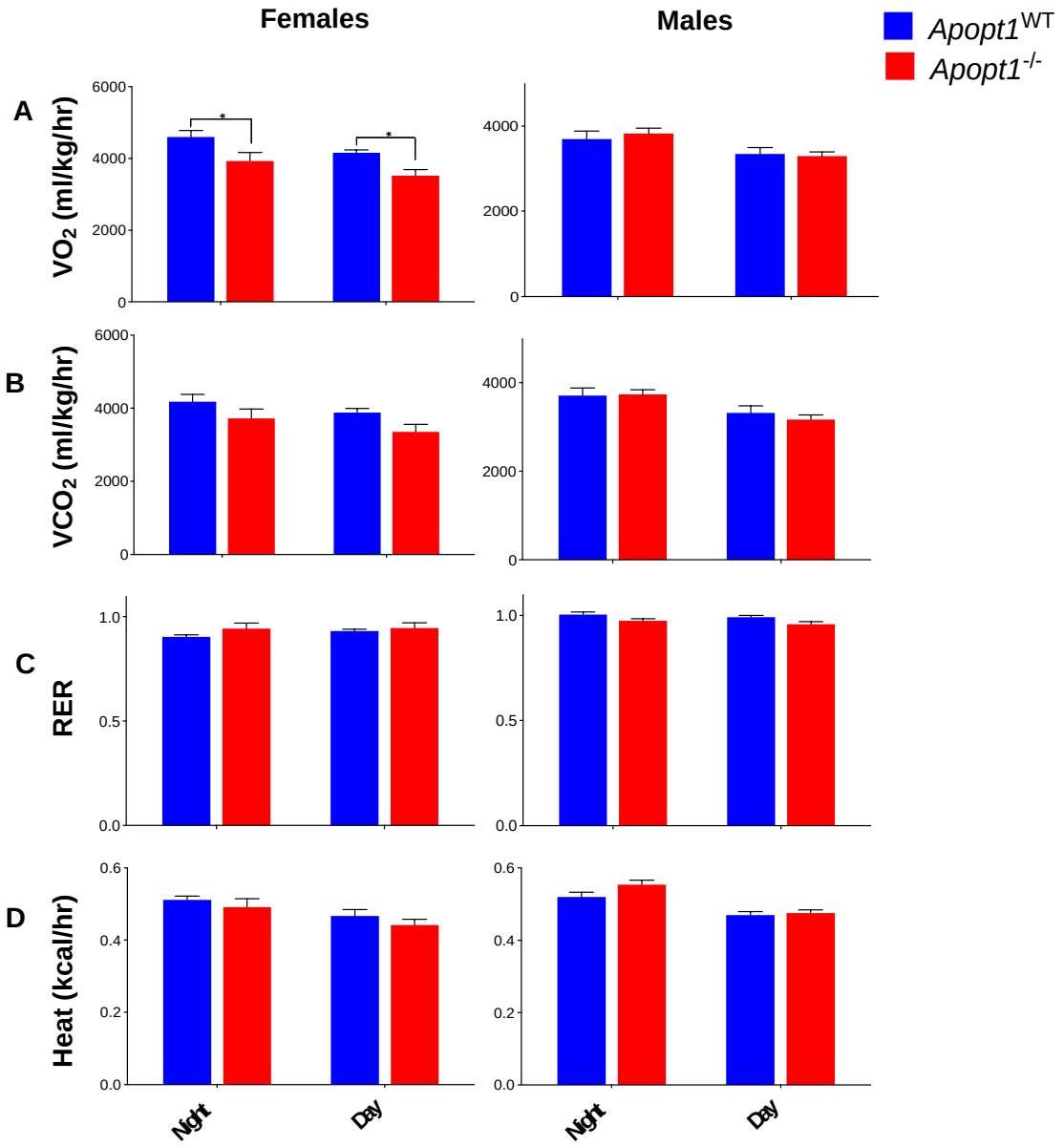

Figure 4.6

Figure 4.6 Energy metabolism at three months of age. (**A**) Volume of oxygen (ml/kg/hr) consumed in female and male animals at 3 months of age. (**B**) Volume of carbon dioxide (ml/kg/hr) produced in female and male animals at 3 months of age. (**C**) Respiratory exchange ratio (RER) in female and male animals at 3 months of age. (**D**) Heat (Kcal/hr) produced by female and male animals at 3 months of age. Data measured in the CLAMS™ system. Data are presented as mean ± SEM. * $p < 0.05$ (two-way ANOVA Sidak's multiple comparisons test). *Apopt1*^{WT} (n = 10): control group composed of *Apopt1*$^{+/+}$ and *Apopt1*$^{+/-}$ individuals. *Apopt1*$^{-/-}$ (n = 5): homozygous *Apopt1* KO mice.

In addition, no differences were found in either food or water intake (data not shown) and, consequently, *Apopt1*$^{-/-}$ male and female mice did not display any differences in weight at 3, 6 or 12 months of age (**Figure 4.7**).

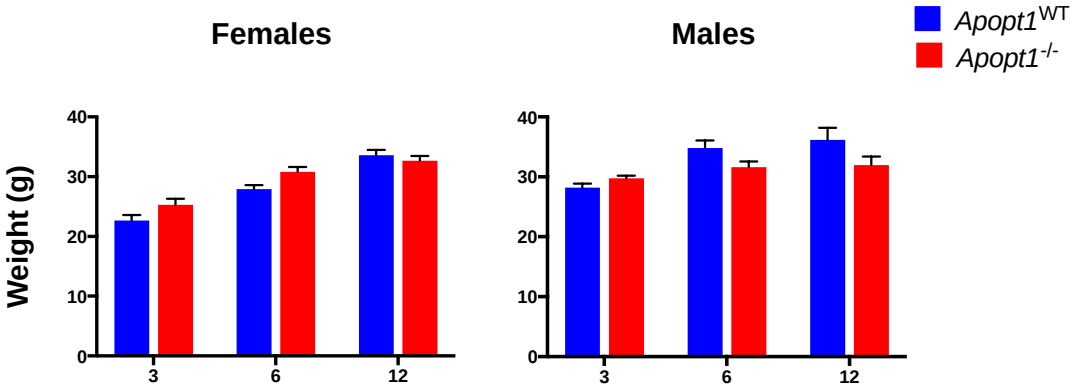

Figure 4.7 Weight at 3, 6 and 12 months of age. Female and male mice weight at 3-, 6- and 12-months of age. Data are presented as mean ± SEM. *Apopt1*^{WT} (n = 10): control group composed of *Apopt1*$^{+/+}$ and *Apopt1*$^{+/-}$ individuals. *Apopt1*$^{-/-}$ (n = 10): homozygous *Apopt1* KO mice.

4.2.3 *Apopt1*$^{-/-}$ mice displayed impaired motor performance

Mutations in the human *APOPT1* gene are associated with neuromuscular disorder, with symptoms noticeable from a young age, characterised by spastic tetraparesis (i.e. muscular weakness and stiffness affecting all four extremities). In some of the cases, a mild to severe cognitive impairment was also observed (Melchionda *et al.*, 2014). To determine whether the mutated mice presented a similar clinical phenotype, motor performance and coordination were evaluated using the treadmill and rotarod tests at different ages. Both male and female *Apopt1*$^{-/-}$ animals performed significantly worse on the treadmill already in their

early adulthood (three months old), reflecting an early onset of muscular weakness (**Figure 4.8A**). Their difficulty to use the four extremities was noticeable also during the rotarod test, assessing coordination, in which *Apopt1* KO mice also performed worse at three months of age (**Figure 4.8B**). In order to assess the progression of the phenotype, the rotarod test was repeated with six- and twelve-month-old mice and the treadmill test was repeated at twelve months of age. No significant changes were observed in their motor performance as they aged (**Figure 4.8A and B**), similar to the clinical course observed in patients, which also tended to stabilise (Melchionda *et al.*, 2014).

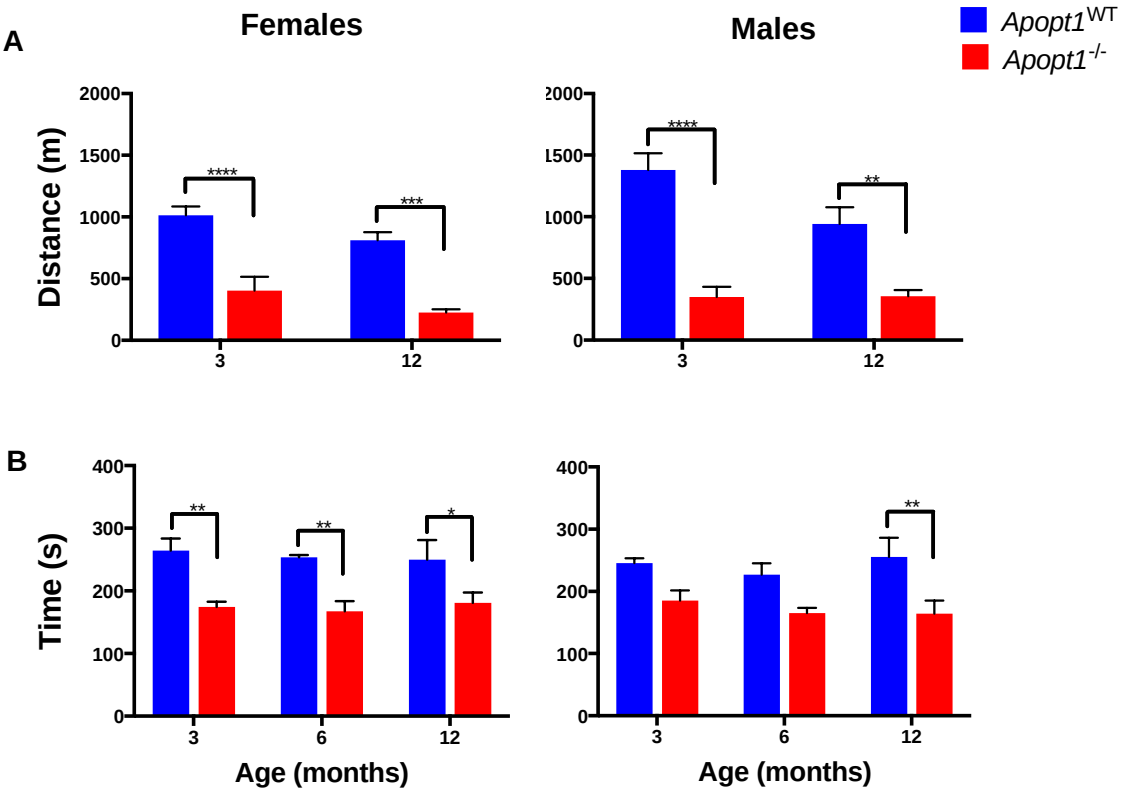

Figure 4.8 Motor performance and coordination. (**A**) Distance run by the tested female and male mice on the treadmill at three and twelve months of age. (**B**) Time in seconds spent by the female and male mice on the Rotarod cylinders before falling at three, six and twelve months of age. < 0.005, * p < 0.05 (two-way ANOVA Sidak's multiple comparisons test). *Apopt1*^{WT} (n = 10): control group composed of *Apopt1*$^{+/+}$ and *Apopt1*$^{+/-}$ individuals. *Apopt1*$^{-/-}$ (n = 5): homozygous *Apopt1* KO mice.

4.2.4 Age-related impairment of spontaneous activity and exploratory behaviour in *Apopt1*$^{-/-}$ mice

The CLAMS™ system also makes it possible to monitor changes in spontaneous activity (including locomotor and exploratory behaviour) to assess mouse cognitive function. Total, ambulatory and rear movements were monitored in this way in three-month-old mice. Total movements were defined as all infrared beam interruptions detected (all counts). When mice broke a series of infrared beams in sequence, meaning that they were moving deliberately (like traversing the cage), counts were defined as ambulatory movements. Movements that broke the same infrared beam repeatedly, for example when grooming or scratching, were not counted as ambulatory movements. All beam interruptions detected in the y-axis, i.e. when mice were standing upright on the hind-legs in order to visually explore their environment, were counted as rear movements. No significant differences in total, ambulatory or rear movements were observed between control and KO mice at three months of age (**Figure 4.9**).

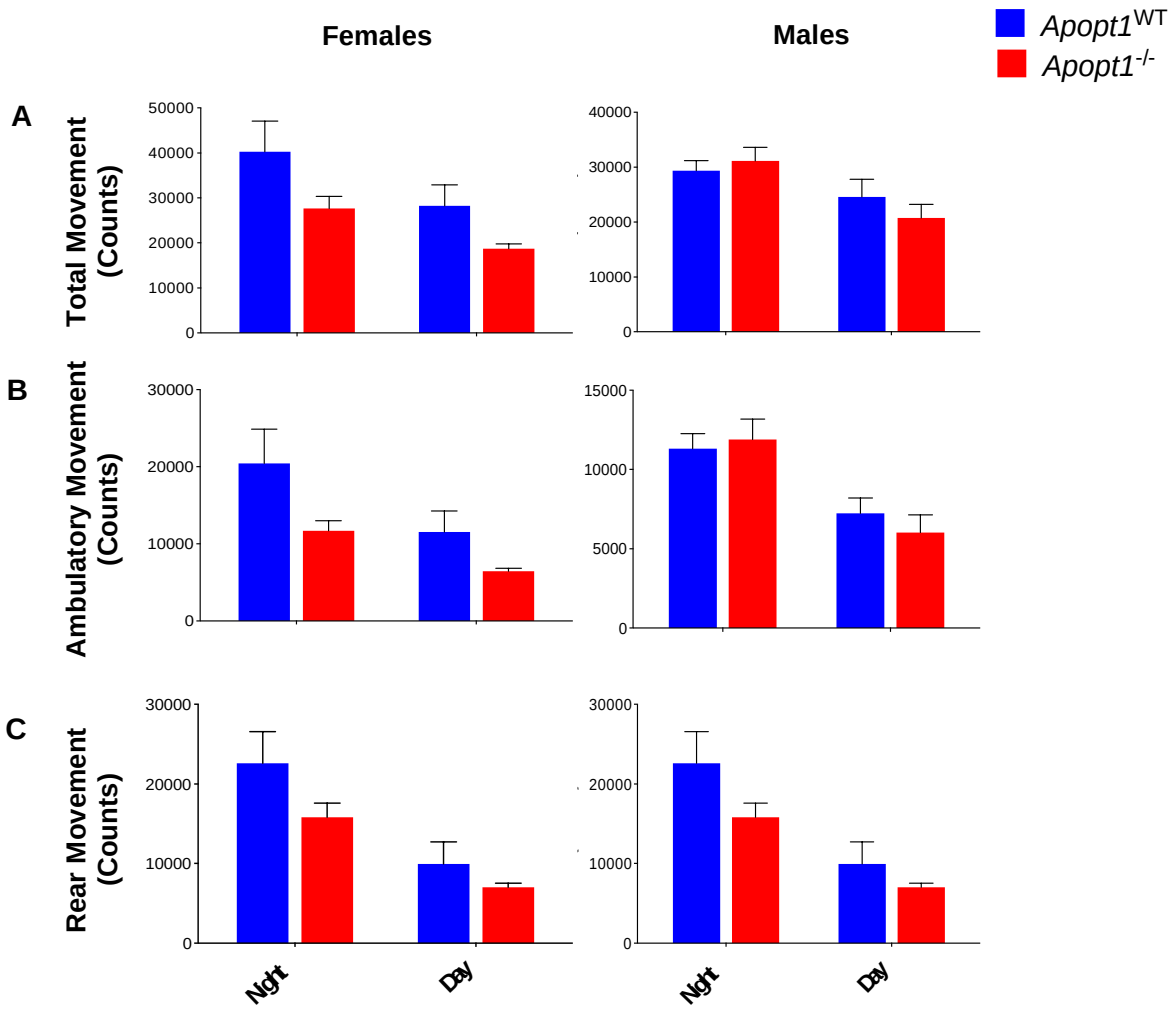

Figure 4.9 Movements at three months of age. (**A**) Total movements of female and male animals at three months of age. (**B**) Ambulatory movements of female and male animals at three months of age. (**C**) Rear movements of female and male animals at three months of age. Data measured in the CLAMS™ system. Data are presented as mean ± SEM. *Apopt1*^{WT} (n = 10): control group composed of *Apopt1*$^{+/+}$ and *Apopt1*$^{+/-}$ individuals. *Apopt1*$^{-/-}$ (n = 5): homozygous *Apopt1* KO mice.

Spontaneous activity was re-assessed at twelve months of age. In this case, horizontal and vertical movements of mice placed in a new environment were monitored for 30 minutes in an 'activity cage'. This test allows the evaluation of the exploratory behaviour, i.e. the tendency of mice to investigate and acquire information about a new environment. Horizontal movements were found strongly reduced in KO animals indicating that they were less motivated than WT mice to investigate their environment (**Figure 4.10**). A decreasing tendency was

observed also for vertical movements, meaning that *Apopt1*$^{-/-}$ mice spent less time obtaining visual information about their environment (**Figure 4.10**).

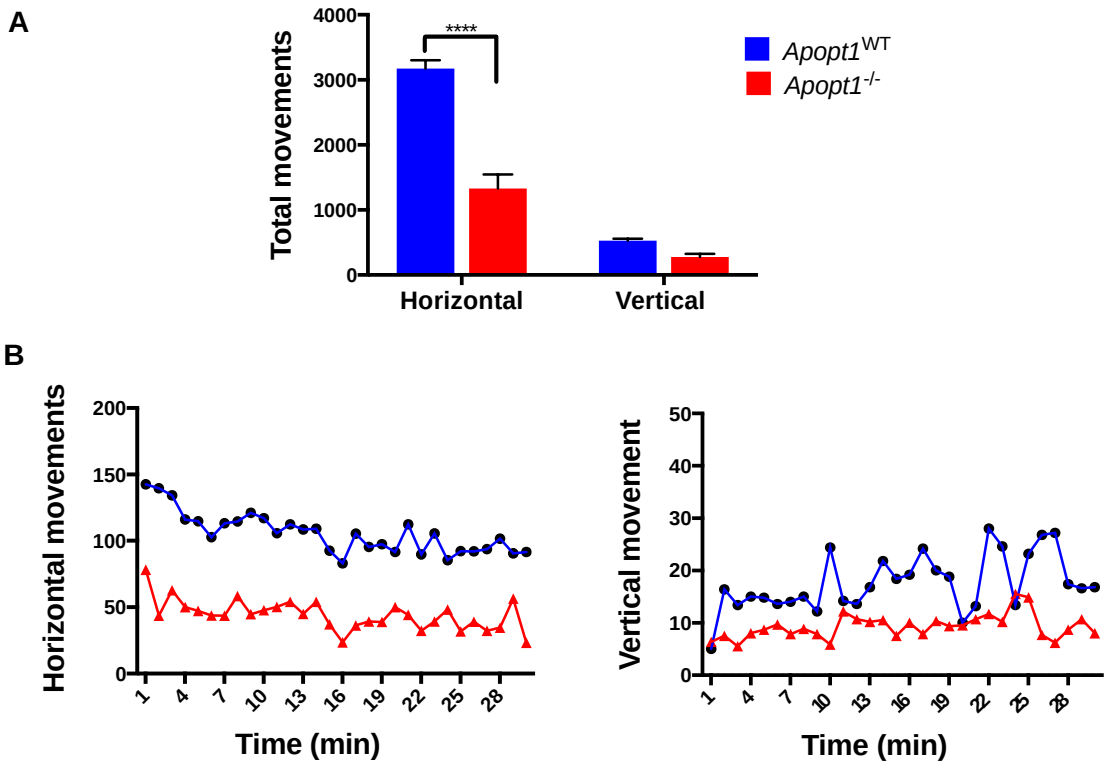

Figure 4.10 Movements at twelve months of age. (**A**) Total spontaneous horizontal and vertical movements of twelve-month-old mice measured in an activity cage for 30 minutes. (**B**) Same data represented as horizontal movements per minute (left) and vertical movements per minute (right). Data are presented as mean ± SEM. **** $p < 0.0001$ (two-way ANOVA Sidak's multiple comparisons test). *Apopt1*^{WT} (n = 5): control group composed of *Apopt1*$^{+/+}$ and *Apopt1*$^{+/-}$ individuals. *Apopt1*$^{-/-}$ (n = 5): homozygous *Apopt1* KO mice.

The decrease in exploratory behaviour was also evident when running the Y maze test. The total number of entries (count of the arms explored in 5 minutes), although not significantly reduced at three months, was much lower in *Apopt1*$^{-/-}$ mice than in the WT littermates at six and twelve months of age (**Figure 4.11**).

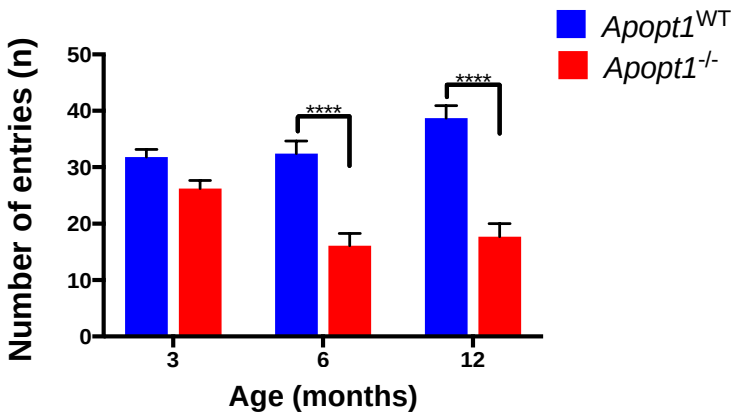

Figure 4.11 Number of arms explored in the Y maze test. Number of entries in each arm of the Y maze performed at different ages. Data are presented as mean ± SEM. **** $p < 0.0001$ (two-way ANOVA Sidak's multiple comparisons test). *Apopt1*^{WT} (n = 12): control group composed of *Apopt1*$^{+/+}$ and *Apopt1*$^{+/-}$ individuals. *Apopt1*$^{-/-}$ (n = 7): homozygous *Apopt1* KO mice.

4.2.5 Other neurological indicators were normal in the *Apopt1*$^{-/-}$ mice

The Y maze test was also used to investigate the contribution of *Apopt1* to spatial learning and memory in mice. However, the percentage of alternation was the same for all animals at all ages measured, which means that *Apopt1* KO mice were able to recognize the last arm explored and choose a new one to visit (**Figure 4.12**).

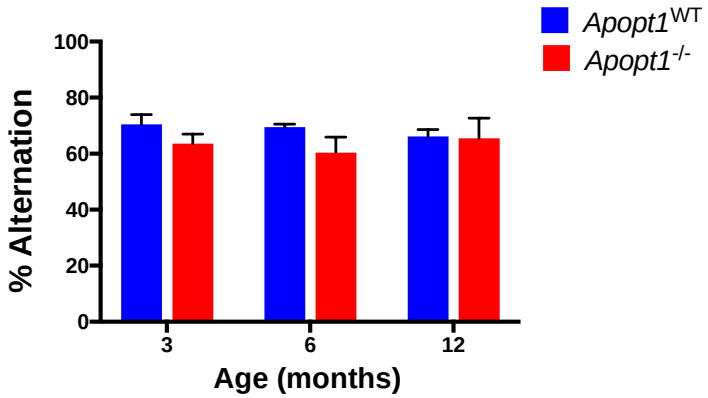

Figure 4.12 Results of the Y maze alternation test. Percentage of alternation scored in the Y maze by the female and male mice at different ages. Data are presented as mean ± SEM. *Apopt1*^{WT} (n = 12): control group composed of *Apopt1*$^{+/+}$ and *Apopt1*$^{+/-}$ individuals. *Apopt1*$^{-/-}$ (n = 7): homozygous *Apopt1* KO mice.

Spastic tetraparesis is associated with clumsy movements and walking difficulties, which was observed in several *APOPT1* patients (Melchionda *et al.*, 2014). However, *Apopt1* KO mice showed normal gait and posture at all ages (data not shown) and did not display feet clasping either, a common sign of neurological conditions in mouse models (**Figure 4.13**).

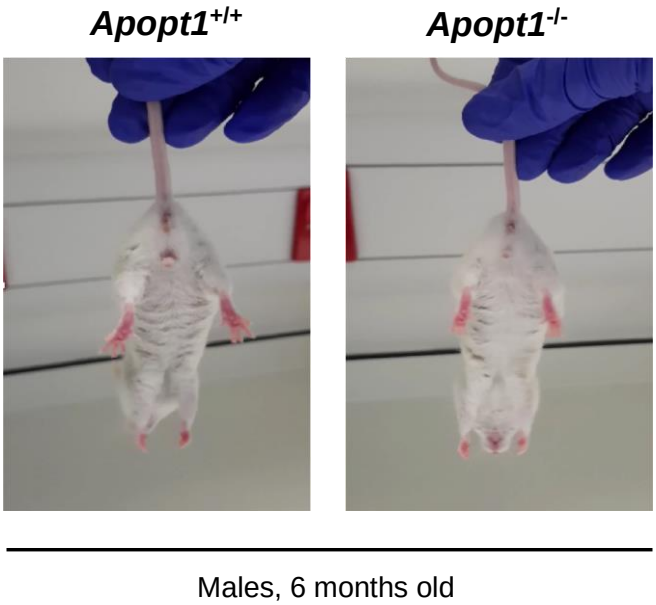

Figure 4.13 Feet clasping. Photographs of the typical posture of six-month-old homozygous WT mice (*Apopt1*$^{+/+}$) compared to homozygous KO mice (*Apopt1*$^{-/}$) when were suspended by the tail.

We then used the pole-test to measure proprioception, which involves sensory neurons from the inner ear (motion and orientation) and from the stretch receptors in the muscles and the joint-supporting ligaments (stance). However, similarly to *Apopt1*^{WT} littermates, *Apopt1*$^{-/-}$ mice required less than 10 seconds to descend the pole, which is the expected time for healthy normal mice, and did not fall of it regardless of the age (**Figure 4.14**).

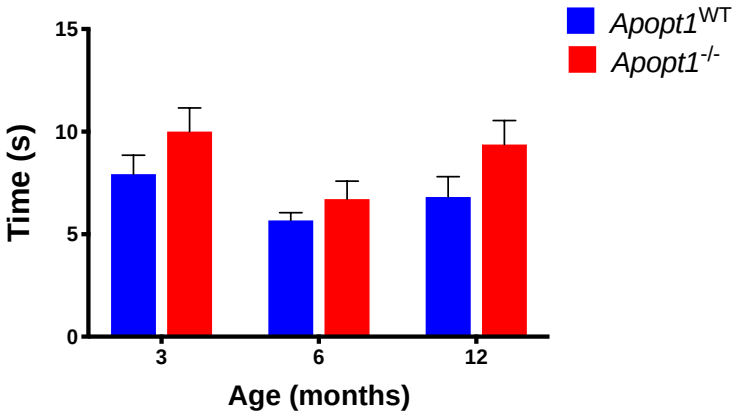

Figure 4.14 Pole-test motor ability test. Time in seconds spent by female and male mice to descend a pole at different ages. Data are presented as mean ± SEM. *Apopt1*^{WT} (n = 8): control group composed of *Apopt1*$^{+/+}$ and *Apopt1*$^{+/-}$ individuals. *Apopt1*$^{-/-}$ (n = 8): homozygous *Apopt1* KO mice.

4.2.6 Skeletal muscle showed no histological alterations in *Apopt1*$^{-/-}$ mice

Hematoxylin and eosin (H&E) staining in skeletal muscle showed normal fibre morphology and size in *Apopt1*$^{-/-}$ animals at three (**Figure 4.15A**) and twelve months of age (data not shown). No centralised nuclei, which represent degenerative-regenerative fibres commonly observed in several types of myopathies (Folker and Baylies, 2013), were detected either (**Figure 4.15A**). When muscle was stained with the modified Gömöri trichrome stain, no ragged red fibres, which are a common marker for mitochondrial myopathies (Nardin and Johns, 2001), were observed (**Figure 4.15B**).

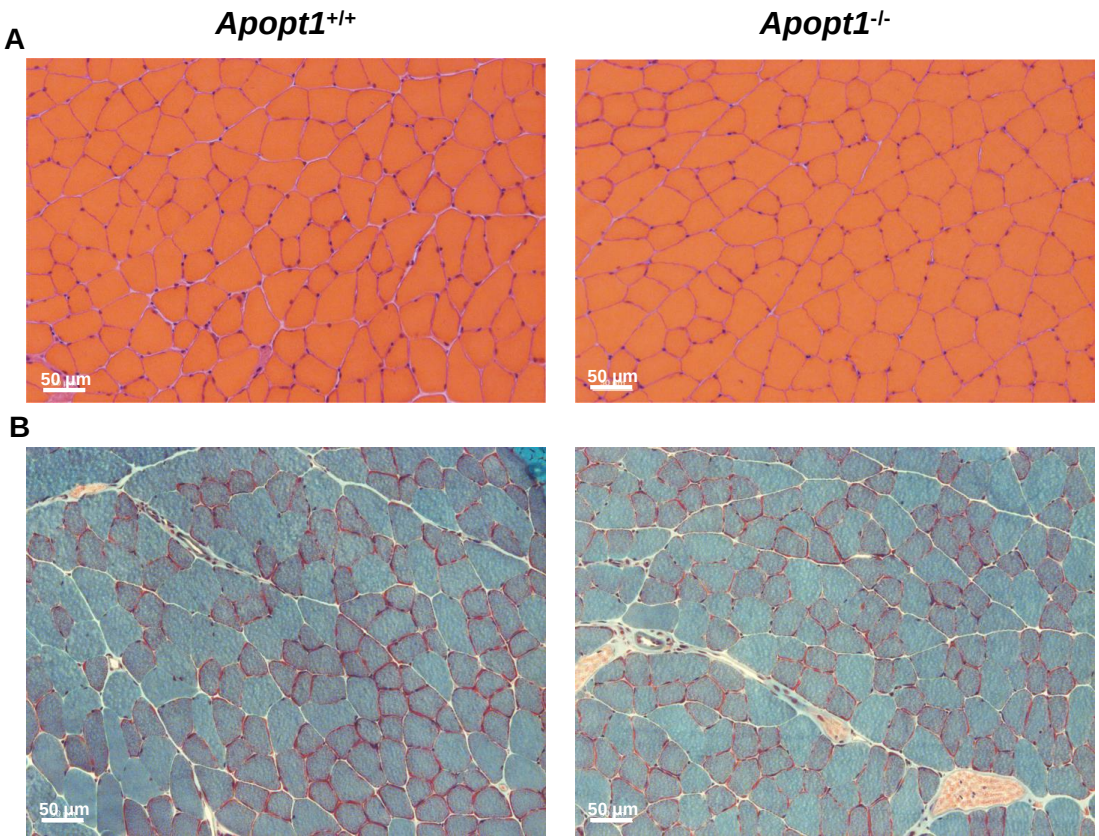

Figure 4.15 Histological examination of mouse skeletal muscle. (**A**) Representative H&E staining in skeletal muscle of three-month-old individuals. (**B**) Representative modified Gömöri trichrome staining in skeletal muscle of three-month-old individuals. *Apopt1*$^{+/+}$: homozygous WT mice, *Apopt1*$^{-/-}$: homozygous *Apopt1* KO mice. Raffaele Cerutti performed these experiments.

4.2.7 Lack of histopathological alterations in *Apopt1*$^{-/-}$ mice brains

For the evaluation of neurodegeneration, neuronal nuclear protein (NeuN) was used as a marker of neuronal differentiation (NeuN is not present in immature neural progenitor cells) and neuronal death (disappearance of NeuN immunoreactivity). Immunostaining of NeuN in *Apopt1*$^{-/-}$ mice in the frontal and occipital cortex showed neither undifferentiated neurons nor neuronal loss (**Figure 4.16**). The same was found when analysing the hippocampus, the basal ganglia and the mesencephalon (data not shown).

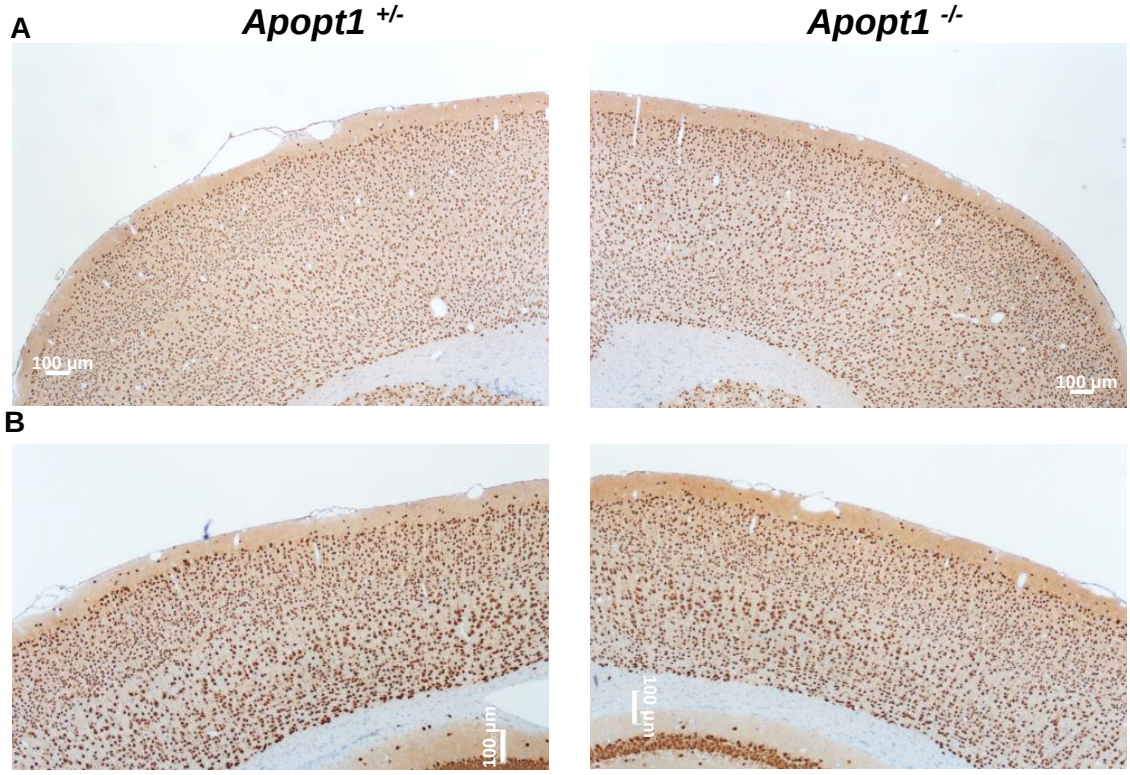

Figure 4.16 NeuN immunohistochemical staining. Representative NeuN staining of the frontal cortex (**A**) and occipital cortex (**B**) of three-month-old mice. *Apopt1*$^{+/-}$: heterozygous *Apopt1* mice, *Apopt1*$^{-/-}$: homozygous *Apopt1* KO mice. Raffaele Cerutti performed these experiments.

Neuronal necrosis and degeneration were examined using the cresyl violet (CV) staining. However, no brain damage was found neither in the frontal nor in the hippocampus (**Figure 4.17**), nor in the occipital cortex (data not shown) of *Apopt1* homozygous KO mice.

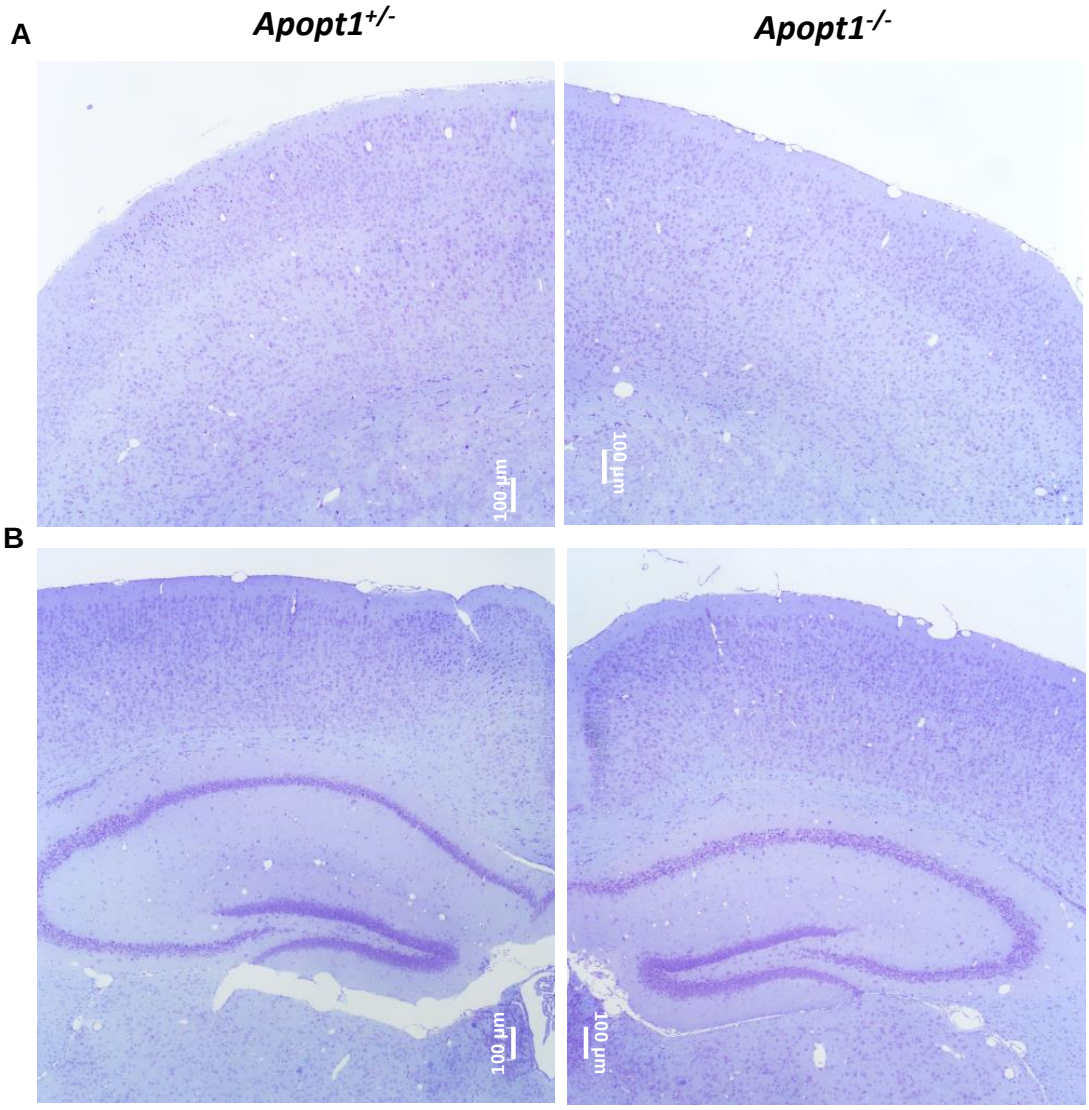

Figure 4.17 Cresyl violet immunohistochemical staining. Representative CV staining of the frontal cortex (**A**) and hippocampus (**B**) of three-month-old mice. *Apopt1*$^{+/-}$: heterozygous *Apopt1* mice, *Apopt1*$^{-/-}$: homozygous *Apopt1* KO mice. Raffaele Cerutti performed these experiments.

4.2.8 *Apopt1*$^{-/-}$ mice showed pan-tissue isolated COX deficiency

Histochemical analyses were used to determine the impact of Apopt1 ablation on COX activity in post-mitotic tissues. As shown in **Figure 4.18,** COX staining was clearly reduced in skeletal muscle, in several regions of the brain and in kidney from three-month-old mice, whereas succinate dehydrogenase (SDH) staining was normal in all the analysed tissues. The same COX reduction was observed in tissues from one-year-old mice (data not shown).

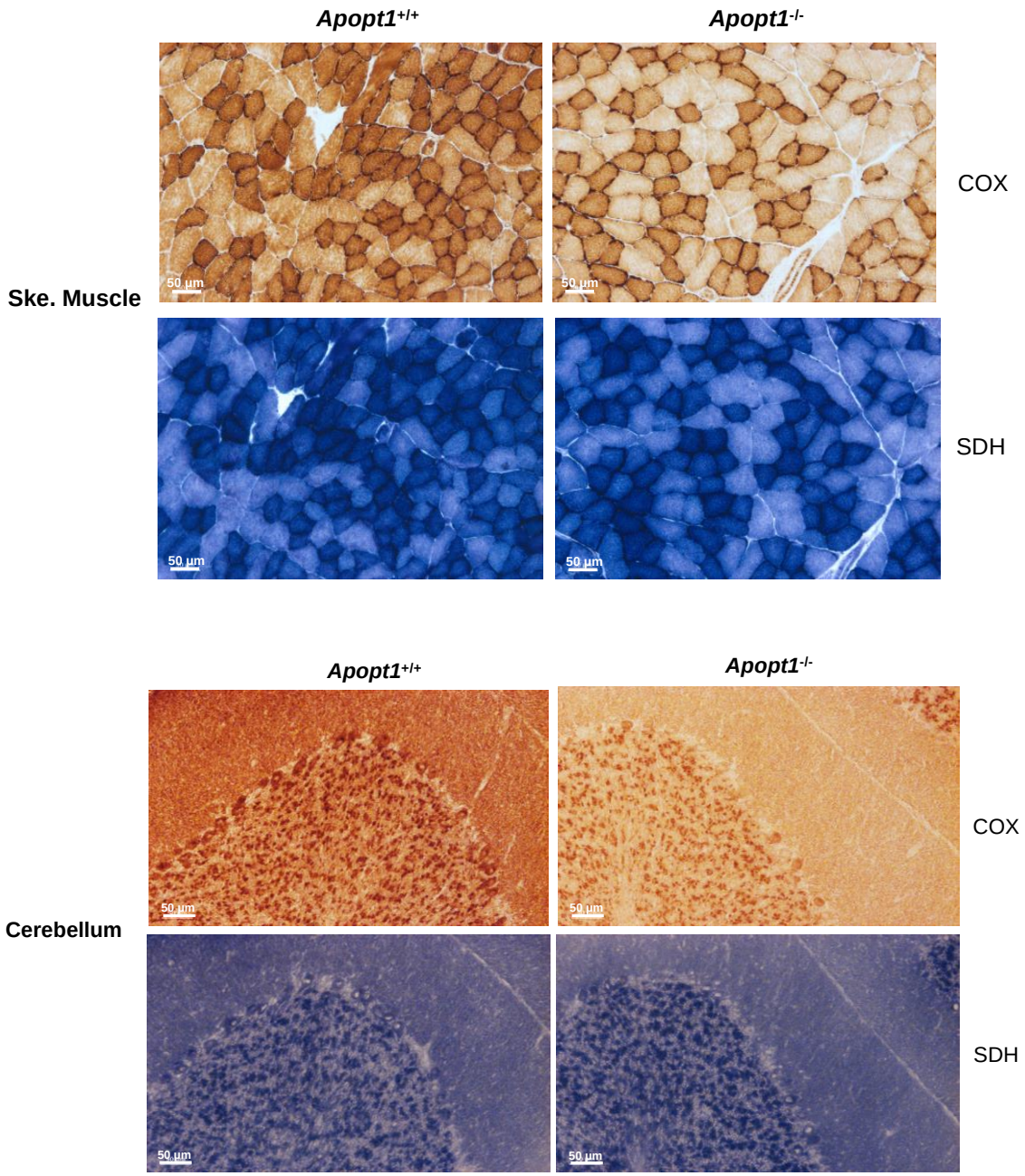
Apopt1+/+
Apopt1-/-
COX
Ske. Muscle
SDH
50 µm
Apopt1+/+
Apopt1-/-
COX
Cerebellum
SDH
50 µm

Figure 4.18

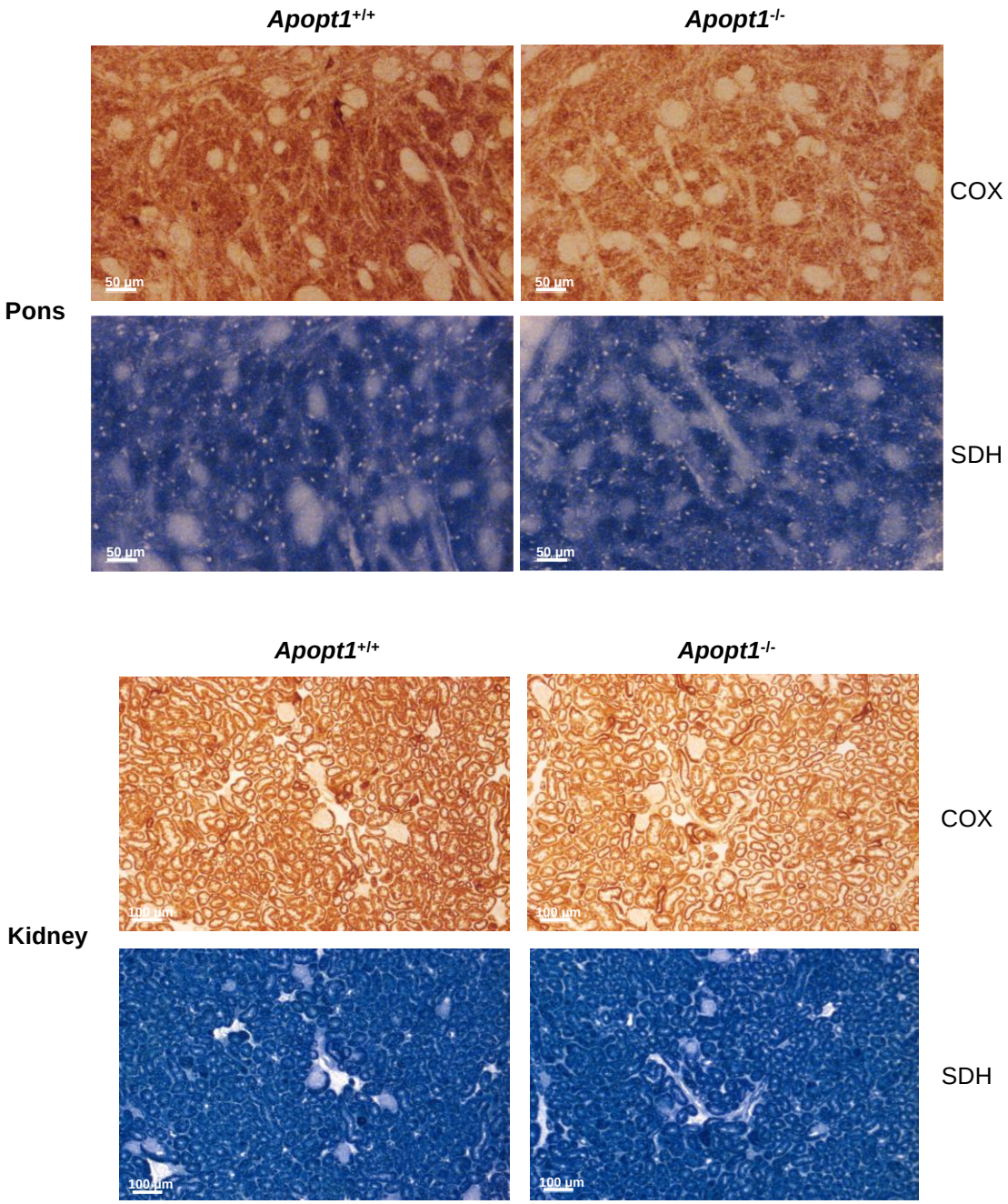

Figure 4.18 Histochemical analysis in mouse tissues. Representative histochemical reactions specific to COX and SDH in skeletal muscle (**A**), in cerebellar cortex and the pons region of the brainstem (**B** and **C**, respectively) and in kidney (**D**) of three-month-old individuals. *Apopt1*$^{+/+}$: homozygous WT mice, *Apopt1*$^{-/-}$: homozygous *Apopt1* KO mice. Raffaele Cerutti performed these experiments.

To quantify the extent of the COX deficiency in the *Apopt1*$^{-/-}$ tissues, kinetic measurements of COX enzymatic activity were performed in tissue homogenates. The activity was reduced by 40 to 60% of controls in skeletal

muscle, kidney, heart, brain and liver of three-month-old *Apopt1*$^{-/-}$ mice compared with *Apopt1*$^{+/+}$ or *Apopt1* $^{+/-}$ controls, in which COX activity was indistinguishable (**Figure 4.19**). One-year old skeletal muscle, liver and brain still showed significant COX deficiency compared with age matched WT animals (**Figure 4.19**).

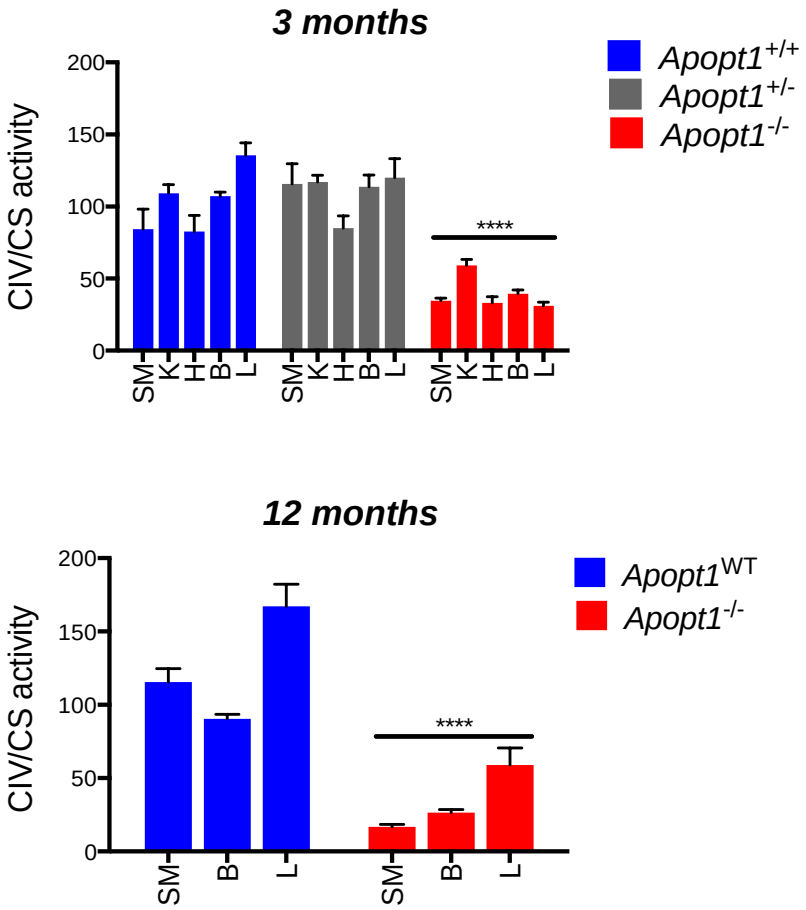

Figure 4.19 Biochemical analysis in mouse tissues. COX (CIV) enzymatic activity normalised to the activity of citrate synthase (CS) measured in kidney (K), heart (H), skeletal muscle (SM), cerebellar cortex (B) and liver (L) from three- and twelve-month-old mice. Data are presented as mean ± SEM (n = 5 mice per genotype). **** $p < 0.0001$ (two-way ANOVA Sidak's multiple comparisons test). *Apopt1*$^{+/+}$: homozygous WT mice, *Apopt1*$^{+/-}$: heterozygous mice, *Apopt1*$^{-/-}$: homozygous *Apopt1* KO mice, *Apopt1*^{WT}: control group composed of *Apopt1*$^{+/+}$ and *Apopt1*$^{+/-}$ individuals.

The activities of other respiratory chain complexes and of citrate synthase were the same as controls in all the analysed tissues, except for complexes I and III, which were slightly reduced in the *Apopt1*$^{-/-}$ liver samples and complex II

activity, which was slightly increased in the skeletal muscle and kidney of *Apopt1*$^{-/-}$ mice (**Figure 4.20**).

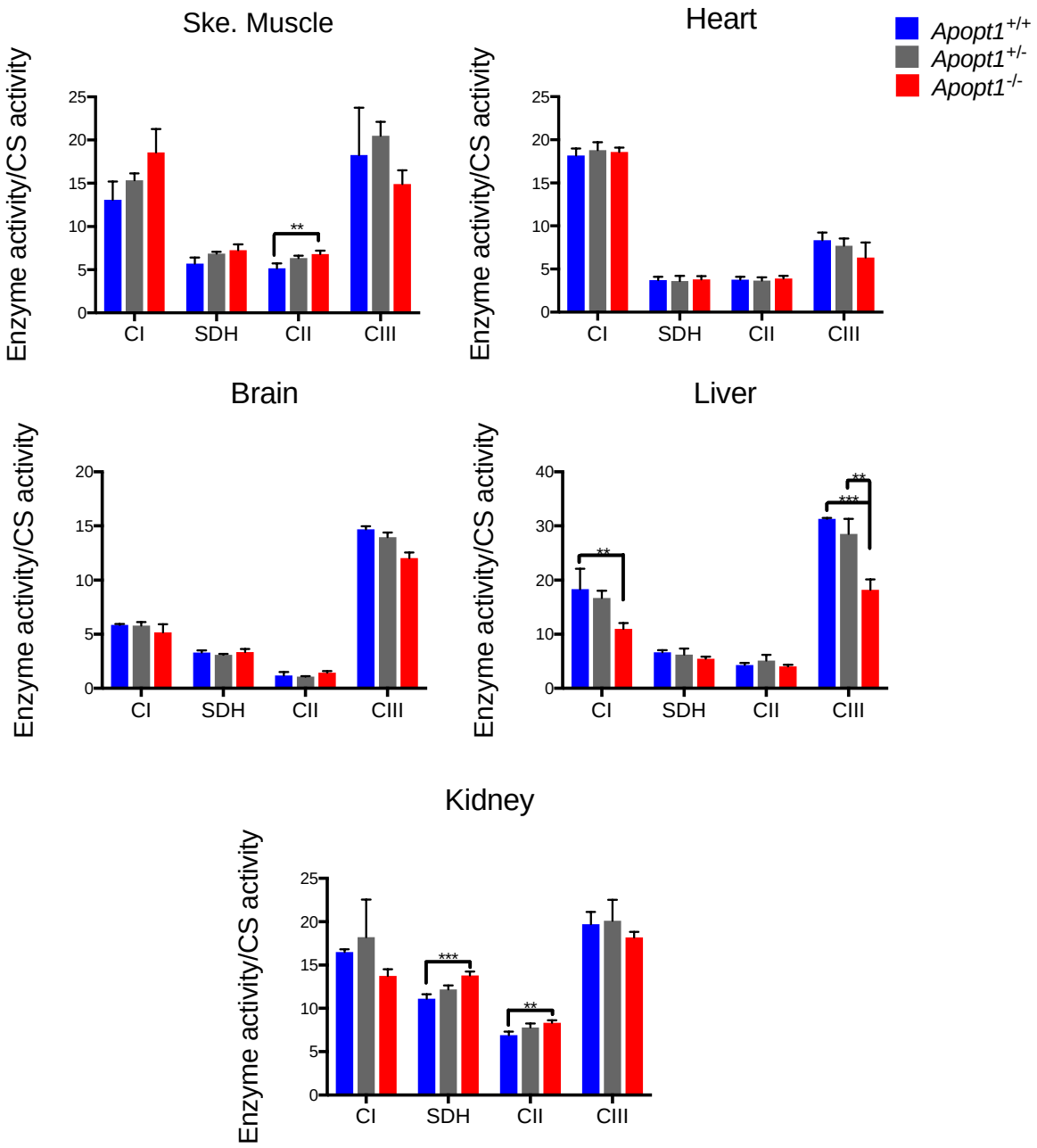

Figure 4.20 Biochemical analysis in mouse tissues. Complex I (CI), succinate dehydrogenase (SDH), complex II (CII) and complex III (CIII) enzymatic activities normalised to the activity of citrate synthase (CS) measured in kidney, heart, skeletal muscle, cerebellar cortex and liver from three-month-old mice. Data are presented as mean ± SEM (n = 3 mice per genotype). *** $p < 0.0005$, ** $p < 0.005$ (two-way ANOVA Sidak's multiple comparisons test). *Apopt1*$^{+/+}$: homozygous WT mice, *Apopt1*$^{+/-}$: heterozygous mice, *Apopt1*$^{-/-}$: homozygous *Apopt1* KO mice.

4.2.9 COX subunit steady-state levels were reduced in the *Apopt1*$^{-/-}$ mice tissues

Considering the COX enzymatic deficiency, we then checked the steady-state protein levels of several structural COX subunits, which were all found decreased in *Apopt1*$^{-/-}$ liver, whereas subunits of complex I (Ndufs1) and complex III (Uqcrc2) were unchanged (**Figure 4.21**). Interestingly, the late (Mt-Co3 and Cox6b) and intermediate (Mt-Co2 and Cox5b) assembly subunits, as well as Mt-Co1, were more decreased than the subunits that assemble earlier (Cox4 and Cox5a) (**Figure 4.21, graph**), suggesting that the assembly defect is predominantly affecting the middle to last steps of the COX assembly pathway (Vidoni *et al.*, 2017).

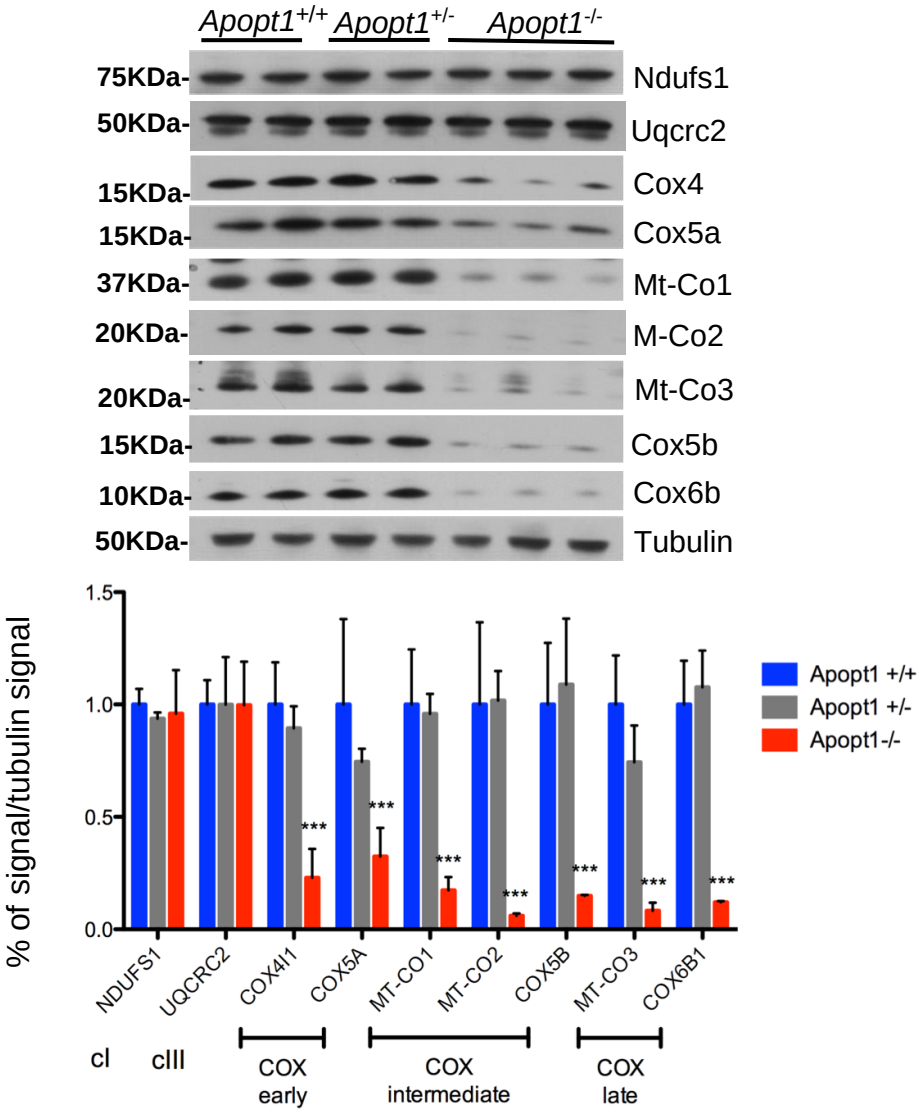

Figure 4.21

Figure 4.21 Reduced COX subunits protein levels in mouse liver. Western blot and immunodetection analysis of SDS-PAGE of total lysates from liver from the indicated genotypes, each lane showing the results for one animal. The graph shows the densitometric quantification of the signal intensities normalised to tubulin signal. Data are presented as mean ± SEM. *** $p < 0.0005$ (two-way ANOVA Sidak's multiple comparisons test). *Apopt1*$^{+/+}$ (n = 2): homozygous WT mice, *Apopt1*$^{+/-}$ (n = 2): heterozygous mice, *Apopt1*$^{-/-}$ (n = 3): homozygous *Apopt1* KO mice.

COX structural subunit protein levels were also decreased in *Apopt1*$^{-/-}$ skeletal muscle and brain, as well as in cultured MEFs (**Figure 4.22**), confirming the specific reduced amounts of COX components in all the analysed mouse tissues and cells.

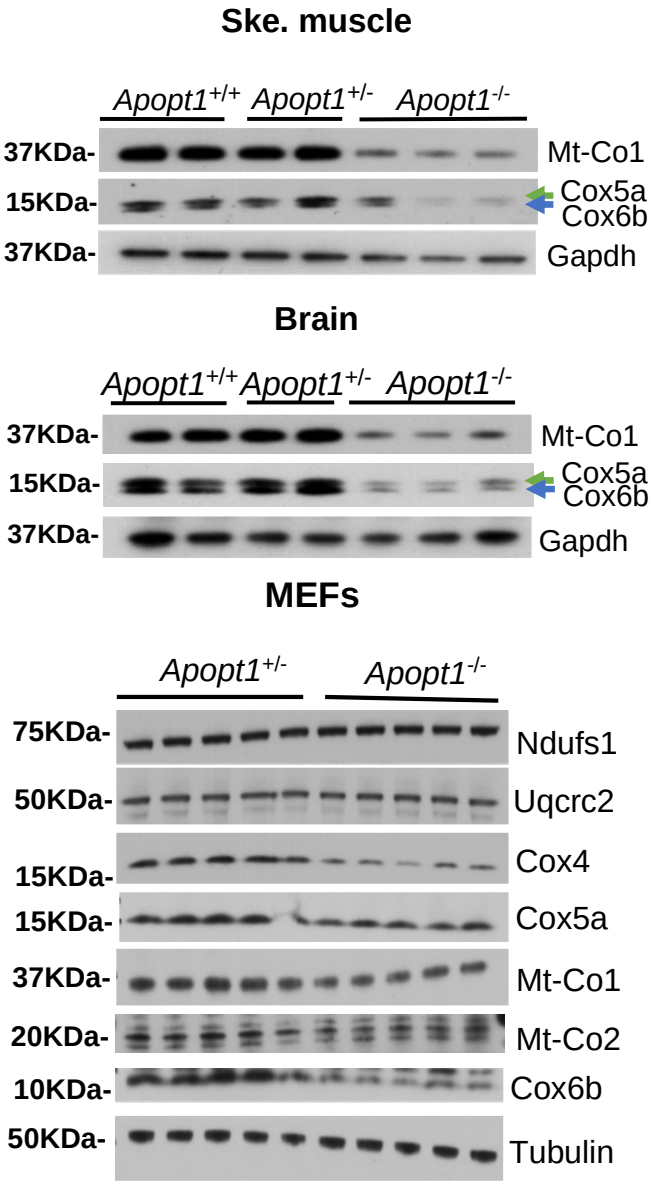

Figure 4.22

Figure 4.22 Reduced COX subunits protein levels in brain, skeletal muscle and MEFs. Western blot and immunodetection analysis of SDS-PAGE of total lysates from skeletal muscle, brain and mouse embryonic fibroblasts (MEFs) from the indicated genotypes, each lane showing the results for one animal. *Apopt1*$^{+/+}$: homozygous WT mice, *Apopt1*$^{+/-}$: heterozygous mice, *Apopt1*$^{-/-}$: homozygous *Apopt1* KO mice.

In order to exclude the possibility that the COX defect in Apopt1-less tissues could be due to a role of *Apopt1* in transcription of COX subunits, the transcript levels of mtDNA-encoded Mt-Co1 (CIV subunit) and Mt-Nd1 (CI subunit) were measured in skeletal muscle of three-month-old animals. No significant changes were detected in mRNA levels between WT and KO mice (**Figure 4.23**), suggesting that the reduction in protein levels occurs either at the translational or post-translational level.

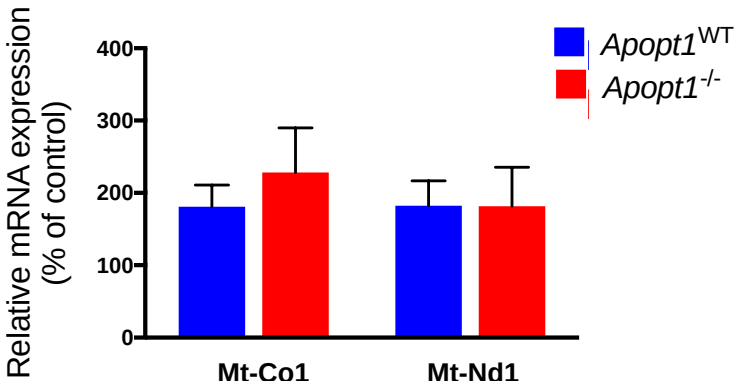

Figure 4.23 Quantification of mt-mRNA levels. Relative mRNA expression of one COX (CIV) subunit (Mt-Co1) and one CI subunit (Mt-Nd1) in skeletal muscle from three-month old WT and KO mice, normalised to the expression of Gapdh and expressed as percentage of the WT. Data are presented as mean ± SEM. *Apopt1*^{WT} (n = 12): control group composed of *Apopt1*$^{+/+}$ and *Apopt1*$^{+/-}$ individuals. *Apopt1*$^{-/-}$ (n = 6): homozygous *Apopt1* KO mice.

4.2.10 Impaired COX assembly in the *Apopt1*$^{-/-}$ mice

BN-PAGE combined with Western blot and immunodetection was used to analyse the levels of fully assembled COX and of the other protein complexes of the respiratory chain. Complex IV amounts were significantly lower in skeletal muscle from *Apopt1*$^{-/-}$ mice of three (**Figure 4.24A**) and twelve (**Figure 4.24B**)

months of age. The assembly defect was specific for COX, as respiratory complexes I, II and III were unaffected.

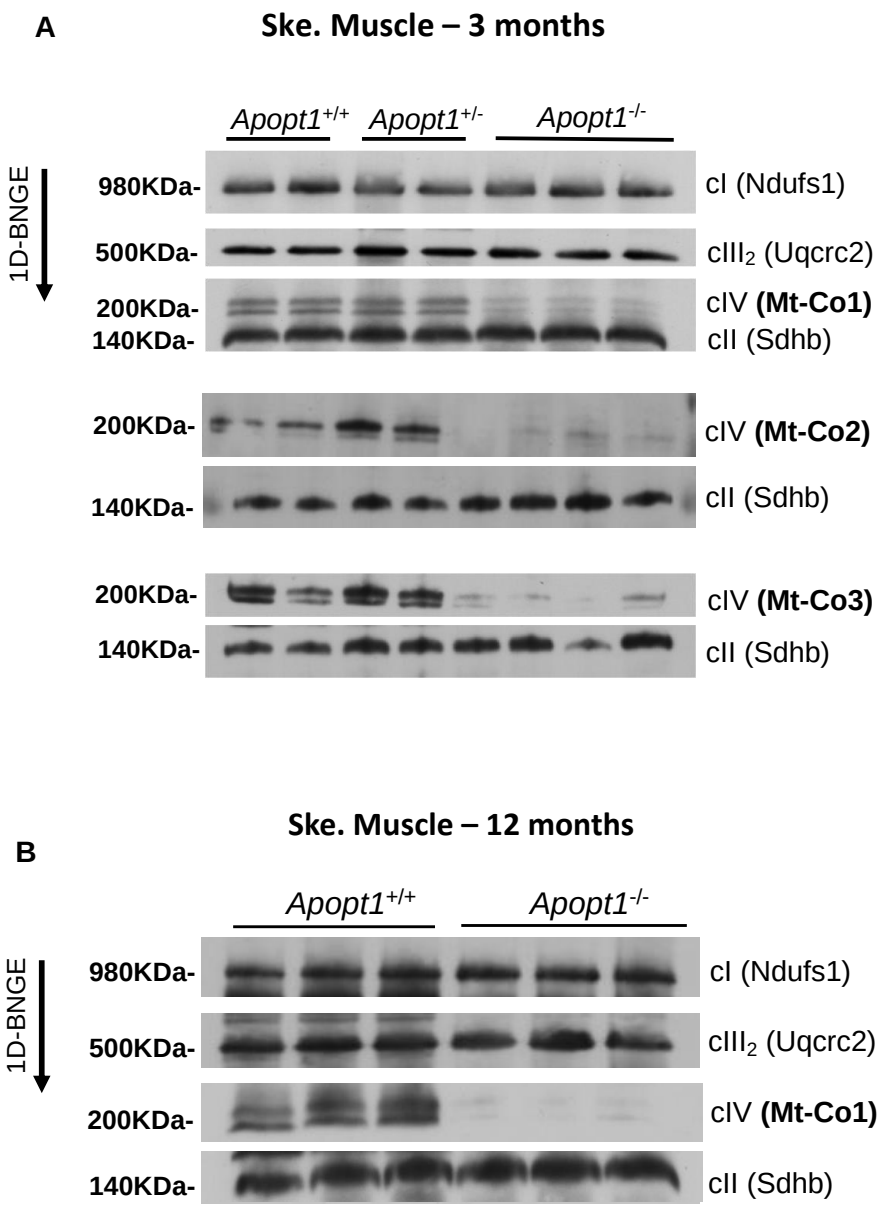

Figure 4.24 COX assembly in skeletal muscle – 1D. Western blot analysis of 1D BN-PAGE of mitochondria from skeletal muscle from three-month-old mice (**A**) and twelve-month-old mice (**B**) from the indicated genotypes, each lane showing the results from one animal. Complex I (cI), II (cII), III dimer ($cIII_2$) and IV (cIV) were visualised immunodetecting against subunits Ndufs1, Sdhb, Uqcrc2 and mt-Co1/mt-Co2/mt-Co3, respectively. *Apopt1*$^{+/+}$: homozygous WT mice, *Apopt1*$^{+/-}$: heterozygous mice, *Apopt1*$^{-/-}$: homozygous *Apopt1* KO mice.

Low levels of fully assembled complex IV were also observed in cultured MEFs by 1D BN-PAGE, indicating that COX biogenesis is profoundly affected also in Apopt1-deficient proliferating cells (**Figure 4.25**).

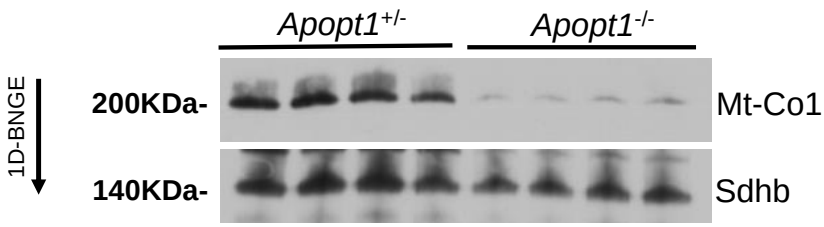

Figure 4.25 COX assembly in MEFs. Western blot analysis of 1D BN-PAGE of mitochondria from MEFs from the indicated genotypes, each lane showing the results from one animal. COX was visualised immunodetecting against subunit Mt-Co1. Sdhb was used as a normalization and MW standard signal. *Apopt1*$^{+/-}$: heterozygous mice, *Apopt1*$^{-/-}$: homozygous *Apopt1* KO mice.

To evaluate the assembly status of the residual COX, 2D BN-PAGE, Western blot and specific immunodetection against COX subunits assembling in different modules was performed. This analysis revealed an accumulation of subcomplexes containing Mt-Co1 and an accumulation of free Cox5a in skeletal muscle from three-month-old *Apopt1*$^{-/-}$ mice (**Figure 4.26**).

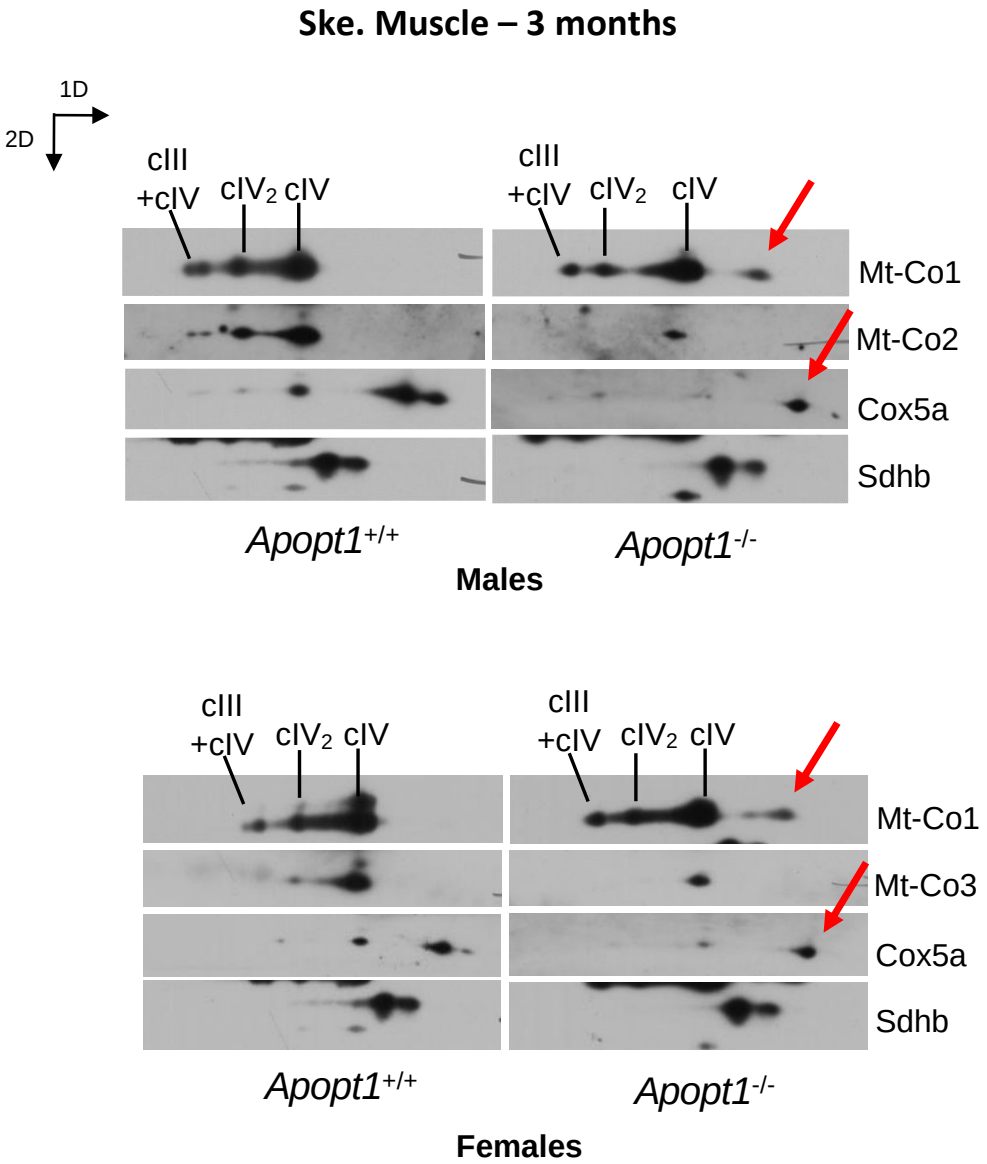

Figure 4.26 COX assembly status in skeletal muscle – 2D. Western blot analysis of 2D BN-PAGE of mitochondria from skeletal muscle (three-month-old mice) from the indicated genotypes, each lane showing the results from one animal. COX was visualised immunodetecting against subunits Cox5a, mt-Co1, mt-Co2 and mt-Co3. Sdhb was used as a normalization and MW standard signal. Red arrows point to the accumulation of subcomplexes containing Mt-Co1 and to the accumulated free Cox5a in *Apopt1*$^{-/-}$ mice. *Apopt1*$^{+/-}$: heterozygous mice, *Apopt1*$^{-/-}$: homozygous *Apopt1* KO mice.

4.2.11 ROS production and antioxidant defences were unaffected in *Apopt1*$^{-/-}$ mice

Absence of APOPT1 was suggested to contribute to higher ROS production in APOPT1-null patient cultured skin fibroblasts stressed with H_2O_2 (Melchionda *et al.*, 2014). In addition, yeast strains displaying COX defects showed increased sensitivity to H_2O_2, which was attributed to the presence of pro-oxidant Cox1p-containing assembly intermediates (Khalimonchuk, Bird and Winge, 2007). Therefore, we hypothesised that ROS production might be increased in *Apopt1*$^{-/-}$ mouse tissues due to the accumulation of Mt-Co1-containing subassemblies, which may have pro-oxidant activity. To investigate this, we measured H_2O_2 production in isolated brain and heart mitochondria from three-month-old mice by monitoring the oxidation of the fluorogenic indicator Amplex red in the presence of horseradish peroxidase using the fluorometry module fitted to the O2k-respirometer (see Chapter 2 for more details). The H_2O_2 production was initiated by addition of succinate without ADP (resting state or state 4), which produces high amounts of ROS at the level of complex I by the so-called reverse electron transfer (RET) (Tretter, Patocs and Chinopoulos, 2016). The ADP-induced stimulation of respiration (state 3) led to a pronounced reduction of the H_2O_2 flux. Complex III was then inhibited by adding antimycin a, which led again to an increase in ROS production (Tretter, Patocs and Chinopoulos, 2016). However, the H_2O_2 rate produced by brain and heart *Apopt1*$^{-/-}$ isolated mitochondria was not significantly different from that of the WT in any of the respiratory states (**Figure 4.27**).

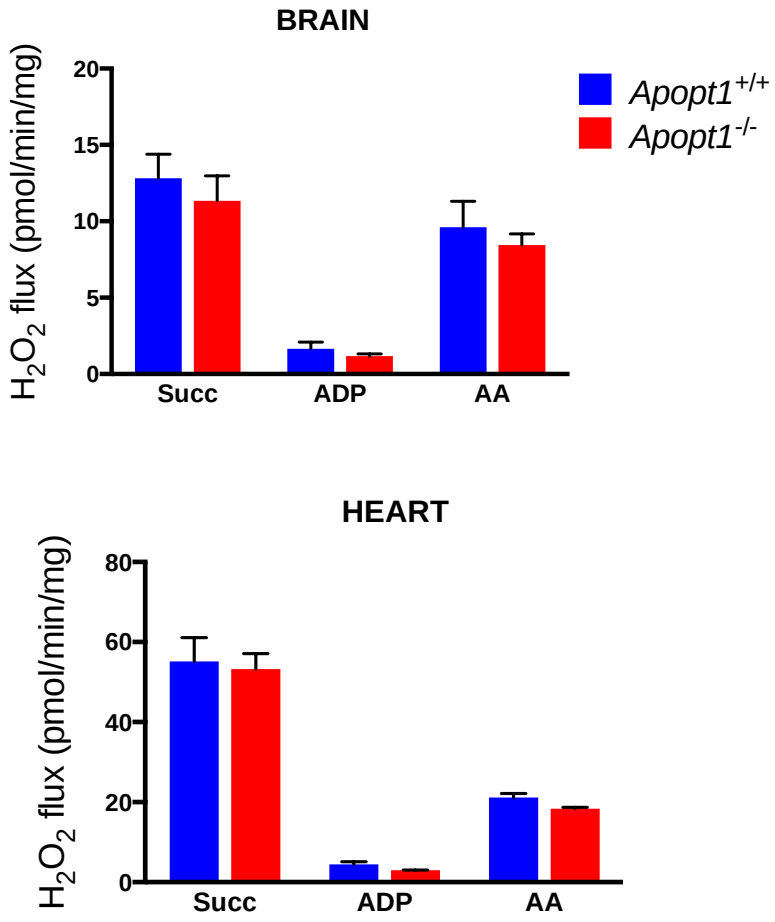

Figure 4.27 ROS production in mouse tissues. H_2O_2 production flux in isolated brain and heart mitochondria from 3-month-old mice determined by monitoring the oxidation of Amplex red in an Oroboros instrument. Measurements were calculated after addition of succinate (Succ), ADP and the complex III inhibitor antimycin a (AA). Data are presented as mean ± SEM (n = 2 mice per genotype). *Apopt1*$^{+/+}$: homozygous WT mice, *Apopt1*$^{-/-}$: homozygous *Apopt1* KO mice.

The fact that no changes were found in ROS production does not necessarily indicates a lack of increased oxidative stress in the *Apopt1*$^{-/-}$ tissues, as this could be compensated by enhanced ROS scavenging. The mitochondrial superoxide dismutase (Sod2) catalyses superoxide into oxygen and hydrogen peroxide and its expression is rapidly activated under oxidative stress conditions, thus being commonly used as an antioxidant defence marker (Murphy, 2009). On the other hand, the mitochondrial aconitase (Aco2) activity is inhibited by H_2O_2 due to the presence of Fe-S clusters in its catalytic centre, which is why it is used as a marker of oxidative damage (Yan, Levine and Sohal, 1997). Sod2 and Aco2 steady-state levels were tested in in mouse liver, brain and skeletal muscle,

however, no significant differences were found between control and mutated mice (**Figure 4.28**).

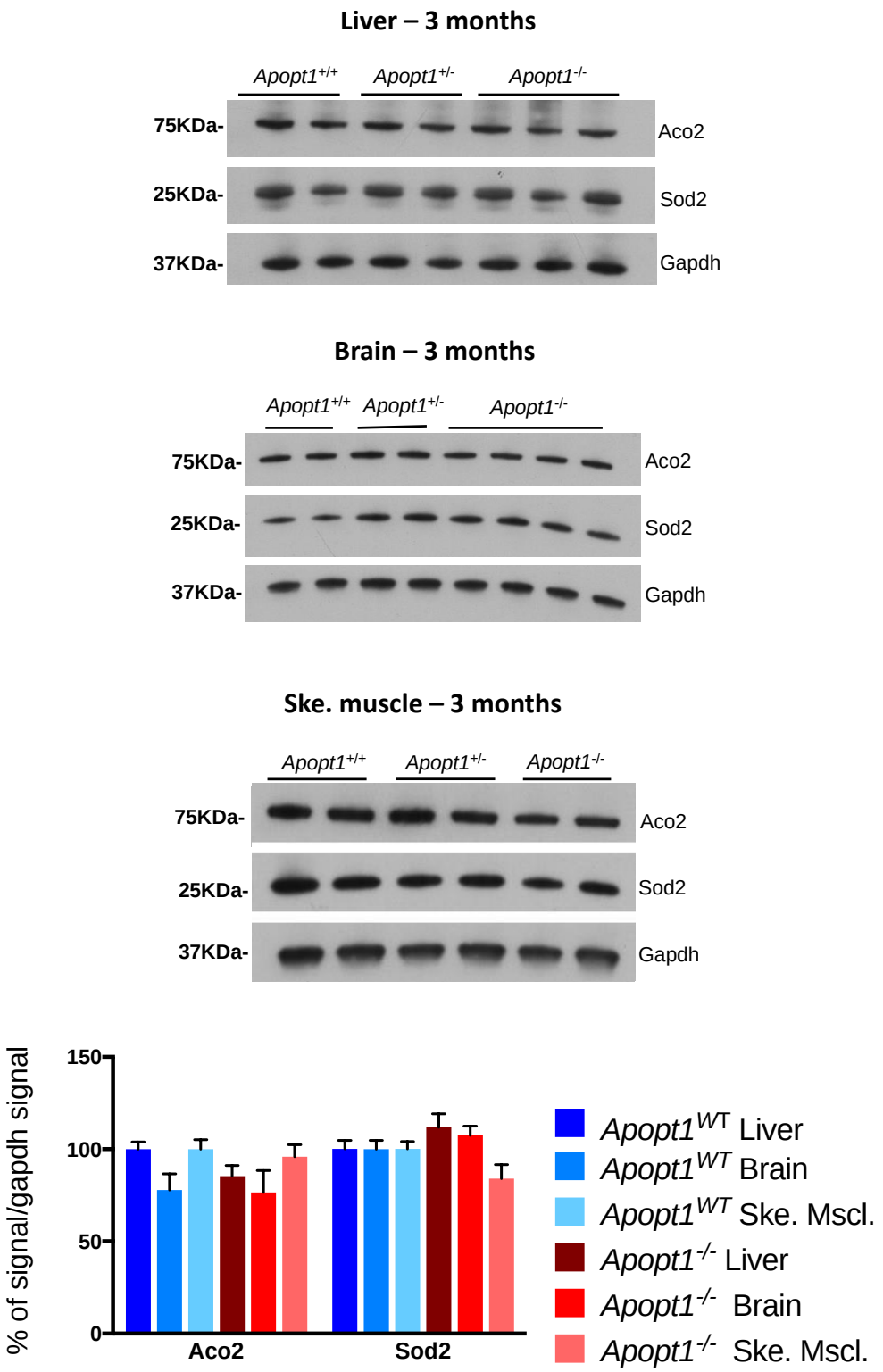

Figure 4.28

Figure 4.28 Protein levels of oxidative stress markers in mouse tissues. Western blot and immunodetection analysis of SDS-PAGE of total lysates from liver, brain and skeletal muscle (three-month-old mice) from the indicated genotypes, showing the signal for aconitase 2 (ACO2) and superoxide dismutase 2 (SOD2). *Apopt1*$^{+/+}$: homozygous WT mice, *Apopt1*$^{+/-}$: heterozygous mice, *Apopt1*$^{-/-}$: homozygous *Apopt1* KO mice. The graph shows the densitometric quantification of the signals obtained for WT mice (n = 8): control group composed of *Apopt1*$^{+/+}$ and *Apopt1*$^{+/-}$ individuals and for KO mice (n = 6): homozygous *Apopt1* KO mice.

4.3 Conclusions

- The homozygous *Apopt1* KO mice, generated by CRISPR/Cas9, showed markedly reduced levels of *Apopt1* mRNA transcripts carrying Mutation #1, an indel producing a frameshift and a premature stop codon.

- The breeding of *Apopt1* heterozygous individuals generated Mendelian ratios of homozygous WT, heterozygous and homozygous *Apopt1* KO mice, confirming the autosomal recessive inheritance observed in patients (Melchionda *et al.*, 2014).

- *Apopt1* KO mice presented significantly impaired motor endurance and coordination skills in the treadmill and rotarod test, respectively.

- *Apopt1*$^{-/-}$ mice showed a decrease in spontaneous and exploratory behaviour at six and twelve months old, indicating a decline of some cognitive functions with age.

- More complex cognitive tasks, such as memory (assessed by the Y maze), were not affected in the *Apopt1* KO mice at any age.

- Normal gait and posture and no feet clasping were observed in the *Apopt1* KO mice.

- The pole-test results were normal in the *Apopt1* KO mice at any age analysed, suggesting that their sensory nervous system was not damaged.

- No histological alterations, such as centralised nuclei or ragged red fibers, were found in the skeletal muscle of three- and twelve-month-old *Apopt1*$^{-/-}$ mice.

- The histopathological study performed in the brain of three-month-old *Apopt1*$^{-/-}$ *mice* showed no neuronal loss, necrosis or any other brain histological abnormality.

- *Apopt1*$^{-/-}$ mice showed global, isolated COX deficiency and reduced steady-state levels of COX structural subunits, which was not caused by a transcriptional defect.

- Apopt1-null tissues presented defective COX assembly, which involved the accumulation of early assembly subunits (Cox4 and Cox5a) and of the Mt-Co1 module (or MITRAC complex), suggesting that Apopt1 must play a role in the intermediate steps of COX assembly.

- Normal levels of ROS production and antioxidant defences were found in Apopt1-less mouse tissues.

CHAPTER 5

Characterisation of the APOPT1 protein in cellular models

5.1 Introduction

The work presented in this chapter builds up from data produced in the preliminary characterisation of APOPT1 pathological role (Melchionda *et al.*, 2014). Similar to what is described in Chapter 4 for mouse tissues, absence of APOPT1 in patient-derived fibroblasts was associated with reduced COX activity and a decrease of fully assembled complex IV (Melchionda *et al.*, 2014). However, complementation assays in these cells were complicated since the expression systems used could not maintain a stable expression of the recombinant wild-type APOPT1. Indeed, $APOPT1^{HA}$ expression was only detectable when cells were stressed with H_2O_2 or treated with the proteasome inhibitor MG132 (Melchionda *et al.*, 2014).

In this chapter, I describe how several APOPT1 alternative splicing isoforms tagged with C-terminal HA and GFP sequences were delivered and successfully expressed in control and patient-derived cells by using a second-generation lentiviral system. These cellular models were then used for complementation assays, as well as for investigating the subcellular and sub-mitochondrial localisation of APOPT1 and the post-translational mechanisms that regulate its protein levels in the cytosol and in the mitochondria.

5.2 Results

5.2.1 Overexpression of HA- and GFP-tagged APOPT1 did not affect cell survival

In order to identify which isoforms of *APOPT1* are actually expressed in human cells, APOPT1 cDNA was amplified from two cell lines: HeLa and HEK 293T. Two different isoforms were detected after cloning and sequencing the PCR fragments. The first isoform was the transcript containing five coding exons, annotated as APOPT1-201 in Ensembl (www.ensembl.org) with Transcript ID ENST00000409074.6, encoding the full- length protein (Uniprot Q96IL0). The second isoform was APOPT1-203, lacking exon 3 and with Transcript ID

ENST00000458117.5, encoding a truncated protein (Uniprot H7C2Z1). To better characterise these two isoforms, we cloned them starting from each of the two putative ATG start codons present in the open reading frame: M1 and M14. The resulting four different cDNAs were fused to GFP in the C-terminus and expressed in three different human cell lines: HeLa, 143B osteosarcoma cells and immortalised control skin fibroblasts. Cells transduced with the pWPXLd-ires-Puro^{R} 'empty vector' or the GFP protein alone were used as controls. APOPT1-201-M1^{GFP} and APOPT1-201-M14^{GFP} produced the same size mature protein (**Figure 5.1 and Table 5.1**), detected at a position corresponding to a size of approximately 40 kDa in all cell lines tested (as shown for 143B cells in **Figure 5.1**). APOPT1-203-M1^{GFP} and APOPT1-203-M14^{GFP} also produced the same band corresponding to the mature protein (**Figure 5.1 and Table 5.1**), detected at a size corresponding to 30 kDa in all cell lines tested (as shown for 143B cells in **Figure 5.1**). The GFP protein was detected at around 27 kDa (**Figure 5.1**).

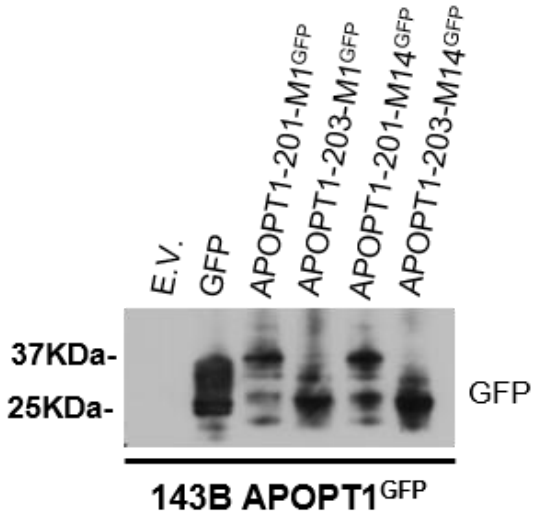

Figure 5.1 GFP-tagged APOPT1 constructs overexpressed in 143B cells. SDS-PAGE (4-12 % NuPAGE Bis-Tris, Thermo Fisher Scientific) and WB analysis of total lysates from 143B cells transduced with either the pWPXLd-ires-Puro^{R} empty vector (E.V.), the GFP protein alone (GFP), APOPT1-201-M1^{GFP}, APOPT1-201-M14^{GFP}, APOPT1-203-M1^{GFP} or APOPT1-203-M14^{GFP}. 20 µg of protein were loaded.

Table 5.1 APOPT1 predicted molecular mass. The table below indicates the molecular mass for the precursor and mature form of each of the APOPT1 versions, with and without including the molecular mass of the GFP protein (27 kDa).

APOPT1 construct	MTS processing	Predicted molecular mass	Predicted molecular mass with the GFP tag
APOPT1-201-M1	Precursor	24.2 kDa	51.2 KDa
	Mature	20.1 KDa	47.1 KDa
APOPT1-201-M14	Precursor	23.0 KDa	50.0 kDa
	Mature	20.1 KDa	47.1 KDa
APOPT1-203-M1	Precursor	14.3 KDa	41.3 KDa
	Mature	10.2 KDa	37.2 KDa
APOPT1-203-M14	Precursor	13.1 KDa	40.1 KDa
	Mature	10.2 KDa	37.2 KDa

In order to investigate the cellular localisation of the proteins encoded in these four constructs, immunofluorescence on fixed cells was performed. All four APOPT1 proteins showed mitochondrial localisation (**Figure 5.2A and B**), whereas the signal of the GFP protein alone was spread around all the cell (**Figure 5.2C**). However, since the constructs starting from the second putative ATG start codon (APOPT1-201-M14^{GFP} and APOPT1-203-M14^{GFP}) produced a protein perfectly able to translocate to the mitochondria, we concluded that the actual starting methionine must be M14, as proposed previously (Melchionda *et al.*, 2014), and that the sequence before that ATG codon corresponds to the APOPT1 mRNA 5'-UTR.

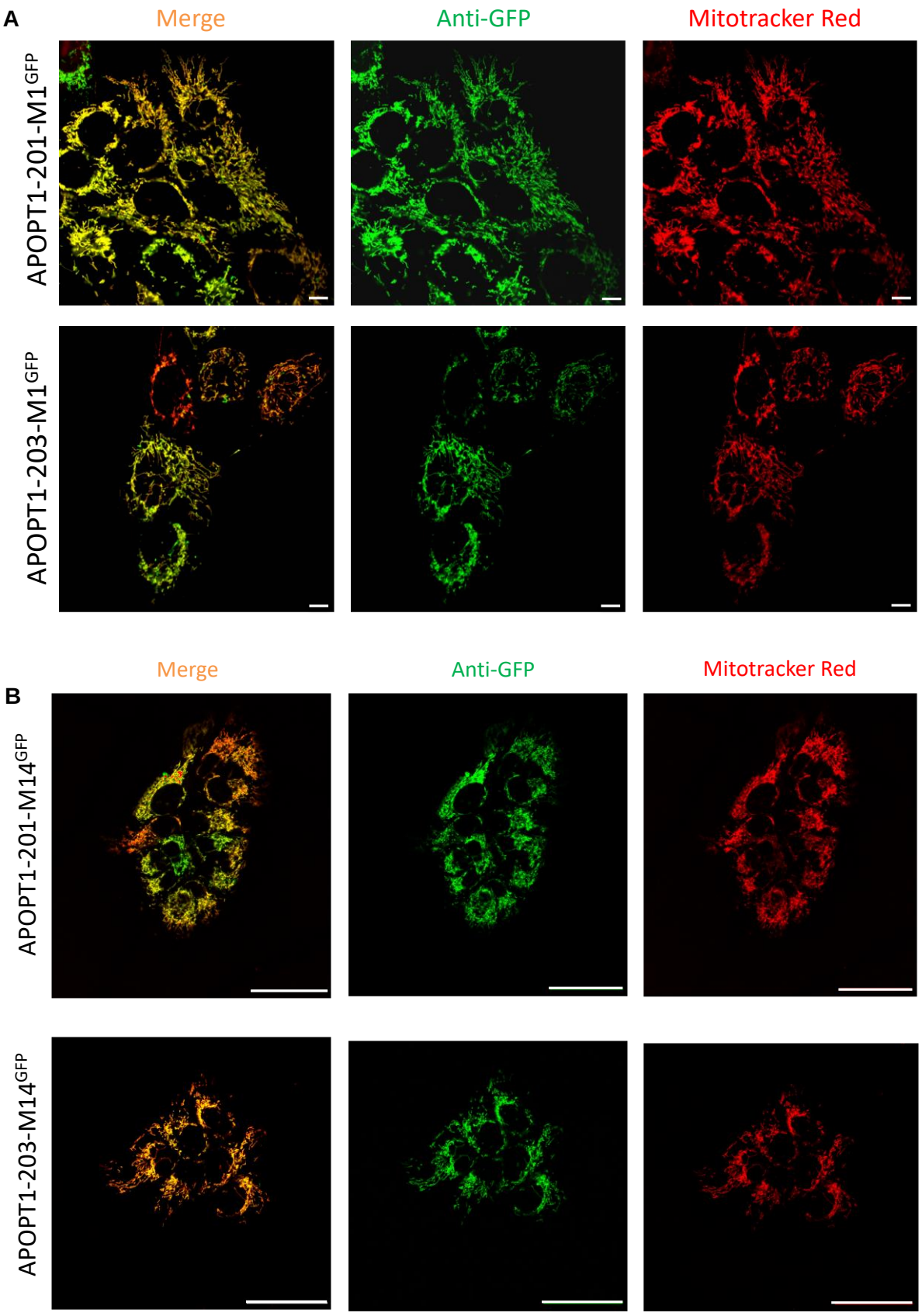
A
Merge
Anti-GFP
Mitotracker Red
APOPT1-201-M1GFP
APOPT1-203-M1GFP
B
Merge
Anti-GFP
Mitotracker Red
APOPT1-201-M14GFP
APOPT1-203-M14GFP

Figure 5.2

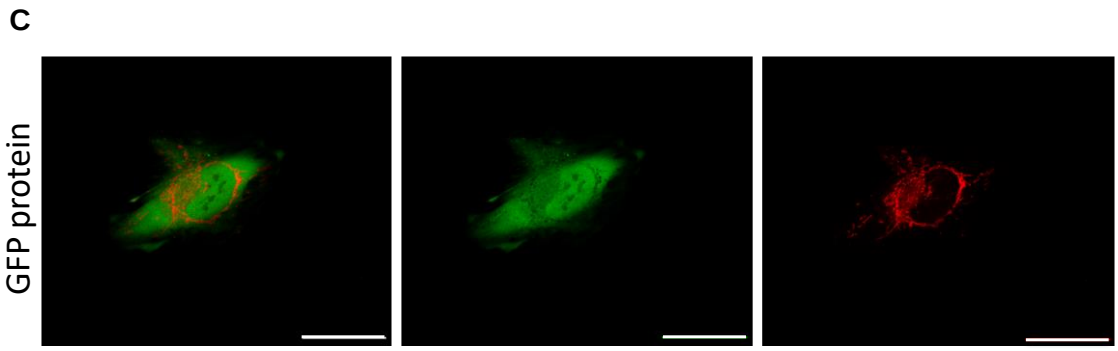

Figure 5.2 Immunofluorescence assays in 143B cells. Confocal images comparing the signal of GFP (**C**), APOPT1-201-M1^{GFP} (**A**), APOPT1-203-M1^{GFP} (**A**), APOPT1-201-M14^{GFP} (**B**) or APOPT1-203-M14^{GFP}(**B**), immunostained with primary anti-GFP antibody (Abcam) and secondary Alexa fluor 488 anti-rabbit (Invitrogen), to that of MitoTracker®RedCMXRos (Invitrogen), used to visualise the mitochondrial network. The pattern of all GFP-tagged APOPT1 constructs shows co-localisation with that obtained with MitoTracker Red. Bars (A): 10 µm; (B and C): 50 µm.

Moreover, and contrary to the original report on the identification of APOPT1 (Yasuda *et al.*, 2006), no induction of cell death or effect on cell survival were observed after transduction of the GFP-tagged APOPT1 versions in any of the cell lines tested, including HeLa (used in that report). Some of the images taken by the IncuCyte ZOOM instrument (Essen Bioscience, UK), monitoring the cell growth and protein expression of HeLa cells immediately after transduction of the APOPT1-201-M1^{GFP} construct, are shown in **Figure 5.3**.

Figure 5.3

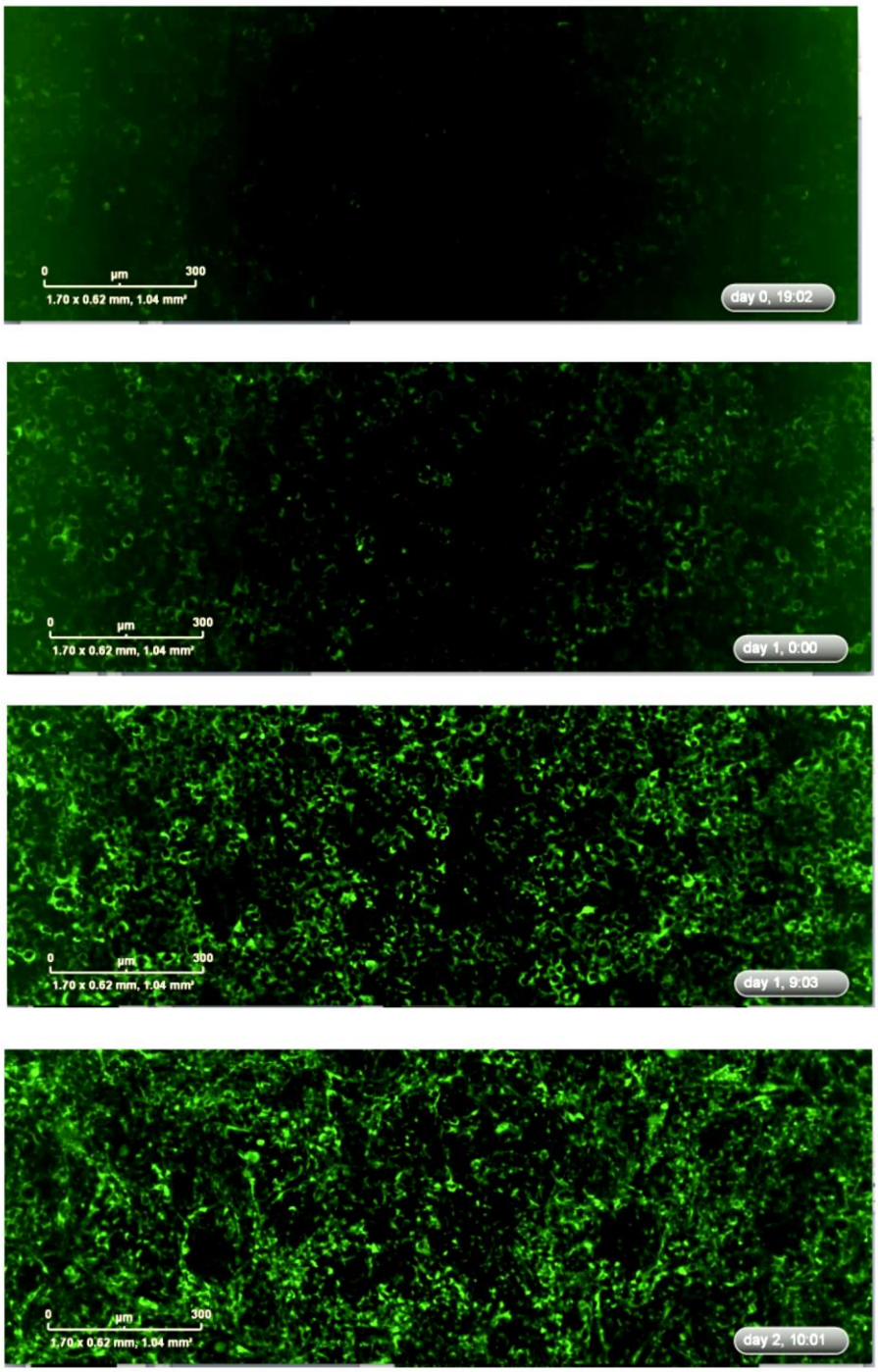

Figure 5.3 Normal cell growth and protein expression after transduction with APOPT1-201-M1^{GFP}. An IncuCyte ZOOM instrument (Essen Bioscience, UK), was used to monitor cell confluency and GFP expression by detection of green fluorescence. The images shown were taken 0, 14, 19, 24, 33 and 58 hours after transduction of HeLa cells with the APOPT1-201-M1^{GFP} construct. 10X magnification. All the images collected were compiled in several videos (available upon request).

In addition to the GFP tag, a C-terminal HA tag was added to the APOPT1-201-M1 and APOPT1-203-M1 cDNA sequences previously described, which were then transfected into 143B cells. The M1 constructs were used in order to keep what we assumed was the APOPT1 mRNA 5'-UTR, which could help maintain a more physiological structure and possibly expression of the protein. Cells transduced with the pWPXLd-ires-Puro^{R} 'empty vector' were used as controls. By using the anti-HA antibody in optimal conditions, i.e. at a high concentration and long exposure of the X-ray films, we were able to immunovisualise two bands for the APOPT1-201-M1^{HA} construct, most likely corresponding to the mature form, with a molecular mass of approximately 21 kDa, and the precursor form, of around 25 kDa (**Figure 5.4 and Table 5.2**). Note that the HA-tagged protein expression was hardly detectable in HeLa and fibroblasts when tested previously (Melchionda *et al.*, 2014). The protein product of APOPT1-203-M1^{HA} was undetectable (**Figure 5.4**), which led to the conclusion that the APOPT1-203 isoform was not functional. This idea was reinforced by the fact that deletion of *APOPT1* exon 3 causes the pathological phenotype of COX deficiency and encephalopathy (Melchionda *et al.*, 2014; Sharma *et al.*, 2018). Therefore, we decided not to continue using the HA- and GFP-tagged APOPT1-203 constructs in further experiments and to designate the APOPT1-201-M1^{HA} and APOPT1-201-M1^{GFP} proteins as APOPT1^{GFP} and APOPT1^{HA}.

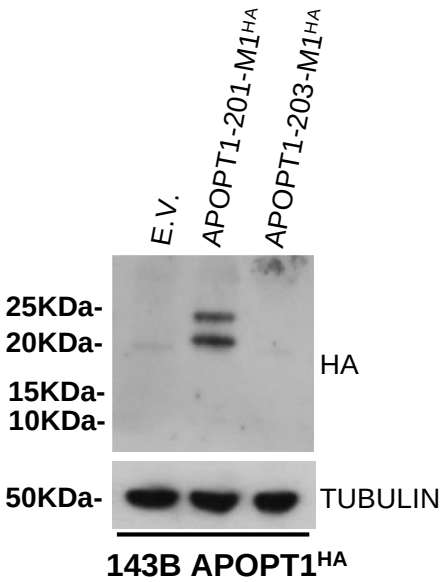

Figure 5.4

Figure 5.4 HA-tagged APOPT1 constructs overexpressed in 143B cells. SDS-PAGE (4-12 % NuPAGE Bis-Tris, Thermo Fisher Scientific) and WB analysis of total lysates from 143B cells transduced with either the pWPXLd-ires-Puro^{R} empty vector (E.V.), APOPT1-201-M1^{HA} or APOPT1-203-M1^{HA}. 40 µg of protein were loaded.

Table 5.2 APOPT1 predicted molecular mass. The table below indicates the molecular mass for the precursor and mature form of each of the HA-tagged APOPT1 versions, with and without including the molecular mass of the HA tag (10 kDa).

APOPT1 construct	MTS processing	Predicted molecular mass	Predicted molecular mass with the HA tag
APOPT1-201-M1	Precursor	24.2 kDa	25.2 KDa
	Mature	20.1 KDa	21.1 KDa
APOPT1-203-M1	Precursor	14.3 KDa	15.3 KDa
	Mature	10.2 KDa	11.2 KDa

Immunofluorescence on fixed cells validated the mitochondrial localisation of the APOPT1-201-M1^{HA} protein and the absence of signal for the APOPT1-203-M1^{HA} isoform (**Figure 5.5**). However, we noticed that the protein expression levels of the APOPT1 tagged with HA were much lower than those of the APOPT1 tagged with GFP, confirming the intrinsic instability of the HA-tagged protein previously reported by Melchionda et al., which is somehow corrected in the GFP chimeric variants.

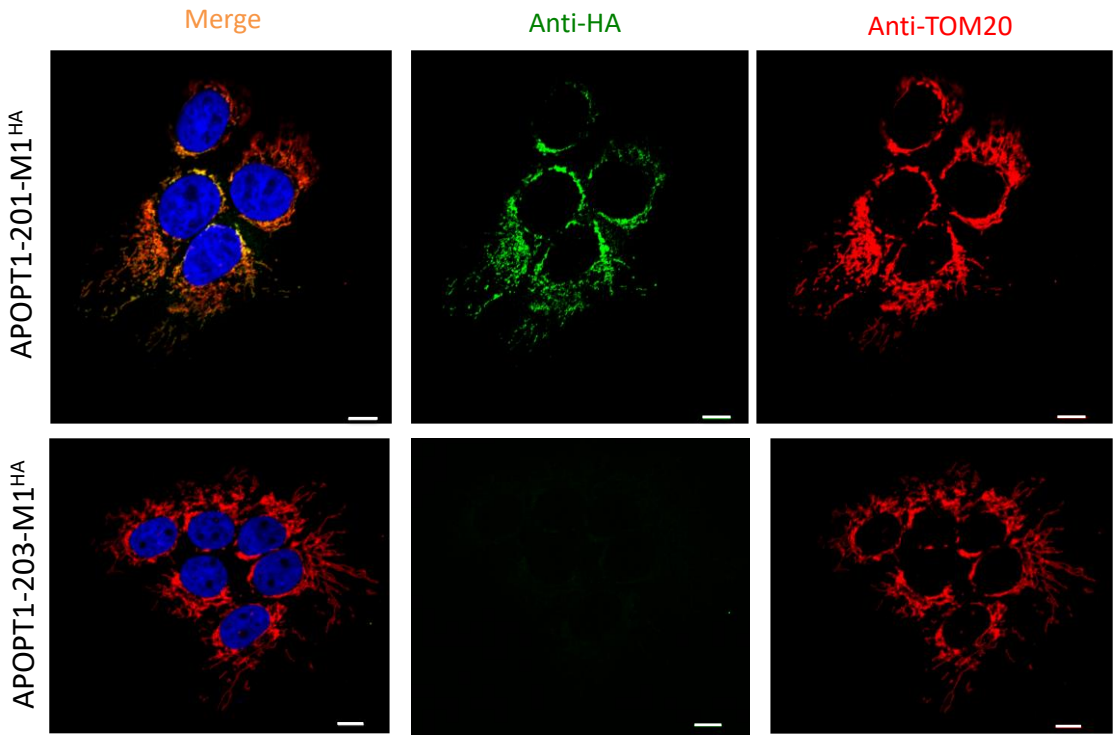

Figure 5.5 Immunofluorescence assay in 143B cells. Confocal images comparing the signal of APOPT1-201-M1^{HA} or APOPT1-203-M1^{HA}, immunostained with primary anti-HA antibody (Roche) and secondary Alexa fluor 488 anti-rat (Invitrogen), to that of TOM20, immunostained with primary anti-TOM20 antibody (Abcam) and secondary Alexa fluor 594 anti-rabbit (Invitrogen). Nuclei were stained with DAPI. The pattern of APOPT1-201-M1^{HA} coincides perfectly with that obtained for TOM20, which was used as a marker for the mitochondrial network. Bars: 10 µm.

The effect of APOPT1^{HA} overexpression in the growth and survival of 143B cells was also investigated by generating growth curves right after the transduction with the lentiviral vectors. However, no changes in cell viability were observed (**Figure 5.6**).

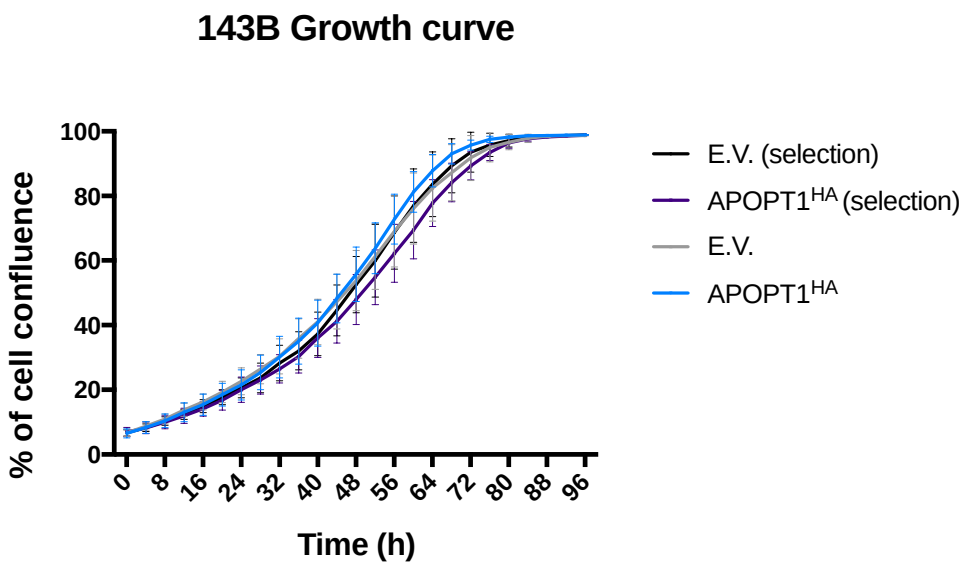

Figure 5.6 Normal cell growth after transduction with APOPT1^{HA}. An IncuCyte ZOOM instrument (Essen Bioscience, UK), was used to monitor cell confluency to calculate the growth curves of 143B cells transduced either with the empty vector or APOPT1^{HA}. Data are presented as mean ± SD (n = 4).

5.2.2 Human APOPT1 immunodetection trials

Detection of the endogenous APOPT1 protein was attempted with four different antibodies (see Chapter 2 for more details). APOPT1is synthesized as a 22.9 kDa precursor including a mitochondrial targeting sequence of 26 amino acids that is cleaved off when imported (Melchionda *et al.*, 2014), producing a mature protein with a predicted molecular mass of 20.1 kDa,. Two antibodies were commercial: one raised against a synthetic human APOPT1 peptide (Antibodies Online), which detect neither the endogenous nor the overexpressed protein (data not shown); and one raised against the full-length human APOPT1 (anti-C14orf153) by Proteintech, which we were allowed to test before it was available for the general public and detected both the endogenous and overexpressed protein (**Figure 5.7**). To demonstrate this, immortalised fibroblasts derived from patients S2 and S6, carrying homozygous p.Arg79* and heterozygous p.Arg79*/p.Glu124del truncating mutations, respectively (Melchionda *et al.*, 2014), were immunostained with the Proteintech antibody. A drastic reduced signal of the band corresponding to the size of mature APOPT1 (22.9 kDa), was observed (**Figure 5.7**). However, the presence or absence of the

endogenous precursor protein was impossible to determine as an intense unspecific band of the same electrophoretic mobility as pre-APOPT1 cross-reacts with the anti-APOPT1 antibody (**Figure 5.7**). The bands corresponding to the precursor and mature forms of APOPT1^{HA} were also detected by this antibody, as shown in **Figure 5.7**.

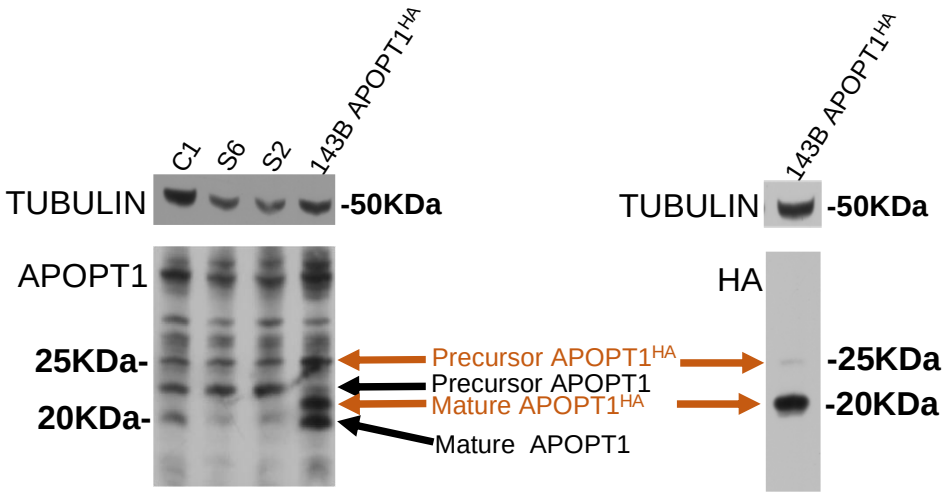

Figure 5.7 Immunodetection of APOPT1 with the Proteintech antibody. SDS-PAGE (12 % NuPAGE Bis-Tris, Thermo Fisher Scientific) and WB analysis of total lysates from 143B cells transduced with APOPT1^{HA} and of patient-derived (S2 and S6) and control (C1) immortalised fibroblasts. 50 µg of protein were loaded. The left blot was immunodetected with an antibody raised against the full-length human APOPT1 (Proteintech 27300-1-AP). The right blot was immunodetected with anti-HA (Roche). Tubulin was used as a loading control.

The other two tested antibodies were custom-made: one raised against a synthetic human APOPT1 peptide (Agrisera), which only detected the GFP-tagged overexpressed protein (**Figure 5.8**); and one raised against the full-length human APOPT1 mature protein (ProteoGenix), which detected both the endogenous and the overexpressed protein. However, the obtained pattern showed even a higher number of unspecific bands than the one made available by Proteintech (data not shown).

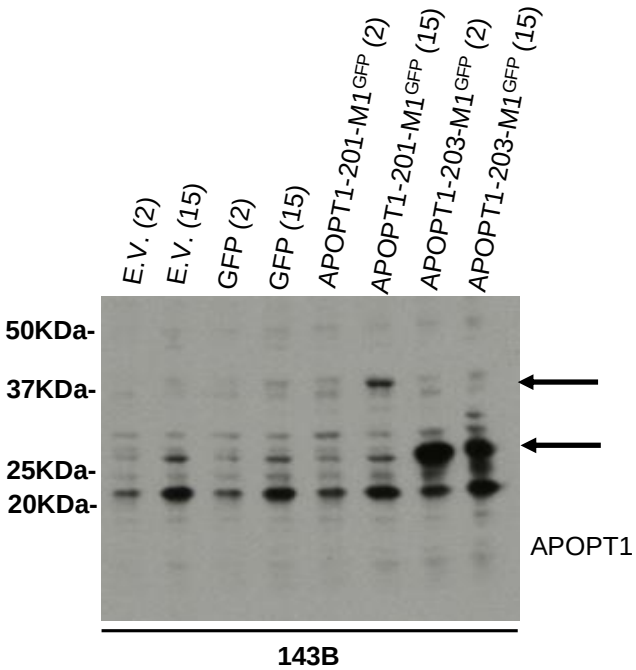

Figure 5.8 Immunodetection of APOPT1 with the Agrisera antibody. SDS-PAGE (4-12 % NuPAGE Bis-Tris, Thermo Fisher Scientific) and WB analysis of total lysates from 143B cells 2 days (2) and 15 days (15) after transduction with either the 'empty vector', the GFP protein alone, APOPT1-201-M1^{GFP} or APOPT1-203-M1^{GFP}, immunodetected with an antibody raised against a synthetic human APOPT1 peptide (Agrisera 2218). 30 µg of protein were loaded. The arrows indicate the signal for APOPT1-201-M1^{GFP} (around 40 kDa) and APOPT1-203-M1^{GFP} (around 30 kDa). The strong signal at around 22 kDa, which could correspond to the endogenous APOPT1 protein, was found to be a cytosolic protein when subcellular studies were performed later on.

5.2.3 APOPT1 is an inner mitochondrial membrane protein that does not stably interact in a high-molecular weight complex

To determine the subcellular and sub-mitochondrial localisation of the endogenous and overexpressed tagged APOPT1, mitochondria were isolated from HEK293 human cells and from 143B cells expressing either APOPT1^{HA} or APOPT1^{GFP}. First, APOPT1 association to the mitochondrial membranes was tested separating the soluble and membrane fractions by sonication and ultracentrifugation. Virtually all the endogenous, as well as the HA- and GFP-tagged APOPT1 species, were found exclusively in the mitochondrial membrane pellet fractions (**Figure 5.9**). However, a large proportion of the protein was released to the supernatant after alkaline carbonate extraction (**Figure 5.9**).

These results indicate that APOPT1 is associated with but not integral to the mitochondrial membranes.

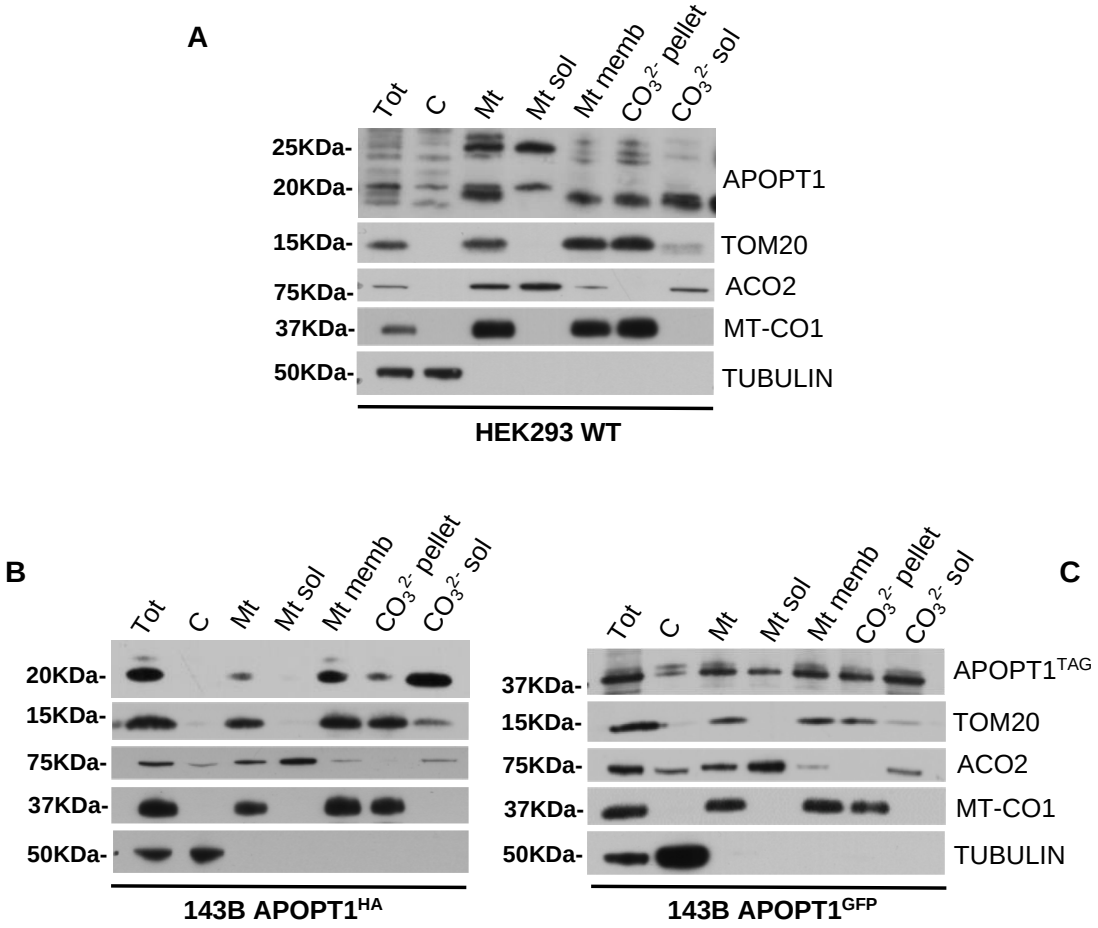

Figure 5.9 Subcellular localisation of APOPT1. SDS-PAGE (4-12 % NuPAGE Bis-Tris, Thermo Fisher Scientific) and WB analysis of different fractions from (**A**) non-transduced HEK cells, (**B**) 143B cells transduced with $APOPT1^{HA}$ and (**C**) 143B cells transduced with $APOPT1^{GFP}$. Tot: total lysate. C: post-mitochondrial fraction (cytoplasm). Mt: isolated mitochondria. Mt sol: Soluble mitochondrial fraction. Mt memb: mitocondrial membranes. CO_3^{2-} pellet: Pellet after carbonate extraction with 0.1 M Na2CO3, pH 10.5 for 30 minutes. CO_3^{2-} sol: soluble fraction after the carbonate extraction. Proteins located in different cellular compartments were immunostained: TOM20 in the outer mitochondrial membrane, aconitase (ACO2) in the mitochondrial matrix, MT-CO1 in the inner mitochondrial membrane and tubulin in the cytosol.

The localisation within the different mitochondrial compartments of the endogenous and HA-tagged APOPT1 was studied in mitoplasts, i.e. mitochondria devoid of the OM, testing the sensitivity of the APOPT1 proteins to trypsin in comparison to markers located in specific sub-compartments: matrix, inner

membrane (IM), intermembrane space (IMS) and outer membrane (OM). AIF (apoptosis inducing factor), which is a protein bound to the inner mitochondrial membrane but protruding towards the intermembrane space, and AK2 (adenylate kinase 2), which is an IMS soluble protein, were partially sensitive to trypsin when mitoplasts were generated exposing the mitochondria to increasing concentrations of the detergent digitonin (**Figure 5.10**). Aconitase 2 (ACO2), a matrix protein, and COX4, an IMM protein, seemed to be protected to trypsin treatment, except at very high digitonin concentrations, which were probably enough to disrupt the IMM (**Figure 5.10**). Endogenous APOPT1 and APOPT1^{HA} showed a sensitivity pattern similar to both AIF and ACO2 (**Figure 5.10**). These results indicate that APOPT1 is clearly an IMM-bound protein, but the exact topology is not well defined.

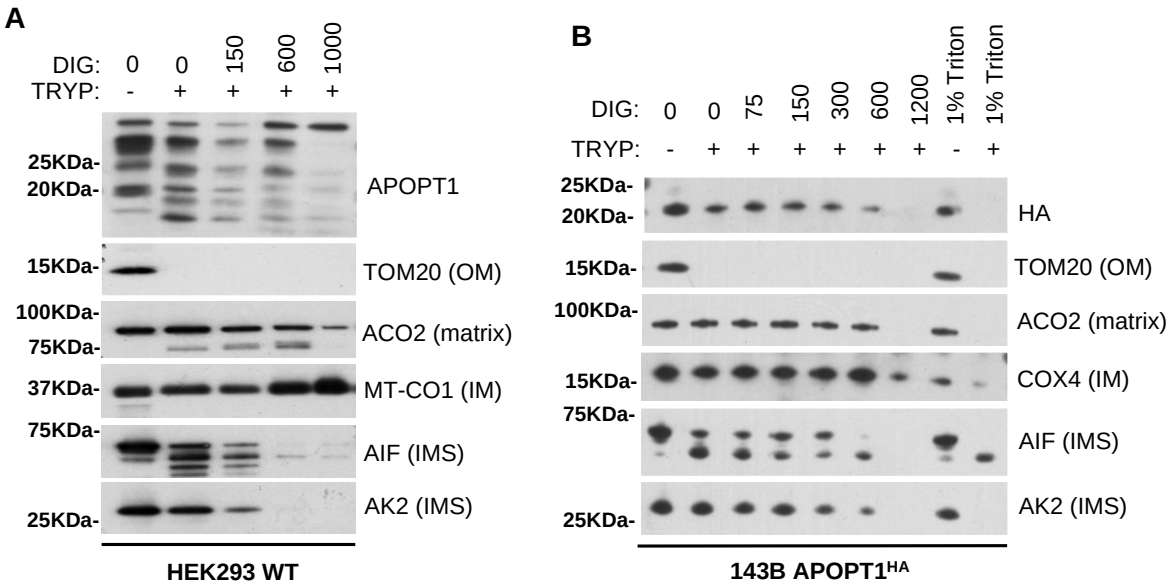

Figure 5.10 Sub-mitochondrial localisation of APOPT1 – digitonin treatment. SDS-PAGE (4-12 % NuPAGE Bis-Tris, Thermo Fisher Scientific) and WB analysis of isolated mitochondria from (**A**) non-transduced HEK cells and (**B**) 143B cells transduced with APOPT1^{HA} exposed to increasing amounts of digitonin (expressed in µg) and 50 µg/ml trypsin. Proteins located in different mitochondrial compartments were immunostained: TOM20 in the outer mitochondrial membrane, aconitase (ACO2) in the mitochondrial matrix, MT-CO1/COX4 in the inner mitochondrial membrane and AIF and AK2 in the intermembrane space.

To further validate whether the IMM-bound APOPT1 is facing the IMS or the matrix, mitoplasts were then generated by incubating mitochondria in

hypotonic buffer solution, which should not affect the IMM in any way, followed by trypsin treatment. The sensitivity of APOPT1^{HA} to proteolysis was compared to markers located in the intermembrane space (AK2), inner membrane facing the IMS (SCO2) and inner membrane (COX4). AK2 was found in the supernatant fractions after hypotonic shock and was fully degraded by trypsin (**Figure 5.11**), confirming that it is a soluble IMS protein. The sensitivity pattern of the mature APOPT1^{HA} protein was similar to COX4, an IMM, while SCO2 was more sensitive to trypsin and a soluble peptide of around 19 kDa was detected in the supernatant fractions under these conditions (**Figure 5.11**). No soluble APOPT1 was found in the supernatant fractions after trypsin treatments (**Figure 5.11**). These results suggest that APOPT1, bound to the IMM, has its C-terminus protruding to the matrix.

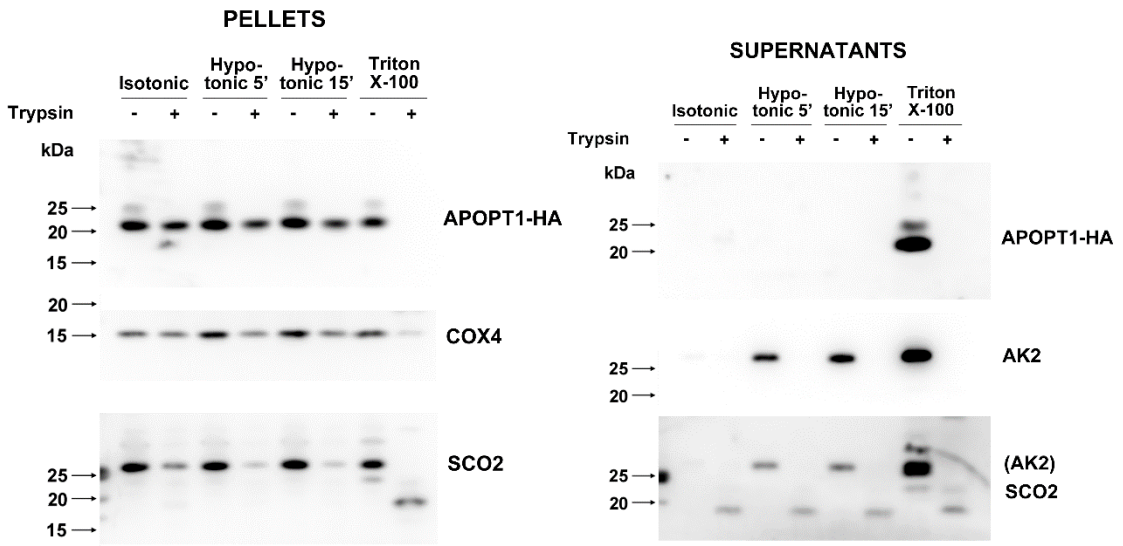

Figure 5.11 Sub-mitochondrial localisation of APOPT1 – hypotonic shock. SDS-PAGE (4-12 % NuPAGE Bis-Tris, Thermo Fisher Scientific) and WB analysis of the pellet and supernatant fractions of isolated mitochondria from 143B cells transduced with APOPT1^{HA} incubated with hypotonic buffer (5 mM sucrose, 10 mM Tris-HCl, pH 7.4, 1 mM EDTA) for 5 and 15 minutes, and with (+) or without (-) 50 µg/ml trypsin. Proteins located in different mitochondrial compartments were immunostained: COX4 in the IMM, AK2 in the intermembrane space and SCO2 in the IMM facing the IMS. Experiment performed by Erika Fernandez-Vizarra.

In order to analyse whether APOPT1 interacts with other proteins in a high-molecular complex, I performed Western-blot of 2D BN-PAGE of samples

solubilised with the two commonly used neutral detergents, DDM and digitonin. In both conditions, the two tagged proteins (APOPT1^{HA} and APOPT1^{GFP}) migrated to the bottom of the gel (**Figure 5.12**), indicating no interaction with other proteins including the COX assembly intermediates containing MT-CO1 or MT-CO2.

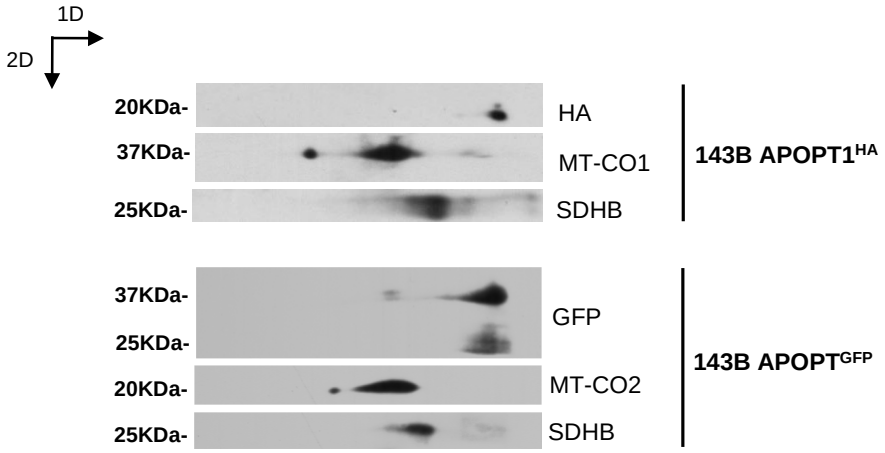

Figure 5.12 APOPT1 is not part of a high molecular weight complex. Western blot analysis of 2D BN-PAGE of DDM-treated mitochondrial fractions from 143B cells transduced either with APOPT1^{HA} or APOPT1^{GFP}. Fully assembled COX was immunovisualised with antibodies recognizing MT-CO1 and MT-CO2. SDHB was used as a normalization and molecular weight standard signal.

5.2.4 Stable expression of wild-type APOPT1 complemented the COX defect in patient-derived fibroblasts

In order to further investigate the function of APOPT1 in COX assembly, we took advantage of the availability of cultured skin fibroblasts from patients S2 and S6 (described in Melchionda et al.). After both cell lines were immortalised by lentiviral transduction with pLOX-Ttag-iresTK (see Chapter 2 for more details), they continued to display the same COX deficiency, of around 50% of the controls. These cells, were then transduced with APOPT1^{HA} and APOPT1^{GFP} lentiviral constructs. Although APOPT1^{HA} was always detectable in both patients, its amounts gradually decreased with time (**Figure 5.13A**). Consequently, although expression of APOPT1^{HA} rescued COX activity in the S6 cells, the complementation in S2 was only partial (**Figure 5.13B**).

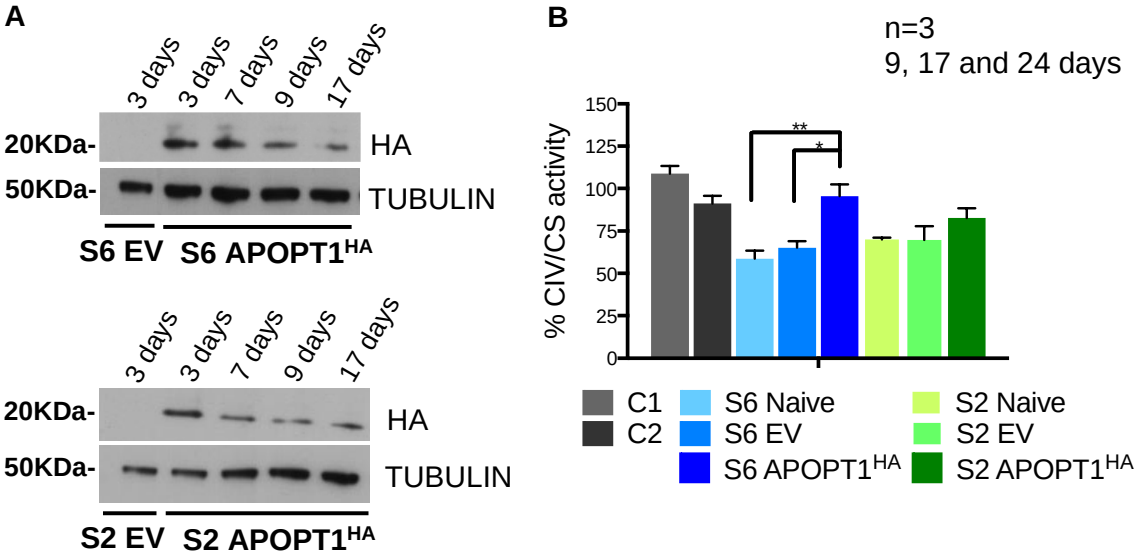

Figure 5.13 APOPT1^{HA} complementation assays. (**A**) SDS-PAGE (4-12 % NuPAGE Bis-Tris, Thermo Fisher Scientific) and WB analysis of total lysates from S6 and S2 patient-derived immortalized fibroblasts transduced with either the empty vector (E.V) or the APOPT1^{HA}-expressing plasmid. The expression levels of APOPT1^{HA} were tested at different days after transduction. (**B**) COX (CIV) enzymatic activity normalised to the activity of citrate synthase (CS) measured in control fibroblasts (C1 and C2) and patient cells (S6 and S2) either non-transduced (naïve) or transduced with the empty vector (E.V) or the APOPT1^{HA} construct. Data are presented as mean ± SEM (n = 3). ** $p < 0.005$, * $p < 0.05$ (two-way ANOVA Sidak's multiple comparisons test).

On the other hand, the expression of APOPT1^{GFP} was much more robust and stable and therefore, transduced S2 and S6 patient cells showed full recovery of COX subunit levels (**Figure 5.14A**) and COX enzymatic activity (**Figure 5.14B**).

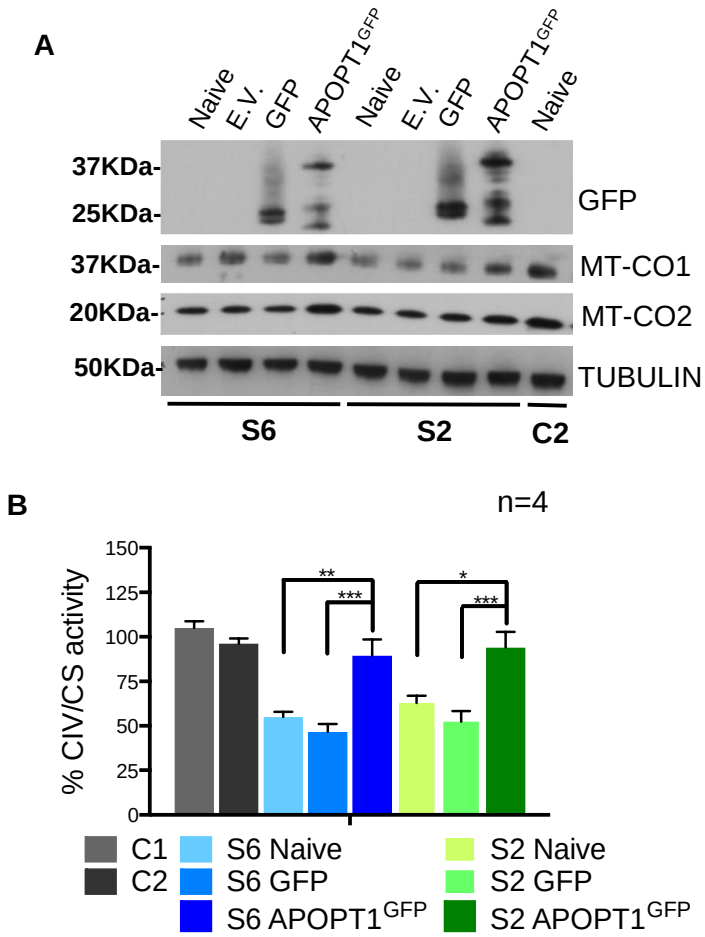

Figure 5.14 APOPT1^{GFP} complementation assays. (**A**) SDS-PAGE (4-12 % NuPAGE Bis-Tris, Thermo Fisher Scientific) and WB analysis of total lysates from control fibroblasts (C2) and S6 and S2 patient cells either non-transduced (naïve) or transduced with the empty vector (E.V), the GFP protein alone (GFP) or the APOPT1^{GFP} construct. (**B**) COX (CIV) enzymatic activity normalised to the activity of citrate synthase (CS) measured in control fibroblasts (C1 and C2) and patient cells (S6 and S2) either non-transduced (naïve) or transduced with the empty vector (E.V), the GFP protein alone (GFP) or the APOPT1^{GFP} construct. Data are presented as mean ± SEM (n = 3). *** $p < 0.0005$, ** $p < 0.005$, * $p < 0.05$ (two-way ANOVA Sidak's multiple comparisons test).

BN-PAGE was then used to analyse the native protein complexes of the respiratory chain. The amounts of fully assembled complex IV were considerably lower in the S2 and S6 patient cells compared to control immortalised fibroblasts (**Figure 5.15**). Moreover, accumulation of subassemblies of the MT-CO1 module (MITRAC) were also observed in the mutated human cells (**Figure 5.15**).

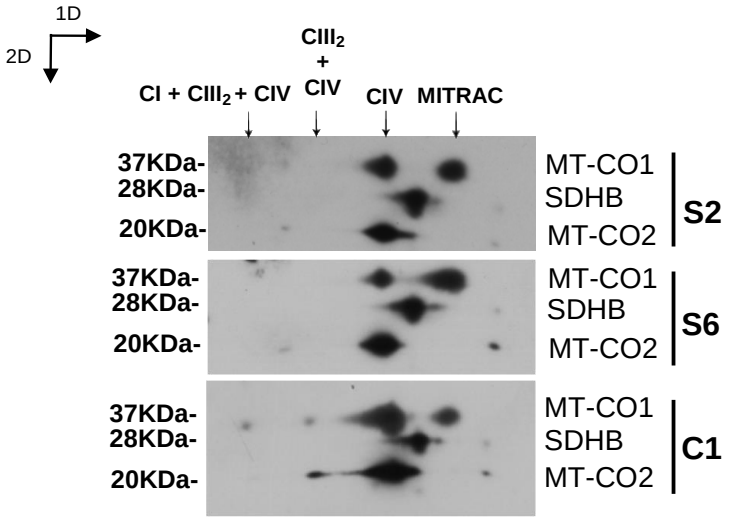

Figure 5.15 Reduced fully assembled CIV and subassembly accumulation in APOPT1-deficient cells. Western blot analysis of 2D BN-PAGE of mitoplasts from control fibroblasts (C1) and patient cells (S2 and S6). Fully assembled COX was immunovisualised with antibodies recognizing MT-CO1, and MT-CO2. The presence of the assembly intermediate 'MITRAC' was also detected (arrow). SDHB was used as a normalization and molecular weight standard signal.

Interestingly, the assembly defect in S2 and S6 cells not only led to an accumulation of MITRAC but it also affected the late COX intermediate composed of subunits COX4 and COX5A plus the MT-CO1 and MT-CO2 modules (also known as 'S3' (Nijtmans *et al.*, 1998; Vidoni *et al.*, 2017), which was markedly reduced in APOPT1-less cells (**Figure 5.16**). The assembly defects observed in patient-derived fibroblasts transfected with the 'empty vector' or the GFP protein alone were reverted by expression of wild-type APOPT1^{GFP} (**Figure 5.16**).

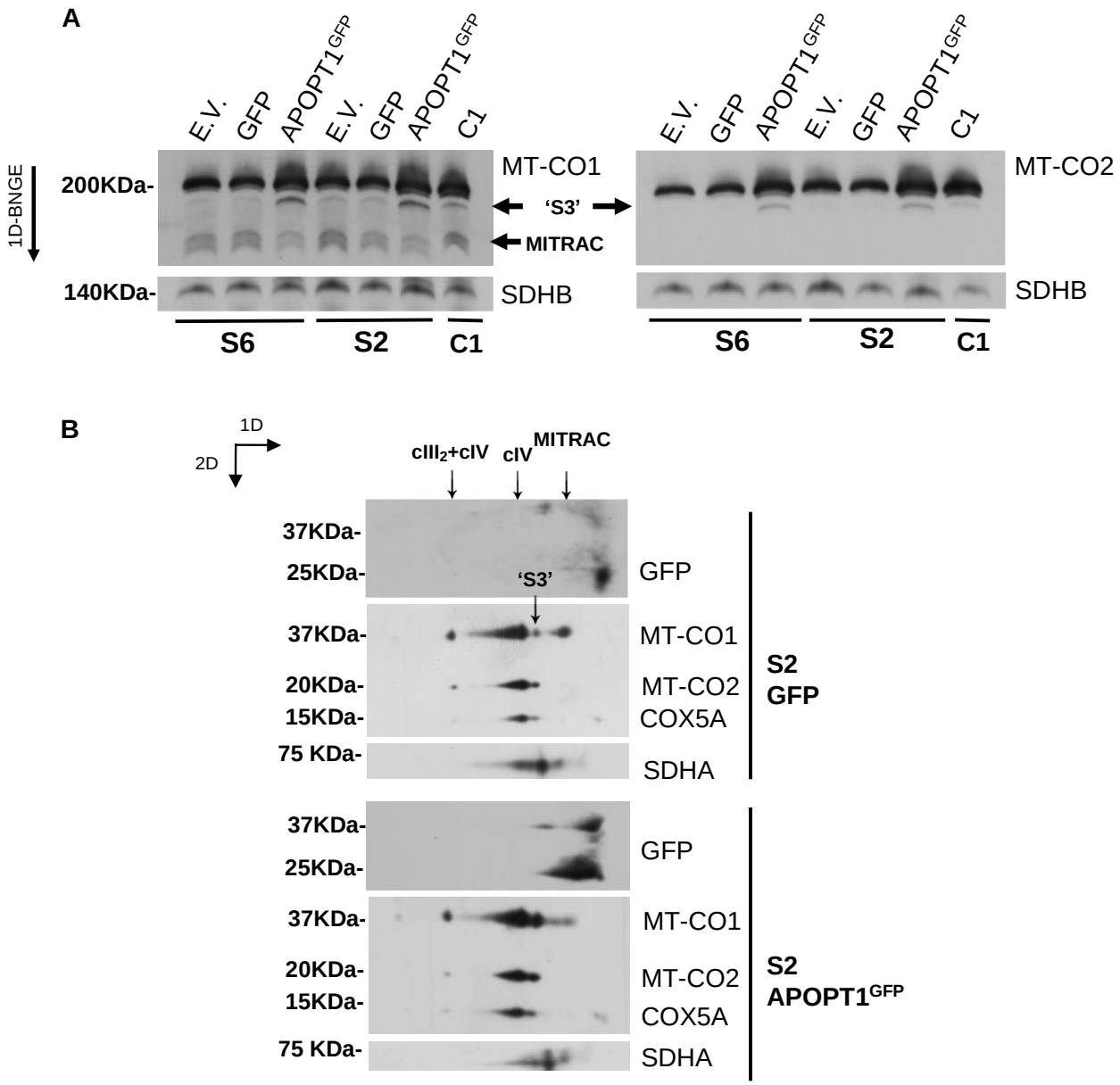

Figure 5.16 COX assembly defect in APOPT1-less cells rescued by APOPT1^{GFP} expression. (**A**) Western blot analysis of 1D BN-PAGE of mitoplasts from control fibroblasts (C1) and patient cells (S2 and S6) transduced with either the empty vector (E.V.), the GFP protein alone (GFP) or the APOPT1^{GFP} construct. (**B**) Western blot analysis of 2D BN-PAGE of mitoplasts from patient fibroblasts (S2) transduced with either the GFP protein alone (GFP) or the APOPT1^{GFP} construct.
Fully assembled COX was immunovisualised with antibodies recognising MT-CO1, MT-CO2 and COX5A. The presence of the assembly intermediates 'MITRAC' and 'S3' was also detected (indicated with arrows). SDHB signal was used for loading normalisation and molecular weight standard. Anti-GFP immunodetection revealed the presence of APOPT1^{GFP} migrating at low molecular weight positions in the 1D gel.

5.2.5 Decreased stability of the mtDNA-encoded COX subunits in APOPT1-less cells

The possibility that the COX defect in APOPT1-less cells could be due to a role of APOPT1 in transcription of COX subunits was evaluated by measuring mRNA levels of several of them. However, no changes were detected in either mtDNA-encoded *MT-CO1* and *MT-CO2* or nuclear-encoded *COX4I1* and *COX6B* mRNA levels (**Figure 5.17**).

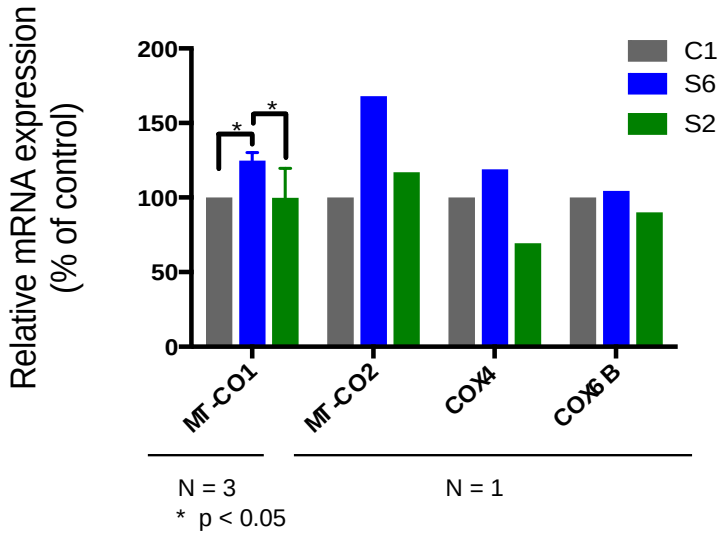

Figure 5.17 Normal COX subunits mRNA levels in patient cells. Relative mRNA expression of several COX subunits (*MT-CO1, MT-CO2, COX4 (isoform 1) and COX6B*) in control fibroblasts (C1) and patient cells (S2 and S6), normalised to the expression of *GAPDH* and expressed as percentage of the control. Data are presented as mean ± SEM (n = 3 for *MT-CO1*, n = 1 for the rest). Each of the biological replicas was measured in triplicate. * $p < 0.05$ (two-way ANOVA Sidak's multiple comparisons test).

Having excluded a role for APOPT1 in transcription of the COX mRNAs, the possibility that the defect could have its origin in decreased translation of mtDNA-encoded subunits was then investigated. The pulse synthesis of ^{35}S-labelled COX proteins was comparable in the non-complemented patient cells (expressing only GFP) and the controls, which were both patient cells transfected with APOPT1^{GFP} and wild-type immortalised fibroblasts (**Figure 5.18**). However, when the stability of the protein products was evaluated at different chase times, the amounts of labelled MT-CO2/MT-CO3 in the non-complemented S2 and S6

cells were significantly lower than in the controls after only three hours of culture in 'cold' medium (without L-[^{35}S]-Met), whereas MT-CO1 protein levels were clearly decreased after six hours (**Figure 5.18**). The differences became even more significant at subsequent time points.

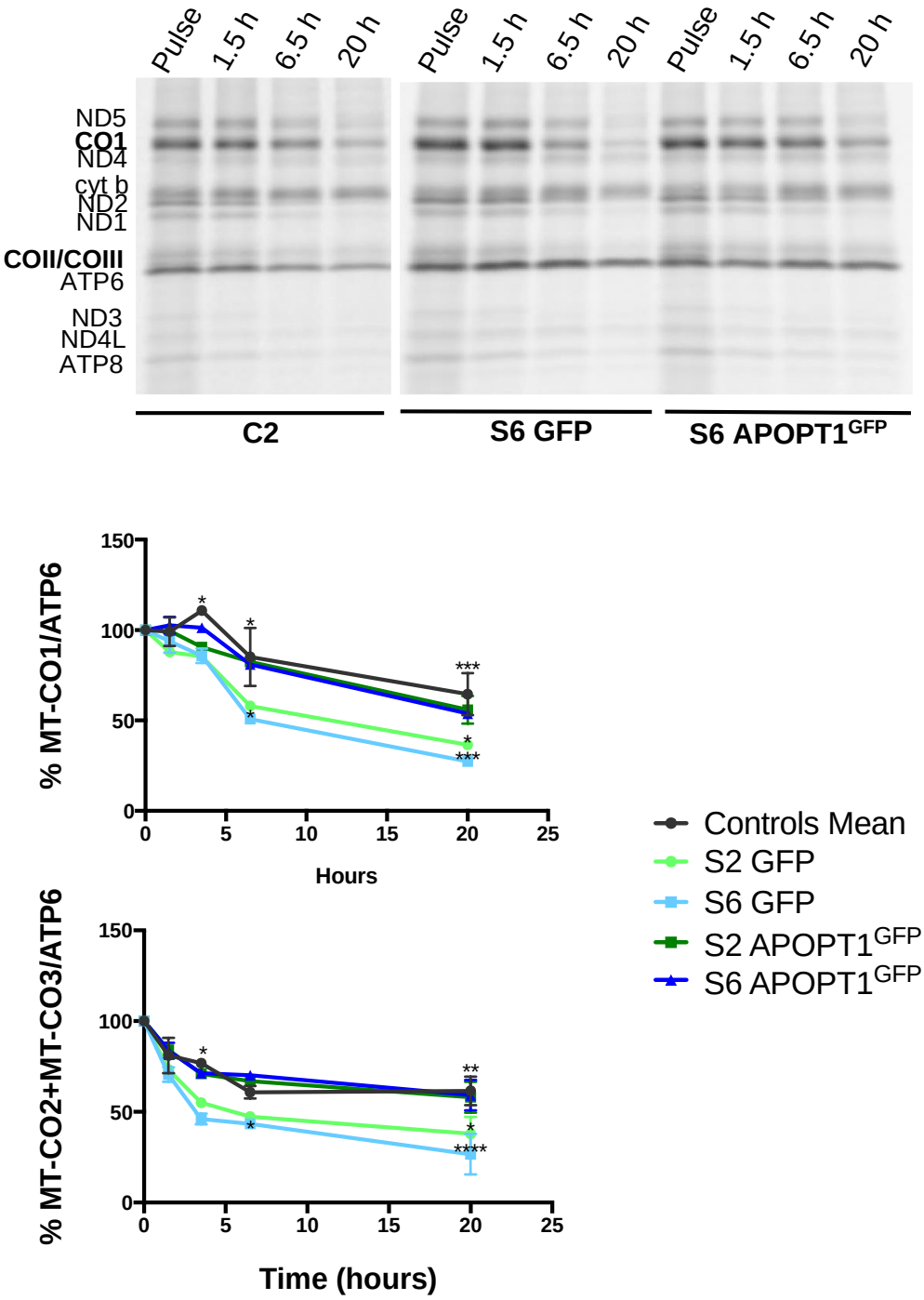

Figure 5.18

Figure 5.18 Decreased stability of mtDNA-encoded COX subunits in APOPT1-deficient patient cells. L-[^{35}S]-Methionine pulse-chase labelling of mtDNA-encoded proteins in control fibroblasts (C1 and C2) and patient cells (S2 and S6) transduced with either the GFP protein alone (GFP) or the APOPT1^{GFP} construct. After a two-hour exposure with the radioactive label (pulse), cells were cultured in cold medium for the indicated chase times. The graphs below show the densitometric quantification of the signal intensities of MT-CO1 (upper graph) and MTCO2+MT-CO3 (bottom graph) normalised to the ATP6 signal over the indicated time points. Data are presented as mean ± SEM (n = 3). **** $p < 0.0001$, *** $p < 0.0005$, ** $p < 0.005$, * $p < 0.05$ (two-way ANOVA Sidak's multiple comparisons test).

5.2.6 APOPT1 cytoplasmic levels are regulated by ubiquitination and proteasome degradation

APOPT1^{HA} was stabilised following treatment with the proteasome inhibitor MG132 (Melchionda *et al.*, 2014). In order to further explore this finding, the newly transduced 143B cells, expressing detectable amounts of APOPT1^{HA} in basal conditions, were treated with 5µM MG132 for different times. An increase in the precursor protein and a corresponding decrease of the mature cleaved form were observed after 2 and 6 hours of treatment (**Figure 5.19**), confirming that the precursor of APOPT1 is degraded by the UPS.

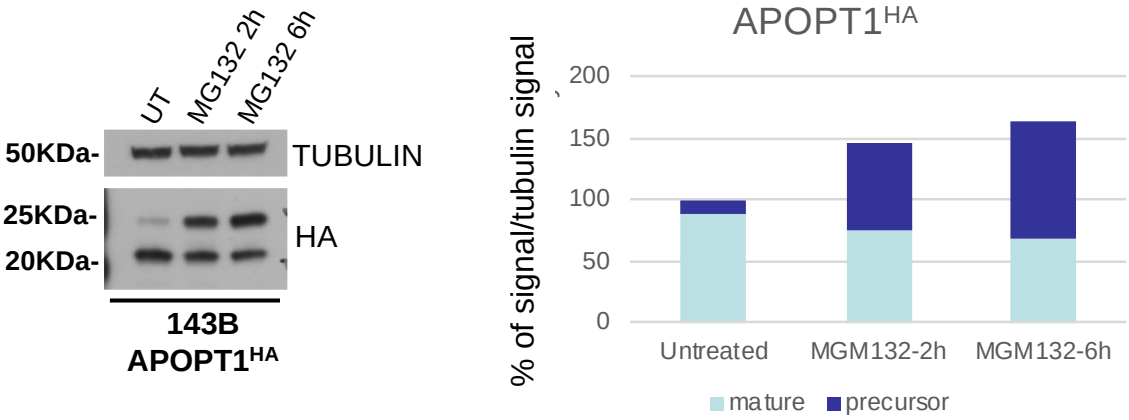

Figure 5.19 The precursor of APOPT^{HA} is accumulated after proteasome inhibition. SDS-PAGE (4-12 % NuPAGE Bis-Tris, Thermo Fisher Scientific) and WB analysis of total lysates from 143B APOPT1^{HA} cells untreated (UT) and treated with 5µM MG132 for 2 and 6 hours. The graph represents the densitometric quantification of the signals for the precursor and mature protein.

In addition, higher molecular mass HA-immunoreactive bands appeared after proteasome inhibition, which corresponded to ubiquitinated forms of APOPT1, as confirmed by immunoblotting for ubiquitin of immunoprecipitated APOPT1^{HA} (**Figure 5.20**).

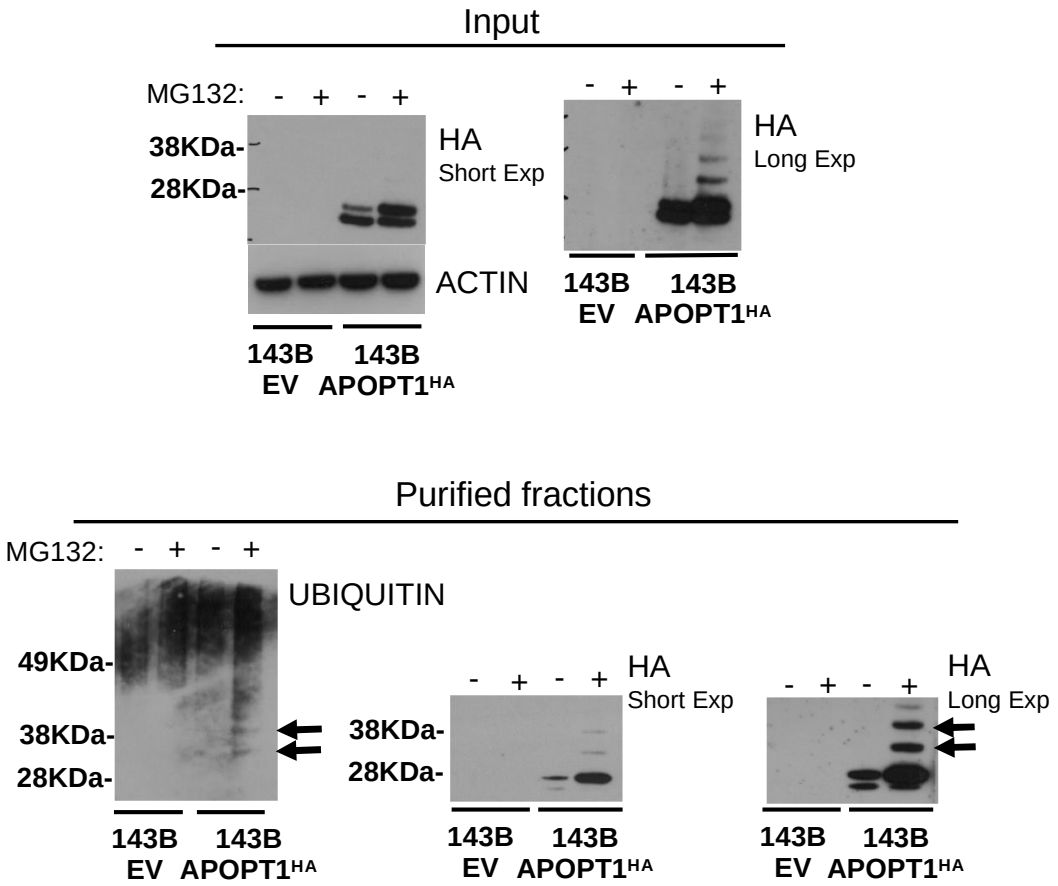

Figure 5.20 APOPT1^{HA} ubiquitinated forms accumulate after proteasome inhibition. The upper part of the panel (Input) shows Western blot analyses of total lysates from 143B cells transduced with either the empty vector (E.V) or APOPT1^{HA}, untreated (-) and treated with MG132 (+). Higher molecular mass bands appeared upon longer exposure in the samples treated with the proteasome inhibitor. The bottom part of the panel (Purified fractions) shows the analysis of fractions from the same cells immunoprecipitated with anti-HA. The higher molecular weight species (arrows) are cross-reacting with both anti-HA and anti-ubiquitin. Experiments performed by Anna S. Dickson (Cambridge Institute for Medical Research, CIMR, Cambridge, UK).

5.2.7 Mature APOPT1 is stabilised in oxidative stress conditions

APOPT1 was also stabilised when H_2O_2 was added to the cells directly in the culture medium, suggesting a role for APOPT1 in oxidative stress response (Melchionda *et al.*, 2014). To further explore this phenomenon, we stressed 143B cells overexpressing APOPT1^{HA} and APOPT1^{GFP} with 100 µM H_2O_2, the lowest concentration that has been shown to produce oxidative stress both in the cytosol and in the mitochondria (Hinchy *et al.*, 2018). The levels of both APOPT1^{HA} and APOPT1^{GFP} increased five to ten minutes after starting the treatment. Tagged APOPT1 amounts continued to be increased after three hours and returned to the initial levels at the six-hour time point (**Figure 5.21**), most likely due to the total elimination of extracellular H_2O_2 by the peroxide-removal systems in the cell (peroxiredoxins, glutathione peroxidases, catalases, etc.) (Chance, Sies and Boveris, 1979; Wagner *et al.*, 2013). Conversely, other mitochondrial proteins, including structural subunits (NDUFS1, UQCRC2, MT-CO1) and assembly factors (MR-1S), or proteins involved in the cytoplasmic heat-shock protein response (HSP70) did not increase under these conditions (**Figure 5.21**).

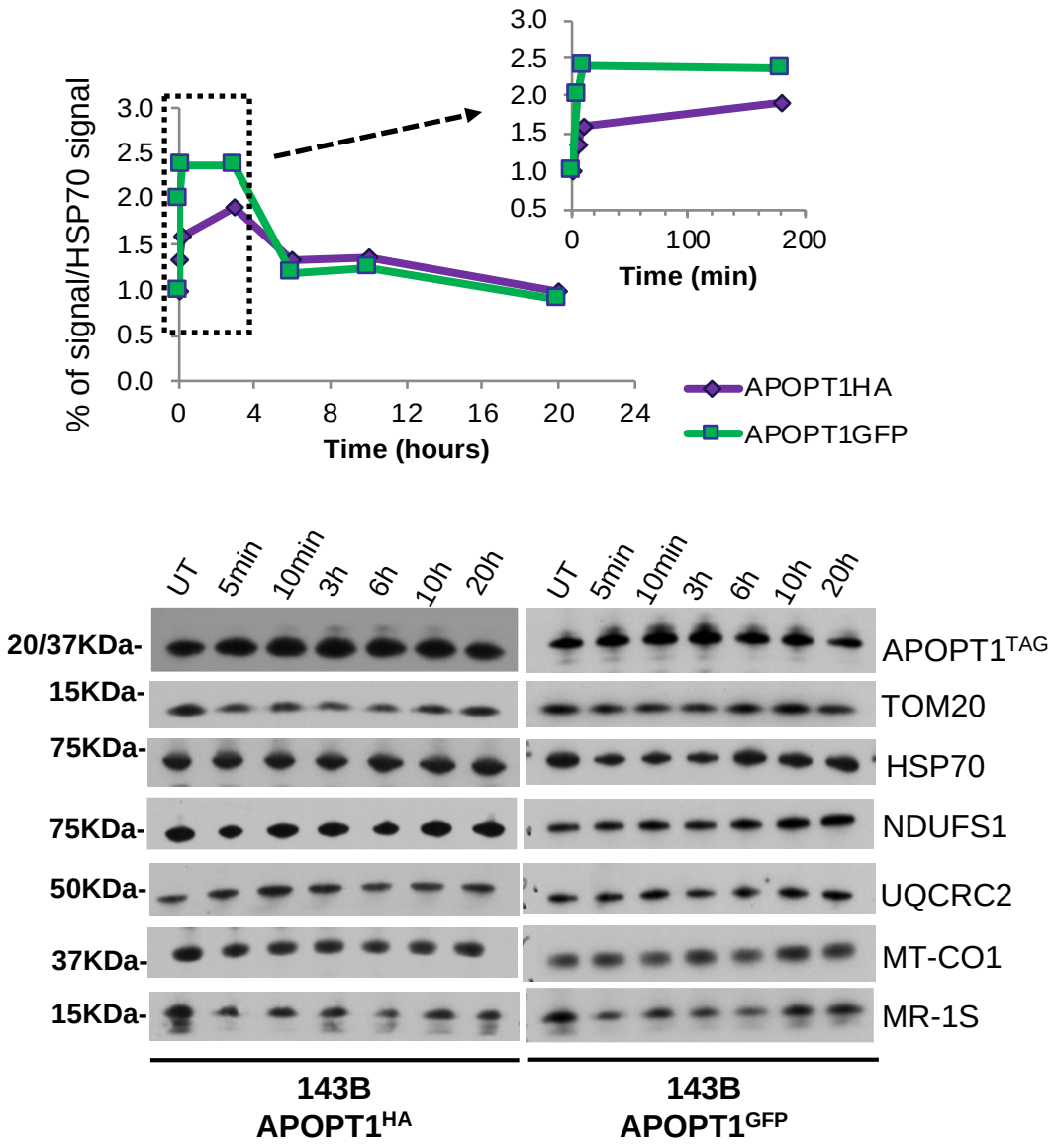

Figure 5.21 APOPT1 is stabilised by H_2O_2. SDS-PAGE (4-12 % NuPAGE Bis-Tris, Thermo Fisher Scientific) and WB analysis of total lysates from 143B cells overexpressing tagged APOPT1 (as indicated) untreated (UT) and exposed to 100 μM H_2O_2 for the indicated times. The upper graphs represent the densitometric quantification of the tagged APOPT1 signal normalized to the HSP70 signal at each time point. The graph inset shows that the increase of APOPT1 occurs in the first minutes after the exposure to H_2O_2.

To test whether this effect could be reproduced when ROS were selectively generated within mitochondria, we used MitoPQ (kindly provided by Michael Murphy and Elizabeth Hinchy), which is specifically imported into the organelle and generates superoxide ($O2^{\bullet-}$) within the mitochondrial matrix (Robb *et al.*, 2015). ROS generated within the organelle could directly or indirectly affect intramitochondrial APOPT1. On the other hand, it has been shown that the ROS produced by MitoPQ do not reach the cytosol (Hinchy *et al.*, 2018). However, the oxidative signal generated within the mitochondria could still be transferred to the cytosol through redox-relay reactions among redox-sensitive proteins that eventually interact with the target protein, in this case the cytosolic APOPT1 precursor (Herrmann and Riemer, 2012; Sobotta *et al.*, 2015a). Treatment with 5 µM MitoPQ in 143B cells overexpressing $APOPT1^{HA}$ and $APOPT1^{GFP}$ also promoted the rapid stabilisation of the mature APOPT1 form after only ten minutes (**Figure 5.22**), which continued for the first hours. APOPT1 amounts went back to the initial, or even lower, levels after 6 to 20 hours of treatment (**Figure 5.22**). Again, other mitochondrial proteins, including structural subunits (NDUFS1, UQCRC2, MT-CO1) and assembly factors (MR-1S), or proteins involved in the cytosolic heat-shock protein response (HSP70) did not increase under these conditions (**Figure 5.22**).

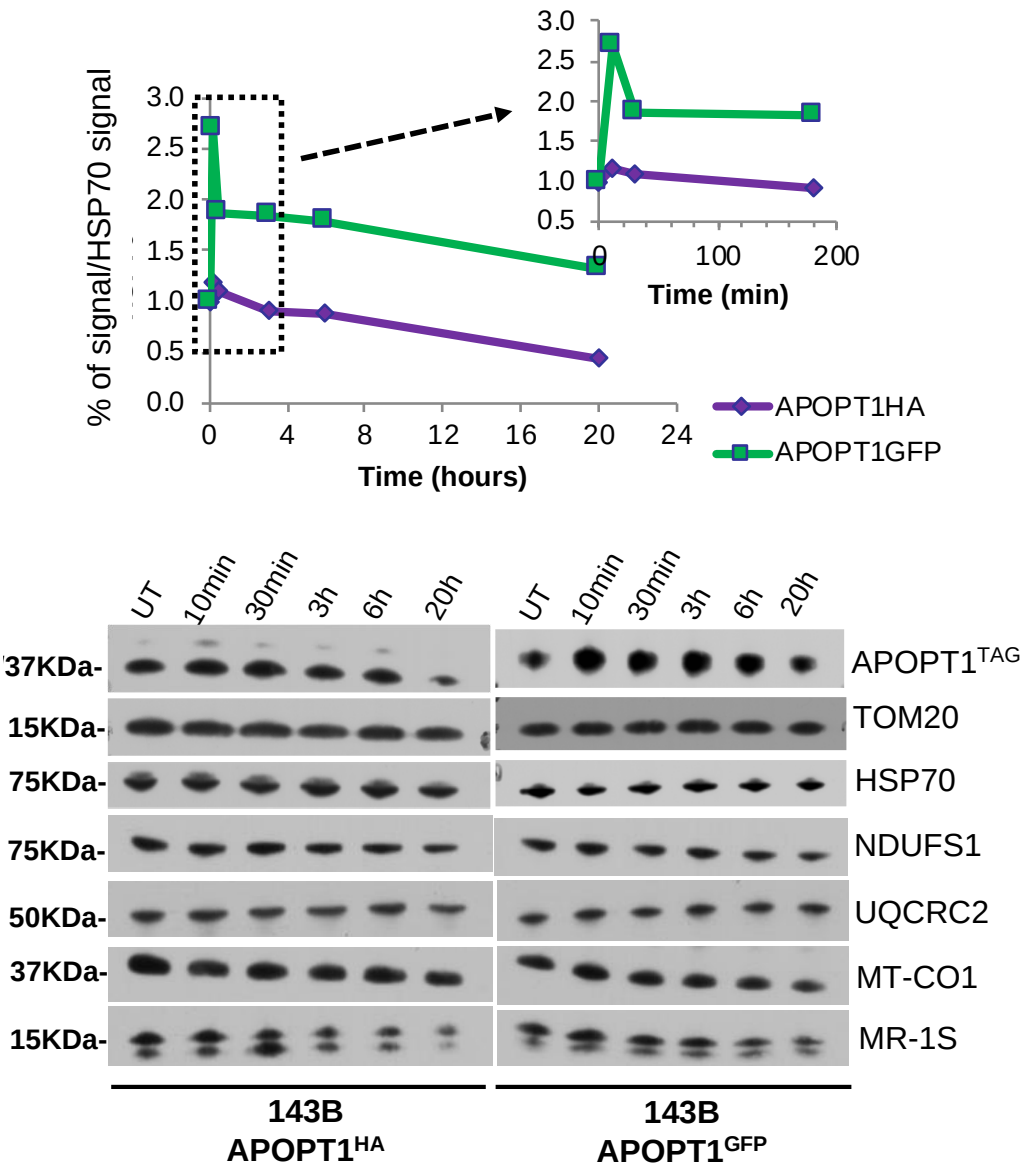

Figure 5.22 APOPT1 is stabilised by oxidative stress produced by MitoPQ. SDS-PAGE (4-12 % NuPAGE Bis-Tris, Thermo Fisher Scientific) and WB analysis of total lysates from 143B cells overexpressing tagged APOPT1 (as indicated) untreated (UT) and exposed to 5 µM MitoPQ for the indicated times. The upper graphs represent the densitometric quantification of the tagged APOPT1 signal normalized to the HSP70 signal at each time point. The graph inset shows that the increase of APOPT1 occurs in the first minutes after exposure to MitoPQ.

The increase in APOPT1 protein levels observed after treatment with H_2O_2 and MitoPQ could not be due to an increased synthesis, as the expression of the recombinant APOTP1 protein was under the control of a constitutive exogenous promoter. The stabilisation effect could not be a consequence of proteasome inactivation by oxidative stress either (Livnat-Levanon *et al.*, 2014; Segref *et al.*,

2014), since pharmacological proteasome inhibition clearly led to the preferential accumulation of the APOPT1 precursor (**Figure 5.19**), whereas addition of H_2O_2 and MitoPQ increased the amounts of the mature species (**Figure 5.21 and 5.21**). We further confirmed this by analysing the ubiquitinated protein levels in stressed and non-stressed cells. However, we did not find an increase in general ubiquitination in 143B cells overexpressing APOPT1^{HA} and APOPT1^{GFP} under exposure to 100 µM H_2O_2 or 5 µM MitoPQ (**Figure 5.23**).

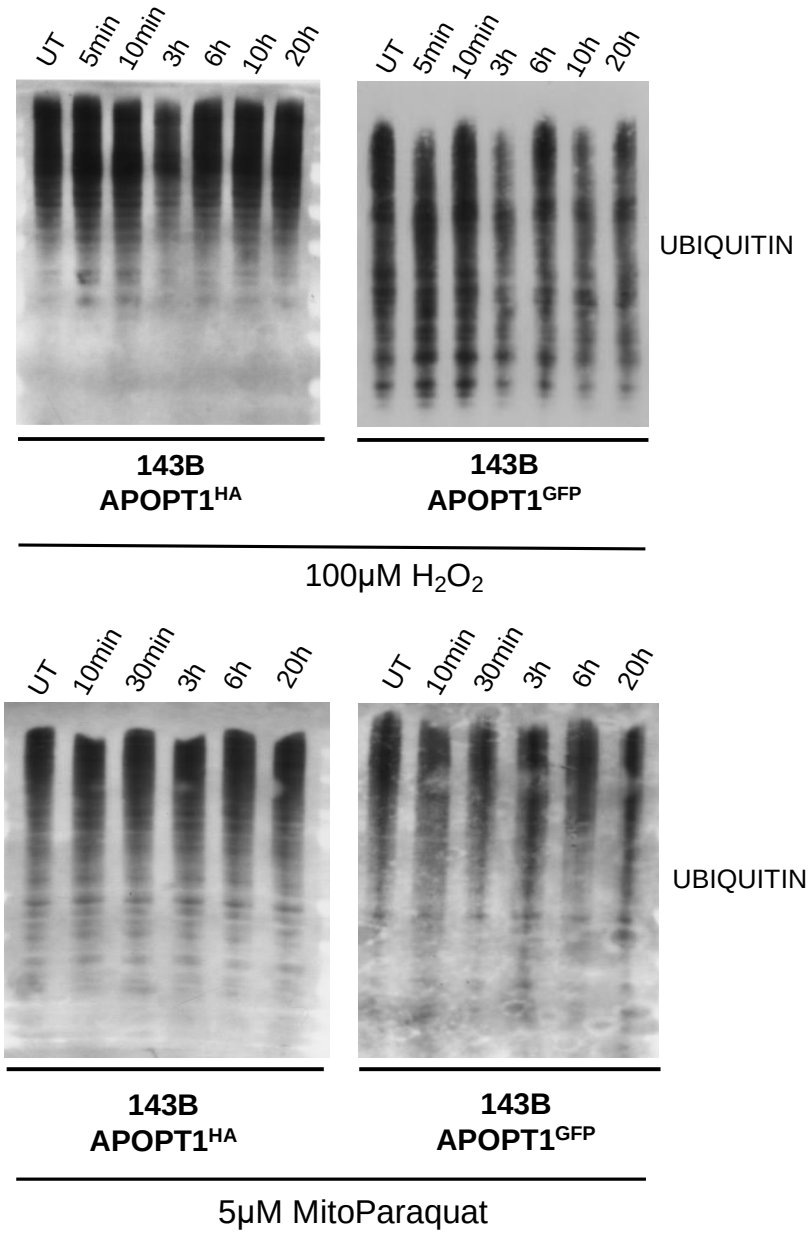

Figure 5.23

Figure 5.23 Ubiquitination analysis of cells stressed with oxidants. SDS-PAGE (4-12 % NuPAGE Bis-Tris, Thermo Fisher Scientific) and WB analysis of total lysates from 143B cells overexpressing tagged APOPT1 (as indicated) untreated (UT) and treated with (**A**) H_2O_2 or (**B**) MitoPQ for the indicated times. No increase in ubiquitinated proteins was observed with any of the treatments.

5.2.8. APOPT1 protects COX subunits from oxidatively-induced degradation

In order to analyse the possible effect of APOPT1 on COX under oxidative stress conditions, control fibroblasts and patient-derived cells transduced either with the GFP protein alone or the APOPT1^{GFP} construct, were treated with 5 µM MitoPQ for different times. Similar to what was observed in 143B cells, APOPT1^{GFP} levels increased around 4-fold in the complemented fibroblasts after 10 minutes from the start of MitoPQ treatment, reaching a maximum of 8-fold after 30 minutes to eventually decrease to pre-treatment levels after 20 hours of incubation (**Figure 5.24**). Interestingly, the addition of MitoPQ to the culture medium of APOPT1-deficient cells resulted in a gradual decrease of the levels of MT-CO2 and MT-CO1, being the reduction in the latter statistically significant after 20 hours of MitoPQ exposure (**Figure 5.24**). Conversely, wild-type immortalized fibroblasts and APOPT1^{GFP}-complemented patient cells showed no decrease in the amounts of MT-CO1 and MT-CO2, or even a slight increase, following MitoPQ treatment (**Figure 5.24**). The levels of a complex III structural subunit (UQCRC2) were unaffected, while complex I NDUFS1 was clearly reduced at the 20 h point, although this was independent on the presence or absence of APOPT1 (**Figure 5.24**).

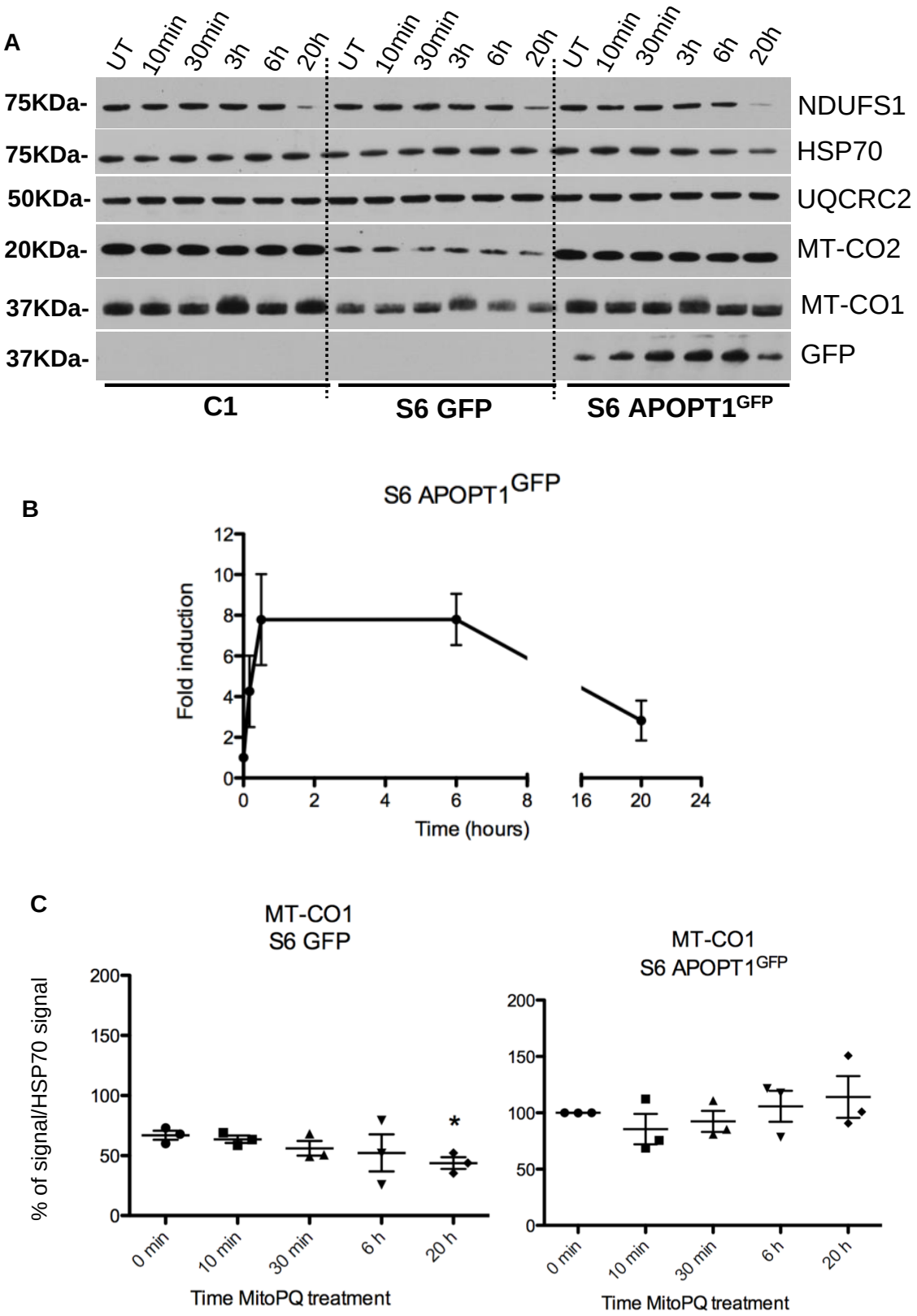
A
UT
10min
30min
3h
6h
20h
75KDa-
75KDa-
50KDa-
20KDa-
37KDa-
37KDa-
NDUFS1
HSP70
UQCRC2
MT-CO2
MT-CO1
GFP
C1
S6 GFP
S6 APOPT1GFP
B
S6 APOPT1GFP
Fold induction
Time (hours)
C
MT-CO1
S6 GFP
MT-CO1
S6 APOPT1GFP
% of signal/HSP70 signal
0 min
10 min
30 min
6 h
20 h
Time MitoPQ treatment

Figure 5.24

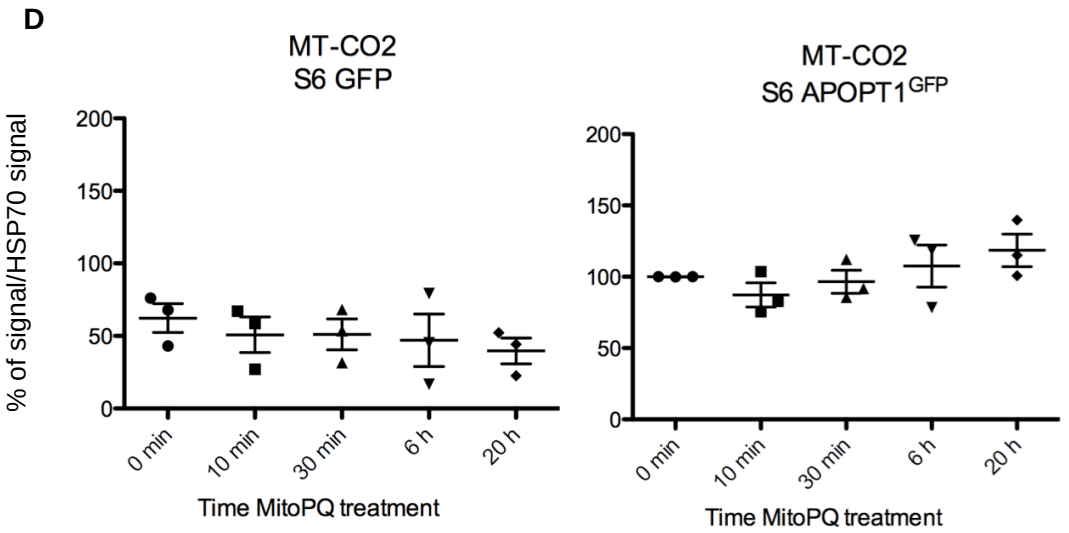

Figure 5.24 Effects of MitoPQ treatment in the absence or presence of APOPT1. (**A**) SDS-PAGE (4-12 % NuPAGE Bis-Tris, Thermo Fisher Scientific) and WB analysis of total lysates from control fibroblasts (C1) and patient cells transduced with the GFP protein alone (S6 GFP) or the APOPT1^{GFP} construct (S6 APOPT1^{GFP}), untreated (UT) or treated with 5 μM MitoPQ at the indicated times. (**B**) Densitometric quantification of the APOPT1^{GFP} signal during the treatment in two biological replicas. (**C**) Densitometric quantification of the MT-CO1 signal in the non-complemented APOPT1-less cells (S6 GFP) vs. the complemented cells (S6 APOPT1GFP). Three biological replicas and two technical replicates were carried out for each cell line. The signals in UT S6 APOPT1^{GFP} were considered 100% in each independent experiment. (**D**) Densitometric quantification of the MT-CO2 signal in the non-complemented APOPT1-less cells (S6 GFP) vs. the complemented cells (S6 APOPT1GFP). Three biological replicas and two technical replicates were carried out for each cell line. The signals in UT S6 APOPT1^{GFP} were considered 100%. Data are presented as mean ± SEM. * $p < 0.05$ (unpaired two-tailed Student's t-test).

5.2.9 APOPT1 levels decrease in hypoxic conditions

In order to investigate if other conditions in which the oxidative state of the cell changes also affect APOPT1 protein levels, we cultured the APOPT1^{HA} and APOPT1^{GFP}-expressing 143B cells in a hypoxic atmosphere with 5% O_2. APOPT1^{HA} and APOPT^{GFP} levels gradually decreased under these conditions, being their levels strongly reduced after 5 hours and almost undetectable after 29 hours (**Figure 5.25**). Conversely, the protein levels of MT-CO2 and of another COX assembly factor (SURF1) did not change and even seemed to be slightly increased after 29 hours of hypoxia (**Figure 5.25**). HIF-1α protein levels, which were undetectable under normoxia but markedly and moderately increased after

2 and 5 hours, respectively, confirmed the cellular adaptive response to hypoxia (**Figure 5.25**).

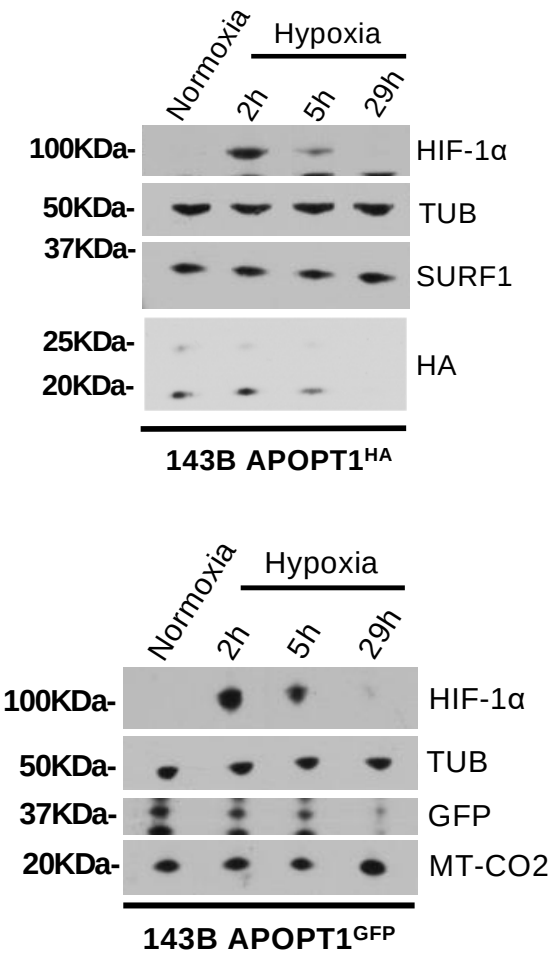

Figure 5.25 Hypoxia-induced APOPT1 degradation. SDS-PAGE (12 % NuPAGE Bis-Tris, Thermo Fisher Scientific) and WB analysis of total lysates from confluent 143B cells overexpressing tagged APOPT1 (as indicated) and cultured under normoxia (21% O_2; 5% CO_2) or hypoxia (5% O_2; 5% CO_2) for 2, 6 and 29 hours in an INVIVO2 300 hypoxia chamber (Ruskinn, Pencoed, UK).

5.3 Conclusions

- The transcript containing five coding exons, annotated as APOPT1-201 in Ensembl (www.ensembl.org) with Transcript ID ENST00000409074.6, encodes a functional protein able to complement the COX defect in APOPT1-null human cells.

- No cell death or growth arrest were observed when overexpressing APOPT1 in three different human cell lines, including HeLa transduced with APOPT1 tagged with a C-terminal GFP, as originally reported (Yasuda *et al.*, 2006).

- APOPT1 does not stably interact in a high-molecular weight complex, including COX subassembly intermediates.

- Stable translation of wild-type human $APOPT1^{HA}$ and $APOPT1^{GFP}$ in different human tumour cell lines and immortalised fibroblasts was achieved by using a second-generation lentiviral expression system.

- The mature APOPT1 protein is an IMM-bound protein apparently protruding to the matrix.

- Defective APOPT1 is undoubtedly the cause of isolated COX deficiency in patients S2 and S6.

- APOPT1-deficiency is associated with reduced levels of fully assembled COX, characterised by the accumulation of MT-CO1 containing subassemblies and reduced levels of the ‘S3’ intermediate. This suggests that APOPT1 participates in the intermediate steps of COX assembly, most likely in the joining of MITRAC to the MT-CO2 module in order to form the ‘S3’ intermediate.

- Absence of APOPT1 compromises the stability of the mtDNA-encoded COX subunits.

- A significant proportion of newly synthesized APOPT1 is ubiquitinated and degraded by the proteasome under normal conditions.

- Oxidative stress conditions, induced by direct addition of H_2O_2 or MitoPQ in the cell culture medium, rapidly increase the amounts of mature APOPT1.

- APOPT1-null cells showed reduction in COX subunit levels in oxidative stress conditions. The presence of APOPT1 protected COX from this damage.

- APOPT1 protein levels decrease in long-term hypoxia.

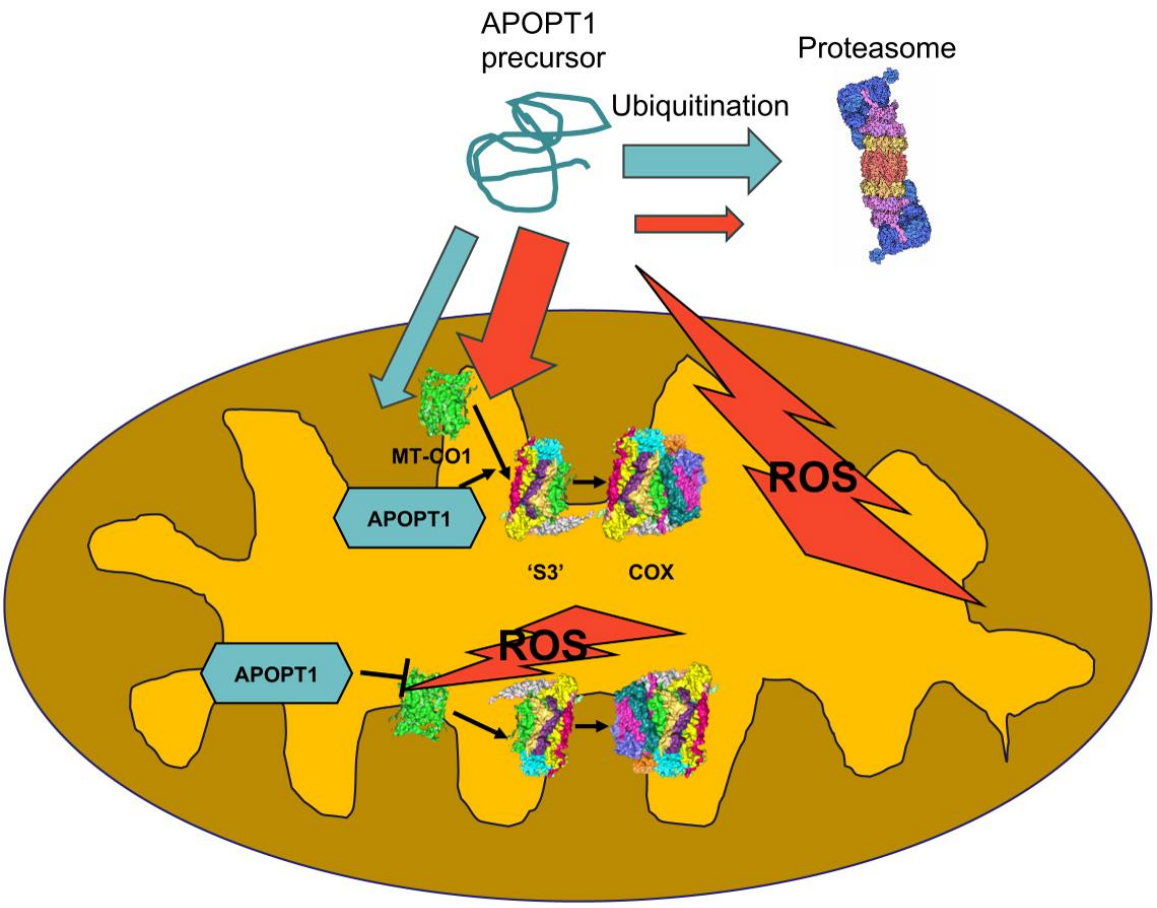

Figure 5.26 Visual summary of APOPT1-related findings. The cartoon depicts APOPT1 opposite regulation by UPS and ROS, as well as its potential intra-mitochondrial localisation in the IMM facing the matrix and its main function assisting the intermediate steps of COX assembly. It also shows the effect of oxidative stress in the absence of APOPT1, which results in enhanced degradation of COX structural subunits.

CHAPTER 6

Discussion and future aims

6.1 Discussion

COX biogenesis and regulation has been extensively studied owing to its fundamental role as the terminal oxidase of the mitochondrial respiratory chain. Studies in *Saccharomyces cerevisiae* have been fundamental to understand the assembly process of this enzyme. *Saccharomyces cerevisiae* is easy to be genetically manipulated and is a facultative anaerobic organism; both these features make it an ideal model organism for mitochondrial research. Indeed, the availability of an extensive collection of COX-defective mutant strains has allowed the identification of many assembly factors (Tzagoloff and Dieckmann, 1990; Barrientos, 2003; Barrientos *et al.*, 2009). The search for homologues of these factors in human cells resulted in the identification of several genes encoding the corresponding human proteins and eventually the discovery of pathological mutations associated with COX deficiency (Petruzzella *et al.*, 1998; Barrientos, 2003; Barrientos *et al.*, 2009; Szklarczyk *et al.*, 2012). During the past few years, more sophisticated genetic diagnostic approaches have allowed the identification of factors involved in COX biogenesis encoded by genes present only in animals without any obvious orthologs in yeast, such as LRPPRC (Mootha *et al.*, 2003), TACO1 (Weraarpachai *et al.*, 2009), APOPT1 (Melchionda *et al.*, 2014) and COA7 (Lyons *et al.*, 2016). This could be related to the fact that COX assembly and regulation is more complex in higher organisms and, therefore, requires the existence of animal-specific and even vertebrate-specific assembly factors. New strategies aimed to identify these specific proteins relevant to human disease must be implemented by using mammalian systems in our research. Two complementary strategies, proteomics and genomics, allowed us to identify the two animal-specific COX assembly factors discussed in this dissertation, MR-1S and APOPT1.

For the identification of novel factors in human cells, we performed quantitative proteomic analysis of the subassemblies accumulated in a *MT-CO3* mutant cybrid cell line (Tiranti *et al.*, 2000). As a starting point, we reasoned that some assembly factors may remain associated to the partially assembled species and that this strategy would unravel their identity (Andrews *et al.*, 2013). As a

result of these analyses, MR-1S was picked out as a putative COX assembly factor encoded by *PNKD*, a vertebrate-specific gene that is transcribed into three different isoforms (MR-1L, MR-1M and MR-1S). Knock-down expression of MR-1S in human cells resulted in decreased respiration and COX activity as well as defective assembly of the enzyme (Vidoni *et al.*, 2017), confirming its role in COX assembly and/or stability. Furthermore, we found that MR-1S interacts with COX structural subunits belonging to the early and intermediate assembly groups (Nijtmans *et al.*, 1998; Vidoni *et al.*, 2017) and that the advanced subcomplex 'S3' and fully assembled COX were less abundant in the MR-1S knockdown cells. Taken together, these results suggest a role for MR-1S in the intermediate assembly steps of COX. In addition, we found that MR-1S co-immunoprecipitates with PET100, a known COX assembly factor (Church *et al.*, 2005; Lim *et al.*, 2014; Oláhová *et al.*, 2015), and vice versa. Yeast Pet100 is necessary for COX assembly and has been reported to form a subcomplex with Cox7 (COX7A), Cox7a (COX6C), and Cox8 (COX7C) (Church, Chapon and Poyton, 1996; Church *et al.*, 2005). Interestingly, two of the human ortholog subunits (COX6C and COX7A2) were present in the same fractions as PET100 when MR-1S^{HA} was immunoprecipitated. Human skin fibroblasts deficient in PET100 (PET100^{G48*}) show profoundly reduced COX levels (Lim *et al.*, 2014; Oláhová *et al.*, 2015). In these cells MT-CO2 was found drastically reduced, whereas MT-CO1 was also low, but to a lesser extent (Oláhová *et al.*, 2015). In fibroblasts carrying the only other PET100 pathological mutation ever described (PET100$^{M1?}$) the turnover of MT-CO2 and MT-CO3 was much higher than in control cells (Lim *et al.*, 2014). This is totally consistent with the idea that PET100 is important for the formation and/or stabilisation of the intermediate steps of COX assembly, i.e. the subassembly structure produced when the COX4I1 + COX5A and the MT-CO1 module joins the MT-CO2-containing modules, before the incorporation of MT-CO3 and its partners. This is the same step in which we propose that MR-1S binds the COX subassemblies. In addition to PET100, MR-1S co-immunoprecipitated with PET117, a human ortholog of the yeast Pet117, also necessary for COX assembly (McEwen *et al.*, 1993; Szklarczyk *et al.*, 2012). The involvement of PET117 in COX biogenesis in human cells was never described before. Interestingly, by using the PET100^{G48*} mutant cells, we were able to

determine that the interactions among MR-1S, PET117, and COX structural subunits require the presence of PET100.

Regarding pathogenic variants found in the *PNKD* gene, mutations in exon 1, encoding the MTS of the two mitochondrially-targeted proteins (MR-1S and MR-1L), have been associated with the autosomal-dominant neurological disease paroxysmal non-kinesigenic dyskinesia (PNKD) (Ghezzi, Viscomi, *et al.*, 2009). Lower oxygen consumption rate was found in fibroblasts from one of the patients with mutations in the MTS of MR-1S and MR-1L (mutation c.26C>T resulting in an amino acid change p.Ala9Val, reference sequence NM_015488.4) (Ghezzi *et al.*, 2015). However, the molecular pathogenic mechanisms of PNKD remained elusive, since mutations in the MTS were shown to affect neither mitochondrial import nor protein maturation of MR-1S and MR-1L (Ghezzi, Viscomi, *et al.*, 2009). The function of both MR-1L, which localises to mitochondria and is only expressed in the brain, and MR-1M, which localises to the Golgi apparatus and endoplasmic reticulum, remains unknown but is likely not related to the COX-specific chaperone role that we have demonstrated for MR-1S, since the C-terminal sequences and functional domains of the MR-1L are the same of those of MR-1M, and completely different from those of MR-1S.

Genomic screening of mitochondrial encephalopathy patients, showing a characteristic MRI pattern and isolated COX deficiency, allowed the identification of pathogenic mutations in APOPT1 (Melchionda et al., 2014; Sharma et al., 2018). Although the genetic association was well established at the time, the biochemical link between APOPT1 and COX was unclear. APOPT1 was firstly described as an apoptosis-inducing factor identified as overexpressed at the mRNA level in smooth muscle cells from atherosclerotic plaques of Apolipoprotein E-deficient mice (Yasuda *et al.*, 2000). Exogenous expression of the mouse Apopt1 protein fused to GFP at its C-terminus revealed mitochondrial localisation (Yasuda *et al.*, 2006). However, overexpression of both the wild-type and the tagged protein was shown to induce apoptosis in cultured vascular smooth muscle and HeLa cells in a time frame of less than 24 hours after transfection (Yasuda *et al.*, 2006; Sun *et al.*, 2008). These contradictory findings and the inability to prove the biochemical link with COX in cultured cell models, due to difficulties in re-expressing the WT protein in patient-derived fibroblasts

(Melchionda *et al.*, 2014), prompted us to generate an *Apopt1* KO mouse model to study the function of APOPT1. The CRISPR/Cas9 technology was chosen for the genomic modification of mouse embryos. This system presents a great advantage over other genome editing technologies also based on nucleases, such as TALENs and ZNFs. The target specificity of those technologies relies on protein/DNA recognition, which means that the DNA-binding motif of the nuclease enzyme, encoded by large DNA fragments of 500-1500 bp, must be modified for each target, which is a very laborious task (Wood *et al.*, 2011). Instead, CRISPR/Cas9 can easily be adapted to new targets by just changing the 20 nucleotides spacer sequence, while the Cas protein remains unchanged (Rath *et al.*, 2015). The traditional transgenic mouse generation system based on embryonic stem cells (ESCs) and homologous recombination is extremely time-consuming, less efficient and much more complex (Capecchi, 1989; Hall, Limaye and Kulkarni, 2009). Generation of the construct plus target and validation of selected clones can take many months. Moreover, this technique requires manipulation of established ES cell lines, limiting the availability of strains for the initial engineering. Although this problem can be overcome by performing gene editing on a strain for which mouse ES cells already exist, followed by backcrosses to the desired background, the process would take more than a year (Liu *et al.*, 2017). Finally, engineering of multiple loci cannot be accomplished by this approach, unless knock-in individuals are selected through serial crosses or laborious manipulations (Liu *et al.*, 2017).

The availability of an *Apopt1* KO mouse model, allowed us to unequivocally establish the association of this protein with COX biogenesis. All the analysed tissues showed isolated COX deficiency with reduced enzymatic activity, low steady-state levels of structural subunits and defective assembly of COX, whereas the rest of the complexes of the respiratory chain were spared. The *in vivo* mouse model was also exploited to evaluate the impact of *Apopt1* deletion on the metabolic, neurological and motor phenotypes. Although *Apopt1* genetic ablation had no major metabolic effects, *Apopt1*$^{-/-}$ mice showed significantly impaired motor coordination and endurance. This was an indication of neurological and muscular involvement in the clinical phenotype similar to that found in human patients (Melchionda *et al.*, 2014), therefore confirming *APOPT1* as a mitochondrial disease gene. The pathological phenotype was expressed in

mice from a very young age and no worsening was observed when the analyses were repeated in one-year-old animals. Similarly, the disease has a childhood onset in humans with a clinical course that tends to stabilise and even recover over time. Some of these patients also presented sensorimotor polyneuropathy, which affects both sensory neurons (which convert external stimuli into centripetal action potentials) and motor neurons (which are responsible for muscle contraction and generation of movement) (Melchionda *et al.*, 2014). However, the pole-test results were negative at any age analysed, suggesting that, at least, proprioceptive sensory neurons were not damaged in the recombinant mice. Although mutations in the human *APOPT1* gene were also characterised by cognitive involvement in some patients, such as learning difficulties (Melchionda *et al.*, 2014), mice memory and spatial learning (assessed by the Y maze), were not affected at any age. However, *Apopt1*$^{-/-}$ mice showed reduced motivation to move and explore their environment, reflecting partial neurological impairment. A brain histopathological study, performed on three-month-old mice, showed neither morphological abnormalities nor neuronal loss or necrosis. The possibility that only the peripheral nerves, and not the brain, are affected in mutated mice cannot be ruled out, as some of the patients did present peripheral neuropathy (Melchionda *et al.*, 2014). It is also possible that brain histopathological lesions appear in ageing mice, although the motor and behavioural tests failed to clearly indicate a progressive deterioration of the clinical phenotype.

The initial characterisation of APOPT1 function and regulation was not possible due to the inability to re-express wild-type functional APOPT1 in cultured cells (Melchionda *et al.*, 2014). This was most probably due to the transfection and transduction systems used, which did not allow the stable expression of the HA-tagged APOPT1 protein in human fibroblasts. By optimising the transduction and expression systems with different lentiviral vectors and recombinant constructs, we were able to obtain stable translation of WT human APOPT1^{HA} and APOPT1^{GFP} in different human cell lines: standard tumour cells (HeLa and 143B) and immortalised fibroblasts, from both control subjects and patients. When overexpressing APOPT1 in human cells and contrary previous reports (Yasuda *et al.*, 2006; Sun *et al.*, 2008), we did not observe any cell death or growth arrest, including HeLa transduced with APOPT1 tagged with a C-terminal

GFP, similarly to what was used in the original report. The stable expression of the APOPT1 tagged versions, and the development of polyclonal antibodies recognising the endogenous human protein, enabled us to determine APOPT1 mitochondrial and sub-mitochondrial localisation as a protein associated to the inner membrane with its C-terminal most likely protruding into the matrix. In addition, transduction of WT APOPT1 in immortalised fibroblasts derived from two unrelated patients, S2 and S6 (Melchionda *et al.*, 2014), rescued the enzymatic and assembly COX defect. Altogether, these results allow us to clearly establish a role for APOPT1 in COX biogenesis and exclude its involvement in apoptosis, at least in the cells and tissues considered in our study. Therefore, we propose to change its name into cytochrome *c* oxidase assembly factor (COA) 8 and add it to the collection of already known COX assembly factors named COA 1-7.

The assembly defect shown by all the APOPT1-null models analysed, i.e. *Apopt1*$^{-/-}$ tissues as well as patient-derived immortalised fibroblasts, involves the global down-regulation of COX with an accumulation of subcomplexes including early assembly subunits (COX4 and COX5A) and the MT-CO1 module (MITRAC complex). Consistent with this observation, COX4, COX5A and MITRAC steady-state levels were less reduced than those of the MT-CO2 and MT-CO3 modules, involved in later steps of COX assembly (Timón-Gómez *et al.*, 2017; Vidoni *et al.*, 2017). Moreover, the 'S3' subassembly, containing the MT-CO1 and MT-CO2 modules together, is markedly reduced in the patient-derived cells. Thus, APOPT1/COA8 must play a role in joining or stabilising the MT-CO2 module to COX4-COX5A and MT-CO1. Absence of APOPT1/COA8 did not affect the synthesis of any of the mtDNA-encoded COX subunits. However, the stability of COX subunits was severely compromised, being probably actively degraded owing to impaired incorporation into the nascent complex. The same phenomenon has been consistently observed when different COX assembly factors, such as SCO1, COX20, CMC1 or COX18, are mutated or absent in human cells, determining the stalling in the assembly of the MT-CO1 module (Leary *et al.*, 2009; Bourens *et al.*, 2014; Bourens and Barrientos, 2017b, 2017a). Accordingly, it has been shown that COX deficient *S. cerevisia*e strains showing high sensitivity to hydrogen peroxide and an accumulation of subassemblies containing haemylated Cox1 (Khalimonchuk, Bird and Winge, 2007; Veniamin *et*

al., 2011) display a faster turnover of unassembled COX subunits, which is mediated by the ATPase Afg1 (Khalimonchuk, Bird and Winge, 2007). Interestingly, LACE1, the human orthologue of Afg1, is also involved in the degradation of nuclear-encoded COX subunits (Cesnekova *et al.*, 2016). These lines of evidence strongly suggest that there is a regulatory mechanism of COX assembly that links the accumulation of MT-CO1 containing subassemblies with faster degradation of unassembled COX subunits.

Concerning the regulation of APOPT1/COA8, the results presented here indicate active ubiquitination and proteasome-mediated degradation of the APOPT1/COA8 precursor in the cytoplasm under normal conditions and before mitochondrial import. Proteasome-mediated degradation of mitochondria-targeted proteins, especially those of the IMS, has been proposed as a regulatory mechanism aiming to prevent the accumulation of precursor proteins in the cytoplasm when import fails and to modulate their availability under physiological conditions (Bragoszewski *et al.*, 2013; Wrobel *et al.*, 2015). Therefore, the UPS could be involved in the mechanisms regulating COX assembly and function through APOPT1/COA8.

Short-term and mild oxidative stress, induced by direct addition of H_2O_2 in the cell culture medium or via MitoPQ, seem to enhance APOPT1/COA8 import or stabilisation inside mitochondria, since the amounts of mature APOPT1/COA8 increase in these conditions. This phenomenon cannot be attributed to direct proteasome inhibition by H_2O_2 (Livnat-Levanon *et al.*, 2014; Segref *et al.*, 2014) as we did not observe signs of accumulation of ubiquitinated proteins or increased heat-shock protein response. Moreover, pharmacological inhibition of the proteasome produced the preferential accumulation of APOPT1/COA8 precursor and not of the mature protein, as we observed under oxidative stress conditions. It has been shown that MitoPQ continuously and cumulatively generates ROS within mitochondria by redox cycling at the flavin site of complex I (Robb *et al.*, 2015), but that these ROS do not diffuse to the cytosol (Hinchy *et al.*, 2018). This could indicate that oxidants only have an effect on the intramitochondrial APOPT1/COA8, i.e. stabilise the mature form of APOPT1/COA8 without affecting its import. Addition of MitoPQ to the cell culture medium induces the redox-dependent dimerisation of mitochondrial matrix peroxiredoxins, which is reversed after 6 to 20 hours (Hinchy *et al.*, 2018), the

same time-frame in which we observed the return of APOPT1/COA8 to basal levels. Thus, an interesting possibility, worth testing in the future, is that the stabilisation of APOPT1/COA8 could be mediated by the matrix pool of peroxiredoxins, which are peroxidase enzymes in which the catalytic site contains two well conserved redox active cysteines involved in cellular redox homeostasis (Rhee, 2016). Indeed, it has already been shown that thiol peroxidases are involved in the transformation of oxidative equivalents (the peroxide) into transmittable signals, such as the formation of disulphide bonds in target proteins. This sensor-transducer mechanism has been reported in both yeast (Pflieger, Vinh and Toledano, 2002) and mammals (Sobotta *et al.*, 2015b). Another possibility is that the oxidative signal generated within the mitochondria is transferred to the cytosol by redox-relay interactions among redox-sensitive proteins, eventually modifying the cytosolic precursor of APOPT1/COA8 and favouring its import. Human APOPT1/COA8 has cysteine residues eleven amino acids upstream and nineteen amino acids downstream of the predicted MTS cleavage site, which are well conserved in other mammalian species and could therefore be involved in redox modifications that modulate its import and/or stability. Another indication that the peri-MTS cysteine residues could be involved in the regulation of APOPT1/COA8 import comes from a bioinformatic prediction using the Mitofates online tool (http://mitf.cbrc.jp/MitoFates/cgi-bin/top.cgi), which indicates that the two conserved cysteines in APOPT1/COA8 are part of or in close proximity to TOM20 recognition motifs (**Figure 6.1**). TOM20, a 20-kDa peripheral subunit of the TOM complex, interacts with the N-terminal MTS of cytosolic precursor proteins destined to the mitochondrial matrix and IMM (Söllner *et al.*, 1989; Ramage *et al.*, 1993; Rapaport, 2003) and recognises a 5–6-residue common motif, distinguishing them from other non-mitochondrial proteins and allowing their import into the organelle (Moczko *et al.*, 1997; Obita *et al.*, 2003).

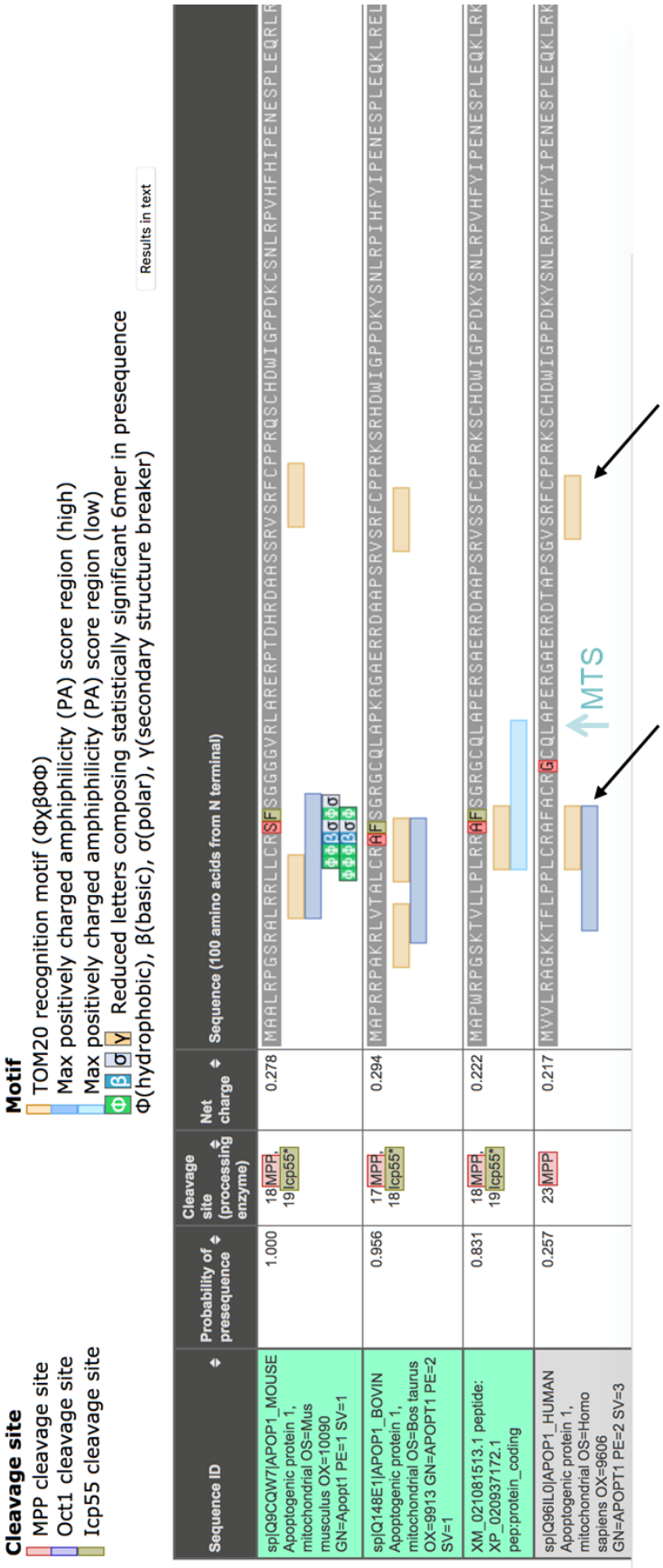
Cleavage site
MPP cleavage site
Oct1 cleavage site
Icp55 cleavage site
Motif
TOM20 recognition motif (ΦχβΦΦ)
Max positively charged amphiphilicity (PA) score region (high)
Max positively charged amphiphilicity (PA) score region (low)
Φ β σ γ Reduced letters composing statistically significant 6mer in presequence
Φ(hydrophobic), β(basic), σ(polar), γ(secondary structure breaker)
Results in text
Sequence ID
Probability of presequence
Cleavage site (processing enzyme)
Net charge
Sequence (100 amino acids from N terminal)
spQ9CQW7APOP1_MOUSE Apoptogenic protein 1, mitochondrial OS=Mus musculus OX=10090 GN=Apopt1 PE=1 SV=1
1.000
18MPP, 19Icp55*
0.278
MAALRPGSRALRRLLCRSFSGGGVRLARERPTDHRDAASSRVSRFCPPRQSCHDWIGPPDKCSNLRPVHFHIPENESPLEQRLR
spQ148E1APOP1_BOVIN Apoptogenic protein 1, mitochondrial OS=Bos taurus OX=9913 GN=APOPT1 PE=2 SV=1
0.956
17MPP, 18Icp55*
0.294
MAPRRPAKRLVTALCRAFSGRGCQLAPKRGAERRDAAPSRVSRFCPPRKSRHDWIGPPDKYSNLRPIHFYIPENESPLEQKLREL
XM_021081513.1 peptide: XP_020937172.1 pep:protein_coding
0.831
18MPP, 19Icp55*
0.222
MAPWRPGSKTVLLPLRRAFSGRGCQLAPERSAERRDAAPSRVSSFCPPRKSCHDWIGPPDKYSNLRPVHFYIPENESPLEQKLRK
spQ96IL0APOP1_HUMAN Apoptogenic protein 1, mitochondrial OS=Homo sapiens OX=9606 GN=APOPT1 PE=2 SV=3
0.257
23MPP
0.217
MVVLRAGKKTFLPPLCRAFACRGCQLAPERGAERRDTAPSGVSRFCPPRKSCHDWIGPPDKYSNLRPVHFYIPENESPLEQKLRK
MTS

Figure 6.1

Figure 6.1 Mitofates prediction software. The output shows the N-terminal 100 amino acids of the mouse, bovine, pig and protein with the following features: predicted cleaved site, region having the maximum score of positively charged amphiphilicity score in N-terminal 30 residues (high and low mean that the score is higher and lower than the sensitivity and specificity versus cut off value, respectively), regions matching to known TOM20 recognition motif (ΦXβΦΦ) and regions matching to any of 14 types of statistically significant 6-mers in N-terminal 30 residues: ΦΦσβΦΦ, ΦΦβσΦΦ, ΦΦΦβσΦ, ΦΦβσΦβ, ΦβΦΦβγ, βΦΦσσσ, ΦΦΦββΦ, ΦΦβΦΦβ, ΦσβΦΦσ, σΦΦβσΦ, ΦβΦΦγβ, ΦΦΦΦββ, ΦΦβσΦσ, βσΦβΦΦ. Φ indicates hydrophobic amino acid (L, F, I, V, W, Y, M, C, A), β indicates basic amino acid (R, K, H), σ indicates polar aminoacid (S, T, N, Q) and γ indicates secondary structure breaker amino acid (P, G).

Preliminary results shown in Chapter 5 indicate that APOPT1/COA8 amounts decrease in long-term hypoxia, confirming that the levels of this protein are strongly affected by the cellular redox state. HIF-1α can directly regulate gene expression by binding to hypoxia response elements (HRE), which are located upstream of transcriptional sites of target genes (Semenza and Wang, 1992). However, since gene expression of APOPT1^{HA} and APOPT1^{GFP} is not controlled by the endogenous promotor, the decrease in protein levels is most likely to be consequence of an increased proteolytic degradation, which could be controlled by the UPS and/or by mitochondrial proteases. For example, the matrix LON protease was reported to be involved in COX turnover under hypoxic conditions by degradation of phosphorylated COX4I1 and COX5B subunits (Sepuri *et al.*, 2017).

In the case of APOPT1/COA8 deficiency, neither the human cultured cells nor mouse tissues showed increased H_2O_2 production in non-induced conditions, however, when the patient-derived fibroblasts were oxidatively challenged they showed a significant increase in ROS production compared to the controls (Melchionda *et al.*, 2014), which argues in favour of a ‘pro-oxidant state’ in the absence of APOPT1/COA8. Interestingly, of the seven reported patients with mutations in APOPT1/COA8, 3 had an onset of the disease after a febrile illness or infection. It is well-known that both viral and bacterial infections trigger ROS production, which can in turn trigger the development or manifestation of other diseases (Schwarz, 1996; Ivanov, Bartosch and Isaguliants, 2017). In line with oxidative stress worsening the clinical phenotype of the patients, these same APOPT1-null cells showed further reduction in COX levels when oxidants were

added to the culture medium. The presence of APOPT1/COA8 in control cells (both complemented patient and control fibroblasts) protected COX from this damage. These observations underscore the association of APOPT1/COA8 function with COX assembly and stabilisation, as well as with the protection of the nascent enzyme from oxidative damage, which leads to degradation of its structural components.

In summary, we have demonstrated that quantitative proteomic analysis of subassemblies accumulated in cells with defective COX assembly, is a useful tool to identify new assembly factors that remain associated to the intermediates. In this way, we found MR-1S, a vertebrate-specific protein that interacts with COX subunits and the highly conserved PET100 and PET117 assembly factors. On the other hand, we have clearly demonstrated that genetic ablation of *APOPT1* is directly related to COX deficiency and mitochondrial disease. Moreover, we propose a mechanism of modulation of COX assembly that is mediated by regulating the levels of APOPT1/COA8, first in the cytoplasm by degrading it through the ubiquitin-proteasome system and secondly by ROS, which increases its intramitochondrial form to promote COX assembly at intermediate steps by stabilising and/or protecting the COX subassemblies from oxidative damage.

6.2 Future aims

- Characterisation of the function of human PET117 by knocking-down and/or knocking out its expression and evaluating the effect on COX activity and assembly. Additional studies, such as sub-mitochondrial localisation and PET117 protein levels upon knocking-down MR-1S or COX11, would be very useful to better understand the role of this protein in the intermediate steps of human COX maturation.

- To study the possible histopathological alterations in ageing *Apopt1*$^{-/-}$ brains, as differences in exploratory behaviour, which are related to cognitive functions, became evident in six-month old and older mice.

- Further characterisation of the neurological phenotype of *Apopt1* KO ageing mice by using more sophisticated behavioural tests such as 2-object novel object recognition, which measures the spontaneous tendency of mice to spend more time exploring new objects than familiar ones, or the visual acuity test, which assesses visual discrimination and clarity.

- Investigation of the *Apopt1*$^{-/-}$ mice phenotypical and biochemical changes induced by oxidative stress. The mice could be treated with acetaminophen, which has been shown to induce oxidative stress in liver (Jaeschke, McGill and Ramachandran, 2012), or MitoPQ, which has not been tested *in vivo* yet. Since human APOPT1/COA8 protects COX from oxidatively-induced degradation, a worsening of the phenotype in *Apopt1* KO mice is expected.

- Measurement of the H_2O_2 levels produced in mouse isolated mitochondria from oxidatively stressed tissues *in vivo* and the effects of direct addition of oxidants to the isolated mitochondria.

- Investigation of the APOPT1/COA8 interactome by immunoprecipitation of the tagged proteins using anti-HA and anti-GFP affinity agarose beads. Quantitative mass spectrometry using SILAC could be used to compare patient-derived fibroblasts mock-transfected and overexpressing APOPT1^{GFP}. In addition, cells could be stressed with H_2O_2 or MitoPQ prior to the immunoprecipitation, in order to investigate whether APOPT1/COA8 interacts with other proteins, such as COX assembly factors or COX subunits, under these conditions.

- BN-PAGE-based kinetic studies of the incorporation of newly synthesised radio-labelled mtDNA-encoded COX subunits to understand exactly in which point COX assembly is disrupted in APOPT1-null cells and whether the structural subunits are degraded after being incorporated (due to an

unstable fully-assembled COX) or if they are accumulated and degraded before joining the nascent complex.

- A significant proportion of the APOPT1/COA8 precursor seems to be ubiquitinated and degraded by the proteasome under normal conditions. However, complementary experiments, such as WB analysis of the potential gradual degradation of APOPT1/COA8 by the UPS after cytosolic protein synthesis inhibition, need to be performed in order to validate this observation.

- Further analysis of the effect of oxidants on the COX in APOPT1-null cells, such as BN-PAGE analysis and COX enzymatic activity, are necessary in order to better understand the role of this protein in COX maturation under oxidative stress.

- Investigation of the role of the cysteines proximal to the APOPT1/COA8 MTS in relation to the import and/or intramitochondrial stabilisation of the protein. These specific residues will be substituted by alanines by site-directed-mutagenesis in order to investigate whether they are involved in direct post-translational modifications by H_2O_2 or by interaction with other redox-sensitive proteins. Furthermore, the redox state of the cysteines will also be investigated by electrophoretic mobility shift assays in which the redox-modified cysteine residues are tagged with a large group, such as a polyethylene glycol (PEG) polymer (van Leeuwen *et al.*, 2017). In addition, the APOPT1/COA8 MTS will be replaced by a classic MTS (with no cysteine residues) and the functionality and localisation of the protein will then be analysed in transfected cells with this hybrid construct. Also, the effect of oxidants on the regulation of this protein lacking the natural APOPT1/COA8 MTS will be investigated.

- Expand the analysis of APOPT1/COA8 protein levels in hypoxia. This preliminary observation will be confirmed by replicating the experiment and analysing APOPT1/COA8 protein levels at more time points. The

implication of the hypoxic signalling pathways in the observed effect will be analysed (Clerici and Matthay, 2000; Pham *et al.*, 2002). The proteolytic pathways leading to APOPT1/COA8 decrease in hypoxic conditions will also be investigated.

7. References

Abhishek Aich, Cong Wang, Arpita Chowdhury, Christin Ronsör, D., Pacheu-Grau1, Ricarda Richter-Dennerlein, S. D. & P. and Rehling (1978) 'COX16 promotes COX2 metallation and assembly during respiratory complex IV biogenesis', p. 3.

Abrahams, J. *et al.* (1994) 'Structure at 2.8 A resolution of F1-ATPase from bovine heart mitochondria', *Nature Publishing Group*, 370, pp. 621–628.

Acín-Pérez, R. *et al.* (2008) 'Respiratory Active Mitochondrial Supercomplexes', *Molecular Cell*, 32(4), pp. 529–539. doi: 10.1016/j.molcel.2008.10.021.

Ackerman, S. H. and Tzagoloff, A. (1990) 'Identification of two nuclear genes (ATPJ1, ATP12) required for assembly of the yeast F1-ATPase', *Biochemistry*, 87(July), pp. 4986–4990.

Ademowo, O. S. *et al.* (2017) 'Lipid (per) oxidation in mitochondria: an emerging target in the ageing process?', *Biogerontology*. Springer Netherlands, 18(6), pp. 859–879. doi: 10.1007/s10522-017-9710-z.

Aguileta, M. A. *et al.* (2015) 'The E3 ubiquitin ligase parkin is recruited to the 26 S proteasome via the proteasomal ubiquitin receptor Rpn13', *Journal of Biological Chemistry*, 290(12), pp. 7492–7505. doi: 10.1074/jbc.M114.614925.

Aich, A. *et al.* (2018) 'COX16 promotes COX2 metallation and assembly during respiratory complex IV biogenesis', *eLife*, 7, pp. 1–18. doi: 10.7554/eLife.32572.

Ajioka, R. S., Phillips, J. D. and Kushner, J. P. (2006) 'Biosynthesis of heme in mammals', *Biochimica et Biophysica Acta - Molecular Cell Research*, 1763(7), pp. 723–736. doi: 10.1016/j.bbamcr.2006.05.005.

Ambivero, C. T. *et al.* (2014) 'Mulan E3 ubiquitin ligase interacts with multiple E2 conjugating enzymes and participates in mitophagy by recruiting GABARAP', *Cellular Signalling*. Elsevier Inc., 26(12), pp. 2921–2929. doi: 10.1016/j.cellsig.2014.09.004.

Andrews, B. *et al.* (2013) 'Assembly factors for the membrane arm of human

complex I', *Proceedings of the National Academy of Sciences*, 110(47), pp. 18934–18939. doi: 10.1073/pnas.1319247110.

Andreyev, A. Y., Kushnareva, Y. E. and Starkov, A. A. (2005) 'Mitochondrial metabolism of reactive oxygen species', *{B}iochemistry ({M}oscow)*, 70(2), pp. 200–214. doi: 10.1007/s10541-005-0102-7.

Anesti, V. and Scorrano, L. (2006) 'The relationship between mitochondrial shape and function and the cytoskeleton', 1757, pp. 692–699. doi: 10.1016/j.bbabio.2006.04.013.

Antonicka, H., Ogilvie, I., *et al.* (2003) 'Identification and Characterization of a Common Set of Complex I Assembly Intermediates in Mitochondria from Patients with Complex I Deficiency', *Journal of Biological Chemistry*, 278(44), pp. 43081–43088. doi: 10.1074/jbc.M304998200.

Antonicka, H., Leary, S. C., *et al.* (2003) 'Mutations in COX10 result in a defect in mitochondrial heme A biosynthesis and account for multiple, early-onset clinical phenotypes associated with isolated COX deficiency', *Human Molecular Genetics*, 12(20), pp. 2693–2702. doi: 10.1093/hmg/ddg284.

Antonicka, H., Mattman, A., *et al.* (2003) 'Mutations in COX15 Produce a Defect in the Mitochondrial Heme Biosynthetic Pathway, Causing Early-Onset Fatal Hypertrophic Cardiomyopathy', *The American Journal of Human Genetics*, 72(1), pp. 101–114. doi: 10.1086/345489.

Arnold, S., Goglia, F. and Kadenbach, B. (1998) '3,5-Diiodothyronine binds to subunit Va of cytochrome-c oxidase and abolishes the allosteric inhibition of respiration by ATP', *European Journal of Biochemistry*, 252(2), pp. 325–330. doi: 10.1046/j.1432-1327.1998.2520325.x.

Arnold, S. and Kadenbach, B. (1997) 'Cell respiration is controlled by ATP, an allosteric inhibitor of cytochrome-c oxidase', *European Journal of Biochemistry*, 249(1), pp. 350–354. doi: 10.1111/j.1432-1033.1997.t01-1-00350.x.

Arnold, S. and Kadenbach, B. (1999) 'The intramitochondrial ATP/ADP-ratio controls cytochrome c oxidase activity allosterically', *FEBS Letters*, 443(2), pp. 105–108. doi: 10.1016/S0014-5793(98)01694-9.

Atkinson, A. *et al.* (2011) 'The LYR Protein Mzm1 Functions in the Insertion of the Rieske Fe/S Protein in Yeast Mitochondria', *Molecular and Cellular Biology*, 31(19), pp. 3988–3996. doi: 10.1128/MCB.05673-11.

Aufschnaiter, A., Kohler, V., Diessl, J. and Peselj, C. (2017) 'Mitochondrial lipids in neurodegeneration', *Cell and Tissue Research*. Cell and Tissue Research, pp. 125–140. doi: 10.1007/s00441-016-2463-1.

Aufschnaiter, A., Kohler, V., Diessl, J., Peselj, C., *et al.* (2017) 'Mitochondrial lipids in neurodegeneration', *Cell and Tissue Research*. Cell and Tissue Research, 367(1), pp. 125–140. doi: 10.1007/s00441-016-2463-1.

Ayala, A., Muñoz, M. F. and Argüelles, S. (2014) 'Lipid peroxidation: Production, metabolism, and signaling mechanisms of malondialdehyde and 4-hydroxy-2-nonenal', *Oxidative Medicine and Cellular Longevity*, 2014. doi: 10.1155/2014/360438.

Bacman, S. R. *et al.* (2014) 'The Use of Mitochondria-Targeted Endonucleases to Manipulate mtDNA', *Methods Enzymol*, 547, pp. 373–397. doi: 10.1016/B978-0-12-801415-8.00018-7.The.

Balsa, E. *et al.* (2012) 'NDUFA4 is a subunit of complex IV of the mammalian electron transport chain', *Cell Metabolism*. doi: 10.1016/j.cmet.2012.07.015.

Banci, L. *et al.* (2004) 'Solution structure of Cox11, a novel type of β-immunoglobulin-like fold involved in CuB site formation of cytochrome c oxidase', *Journal of Biological Chemistry*, 279(33), pp. 34833–34839. doi: 10.1074/jbc.M403655200.

Baradaran, R. *et al.* (2013) 'Crystal structure of the entire respiratory complex i', *Nature*, 494(7438), pp. 443–448. doi: 10.1038/nature11871.

Barca, E. and Garcia-diaz, B. (2018) 'Deoxycytidine and deoxythymidine treatment for thymidine kinase 2 deficiency', 81(5), pp. 641–652. doi: 10.1002/ana.24922.Deoxycytidine.

Barel, O. *et al.* (2008) 'Mitochondrial Complex III Deficiency Associated with a Homozygous Mutation in UQCRQ', *American Journal of Human Genetics*, 82(5), pp. 1211–1216. doi: 10.1016/j.ajhg.2008.03.020.

Barrientos, A. (2003) ‘Yeast models of human mitochondrial diseases’, *IUBMB Life*, 55(2), pp. 83–95. doi: 10.1080/1521654031000098122.

Baughman, J. M. *et al.* (2008) ‘Integrative genomics identifies MCU as an essential component of the mitochondrial calcium uniporter’, *Nano*, 6(9), pp. 2166–2171. doi: 10.1021/nl061786n.Core-Shell.

Benard, G. *et al.* (2010) ‘IBRDC2, an IBR-type E3 ubiquitin ligase, is a regulatory factor for Bax and apoptosis activation’, *EMBO Journal*. Nature Publishing Group, 29(8), pp. 1458–1471. doi: 10.1038/emboj.2010.39.

Bender, E. and Kadenbach, B. (2000) ‘The allosteric ATP-inhibition of cytochrome c oxidase activity is reversibly switched on by cAMP-dependent phosphorylation’, *FEBS Letters*, 466(1), pp. 130–134. doi: 10.1016/S0014-5793(99)01773-1.

Bezawork-Geleta, A. *et al.* (2015) ‘LON is the master protease that protects against protein aggregation in human mitochondria through direct degradation of misfolded proteins’, *Scientific Reports*. Nature Publishing Group, 5(October), pp. 1–13. doi: 10.1038/srep17397.

Bianciardi, L. *et al.* (2016) ‘Exome sequencing coupled with mRNA analysis identifies NDUFAF6 as a Leigh gene’, *Molecular Genetics and Metabolism*. Elsevier B.V., 119(3), pp. 214–222. doi: 10.1016/j.ymgme.2016.09.001.

Bingol, B. *et al.* (2014) ‘The mitochondrial deubiquitinase USP30 opposes parkin-mediated mitophagy’, *Nature*. Nature Publishing Group, 510(7505), pp. 370–375. doi: 10.1038/nature13418.

Blaza, J. N. *et al.* (2014) ‘Kinetic evidence against partitioning of the ubiquinone pool and the catalytic relevance of respiratory-chain supercomplexes’, *Proceedings of the National Academy of Sciences*, 111(44), pp. 15735–15740. doi: 10.1073/pnas.1413855111.

Bode, M. *et al.* (2015) ‘Redox-regulated dynamic interplay between Cox19 and the copper-binding protein Cox11 in the intermembrane space of mitochondria facilitates biogenesis of cytochrome c oxidase’, *Molecular Biology of the Cell*, 26(13), pp. 2385–2401. doi: 10.1091/mbc.E14-11-1526.

Bogenhagen, D. F. (2012) ‘Mitochondrial DNA nucleoid structure ☆’, *BBA - Gene Regulatory Mechanisms*. Elsevier B.V., 1819(9–10), pp. 914–920. doi: 10.1016/j.bbagrm.2011.11.005.

Bottani, E. *et al.* (2017) ‘TTC19 Plays a Husbandry Role on UQCRFS1 Turnover in the Biogenesis of Mitochondrial Respiratory Complex III’, *Molecular Cell*. Elsevier Inc., 67(1), p. 96–105.e4. doi: 10.1016/j.molcel.2017.06.001.

Bourens, M. *et al.* (2013) ‘Redox and Reactive Oxygen Species Regulation of Mitochondrial Cytochrome *c* Oxidase Biogenesis’, *Antioxidants & Redox Signaling*, 19(16), pp. 1940–1952. doi: 10.1089/ars.2012.4847.

Bourens, M. *et al.* (2014) ‘Human COX20 cooperates with SCO1 and SCO2 to mature COX2 and promote the assembly of cytochrome c oxidase’, *Human Molecular Genetics*, 23(11), pp. 2901–2913. doi: 10.1093/hmg/ddu003.

Bourens, M. and Barrientos, A. (2017a) ‘A *CMC1* -knockout reveals translation-independent control of human mitochondrial complex IV biogenesis’, *EMBO reports*, 18(3), pp. 477–494. doi: 10.15252/embr.201643103.

Bourens, M. and Barrientos, A. (2017b) ‘Human mitochondrial cytochrome c oxidase assembly factor COX18 acts transiently as a membrane insertase within the subunit 2 maturation module’, *Journal of Biological Chemistry*, 292(19), pp. 7774–7783. doi: 10.1074/jbc.M117.778514.

Boveris, A., Cadenas, E. and Stoppani, A. O. M. (1976) ‘Role of ubiquinone in the mitochondrial generation of hydrogen peroxide’, *Biochemical Journal*, 156(2), pp. 435–444. doi: 10.1042/bj1560435.

Bragoszewski, P. *et al.* (2013) ‘The Ubiquitin-Proteasome System Regulates Mitochondrial Intermembrane Space Proteins’, *Molecular and Cellular Biology*, 33, pp. 2136–2148. doi: 10.1128/MCB.01579-12.

Bragoszewski, P. *et al.* (2015) ‘Retro-translocation of mitochondrial intermembrane space proteins’, *Proceedings of the National Academy of Sciences*, 112(25), pp. 7713–7718. doi: 10.1073/pnas.1504615112.

Bragoszewski, P., Turek, M. and Chacinska, A. (2017) ‘Control of mitochondrial biogenesis and function by the ubiquitin–proteasome system’, *Open Biology*. doi:

10.1098/rsob.170007.

Brandt, U. *et al.* (1993) 'The mitochondrial targeting presequence of the Rieske iron-sulfur protein is processed in a single step after insertion into the cytochrome bc1 complex in mammals and retained as a subunit in the complex', *Journal of Biological Chemistry*, 268(12), pp. 8387–8390.

Braschi, E., Zunino, R. and McBride, H. M. (2009) 'MAPL is a new mitochondrial SUMO E3 ligase that regulates mitochondrial fission', *EMBO Reports*, 10(7), pp. 748–754. doi: 10.1038/embor.2009.86.

Braymer, J. J. and Lill, R. (2017) 'Iron–sulfur cluster biogenesis and trafficking in mitochondria', *Journal of Biological Chemistry*, 292(31), pp. 12754–12763. doi: 10.1074/jbc.R117.787101.

Brieger, K. *et al.* (2012) 'Reactive oxygen species: from health to disease', *Swiss Medical Weekly*, (August), pp. 1–14. doi: 10.4414/smw.2012.13659.

Bruno, C. *et al.* (1999) 'A Stop-Codon Mutation in the Human mtDNA Cytochrome c Oxidase I Gene Disrupts the Functional Structure of Complex IV', pp. 611–620.

Brzóska, K., Męczyńska, S. and Kruszewski, M. (2006) 'Iron-sulfur cluster proteins: Electron transfer and beyond', *Acta Biochimica Polonica*, 53(4), pp. 685–691. doi: 20061382 [pii].

Bulteau, A. L. *et al.* (2017) 'Dysfunction of mitochondrial Lon protease and identification of oxidized protein in mouse brain following exposure to MPTP: Implications for Parkinson disease', *Free Radical Biology and Medicine*. Elsevier B.V., 108(March), pp. 236–246. doi: 10.1016/j.freeradbiomed.2017.03.036.

Bulteau, A. L., Ikeda-Saito, M. and Szweda, L. I. (2003) 'Redox-Dependent Modulation of Aconitase Activity in Intact Mitochondria', *Biochemistry*, 42(50), pp. 14846–14855. doi: 10.1021/bi0353979.

Buskiewicz, I. A. *et al.* (2016) 'Reactive oxygen species induce virus-independent MAVS oligomerization in systemic lupus erythematosus', 9(456). doi: 10.1126/scisignal.aaf1933.Reactive.

Calvo, S. E. *et al.* (2010) 'High-throughput, pooled sequencing identifies mutations in NUBPL and FOXRED1 in human complex i deficiency', *Nature Genetics*. Nature Publishing Group, 42(10), pp. 851–858. doi: 10.1038/ng.659.

Calvo, S. E. and Mootha, V. K. (2010) 'The Mitochondrial Proteome and Human Disease', *Annu Rev Genomics Hum Genet*, 11, pp. 25–44. doi: 10.1146/annurev-genom-082509-141720.The.

Camara, Y. *et al.* (2014) 'Administration of deoxyribonucleosides or inhibition of their catabolism as a pharmacological approach for mitochondrial DNA depletion syndrome', *Human Molecular Genetics,* 23(9), pp. 2459–2467. doi: 10.1093/hmg/ddt641.

Campello, S. and Scorrano, L. (2010) 'Mitochondrial shape changes: orchestrating cell pathophysiology', 11(9). doi: 10.1038/embor.2010.115.

Carlson, C. G. *et al.* (2003) 'COX16 encodes a novel protein required for the assembly of cytochrome oxidase in Saccharomyces cerevisiae.', *The Journal of biological chemistry*, 278(6), pp. 3770–5. doi: 10.1074/jbc.M209893200.

Carroll, C. J. *et al.* (2014) 'Next-generation sequencing for mitochondrial disorders', pp. 1837–1853. doi: 10.1111/bph.12469.

Carroll, J. *et al.* (2006) 'Bovine complex I is a complex of 45 different subunits', *Journal of Biological Chemistry*, 281(43), pp. 32724–32727. doi: 10.1074/jbc.M607135200.

Carrozzo, R. *et al.* (2006) 'Subcomplexes of human ATP synthase mark mitochondrial biosynthesis disorders', *Annals of Neurology*, 59(2), pp. 265–275. doi: 10.1002/ana.20729.

Cavalier-Smith, T. (2006) 'Origin of mitochondria by intracellular enslavement of a photosynthetic purple bacterium', *Proceedings of the Royal Society B: Biological Sciences*, 273(1596), pp. 1943–1952. doi: 10.1098/rspb.2006.3531.

Cerqua, C. *et al.* (2018) 'COX16 is required for assembly of cytochrome c oxidase in human cells and is involved in copper delivery to COX2', *Biochimica et Biophysica Acta (BBA) - Bioenergetics*. Elsevier, 1859(4), pp. 244–252. doi: 10.1016/j.bbabio.2018.01.004.

Cerutti, R. *et al.* (2014) 'NAD+-Dependent Activation of Sirt1 Corrects the Phenotype in a Mouse Model of Mitochondrial Disease', *Cell Metabolism*, 1(1), pp. 1042–1049. doi: 10.1016/j.cmet.2014.04.001.

Chacinska, A. *et al.* (2009) 'Importing Mitochondrial Proteins: Machineries and Mechanisms', *Cell*. doi: 10.1016/j.cell.2009.08.005.

Chem, J. B. *et al.* (2015) 'The mitochondrial calcium uniporter is a highly selective ion channel', 427(January 2004), pp. 1874–1878.

Chen, Q., Kang, J. and Fu, C. (2018) 'The independence of and associations among apoptosis, autophagy, and necrosis', *Signal Transduction and Targeted Therapy*. Springer US, 3(1), p. 18. doi: 10.1038/s41392-018-0018-5.

Chen, Y. *et al.* (2012) 'Identification of a protein mediating respiratory supercomplex stability', *Cell Metabolism*, 15(3), pp. 348–360. doi: 10.1016/j.cmet.2012.02.006.Identification.

Chinnery, P. F. and Hudson, G. (2013) 'Mitochondrial genetics', *British Medical Bulletin*, 106(1), pp. 135–159. doi: 10.1093/bmb/ldt017.

Chouchani, E. T. *et al.* (2016) 'A unifying mechanism for mitochondrial superoxide production during ischemia-reperfusion injury', *Cell Metabolism*. Elsevier, 23(2), pp. 254–263. doi: 10.1016/j.cmet.2015.12.009.

Choudhary, C. *et al.* (2009) 'Lysine acetylation targets protein complexes and co-regulates major cellular functions', *Science*, 325(5942), pp. 834–840. doi: 10.1126/science.1175371.

Christoph Maack, B. O. (2013) 'Excitation-contraction coupling and mitochondrial energetics Christoph', 6(8), pp. 369–392. doi: 10.1021/nn300902w.Release.

Church, C. *et al.* (2005) 'A role for Pet100p in the assembly of yeast cytochrome c oxidase: Interaction with a subassembly that accumulates in a pet100 mutant', *Journal of Biological Chemistry*, 280(3), pp. 1854–1863. doi: 10.1074/jbc.M410726200.

Civiletto, G. *et al.* (2015) 'Opa1 Overexpression Ameliorates the Phenotype of

Two Mitochondrial Disease Mouse Models Article Opa1 Overexpression Ameliorates the Phenotype of Two Mitochondrial Disease Mouse Models', *Cell Metabolism*. The Authors, 21(6), pp. 845–854. doi: 10.1016/j.cmet.2015.04.016.

Čížková, A. *et al.* (2008) 'TMEM70 mutations cause isolated ATP synthase deficiency and neonatal mitochondrial encephalocardiomyopathy', *Nature Genetics*, 40(11), pp. 1288–1290. doi: 10.1038/ng.246.

Cobine, P. A., Pierrel, F. and Winge, D. R. (2006) 'Copper trafficking to the mitochondrion and assembly of copper metalloenzymes', *Biochimica et Biophysica Acta - Molecular Cell Research*, 1763(7), pp. 759–772. doi: 10.1016/j.bbamcr.2006.03.002.

Conte, A. *et al.* (2015) 'The dimerization of the yeast cytochrome bc<inf>1</inf> complex is an early event and is independent of Rip1', *Biochimica et Biophysica Acta - Molecular Cell Research*. Elsevier B.V., 1853(5), pp. 987–995. doi: 10.1016/j.bbamcr.2015.02.006.

Cooper, C. E. and Brown, G. C. (2008) 'The inhibition of mitochondrial cytochrome oxidase by the gases carbon monoxide, nitric oxide, hydrogen cyanide and hydrogen sulfide: Chemical mechanism and physiological significance', *Journal of Bioenergetics and Biomembranes*, 40(5), pp. 533–539. doi: 10.1007/s10863-008-9166-6.

Cornelissen, T. *et al.* (2014) 'The deubiquitinase USP15 antagonizes Parkin-mediated mitochondrial ubiquitination and mitophagy', *Human molecular genetics*, 23(19), pp. 5227–5242. doi: 10.1093/hmg/ddu244.

Couvillion, M. T. *et al.* (2016) 'Synchronized translation programs across compartments during mitochondrial biogenesis', *Nature*, 533(7604), pp. 499–503. doi: 10.1038/nature18015.

Craven, L. *et al.* (2017) 'Recent Advances in Mitochondrial Disease', *Annu. Rev. Genom. Hum. Genet*, 18(2), pp. 57–75.

Crofts, A. R. *et al.* (2008) 'The Q-cycle reviewed: How well does a monomeric mechanism of the bc1complex account for the function of a dimeric complex?', *Biochimica et Biophysica Acta - Bioenergetics*, 1777(7–8), pp. 1001–1019. doi: 10.1016/j.bbabio.2008.04.037.

Cruciat, C. M. *et al.* (1999) 'Bcs1p, an AAA-family member, is a chaperone for the assembly of the cytochrome bc1complex', *EMBO Journal*, 18(19), pp. 5226–5233. doi: 10.1093/emboj/18.19.5226.

Cui, T.-Z. *et al.* (2012) 'Late-Stage Maturation of the Rieske Fe/S Protein: Mzm1 Stabilizes Rip1 but Does Not Facilitate Its Translocation by the AAA ATPase Bcs1', *Molecular and Cellular Biology*, 32(21), pp. 4400–4409. doi: 10.1128/MCB.00441-12.

D'Souza, A. R. and Minczuk, M. (2018) 'Mitochondrial transcription and translation: overview.', *Essays in biochemistry*, 62(3), pp. 309–320. doi: 10.1042/EBC20170102.

Daniela Fornuskova, Lukas Stiburek, Laszlo Wenchich, Kamila Vinsova, Hana Hansikova, J. Z. (2010) 'Novel insights into the assembly and function of human nuclear-encoded cytochrome c oxidase subunits 4, 5a, 6a, 7a and 7b', *Biochemical Journal*, 428 (3), pp. 363–374.

Davies, K. M. *et al.* (2011) 'Macromolecular organization of ATP synthase and complex I in whole mitochondria', *Proceedings of the National Academy of Sciences*, 108(34), pp. 14121–14126. doi: 10.1073/pnas.1103621108.

Davies, K. M., Blum, T. B. and Kühlbrandt, W. (2018) 'Conserved in situ arrangement of complex I and III_2 in mitochondrial respiratory chain supercomplexes of mammals, yeast, and plants', *Proceedings of the National Academy of Sciences*, p. 201720702. doi: 10.1073/pnas.1720702115.

Dennerlein, S. *et al.* (2015) 'MITRAC7 Acts as a COX1-Specific Chaperone and Reveals a Checkpoint during Cytochrome c Oxidase Assembly', *Cell Reports*. doi: 10.1016/j.celrep.2015.08.009.

Dennerlein, S. and Rehling, P. (2015) 'Human mitochondrial COX1 assembly into cytochrome c oxidase at a glance', *Journal of Cell Science*. doi: 10.1242/jcs.161729.

Denton, M. and Martin, B. R. (1972) 'Stimulation by calcium-ions of pyruvate dehydrogenase phosphate phosphatase', *Biochemical Journal*, 128, pp. 161–163.

Denton, R. M. (2009) ‘Regulation of mitochondrial dehydrogenases by calcium ions’, *Biochimica et Biophysica Acta*. Elsevier B.V., 1787, pp. 1309–1316. doi: 10.1016/j.bbabio.2009.01.005.

Diaz, F. *et al.* (2005) ‘Mice lacking COX10 in skeletal muscle recapitulate the phenotype of progressive mitochondrial myopathies associated with cytochrome c oxidase deficiency’, *Human Molecular Genetics*, 14(18), pp. 2737–2748. doi: 10.1093/hmg/ddi307.

Diaz, F. (2010) ‘Cytochrome c oxidase deficiency: Patients and animal models’, *Biochimica et Biophysica Acta - Molecular Basis of Disease*. Elsevier B.V., 1802(1), pp. 100–110. doi: 10.1016/j.bbadis.2009.07.013.

Dogan, S. A. *et al.* (2018) ‘Perturbed Redox Signaling Exacerbates a Article Perturbed Redox Signaling Exacerbates a Mitochondrial Myopathy’, pp. 1–12. doi: 10.1016/j.cmet.2018.07.012.

Dolezal, P. *et al.* (2006) ‘Evolution of the Molecular Machines for Protein Import into Mitochondria’, 313(July), pp. 314–319.

Dudkina, N. V. *et al.* (2005) ‘Structure of a mitochondrial supercomplex formed by respiratory-chain complexes I and III’, *Proceedings of the National Academy of Sciences*, 102(9), pp. 3225–3229. doi: 10.1073/pnas.0408870102.

Dunning, C. J. R. *et al.* (2007) ‘Human CIA30 is involved in the early assembly of mitochondrial complex I and mutations in its gene cause disease’, *EMBO Journal*, 26(13), pp. 3227–3237. doi: 10.1038/sj.emboj.7601748.

Durcan, T. M. *et al.* (2014) ‘USP8 regulates mitophagy by removing K6-linked ubiquitin conjugates from parkin’, *The EMBO Journal*, 33(21), pp. 2473–2491. doi: 10.15252/embj.201489729.

Dwight, T. *et al.* (2017) ‘Analysis of SDHAF3 in familial and sporadic pheochromocytoma and paraganglioma’, *BMC Cancer*, 17(1), pp. 1–12. doi: 10.1186/s12885-017-3486-z.

Efremov, R. G., Baradaran, R. and Sazanov, L. A. (2010) ‘The architecture of respiratory complex I’, *Nature*. Nature Publishing Group, 465(7297), pp. 441–445. doi: 10.1038/nature09066.

El-khoury, R. *et al.* (2010) 'Genetic background influences mitochondrial function : modeling mitochondrial disease for therapeutic development', *Trends in Molecular Medicine*. Elsevier Ltd, 16(5), pp. 210–217. doi: 10.1016/j.molmed.2010.03.001.

Enns, G. M. (2014) 'Treatment of Mitochondrial Disorders : Antioxidants and Beyond', 29(9), pp. 1235–1240. doi: 10.1177/0883073814538509.

Ernster, L. and Schatz, G. (1981) 'Mitochondria : A Historical Review', 91(December).

Falkenberg, M. (2018) 'Mitochondrial DNA replication in mammalian cells: overview of the pathway.', *Essays in biochemistry*, 62(3), pp. 287–296. doi: 10.1042/EBC20170100.

Fang, J. *et al.* (2007) 'Site Specific Phosphorylation of Cytochrome c Oxidase Subunits I, IVi1 and Vb in Rabbit Hearts Subjected to Ischemia/Reperfusion', *FEBS Lett*, 581(7), pp. 1302–1310.

Fassone, E. *et al.* (2010) 'FOXRED1, encoding an FAD-dependent oxidoreductase complex-I-specific molecular chaperone, is mutated in infantile-onset mitochondrial encephalopathy', *Human Molecular Genetics*, 19(24), pp. 4837–4847. doi: 10.1093/hmg/ddq414.

Felici, R. *et al.* (2017) 'Post onset , oral rapamycin treatment delays development of mitochondrial encephalopathy only at supramaximal doses', *Neuropharmacology*. Elsevier Ltd, 117, pp. 74–84. doi: 10.1016/j.neuropharm.2017.01.039.

Fernandez-vizarra, E. *et al.* (2018) 'Mitochondrial complex III Rieske Fe-S protein processing and assembly Mitochondrial complex III Rieske Fe-S protein processing and assembly', *Cell Cycle*. Taylor & Francis, 0(0), pp. 1–7. doi: 10.1080/15384101.2017.1417707.

Fernandez-Vizarra, E. *et al.* (2007) 'Impaired complex III assembly associated with BCS1L gene mutations in isolated mitochondrial encephalopathy', *Human Molecular Genetics*, 16(10), pp. 1241–1252. doi: 10.1093/hmg/ddm072.

Fernández-Vizarra, E., Tiranti, V. and Zeviani, M. (2009) 'Assembly of the

oxidative phosphorylation system in humans: What we have learned by studying its defects', *Biochimica et Biophysica Acta - Molecular Cell Research*. doi: 10.1016/j.bbamcr.2008.05.028.

Fernández-Vizarra, E. and Zeviani, M. (2015) 'Nuclear gene mutations as the cause of mitochondrial complex III deficiency', *Frontiers in Genetics*, 6(APR), pp. 1–11. doi: 10.3389/fgene.2015.00134.

Ferramosca, A. and Zara, V. (2013) 'Biogenesis of mitochondrial carrier proteins: Molecular mechanisms of import into mitochondria', *Biochimica et Biophysica Acta - Molecular Cell Research*. Elsevier B.V., 1833(3), pp. 494–502. doi: 10.1016/j.bbamcr.2012.11.014.

Finley, D. (2009) 'Recognition and Processing of Ubiquitin-Protein Conjugates by the Proteasome Daniel', *Annu Rev Biochem*, 78, pp. 477–513. doi: 10.1016/j.pmrj.2014.02.014.Lumbar.

Finsterer, J. and Zarrouk-Mahjoub, S. (2018) 'Biomarkers for Detecting Mitochondrial Disorders', *Journal of Clinical Medicine*, 7(2), p. 16. doi: 10.3390/jcm7020016.

Flescher, S., Klouwen, H. and Brierley, G. (1961) 'Studies of the Electron Transfer System', *The Journal of biological chemistry*, 236(11).

Follman, K. *et al.* (1998) 'CYTOCHROME C OXIDASE FROM EUCARYOTES BUT NOT FROM PROCARYOTES IS ALLOSTERICALLY INHIBITED BY ATP', *Biochemistry and molecular biology international*, 4(5), pp. 1047–1055.

Fontanesi, F. *et al.* (2006) 'Assembly of mitochondrial cytochrome *c* -oxidase, a complicated and highly regulated cellular process', *American Journal of Physiology-Cell Physiology*, 291(6), pp. C1129–C1147. doi: 10.1152/ajpcell.00233.2006.

Fontanesi, F., Soto, I. C. and Barrientos, A. (2008) 'Cytochrome c oxidase biogenesis: New levels of regulation', *IUBMB Life*, 60(9), pp. 557–568. doi: 10.1002/iub.86.

Formosa, L. E. *et al.* (2015) 'Characterization of mitochondrial FOXRED1 in the assembly of respiratory chain complex I', *Human Molecular Genetics*, 24(10), pp.

2952–2965. doi: 10.1093/hmg/ddv058.

Formosa, L. E. *et al.* (2017) 'Building a complex complex: Assembly of mitochondrial respiratory chain complex I', *Seminars in Cell and Developmental Biology*. Elsevier Ltd. doi: 10.1016/j.semcdb.2017.08.011.

Frangini, M. *et al.* (2013) 'Synthesis of Mitochondrial DNA Precursors during Myogenesis , an Analysis in Purified C2C12 Myotubes * □', 288(8), pp. 5624–5635. doi: 10.1074/jbc.M112.441147.

Frazier, A. E. *et al.* (2006) 'Mitochondrial morphology and distribution in mammalian cells', 387(December), pp. 1551–1558. doi: 10.1515/BC.2006.193.

Friedlander, R. *et al.* (2000) 'A regulatory link between ER-associated protein degradation and the unfolded-protein response', *Nature Cell Biology*, 2(7), pp. 379–384. doi: 10.1038/35017001.

Fujikawa, M. *et al.* (2015) 'Assembly of human mitochondrial ATP synthase through two separate intermediates, F1-c-ring and b-e-g complex', *FEBS Letters*. Federation of European Biochemical Societies, 589(19), pp. 2707–2712. doi: 10.1016/j.febslet.2015.08.006.

Fukuda, R. *et al.* (2007) 'HIF-1 Regulates Cytochrome Oxidase Subunits to Optimize Efficiency of Respiration in Hypoxic Cells', *Cell*, 129(1), pp. 111–122. doi: 10.1016/j.cell.2007.01.047.

Galluzzi, L. *et al.* (2018) 'Molecular mechanisms of cell death: Recommendations of the Nomenclature Committee on Cell Death 2018', *Cell Death and Differentiation*, 25(3), pp. 486–541. doi: 10.1038/s41418-017-0012-4.

Gammage, P. A. *et al.* (no date) 'Genome editing in mitochondria corrects a pathogenic mtDNA mutation in vivo', *Nature Medicine*. Springer US. doi: 10.1038/s41591-018-0165-9.

Garone, C. *et al.* (2014) 'Deoxypyrimidine monophosphate bypass therapy for thymidine kinase 2 deficiency', 6(8), pp. 1016–1027.

Garone, C. and Viscomi, C. (2018) 'Towards a therapy for mitochondrial disease :

an update', 0(September), pp. 1–15.

Gauss, R. *et al.* (2006) 'A complex of Yos9p and the HRD ligase integrates endoplasmic reticulum quality control into the degradation machinery', *Nature Cell Biology*, 8(8), pp. 849–854. doi: 10.1038/ncb1445.

Gellerich, F. N. *et al.* (2010) 'The regulation of OXPHOS by extramitochondrial calcium', *Biochimica et Biophysica Acta - Bioenergetics*, 1797(6–7), pp. 1018–1027. doi: 10.1016/j.bbabio.2010.02.005.

Ghezzi, D. *et al.* (2009) 'SDHAF1, encoding a LYR complex-II specific assembly factor, is mutated in SDH-defective infantile leukoencephalopathy', *Nature Genetics*, 41(6), pp. 654–656. doi: 10.1038/ng.378.

Ghezzi, D. *et al.* (2011) 'Mutations in TTC19 cause mitochondrial complex III deficiency and neurological impairment in humans and flies', *Nature Genetics*, 43(3), pp. 259–263. doi: 10.1038/ng.761.

Ghezzi, D. and Zeviani, M. (2018) 'Human diseases associated with defects in assembly of OXPHOS complexes.', *Essays in biochemistry*, 62(3), pp. 271–286. doi: 10.1042/EBC20170099.

Ghosh, A. *et al.* (2016) 'Mitochondrial disease genes COA6, COX6B and SCO2 have overlapping roles in COX2 biogenesis', *Human molecular genetics*, 25(4), pp. 660–671. doi: 10.1093/hmg/ddv503.

Gladyshev, V. N. (2014) 'The Free Radical Theory of Aging Is Dead. Long Live the Damage Theory!', *Antioxidants & Redox Signaling*, 20(4), pp. 727–731. doi: 10.1089/ars.2013.5228.

Glerum, M., Shtanko, A. and Tzagoloff, A. (1996) 'Characterization of COX17, a yeast gene involved in copper metabolism and assembly of cytochrome oxidase', *Journal of Biological Chemistry*, 271(24), pp. 14504–14509. doi: 10.1074/jbc.271.24.14504.

Gorman, G. S. *et al.* (2016) 'Mitochondrial diseases', *Nature Reviews Disease Primers*. Macmillan Publishers Limited, 2, pp. 1–23. doi: 10.1038/nrdp.2016.80.

Gray, M. W. *et al.* (2012) 'Mitochondrial Evolution', *Cold Spring Harb Perspect Biol.*, 4(9), p. a011403. doi: 10.1101/cshperspect.a011403.

Grivennikova, V. G., Kozlovsky, V. S. and Vinogradov, A. D. (2017) 'Respiratory complex II: ROS production and the kinetics of ubiquinone reduction', *Biochimica et Biophysica Acta - Bioenergetics*. Elsevier B.V., 1858(2), pp. 109–117. doi: 10.1016/j.bbabio.2016.10.008.

Gruschke, S. *et al.* (2011) 'Cbp3-Cbp6 interacts with the yeast mitochondrial ribosomal tunnel exit and promotes cytochrome b synthesis and assembly', *Journal of Cell Biology*, 193(6), pp. 1101–1114. doi: 10.1083/jcb.201103132.

Gruschke, S. *et al.* (2012) 'The Cbp3-Cbp6 complex coordinates cytochrome b synthesis with bc1 complex assembly in yeast mitochondria', *Journal of Cell Biology*, 199(1), pp. 137–150. doi: 10.1083/jcb.201206040.

Gu, J. *et al.* (2016) 'The architecture of the mammalian respirasome', *Nature*. Nature Publishing Group, 537(7622), pp. 639–643. doi: 10.1038/nature19359.

Guarani, V. *et al.* (2014) 'TIMMDC1/C3orf1 Functions as a Membrane-Embedded Mitochondrial Complex I Assembly Factor through Association with the MCIA Complex', *Molecular and Cellular Biology*, 34(5), pp. 847–861. doi: 10.1128/MCB.01551-13.

Guda, P., Guda, C. and Subramaniam, S. (2007) 'Reconstruction of Pathways Associated with Amino Acid Metabolism in Human Mitochondria', *Genomics Proteomics & Bioinformatics*. Beijing Institute of Genomics, 5(3–4), pp. 166–176. doi: 10.1016/S1672-0229(08)60004-2.

Guerrero-Castillo, S. *et al.* (2017) 'The Assembly Pathway of Mitochondrial Respiratory Chain Complex I', *Cell Metabolism*. Elsevier Inc., 25(1), pp. 128–139. doi: 10.1016/j.cmet.2016.09.002.

Guo, R. *et al.* (2017) 'Architecture of Human Mitochondrial Respiratory Megacomplex I2III2IV2', *Cell*. Elsevier Inc., 170(6), p. 1247–1257.e12. doi: 10.1016/j.cell.2017.07.050.

Haack, T. B. *et al.* (2010) 'Exome sequencing identifies ACAD9 mutations as a cause of complex i deficiency', *Nature Genetics*. Nature Publishing Group,

42(12), pp. 1131–1134. doi: 10.1038/ng.706.

Halestrap, A. P. (2009) 'What is the mitochondrial permeability transition pore?', *Journal of Molecular and Cellular Cardiology*. Elsevier Inc., 46(6), pp. 821–831. doi: 10.1016/j.yjmcc.2009.02.021.

Hallmann, K. *et al.* (2016) 'Loss of the smallest subunit of cytochrome c oxidase, COX8A, causes Leigh-like syndrome and epilepsy', *Brain*, 139(2), pp. 338–345. doi: 10.1093/brain/awv357.

Hao, H. *et al.* (2009) 'SDH5, a Gene Required for Flavination of Succinate Dehydrogenase, Is Mutated in Paraganglioma', *Science*, 325(August), pp. 1139–1142.

Harman, D. (1956) 'Aging : a Theory Based on Free Radical and Radiation Chemistry', *J Gerontol*, 11, pp. 298–300.

Häussinger, D. (1990) 'Nitrogen metabolism in liver: structural and functional organization and physiological relevance', *Biochemical Journal*, 267(2), pp. 281–290. doi: 10.1042/bj2670281.

Haut, S. *et al.* (2003) 'A deletion in the human QP-C gene causes a complex III deficiency resulting in hypoglycaemia and lactic acidosis.', *Human genetics*, 113(2), pp. 118–122. doi: 10.1007/s00439-003-0946-0.

Hayashi, T. *et al.* (2015) '*Higd1a* is a positive regulator of cytochrome *c* oxidase', *Proceedings of the National Academy of Sciences*, 112(5), pp. 1553–1558. doi: 10.1073/pnas.1419767112.

Haynes, C. M. *et al.* (2007) 'ClpP Mediates Activation of a Mitochondrial Unfolded Protein Response in C. elegans', *Developmental Cell*, 13(4), pp. 467–480. doi: 10.1016/j.devcel.2007.07.016.

He, J., Carroll, J., *et al.* (2017) 'Permeability transition in human mitochondria persists in the absence of peripheral stalk subunits of ATP synthase', *Proceedings of the National Academy of Sciences*, 114(34), pp. 9086–9091. doi: 10.1073/pnas.1711201114.

He, J., Ford, H. C., *et al.* (2017) ‘Persistence of the mitochondrial permeability transition in the absence of subunit c of human ATP synthase’, *Proceedings of the National Academy of Sciences*, 114(13), pp. 3409–3414. doi: 10.1073/pnas.1702357114.

He, J. *et al.* (2018) ‘Assembly of the membrane domain of ATP synthase in human mitochondria’, *Proceedings of the National Academy of Sciences*, p. 201722086. doi: 10.1073/pnas.1722086115.

Heide, H. *et al.* (2012) ‘Complexome profiling identifies TMEM126B as a component of the mitochondrial complex i assembly complex’, *Cell Metabolism*, 16(4), pp. 538–549. doi: 10.1016/j.cmet.2012.08.009.

Hejzlarová, K. *et al.* (2014) ‘Nuclear genetic defects of mitochondrial ATP synthase.’, *Physiological research / Academia Scientiarum Bohemoslovaca*, 63 Suppl 1(1995), pp. S57-71. Available at: http://www.ncbi.nlm.nih.gov/pubmed/24564666.

Hemion, C., Flammer, J. and Neutzner, A. (2014) ‘Quality control of oxidatively damaged mitochondrial proteins is mediated by p97 and the proteasome’, *Free Radical Biology and Medicine*. Elsevier, 75, pp. 121–128. doi: 10.1016/j.freeradbiomed.2014.07.016.

Henson, J., Tischler, G. and Ning, Z. (2014) ‘Europe PMC Funders Group Next-generation sequencing and large genome assemblies’, 13(8), pp. 901–915. doi: 10.2217/pgs.12.72.Next-generation.

Herbert, M. and Turnbull, D. (2018) ‘Progress in mitochondrial replacement therapies’, *Nature Publishing Group*. Nature Publishing Group, 19(2), pp. 71–72. doi: 10.1038/nrm.2018.3.

Herrmann, J. M. and Riemer, J. (2012) ‘Mitochondrial disulfide relay: Redox-regulated protein import into the intermembrane space’, *Journal of Biological Chemistry*, 287(7), pp. 4426–4433. doi: 10.1074/jbc.R111.270678.

Hildenbeutel, M. *et al.* (2014) ‘Assembly factors monitor sequential hemylation of cytochrome b to regulate mitochondrial translation’, *Journal of Cell Biology*, 205(4), pp. 511–524. doi: 10.1083/jcb.201401009.

Hirst, J. and Roessler, M. M. (2016) ‘Energy conversion, redox catalysis and generation of reactive oxygen species by respiratory complex i’, *Biochimica et Biophysica Acta - Bioenergetics*. The Authors, 1857(7), pp. 872–883. doi: 10.1016/j.bbabio.2015.12.009.

Hiser, L. *et al.* (2000) ‘Cox11p is required for stable formation of the Cu(B) and magnesium centers of cytochrome c oxidase’, *Journal of Biological Chemistry*, 275(1), pp. 619–623. doi: 10.1074/jbc.275.1.619.

Holmström, K. M. and Finkel, T. (2014) ‘Cellular mechanisms and physiological consequences of redox-dependent signalling’, *Nature Reviews Molecular Cell Biology*. Nature Publishing Group, 15(6), pp. 411–421. doi: 10.1038/nrm3801.

Horvath, R. *et al.* (2005) ‘Mutations in mtDNA-encoded cytochrome c oxidase subunit genes causing isolated myopathy or severe encephalomyopathy’, *Neuromuscular Disorders*, 15, pp. 851–857. doi: 10.1016/j.nmd.2005.09.005.

Houtkooper, R. H. and Vaz, F. M. (2008) ‘Cardiolipin, the heart of mitochondrial metabolism’, *Cellular and Molecular Life Sciences*, 65(16), pp. 2493–2506. doi: 10.1007/s00018-008-8030-5.

Hüttemann, M. *et al.* (2007) ‘Regulation of mitochondrial oxidative phosphorylation through cell signaling’, *Biochimica et Biophysica Acta - Molecular Cell Research*, 1773(12), pp. 1701–1720. doi: 10.1016/j.bbamcr.2007.10.001.

Hüttemann, M. *et al.* (2012) ‘Cytochrome c oxidase subunit 4 isoform 2-knockout mice show reduced enzyme activity, airway hyporeactivity, and lung pathology’, *FASEB J*, 26(9), pp. 3916–3930.

Hüttemann, M., Kadenbach, B. and Grossman, L. I. (2001) ‘Mammalian subunit IV isoforms of cytochrome c oxidase’, *Gene*, 267(1), pp. 111–123. doi: 10.1016/S0378-1119(01)00385-7.

Indrieri, A. *et al.* (2012) ‘Mutations in COX7B cause microphthalmia with linear skin lesions, an unconventional mitochondrial disease’, *American Journal of Human Genetics*. The American Society of Human Genetics, 91(5), pp. 942–949. doi: 10.1016/j.ajhg.2012.09.016.

Itakura, E. *et al.* (2016) 'Ubiquilins Chaperone and Triage Mitochondrial Membrane Proteins for Degradation', *Molecular Cell*. MRC Laboratory of Molecular Biology, 63(1), pp. 21–33. doi: 10.1016/j.molcel.2016.05.020.

Iwata, S. *et al.* (1998) 'Complete structure of the 11-subunit bovine mitochondrial cytochrome bc1complex', *Science*, 281(5373), pp. 64–71. doi: 10.1126/science.281.5373.64.

Jacobs, H. T. (2003) 'Disorders of mitochondrial protein synthesis', *Human Molecular Genetics*, 12(suppl 2), pp. R293–R301. doi: 10.1093/hmg/ddg285.

Jonckheere, A. I., Smeitink, J. A. M. and Rodenburg, R. J. T. (2012) 'Mitochondrial ATP synthase: architecture, function and pathology', *Journal of Inherited Metabolic Disease*, 35(2), pp. 211–225. doi: 10.1007/s10545-011-9382-9.

Jovaisaite, V., Mouchiroud, L. and Auwerx, J. (2014) 'The mitochondrial unfolded protein response, a conserved stress response pathway with implications in health and disease', *Journal of Experimental Biology*, 217(1), pp. 137–143. doi: 10.1242/jeb.090738.

Kadenbach, B. (2017) 'Regulation of Mammalian 13-Subunit Cytochrome c Oxidase and Binding of other Proteins: Role of NDUFA4', *Trends in Endocrinology and Metabolism*. Elsevier Ltd, 28(11), pp. 761–770. doi: 10.1016/j.tem.2017.09.003.

Kadenbach, B. (2018) 'Regulation of mitochondrial respiration and ATP synthesis via cytochrome c oxidase', *Rendiconti Lincei*. Springer International Publishing, 29(2), pp. 421–435. doi: 10.1007/s12210-018-0710-y.

Kadenbach, B. and Arnold, S. (1999) 'A second mechanism of respiratory control', *FEBS Letters*, 447(2–3), pp. 131–134. doi: 10.1016/S0014-5793(99)00229-X.

Karbowski, M., Neutzner, A. and Youle, R. J. (2007) 'The mitochondrial E3 ubiquitin ligase MARCH5 is required for Drp1 dependent mitochondrial division', *Journal of Cell Biology*, 178(1), pp. 71–84. doi: 10.1083/jcb.200611064.

Khalimonchuk, O., Bird, A. and Winge, D. R. (2007) 'Evidence for a pro-oxidant

intermediate in the assembly of cytochrome oxidase', *Journal of Biological Chemistry*. doi: 10.1074/jbc.M702379200.

Khan, N. A. *et al.* (2014) 'Effective treatment of mitochondrial myopathy by nicotinamide riboside , a vitamin B 3', 6(6), pp. 721–731.

Kim, H. J. *et al.* (2012) 'Flavinylation and assembly of succinate dehydrogenase are dependent on the C-terminal tail of the flavoprotein subunit', *Journal of Biological Chemistry*, 287(48), pp. 40670–40679. doi: 10.1074/jbc.M112.405704.

Kim, H. J. *et al.* (2013) 'Structure, function, and assembly of heme centers in mitochondrial respiratory complexes Hyung', *Biochim Biophys Acta*, 1823(9), pp. 1604–1616. doi: 10.1016/j.bbamcr.2012.04.008.Structure.

Kirkinezos, I. G. and Moraes, C. T. (2001) 'Reactive oxygen species and mitochondrial diseases', *Seminars in Cell and Developmental Biology*, 12(6), pp. 449–457. doi: 10.1006/scdb.2001.0282.

Klement, P. *et al.* (1995) 'Analysis of oxidative phosphorylation complexes in cultured human fibroblasts and amniocytes by blue-native-electrophoresis using mitoplasts isolated with the help of digitonin', *Analytical Biochemistry*. doi: 10.1006/abio.1995.1523.

Klingenberg, M. (2008) 'The ADP and ATP transport in mitochondria and its carrier', *Biochimica et Biophysica Acta*, 1778, pp. 1978–2021. doi: 10.1016/j.bbamem.2008.04.011.

Kobayashi, M. and Yamamoto, M. (2006) 'Nrf2-Keap1 regulation of cellular defense mechanisms against electrophiles and reactive oxygen species', *Advances in Enzyme Regulation*, 46(1), pp. 113–140. doi: 10.1016/j.advenzreg.2006.01.007.

Kocaturk, N. M. and Gozuacik, D. (2018) 'Crosstalk Between Mammalian Autophagy and the Ubiquitin-Proteasome System', *Frontiers in Cell and Developmental Biology*, 6(October), pp. 1–27. doi: 10.3389/fcell.2018.00128.

Koopman, W. J. H. *et al.* (2012) 'OXPHOS mutations and neurodegeneration', *The EMBO Journal*. Nature Publishing Group, 32(1), pp. 9–29. doi: 10.1038/emboj.2012.300.

Kowalski, L. *et al.* (2018) 'Determinants of the cytosolic turnover of mitochondrial intermembrane space proteins', *BMC Biology*. BMC Biology, 16(1), pp. 1–22. doi: 10.1186/s12915-018-0536-1.

Kubbutat, M. H. G., Jones, S. N. and Vousden, K. H. (1997) 'Regulation of p53 stability by Mdm2', *Nature*, 387(6630), pp. 299–303.

Kukat, C. *et al.* (2011) 'Super-resolution microscopy reveals that mammalian mitochondrial nucleoids have a uniform size and frequently contain a single copy of mtDNA'. doi: 10.1073/pnas.1109263108/-/DCSupplemental.www.pnas.org/cgi/doi/10.1073/pnas.1109263108.

Lane, D. J. R. *et al.* (2015) 'Cellular iron uptake, trafficking and metabolism: Key molecules and mechanisms and their roles in disease', *Biochimica et Biophysica Acta - Molecular Cell Research*. Elsevier B.V., 1853(5), pp. 1130–1144. doi: 10.1016/j.bbamcr.2015.01.021.

Lane, N. and Martin, W. (2010) 'The energetics of genome complexity', *Nature*. Nature Publishing Group, 467(7318), pp. 929–934. doi: 10.1038/nature09486.

Lapuente-Brun, E. *et al.* (2013) 'Supercomplex assembly determines electron flux in the mitochondrial electron transport chain', *Science*, 340(6140), pp. 1567–1570. doi: 10.1126/science.1230381.

Lavie, J. *et al.* (2018) 'Ubiquitin-Dependent Degradation of Mitochondrial Proteins Regulates Energy Metabolism', *Cell Reports*, 23(10), pp. 2852–2863. doi: 10.1016/j.celrep.2018.05.013.

Lazarou, M. *et al.* (2007) 'Analysis of the Assembly Profiles for Mitochondrial- and Nuclear-DNA-Encoded Subunits into Complex I', *Molecular and Cellular Biology*, 27(12), pp. 4228–4237. doi: 10.1128/MCB.00074-07.

Leary, S. C. *et al.* (2004) 'Human SCO1 and SCO2 have independent, cooperative functions in copper delivery to cytochrome c oxidase', *Human Molecular Genetics*, 13(17), pp. 1839–1848. doi: 10.1093/hmg/ddh197.

Leary, S. C. *et al.* (2007) 'The Human Cytochrome c Oxidase Assembly Factors SCO1 and SCO2 Have Regulatory Roles in the Maintenance of Cellular Copper Homeostasis', *Cell Metabolism*, 5(1), pp. 9–20. doi: 10.1016/j.cmet.2006.12.001.

Leary, S. C. *et al.* (2009) 'Human SCO2 is required for the synthesis of CO II and as a thiol-disulphide oxidoreductase for SCO1', *Human Molecular Genetics*, 18(12), pp. 2230–2240. doi: 10.1093/hmg/ddp158.

Lee, H. M. *et al.* (2000) 'Mutations in the putative H-channel in the cytochrome c oxidase from Rhodobacter sphaeroides show that this channel is not important for proton conduction but reveal modulation of the properties of heme a', *Biochemistry*, 39(11), pp. 2989–2996. doi: 10.1021/bi9924821.

Lee, J., Giordano, S. and Zhang, J. (2012) 'Autophagy, mitochondria and oxidative stress: cross-talk and redox signalling', *Biochem. J.*, 441(10), pp. 523–540. doi: 10.1042/BJ20111451.

Lejay, A. *et al.* (2007) 'Skeletal Muscle Mitochondrial Function in Peripheral Arterial Disease : Usefulness of Muscle Biopsy', (Figure 1).

Lemarie, A. and Grimm, S. (2009) 'Mutations in the heme b-binding residue of SDHC inhibit assembly of respiratory chain complex II in mammalian cells', *Mitochondrion*. Mitochondria Research Society, 9(4), pp. 254–260. doi: 10.1016/j.mito.2009.03.004.

Letts, J. A., Fiedorczuk, K. and Sazanov, L. A. (2016) 'The architecture of respiratory supercomplexes', *Nature*. Nature Publishing Group, 537(7622), pp. 644–648. doi: 10.1038/nature19774.

Letts, J. A. and Sazanov, L. A. (2017) 'Clarifying the supercomplex: The higher-order organization of the mitochondrial electron transport chain', *Nature Structural and Molecular Biology*, 24(10), pp. 800–808. doi: 10.1038/nsmb.3460.

Liko, I. *et al.* (2016) 'Dimer interface of bovine cytochrome *c* oxidase is influenced by local posttranslational modifications and lipid binding', *Proceedings of the National Academy of Sciences*, 113(29), pp. 8230–8235. doi: 10.1073/pnas.1600354113.

Lim, S. C. *et al.* (2014) 'A founder mutation in PET100 causes isolated complex IV deficiency in lebanese individuals with Leigh syndrome', *American Journal of Human Genetics*. doi: 10.1016/j.ajhg.2013.12.015.

De Lonlay, P. *et al.* (2001) 'A mutant mitochondrial respiratory chain assembly

protein causes complex III deficiency in patients with tubulopathy, encephalopathy and liver failure', *Nature Genetics*, 29(1), pp. 57–60. doi: 10.1038/ng706.

Lopez-Fabuel, I. *et al.* (2016) 'Complex I assembly into supercomplexes determines differential mitochondrial ROS production in neurons and astrocytes', *Proceedings of the National Academy of Sciences*, 113(46), pp. 13063–13068. doi: 10.1073/pnas.1613701113.

Lu, J. and Gunner, M. R. (2014) 'Characterizing the proton loading site in cytochrome c oxidase', *Proceedings of the National Academy of Sciences*, 111(34), pp. 12414–12419. doi: 10.1073/pnas.1407187111.

Lundin, C. R. *et al.* (2016) 'Regulatory role of the respiratory supercomplex factors in Saccharomyces cerevisiae', *Proceedings of the National Academy of Sciences*, 113(31), pp. E4476–E4485. doi: 10.1073/pnas.1601196113.

Magner, M. *et al.* (2015) 'TMEM70 deficiency: long-term outcome of 48 patients', *Journal of Inherited Metabolic Disease*, 38(3), pp. 417–426. doi: 10.1007/s10545-014-9774-8.

Mahapatra, G. *et al.* (2017) 'Phosphorylation of cytochrome c threonine 28 regulates electron transport chain activity in kidney: Implications for amp kinase', *Journal of Biological Chemistry*, 292(1), pp. 64–79. doi: 10.1074/jbc.M116.744664.

Mahaseth, T. and Kuzminov, A. (2018) 'Potentiation of Hydrogen Peroxide Toxicity', pp. 274–281. doi: 10.1016/j.mrrev.2016.08.006.Potentiation.

Maio, N. *et al.* (2014) 'Cochaperone binding to LYR motifs confers specificity of iron sulfur cluster delivery', *Cell Metabolism*. Elsevier Inc., 19(3), pp. 445–457. doi: 10.1016/j.cmet.2014.01.015.

Maio, N. *et al.* (2016) 'Disease-causing SDHAF1 mutations impair transfer of Fe-S clusters to SDHB', *Cell Metabolism*. Elsevier, 23(2), pp. 292–302. doi: 10.1016/j.cmet.2015.12.005.

Maio, N. *et al.* (2017) 'A Single Adaptable Cochaperone-Scaffold Complex Delivers Nascent Iron-Sulfur Clusters to Mammalian Respiratory Chain

Complexes I–III', *Cell Metabolism*. Elsevier Inc., 25(4), p. 945–953.e6. doi: 10.1016/j.cmet.2017.03.010.

Manfredi, G. *et al.* (1995) 'A NEW MUTATION ASSOCIATED WITH MELAS IS LOCATED IN A', 5(5).

Maranzana, E. *et al.* (2013) 'Mitochondrial Respiratory Supercomplex Association Limits Production of Reactive Oxygen Species from Complex I', *Antioxidants & Redox Signaling*, 19(13). doi: 10.1089/ars.2012.4845.

Margineantu, D. H. *et al.* (2007) 'Hsp90 inhibition decreases mitochondrial protein turnover', *PLoS ONE*, 2(10). doi: 10.1371/journal.pone.0001066.

Martínez-reyes, I. *et al.* (2017) 'TCA cycle and mitochondrial membrane potential are necessary for diverse biological functions Inmaculada', 61(2), pp. 199–209. doi: 10.1016/j.molcel.2015.12.002.TCA.

Massa, V. *et al.* (2008) 'Severe Infantile Encephalomyopathy Caused by a Mutation in COX6B1, a Nucleus-Encoded Subunit of Cytochrome C Oxidase', *American Journal of Human Genetics*, 82(6), pp. 1281–1289. doi: 10.1016/j.ajhg.2008.05.002.

Matsushima, Y. and Kaguni, L. S. (2012) 'Matrix proteases in mitochondrial DNA function', *Biochim Biophys Acta*, 1819((9-10)), pp. 1080–1087. doi: 10.1016/j.immuni.2010.12.017.Two-stage.

McEwen, J. E. *et al.* (1993) 'Sequence and chromosomal localization of two PET genes required for cytochrome c oxidase assembly in Saccharomyces cerevisiae', *Current Genetics*, 23(1), pp. 9–14. doi: 10.1007/BF00336742.

McKenzie, M. *et al.* (2011) 'Mutations in the gene encoding C8orf38 block complex i assembly by inhibiting production of the mitochondria-encoded subunit ND1', *Journal of Molecular Biology*. Elsevier Ltd, 414(3), pp. 413–426. doi: 10.1016/j.jmb.2011.10.012.

De Meirleir, L. *et al.* (2004) 'Respiratory chain complex V deficiency due to a mutation in the assembly gene ATP12', *Journal of Medical Genetics*, 41(2), pp. 120–124. doi: 10.1136/jmg.2003.012047.

Melchionda, L. *et al.* (2014) ‘Mutations in APOPT1, encoding a mitochondrial protein, cause cavitating leukoencephalopathy with cytochrome c oxidase deficiency’, *American Journal of Human Genetics*. doi: 10.1016/j.ajhg.2014.08.003.

Mendell, J. R. *et al.* (2017) ‘Single-Dose Gene-Replacement Therapy for Spinal Muscular Atrophy’, *The new england journal of medicine*, pp. 1713–1722. doi: 10.1056/NEJMoa1706198.

Meng, T. C., Fukada, T. and Tonks, N. K. (2002) ‘Reversible oxidation and inactivation of protein tyrosine phosphatases in vivo’, *Molecular Cell*, 9(2), pp. 387–399. doi: 10.1016/S1097-2765(02)00445-8.

Meo, I. Di *et al.* (2017) ‘AAV9-based gene therapy partially ameliorates the clinical phenotype of a mouse model of Leigh syndrome’, *Nature Publishing Group*. Nature Publishing Group, 24(10), pp. 661–667. doi: 10.1038/gt.2017.53.

Di Meo, I., Lamperti, C. and Tiranti, V. (2015) ‘Mitochondrial diseases caused by toxic compound accumulation: from etiopathology to therapeutic approaches’, *EMBO Molecular Medicine*, 7(10), pp. 1257–1266. doi: 10.15252/emmm.201505040.

Michel, H. (1998) ‘The mechanism of proton pumping by cytochrome c oxidasex127e [comments].’, *Proceedings of the National Academy of Sciences of the United States of America*, 95(22), pp. 12819–24. doi: 10.1073/pnas.95.22.12819.

Mick, D. U. *et al.* (2012) ‘MITRAC links mitochondrial protein translocation to respiratory-chain assembly and translational regulation’, *Cell*. Elsevier Inc., 151(7), pp. 1528–1541. doi: 10.1016/j.cell.2012.11.053.

Milenkovic, D. *et al.* (2017) ‘The Enigma of the Respiratory Chain Supercomplex’, *Cell Metabolism*, 25(4), pp. 765–776. doi: 10.1016/j.cmet.2017.03.009.

Miller, W. L. (2013) ‘Steroid hormone synthesis in mitochondria’, *Molecular and Cellular Endocrinology*. Elsevier Ireland Ltd, 379(1–2), pp. 62–73. doi: 10.1016/j.mce.2013.04.014.

Mills, E. L. *et al.* (2016) ‘Repurposing mitochondria from ATP production to ROS

generation drives a pro-inflammatory phenotype in macrophages that depends on succinate oxidation by complex II', 167(2), pp. 457–470. doi: 10.1016/j.cell.2016.08.064.Repurposing.

Mimaki, M. *et al.* (2012) 'Understanding mitochondrial complex I assembly in health and disease', *Biochimica et Biophysica Acta - Bioenergetics*. Elsevier B.V., 1817(6), pp. 851–862. doi: 10.1016/j.bbabio.2011.08.010.

Mootha, V. K. *et al.* (2003) 'Identification of a gene causing human cytochrome c oxidase deficiency by integrative genomics', *Proc Natl Acad Sci USA*, 100(2), pp. 605–610. Available at: http://www.ncbi.nlm.nih.gov/entrez/query.fcgi?cmd=Retrieve&db=PubMed&dopt=Citation&list_uids=12529507.

Moreno-Lastres, D. *et al.* (2012) 'Mitochondrial complex I plays an essential role in human respirasome assembly', *Cell Metabolism*, 15(3), pp. 324–335. doi: 10.1016/j.cmet.2012.01.015.

Morris, S. M. (2002) 'Regulation of enzymes of the urea cycle and arginine metabolism', *Annual Review of Nutrition*, 22(1), pp. 87–105. doi: 10.1146/annurev.nutr.22.110801.140547.

Mourier, A. *et al.* (2014) 'The respiratory Chain supercomplex organization is independent of COX7A2L isoforms', *Cell Metabolism*, 20(6), pp. 1069–1075. doi: 10.1016/j.cmet.2014.11.005.

Muller, F. L., Liu, Y. and Van Remmen, H. (2004) 'Complex III releases superoxide to both sides of the inner mitochondrial membrane', *Journal of Biological Chemistry*, 279(47), pp. 49064–49073. doi: 10.1074/jbc.M407715200.

Murphy, M. P. (2009) 'How mitochondria produce reactive oxygen species', *Biochemical Journal*. doi: 10.1042/BJ20081386.

Na, U. *et al.* (2014) 'The LYR factors sdhaf1 and SDHAF3 mediate maturation of the iron-sulfur subunit of succinate dehydrogenase', *Cell Metabolism*, 20(2), pp. 253–266. doi: 10.1016/j.cmet.2014.05.014.

Nakamura, N. *et al.* (2006) 'MARCH-V is a novel mitofusin 2- and Drp1-binding protein able to change mitochondrial morphology', *EMBO Reports*, 7(10), pp.

1019–1022. doi: 10.1038/sj.embor.7400790.

Nicholls, D. G. (1974) ‘The Influence of Respiration and ATP Hydrolysis on the Proton-Electrochemical Gradient across the Inner Membrane of Rat-Liver Mitochondria as Determined by Ion Distribution’, 315, pp. 305–315.

Nightingale, H. *et al.* (2016) ‘Emerging therapies for mitochondrial disorders’, *Brain*, 139(6), pp. 1633–1648. doi: 10.1093/brain/aww081.

Nijtmans, L. G. *et al.* (1995) ‘Assembly of mitochondrial ATP synthase in cultured human cells: implications for mitochondrial diseases’, *Biochim Biophys Acta*, 1272(3), pp. 190–198. doi: 10.1016/0925-4439(95)00087-9.

Nijtmans, L. G. J. *et al.* (1998) ‘Assembly of cytochrome-c oxidase in cultured human cells’, *European Journal of Biochemistry*, 254(2), pp. 389–394. doi: 10.1046/j.1432-1327.1998.2540389.x.

Nissanka, N. and Moraes, C. T. (2018) ‘Mitochondrial DNA damage and reactive oxygen species in neurodegenerative disease’, *FEBS Letters*, 592(5), pp. 728–742. doi: 10.1002/1873-3468.12956.

Nouws, J. *et al.* (2010) ‘Acyl-CoA dehydrogenase 9 is required for the biogenesis of oxidative phosphorylation complex I’, *Cell Metabolism*, 12(3), pp. 283–294. doi: 10.1016/j.cmet.2010.08.002.

Nulton-Persson, A. C. and Szweda, L. I. (2001) ‘Modulation of Mitochondrial Function by Hydrogen Peroxide’, *Journal of Biological Chemistry*, 276(26), pp. 23357–23361. doi: 10.1074/jbc.M100320200.

Nunnari, J. R. F. and J. (2014) ‘Mitochondrial form and function’, *Nature.*, 505(1), pp. 1–23. doi: 10.1088/1367-2630/15/1/015008.Fluid.

Ogilvie, I., Kennaway, N. G. and Shoubridge, E. A. (2005) ‘A molecular chaperone for mitochondrial complex I assembly is mutated in a progressive encephalopathy’, *Journal of Clinical Investigation*, 115(10), pp. 2784–2792. doi: 10.1172/JCI26020.

Oláhová, M. *et al.* (2015) ‘A truncating PET100 variant causing fatal infantile lactic

acidosis and isolated cytochrome c oxidase deficiency', *European Journal of Human Genetics*, 23(7), pp. 935–939. doi: 10.1038/ejhg.2014.214.

Oyedotun, K. S. and Lemire, B. D. (2001) 'The Quinone-binding Sites of the Saccharomyces cerevisiae Succinate-ubiquinone Oxidoreductase', *Journal of Biological Chemistry*, 276(20), pp. 16936–16943. doi: 10.1074/jbc.M100184200.

Oyedotun, K. S., Sit, C. S. and Lemire, B. D. (2007) 'The Saccharomyces cerevisiae succinate dehydrogenase does not require heme for ubiquinone reduction', *Biochimica et Biophysica Acta - Bioenergetics*, 1767(12), pp. 1436–1445. doi: 10.1016/j.bbabio.2007.09.008.

Pacheu-Grau, D. *et al.* (2015) 'Cooperation between COA6 and SCO2 in COX2 maturation during cytochrome c oxidase assembly links two mitochondrial cardiomyopathies', *Cell Metabolism*, 21(6), pp. 823–833. doi: 10.1016/j.cmet.2015.04.012.

Pagliarini, D. J. *et al.* (2008) 'A Mitochondrial Protein Compendium Elucidates Complex I Disease Biology', *Cell*, 134(1), pp. 112–123. doi: 10.1016/j.cell.2008.06.016.

Palade, G. E. (1953) 'An electron microscope study of the mitochondrial structure', *The Anatomical Record*, 1(4), pp. 188–211.

Paradies, G. *et al.* (2014) 'Functional role of cardiolipin in mitochondrial bioenergetics', *Biochimica et Biophysica Acta - Bioenergetics*. Elsevier B.V., 1837(4), pp. 408–417. doi: 10.1016/j.bbabio.2013.10.006.

Paulsen, C. E. and Carroll, K. S. (2013) 'Cysteine-mediated redox signaling: Chemistry, biology, and tools for discovery', *Chemical Reviews*, 113(7), pp. 4633–4679. doi: 10.1021/cr300163e.

Peng, M. *et al.* (2015) 'Inhibiting cytosolic translation and autophagy improves health in mitochondrial disease', 24(17), pp. 4829–4847. doi: 10.1093/hmg/ddv207.

Peter, M. (1961) 'Coupling of phosphorylation to electron and hydrogen transfer by a chemi-osmotic type of mechanism'.

Pickart, C. M. and Eddins, M. J. (2004) 'Ubiquitin: Structures, functions, mechanisms', *Biochimica et Biophysica Acta - Molecular Cell Research*, 1695(1–3), pp. 55–72. doi: 10.1016/j.bbamcr.2004.09.019.

Pierrel, F. *et al.* (2007) 'Coa1 links the Mss51 post-translational function to Cox1 cofactor insertion in cytochrome c oxidase assembly', *EMBO Journal*, 26(20), pp. 4335–4346. doi: 10.1038/sj.emboj.7601861.

Pitceathly, R. D. S. *et al.* (2013) 'NDUFA4 Mutations Underlie Dysfunction of a Cytochrome c Oxidase Subunit Linked to Human Neurological Disease', *Cell Reports*. The Authors, 3(6), pp. 1795–1805. doi: 10.1016/j.celrep.2013.05.005.

Pitceathly, R. D. S. and Taanman, J.-W. (2018) 'NDUFA4 (Renamed COXFA4) Is a Cytochrome -c Oxidase Subunit', *Trends in Endocrinology & Metabolism*. Elsevier Ltd, 29(7), pp. 452–454. doi: 10.1016/j.tem.2018.03.009.

Pizzimenti, S. *et al.* (2013) 'Interaction of aldehydes derived from lipid peroxidation and membrane proteins', *Frontiers in Physiology*, 4 SEP(September), pp. 1–17. doi: 10.3389/fphys.2013.00242.

Pizzinat, N. *et al.* (1999) 'Reactive oxygen species production by monoamine oxidases in intact cells', *Naunyn Schmiedebergs Arch.Pharmacol.*, 359(5), pp. 428–431. Available at: http://www.ncbi.nlm.nih.gov/pubmed/10498294.

Poole, A. C. *et al.* (2008) 'The PINK1 / Parkin pathway regulates mitochondrial morphology', 105.

Popović-Bijelić, A. *et al.* (2016) 'Iron-sulfur cluster damage by the superoxide radical in neural tissues of the SOD1G93AALS rat model', *Free Radical Biology and Medicine*, 96, pp. 313–322. doi: 10.1016/j.freeradbiomed.2016.04.028.

Potthast, A. B. *et al.* (2017) 'Alterations of sirtuins in mitochondrial cytochrome c-oxidase deficiency', *PLoS ONE*, 12(10), pp. 1–21. doi: 10.1371/journal.pone.0186517.

Pryde, K. R. and Hirst, J. (2011) 'Superoxide is produced by the reduced flavin in mitochondrial complex I: A single, unified mechanism that applies during both forward and reverse electron transfer', *Journal of Biological Chemistry*, 286(20), pp. 18056–18065. doi: 10.1074/jbc.M110.186841.

Pryor, W. a (1986) ‘OXY-RADICALS AND RELATED SPECIES: Their Formation, Lifetimes, and Reactions’, *Annual Review of Physiology*, 48, pp. 657–667.

Quinlan, C. L. *et al.* (2012) ‘Mitochondrial complex II can generate reactive oxygen species at high rates in both the forward and reverse reactions’, *Journal of Biological Chemistry*, 287(32), pp. 27255–27264. doi: 10.1074/jbc.M112.374629.

Qureshi, M. A., Haynes, C. M. and Pellegrino, M. W. (2017) ‘The mitochondrial unfolded protein response: Signaling from the powerhouse’, *Journal of Biological Chemistry*, 292(33), pp. 13500–13506. doi: 10.1074/jbc.R117.791061.

Radke, S. *et al.* (2008) ‘Mitochondrial protein quality control by the proteasome involves ubiquitination and the protease Omi’, *Journal of Biological Chemistry*, 283(19), pp. 12681–12685. doi: 10.1074/jbc.C800036200.

Rai, P. K. *et al.* (2018) ‘Advances in methods for reducing mitochondrial DNA disease by replacing or manipulating the mitochondrial genome’, *Essays In Biochemistry*, 62(3), pp. 455–465. doi: 10.1042/EBC20170113.

Rak, M. *et al.* (2016) ‘Mitochondrial Cytochrome c Oxidase Deficiency’, 130(6), pp. 393–407. doi: 10.1042/CS20150707.Mitochondrial.

Rehling, P. *et al.* (2003) ‘Protein Insertion into the Mitochondrial Inner Membrane by a Twin-Pore Translocase’, 299(April).

Renkema, G. H. *et al.* (2017) ‘Mutated PET117 causes complex IV deficiency and is associated with neurodevelopmental regression and medulla oblongata lesions’, *Human Genetics*. Springer Berlin Heidelberg, 136(6), pp. 759–769. doi: 10.1007/s00439-017-1794-7.

Rhein, V. F. *et al.* (2013) ‘NDUFAF7 methylates arginine 85 in the NDUFS2 subunit of human complex i’, *Journal of Biological Chemistry*, 288(46), pp. 33016–33026. doi: 10.1074/jbc.M113.518803.

Rhein, V. F. *et al.* (2016) ‘NDUFAF5 hydroxylates NDUFS7 at an early stage in the assembly of human complex I’, *Journal of Biological Chemistry*, 291(28), pp. 14851–14860. doi: 10.1074/jbc.M116.734970.

Richardson, D. R. *et al.* (2010) 'Mitochondrial iron trafficking and the integration of iron metabolism between the mitochondrion and cytosol', *Proceedings of the National Academy of Sciences*, 107(24), pp. 10775–10782. doi: 10.1073/pnas.0912925107.

Richman, T. R. *et al.* (2016) 'Loss of the RNA-binding protein TACO1 causes late-onset mitochondrial dysfunction in mice', *Nature Communications*, 7(May), pp. 1–14. doi: 10.1038/ncomms11884.

Richter-Dennerlein, R. *et al.* (2016) 'Mitochondrial Protein Synthesis Adapts to Influx of Nuclear-Encoded Protein', *Cell*. doi: 10.1016/j.cell.2016.09.003.

Robin, E. D. and Wong, R. (1988) 'Mitochondria1 DNA Molecules and Virtual Number of Mitochondria per Cell in Mammalian Cells'.

Rötig, A. (2011) 'Human diseases with impaired mitochondrial protein synthesis', *Biochimica et Biophysica Acta - Bioenergetics*. Elsevier B.V., 1807(9), pp. 1198–1205. doi: 10.1016/j.bbabio.2011.06.010.

Rouault, T. A. and Maio, N. (2017) 'Biogenesis and functions of mammalian iron-sulfur proteins in the regulation of iron homeostasis and pivotal metabolic pathways', *Journal of Biological Chemistry*, 292(31), pp. 12744–12753. doi: 10.1074/jbc.R117.789537.

Ruiz-pesini, E. *et al.* (2007) 'An enhanced MITOMAP with a global mtDNA mutational phylogeny', 35(December 2006), pp. 823–828. doi: 10.1093/nar/gkl927.

Ruzzenente, B. *et al.* (2012) 'LRPPRC is necessary for polyadenylation and coordination of translation of mitochondrial mRNAs', *EMBO Journal*, 31(2), pp. 443–456. doi: 10.1038/emboj.2011.392.

Saada, A. *et al.* (2008) 'C6ORF66 Is an Assembly Factor of Mitochondrial Complex I', *American Journal of Human Genetics*, 82(1), pp. 32–38. doi: 10.1016/j.ajhg.2007.08.003.

Saada, A. *et al.* (2009) 'Mutations in NDUFAF3 (C3ORF60), Encoding an NDUFAF4 (C6ORF66)-Interacting Complex I Assembly Protein, Cause Fatal Neonatal Mitochondrial Disease', *American Journal of Human Genetics*, 84(6),

pp. 718–727. doi: 10.1016/j.ajhg.2009.04.020.

Sánchez-Caballero, L., Guerrero-Castillo, S. and Nijtmans, L. (2016) 'Unraveling the complexity of mitochondrial complex i assembly: A dynamic process', *Biochimica et Biophysica Acta - Bioenergetics*. Elsevier B.V., 1857(7), pp. 980–990. doi: 10.1016/j.bbabio.2016.03.031.

Sánchez, E. *et al.* (2013) 'LYRM7 / MZM1L is a UQCRFS1 chaperone involved in the last steps of mitochondrial Complex III assembly in human cells', *BBA - Bioenergetics*. Elsevier B.V., 1827(3), pp. 285–293. doi: 10.1016/j.bbabio.2012.11.003.

Santra, S. *et al.* (2004) 'Ketogenic Treatment Reduces Deleted Mitochondrial DNAs in Cultured Human Cells', pp. 662–669. doi: 10.1002/ana.20240.

Sarraf, S. A. *et al.* (2013) 'Landscape of the PARKIN-dependent ubiquitylome in response to mitochondrial depolarization Shireen', *Nature*, 496(7445), pp. 372–376. doi: 10.1038/nature12043.Landscape.

Saxton, R. A. and Sabatini, D. M. (2018) 'mTOR Signaling in Growth, Metabolism, and Disease', 168(6), pp. 960–976. doi: 10.1016/j.cell.2017.02.004.mTOR.

Schägger, H. (2002) 'Respiratory chain supercomplexes of mitochondria and bacteria', *Biochimica et Biophysica Acta - Bioenergetics*, 1555(1–3), pp. 154–159. doi: 10.1016/S0005-2728(02)00271-2.

Schieber, M. and Chandel, N. S. (2014) 'ROS function in redox signaling and oxidative stress', *Current Biology*. Elsevier, 24(10), pp. R453–R462. doi: 10.1016/j.cub.2014.03.034.

Schiff, M. *et al.* (2012) 'Therapies in inborn errors of oxidative metabolism', *Trends Endocrinol Metab*, 23(9), pp. 488–495. doi: 10.1016/j.tem.2012.04.006.Therapies.

Scialò, F. *et al.* (2016) 'Mitochondrial ROS Produced via Reverse Electron Transport Extend Animal Lifespan', *Cell Metabolism*, 23(4), pp. 725–734. doi: 10.1016/j.cmet.2016.03.009.

Sharma, S. *et al.* (2018) 'Cavitating Leukoencephalopathy With Posterior Predominance Caused by a Deletion in the APOPT1 Gene in an Indian Boy', *Journal of Child Neurology*, 33(6), pp. 428–431. doi: 10.1177/0883073818760875.

Sharma, V. *et al.* (2017) 'Insights into functions of the H channel of cytochrome *c* oxidase from atomistic molecular dynamics simulations', *Proceedings of the National Academy of Sciences*, 114(48), pp. E10339–E10348. doi: 10.1073/pnas.1708628114.

Sheftel, A. D. *et al.* (2009) 'Human Ind1, an Iron-Sulfur Cluster Assembly Factor for Respiratory Complex I', *Molecular and Cellular Biology*, 29(22), pp. 6059–6073. doi: 10.1128/MCB.00817-09.

Siebels, I. and Dröse, S. (2013) 'Q-site inhibitor induced ROS production of mitochondrial complex II is attenuated by TCA cycle dicarboxylates', *Biochimica et Biophysica Acta - Bioenergetics*. Elsevier B.V., 1827(10), pp. 1156–1164. doi: 10.1016/j.bbabio.2013.06.005.

Signes, A. and Fernandez-vizarra, E. (2018) 'Assembly of mammalian oxidative phosphorylation complexes I – V and supercomplexes', 0(May), pp. 255–270.

Sinkler, C. A. *et al.* (2017) 'Tissue- and Condition-Specific Isoforms of Mammalian Cytochrome c Oxidase Subunits: From Function to Human Disease', *Oxidative Medicine and Cellular Longevity*, 2017. doi: 10.1155/2017/1534056.

Sjöstrand, F. S. (1953) 'Electron microscopy of mitochondria and cytoplasmic double membranes', *Nature Publishing Group*, 171, pp. 30–32.

Smeitink, J., Heuvel, L. Van Den and Dimauro, S. (2001) 'THE GENETICS AND PATHOLOGY OF OXIDATIVE PHOSPHORYLATION', 2(May), pp. 342–352.

Sobotta, M. C. *et al.* (2015) 'Peroxiredoxin-2 and STAT3 form a redox relay for H<inf>2</inf>O<inf>2</inf> signaling', *Nature Chemical Biology*, 11(1), pp. 64–70. doi: 10.1038/nchembio.1695.

Sofia, A.-E. *et al.* (2010) 'Ketogenic diet slows down mitochondrial myopathy progression in mice', 19(10), pp. 1974–1984. doi: 10.1093/hmg/ddq076.

Sohal, R. S. (1996) ‘Oxidative Stress, Caloric Restriction, and Aging Rajindar’, 273(5271), pp. 59–63. doi: 10.1016/j.dci.2009.07.003.Characterization.

Soto, I. C. *et al.* (2012) ‘Biogenesis and assembly of eukaryotic cytochrome c oxidase catalytic core’, *Biochimica et Biophysica Acta - Bioenergetics*. Elsevier B.V., 1817(6), pp. 883–897. doi: 10.1016/j.bbabio.2011.09.005.

Sousa, J. S. *et al.* (2016) ‘Functional asymmetry and electron flow in the bovine respirasome’, *eLife*, 5(NOVEMBER2016), pp. 1–17. doi: 10.7554/eLife.21290.

Starkov, A. A. *et al.* (2004) ‘Mitochondrial alpha-Ketoglutarate Dehydrogenase Complex Generates Reactive Oxygen Species’, *Journal of Neuroscience*, 24(36), pp. 7779–7788. doi: 10.1523/JNEUROSCI.1899-04.2004.

Stefani, D. De *et al.* (2014) ‘A 40 kDa protein of the inner membrane is the mitochondrial calcium uniporter’, 476(7360), pp. 336–340. doi: 10.1038/nature10230.A.

Stewart, J. B. and Chinnery, P. F. (2015) ‘The dynamics of mitochondrial DNA heteroplasmy: Implications for human health and disease’, *Nature Reviews Genetics*. Nature Publishing Group, 16(9), pp. 530–542. doi: 10.1038/nrg3966.

Stiburek, L. *et al.* (2005) ‘Tissue-specific cytochrome *c* oxidase assembly defects due to mutations in *SCO2* and *SURF1*’, *Biochemical Journal*, 392(3), pp. 625–632. doi: 10.1042/BJ20050807.

Stiburek, L. *et al.* (2006) ‘Biogenesis of eukaryotic cytochrome c oxidase.’, *Physiological research*, 55(2), pp. 27–41. Available at: http://www.ncbi.nlm.nih.gov/pubmed/17298220.

Stock, D. *et al.* (2000) ‘The rotary mechanism of ATP synthase’, *Elsevier Science Ltd.*, 10, pp. 672–679.

Stojanovski, D. *et al.* (2008) ‘The MIA system for protein import into the mitochondrial intermembrane space’, 1783, pp. 610–617. doi: 10.1016/j.bbamcr.2007.10.004.

Strauss, M. *et al.* (2008) ‘Dimer ribbons of ATP synthase shape the inner

mitochondrial membrane', *EMBO Journal*, 27(7), pp. 1154–1160. doi: 10.1038/emboj.2008.35.

Strogolova, V. *et al.* (2012) 'Rcf1 and Rcf2, Members of the Hypoxia-Induced Gene 1 Protein Family, Are Critical Components of the Mitochondrial Cytochrome bc1-Cytochrome c Oxidase Supercomplex', *Molecular and Cellular Biology*, 32(8), pp. 1363–1373. doi: 10.1128/MCB.06369-11.

Stroud, D. A. *et al.* (2015) 'COA6 is a mitochondrial complex IV assembly factor critical for biogenesis of mtDNA-encoded COX2', *Human Molecular Genetics*, 24(19), pp. 5404–5415. doi: 10.1093/hmg/ddv265.

Stroud, D. A. *et al.* (2016) 'Accessory subunits are integral for assembly and function of human mitochondrial complex i', *Nature*. Nature Publishing Group, 538(7623), pp. 123–126. doi: 10.1038/nature19754.

Suárez-Rivero, J. *et al.* (2016) 'Mitochondrial Dynamics in Mitochondrial Diseases', *Diseases*, 5(1), p. 1. doi: 10.3390/diseases5010001.

Sun, F. *et al.* (2005) 'Crystal structure of mitochondrial respiratory membrane protein Complex II', *Cell*, 121(7), pp. 1043–1057. doi: 10.1016/j.cell.2005.05.025.

Sun, R. C. and Denko, N. C. (2014) 'Hypoxic regulation of glutamine metabolism through HIF1 and SIAH2 supports lipid synthesis that is necessary for tumor growth', *Cell Metabolism*. Elsevier Inc., 19(2), pp. 285–292. doi: 10.1016/j.cmet.2013.11.022.

Szklarczyk, R. *et al.* (2012) 'Iterative orthology prediction uncovers new mitochondrial proteins and identifies C12orf62 as the human ortholog of COX14, a protein involved in the assembly of cytochrome c oxidase', *Genome Biology*. BioMed Central Ltd, 13(2), p. R12. doi: 10.1186/gb-2012-13-2-r12.

Szklarczyk, R. *et al.* (2013) 'A mutation in the FAM36A gene, the human ortholog of COX20, impairs cytochrome c oxidase assembly and is associated with ataxia and muscle hypotonia', *Human Molecular Genetics*, 22(4), pp. 656–667. doi: 10.1093/hmg/dds473.

Tait, S. W. G. and Green, D. R. (2013) 'Mitochondrial regulation of cell death.', *Cold Spring Harbor perspectives in biology*, 5(9), p. a008706. doi:

10.1101/cshperspect.a008706.

Tamiy, G. *et al.* (2014) ‘A Mutation of COX6A1 causes a recessive axonal or mixed form of charcot-marie-tooth disease’, *American Journal of Human Genetics*. The American Society of Human Genetics, 95(3), pp. 294–300. doi: 10.1016/j.ajhg.2014.07.013.

Taylor, N. G. *et al.* (2017) ‘The assembly factor Pet117 couples heme a synthase activity to cytochrome oxidase assembly’, *Journal of Biological Chemistry*, 292(5), pp. 1815–1825. doi: 10.1074/jbc.M116.766980.

Tello, D. *et al.* (2011) ‘Induction of the mitochondrial NDUFA4L2 protein by HIF-1α decreases oxygen consumption by inhibiting complex i activity’, *Cell Metabolism*, 14(6), pp. 768–779. doi: 10.1016/j.cmet.2011.10.008.

Thomas, R. E. *et al.* (2014) ‘PINK1-Parkin Pathway Activity Is Regulated by Degradation of PINK1 in the Mitochondrial Matrix’, *PLoS Genetics*, 10(5). doi: 10.1371/journal.pgen.1004279.

Tilokani, L. *et al.* (2018) ‘Mitochondrial dynamics : overview of molecular mechanisms’, 0(July), pp. 341–360.

Timón-Gómez, A. *et al.* (2017) ‘Mitochondrial cytochrome c oxidase biogenesis: Recent developments’, *Seminars in Cell & Developmental Biology*, 76, pp. 163–178. doi: 10.1016/j.semcdb.2017.08.055.

Tiranti, V. *et al.* (1998) ‘Mutations of SURF-1 in Leigh Disease Associated with Cytochrome c Oxidase Deficiency’, *The American Journal of Human Genetics*, 63(6), pp. 1609–1621. doi: 10.1086/302150.

Tiranti, V. *et al.* (2009) ‘Loss of ETHE1 , a mitochondrial dioxygenase , causes fatal sulfide toxicity in ethylmalonic encephalopathy’, 15(2), pp. 200–205. doi: 10.1038/nm.1907.

Trumpower, B. (1990) ‘The protonmotive Q cycle. Energy transduction by coupling of proton translocation to electron transfer by the cytochrome bc1 complex’, *Journal of Biological Chemistry*, 265(20), pp. 11409–11412. doi: 10.3109/10409239409086800.

Tsukihara T, Aoyama H, Yamashita E, Tomizaki T, Yamaguchi H, Shinzawa-Itoh K, Nakashima R, Yaono R, Y. S. (1996) 'The whole structure of the 13-subunit oxidized cytochrome c oxidase at 2.8 A', *Science*, 24(272(5265)), pp. 1136–44.

Tucker, E. J. *et al.* (2013) 'Mutations in the UQCC1-Interacting Protein, UQCC2, Cause Human Complex III Deficiency Associated with Perturbed Cytochrome b Protein Expression', *PLoS Genetics*, 9(12). doi: 10.1371/journal.pgen.1004034.

Turrens, J. F. (2003) 'Mitochondrial formation of reactive oxygen species', *Journal of Physiology*, 552(2), pp. 335–344. doi: 10.1113/jphysiol.2003.049478.

Turrens, J. F., Alexandre, A. and Lehninger, A. L. (1985) 'Ubisemiquinone is the electron donor for superoxide formation by complex III of heart mitochondria', *Archives of Biochemistry and Biophysics*, 237(2), pp. 408–414. doi: 10.1016/0003-9861(85)90293-0.

Twig, G., Hyde, B. and Shirihai, O. S. (2008) 'Mitochondrial fusion, fission and autophagy as a quality control axis: The bioenergetic view', *Biochimica et Biophysica Acta - Bioenergetics*, 1777(9), pp. 1092–1097. doi: 10.1016/j.bbabio.2008.05.001.

Tzagoloff, A. and Dieckmann, C. L. (1990) 'PET genes of *Saccharomyces cerevisiae*.', *Microbiological reviews*, 54(9), pp. 211–225. doi: 10.1001/archderm.140.9.1127.

Ugalde, C., Janssen, R. J. R. J., *et al.* (2004) 'Differences in assembly or stability of complex I and other mitochondrial OXPHOS complexes in inherited complex I deficiency', *Human Molecular Genetics*, 13(6), pp. 659–667. doi: 10.1093/hmg/ddh071.

Ugalde, C., Vogel, R., *et al.* (2004) 'Human mitochondrial complex I assembles through the combination of evolutionary conserved modules: A framework to interpret complex I deficiencies', *Human Molecular Genetics*, 13(20), pp. 2461–2472. doi: 10.1093/hmg/ddh262.

Varanita, T. *et al.* (2015) 'The Opa1-Dependent Mitochondrial Cristae Remodeling Pathway Controls Atrophic , Apoptotic , Article The Opa1-Dependent Mitochondrial Cristae Remodeling Pathway Controls Atrophic , Apoptotic , and Ischemic Tissue Damage', pp. 834–844. doi: 10.1016/j.cmet.2015.05.007.

Vidoni, S. *et al.* (2017) 'MR-1S Interacts with PET100 and PET117 in Module-Based Assembly of Human Cytochrome c Oxidase', *Cell Reports*. ElsevierCompany., 18(7), pp. 1727–1738. doi: 10.1016/j.celrep.2017.01.044.

Vinothkumar, K. R., Zhu, J. and Hirst, J. (2014) 'Architecture of mammalian respiratory complex I', *Nature*. Nature Publishing Group, 515(7525), pp. 80–84. doi: 10.1038/nature13686.

Viscomi, C. *et al.* (2010) 'Combined treatment with oral metronidazole and N-acetylcysteine is effective in ethylmalonic encephalopathy', *Nature Medicine*. Nature Publishing Group, 16(8), pp. 869–871. doi: 10.1038/nm.2188.

Viscomi, C. *et al.* (2011) 'In Vivo Correction of COX Deficiency by Activation of the AMPK / PGC-1 a Axis', *Cell Metabolism*. Elsevier Inc., 14(1), pp. 80–90. doi: 10.1016/j.cmet.2011.04.011.

Viscomi, C. (2016) 'Toward a therapy for mitochondrial disease', 0(June), pp. 1483–1490. doi: 10.1042/BST20160085.

Viscomi, C. and Zeviani, M. (2017) 'MtDNA-maintenance defects: syndromes and genes', *Journal of Inherited Metabolic Disease*. Journal of Inherited Metabolic Disease, 40(4), pp. 587–599. doi: 10.1007/s10545-017-0027-5.

Vogel, R. O. *et al.* (2005) 'Human mitochondrial complex I assembly is mediated by NDUFAF1', *FEBS Journal*, 272(20), pp. 5317–5326. doi: 10.1111/j.1742-4658.2005.04928.x.

Vogel, R. O., Janssen, R. J. R. J., *et al.* (2007) 'Cytosolic signaling protein Ecsit also localizes to mitochondria where it interacts with chaperone NDUFAF1 and functions in complex I assembly', *Genes and Development*, 21(5), pp. 615–624. doi: 10.1101/gad.408407.

Vogel, R. O., Dieteren, C. E. J., *et al.* (2007) 'Identification of mitochondrial complex I assembly intermediates by tracing tagged NDUFS3 demonstrates the entry point of mitochondrial subunits', *Journal of Biological Chemistry*, 282(10), pp. 7582–7590. doi: 10.1074/jbc.M609410200.

Vogel, R. O., van den Brand, M. A. M., *et al.* (2007) 'Investigation of the complex I assembly chaperones B17.2L and NDUFAF1 in a cohort of CI deficient patients',

Molecular Genetics and Metabolism, 91(2), pp. 176–182. doi: 10.1016/j.ymgme.2007.02.007.

Vogel, R. O., Smeitink, J. A. M. and Nijtmans, L. G. J. (2007) 'Human mitochondrial complex I assembly: A dynamic and versatile process', *Biochimica et Biophysica Acta - Bioenergetics*, 1767(10), pp. 1215–1227. doi: 10.1016/j.bbabio.2007.07.008.

Van Vranken, J. G. *et al.* (2014) 'SDHAF4 promotes mitochondrial Succinate dehydrogenase activity and prevents neurodegeneration', *Cell Metabolism*. Elsevier Inc., 20(2), pp. 241–252. doi: 10.1016/j.cmet.2014.05.012.

Van Vranken, J. G. *et al.* (2015) 'Protein-mediated assembly of succinate dehydrogenase and its cofactors', 91(2), pp. 165–171. doi: 10.1016/j.chemosphere.2012.12.037.Reactivity.

Vukotic, M. *et al.* (2012) 'Rcf1 mediates cytochrome oxidase assembly and respirasome formation, revealing heterogeneity of the enzyme complex', *Cell Metabolism*, 15(3), pp. 336–347. doi: 10.1016/j.cmet.2012.01.016.

Vygodina, T. V. *et al.* (2017) 'Cytochrome c oxidase inhibition by calcium at physiological ionic composition of the medium: Implications for physiological significance of the effect', *Biochimica et Biophysica Acta - Bioenergetics*, 1858(12), pp. 982–990. doi: 10.1016/j.bbabio.2017.08.011.

Wagener, N. *et al.* (2011) 'A pathway of protein translocation in mitochondria mediated by the AAA-ATPase Bcs1', *Molecular Cell*. Elsevier Inc., 44(2), pp. 191–202. doi: 10.1016/j.molcel.2011.07.036.

Walker, J. E. (2013) 'The ATP synthase: the understood, the uncertain and the unknown', *Biochemical Society Transactions*, 41(1), pp. 1–16. doi: 10.1042/BST20110773.

Wang, A. *et al.* (2016) 'Rapamycin enhances survival in a Drosophila model of mitochondrial disease', 7(49), pp. 80131–80139.

Wang, L. (2016) 'Mitochondrial purine and pyrimidine metabolism and beyond and beyond'. Taylor & Francis, 7770. doi: 10.1080/15257770.2015.1125001.

Wang, Z. and Ackerman, S. H. (2000) ‘The Assembly Factor Atp11p Binds to the β -Subunit of the Mitochondrial F 1 -ATPase The Assembly Factor Atp11p Binds to the -Subunit of the Mitochondrial F 1 -ATPase *’, *The Journal of biological chemistry*, 275(8), pp. 5767–5772. doi: 10.1074/jbc.275.8.5767.

Wang, Z. G. *et al.* (2000) ‘The alpha-subunit of the mitochondrial F(1) ATPase interacts directly with the assembly factor Atp12p.’, *The EMBO journal*, 19(7), pp. 1486–93. doi: 10.1093/emboj/19.7.1486.

Wang, Z. G., White, P. S. and Ackerman, S. H. (2001) ‘Atp11p and Atp12p are Assembly Factors for the F1-ATPase in Human Mitochondria’, *Journal of Biological Chemistry*, 276(33), pp. 30773–30778. doi: 10.1074/jbc.M104133200.

Wanschers, B. F. J. *et al.* (2014) ‘A mutation in the human CBP4 ortholog UQCC3 impairs complex III assembly, activity and cytochrome b stability’, *Human molecular genetics*, 23(23), pp. 6356–6365. doi: 10.1093/hmg/ddu357.

Wasilewski, M., Chojnacka, K. and Chacinska, A. (2017) ‘Protein trafficking at the crossroads to mitochondria’, *Biochimica et Biophysica Acta - Molecular Cell Research*, 1864(1), pp. 125–137. doi: 10.1016/j.bbamcr.2016.10.019.

Watt, I. N. *et al.* (2010) ‘Bioenergetic cost of making an adenosine triphosphate molecule in animal mitochondria’, *Proceedings of the National Academy of Sciences*, 107(39), pp. 16823–16827. doi: 10.1073/pnas.1011099107.

Weraarpachai, W. *et al.* (2009) ‘Mutation in TACO1, encoding a translational activator of COX I, results in cytochrome c oxidase deficiency and late-onset Leigh syndrome’, *Nature Genetics*. doi: 10.1038/ng.390.

Weraarpachai, W. *et al.* (2012) ‘Mutations in C12orf62, a factor that couples COX i synthesis with cytochrome c oxidase assembly, cause fatal neonatal lactic acidosis’, *American Journal of Human Genetics*. doi: 10.1016/j.ajhg.2011.11.027.

Wiedemann, N., Frazier, A. E. and Pfanner, N. (2004) ‘The Protein Import Machinery of Mitochondria’, *Journal of Biological Chemistry*. doi: 10.1074/jbc.R400003200.

Wikström, M., Krab, K. and Sharma, V. (2018) ‘Oxygen Activation and Energy Conservation by Cytochrome *c* Oxidase’, *Chemical Reviews*, p.

acs.chemrev.7b00664. doi: 10.1021/acs.chemrev.7b00664.

Williams, E. G. *et al.* (2016) 'Systems proteomics of liver mitochondria function', *Science*, 352(6291). doi: 10.1126/science.aad0189.

Wittig, I. *et al.* (2010) 'Assembly and oligomerization of human ATP synthase lacking mitochondrial subunits a and A6L', *Biochimica et Biophysica Acta - Bioenergetics*. Elsevier B.V., 1797(6–7), pp. 1004–1011. doi: 10.1016/j.bbabio.2010.02.021.

Wittig, I. and Schägger, H. (2008) 'Structural organization of mitochondrial ATP synthase', *Biochimica et Biophysica Acta - Bioenergetics*, 1777(7–8), pp. 592–598. doi: 10.1016/j.bbabio.2008.04.027.

Wrobel, L. *et al.* (2015) 'Mistargeted mitochondrial proteins activate a proteostatic response in the cytosol', *Nature*. doi: 10.1038/nature14951.

Wu, M. *et al.* (2016) 'Structure of Mammalian Respiratory Supercomplex I1III2IV1', *Cell*. Elsevier, 167(6), p. 1598–1609.e10. doi: 10.1016/j.cell.2016.11.012.

XU, F. *et al.* (2004) 'The role of the *LRPPRC* (leucine-rich pentatricopeptide repeat cassette) gene in cytochrome oxidase assembly: mutation causes lowered levels of COX (cytochrome *c* oxidase) I and COX III mRNA', *Biochemical Journal*. doi: 10.1042/BJ20040469.

Xu, S. *et al.* (2011) 'The AAA-ATPase p97 is essential for outer mitochondrial membrane protein turnover', *Molecular Biology of the Cell*, 22(3), pp. 291–300. doi: 10.1091/mbc.E10-09-0748.

Yahata, N. *et al.* (2017) 'TALEN-mediated shift of mitochondrial DNA heteroplasmy in MELAS-iPSCs with m . 13513G > A mutation', *Scientific Reports*. Springer US, (March), pp. 1–11. doi: 10.1038/s41598-017-15871-y.

Yang, Y. *et al.* (2000) 'Ubiquitin protein ligase activity of IAPs and their degradation in proteasomes in response to apoptotic stimuli', *Science*, 288(5467), pp. 874–877. doi: 10.1126/science.288.5467.874.

Yaoa, J. and Brinton, R. D. (2011) 'Targeting Mitochondrial Bioenergetics for Alzheimer's Prevention and Treatment', *Curr Pharm Des.*, 17(31), pp. 3474–3479. doi: 10.2217/nnm.12.167.Gene.

Yonashiro, R. *et al.* (2006) 'A novel mitochondrial ubiquitin ligase plays a critical role in mitochondrial dynamics', *EMBO Journal*, 25(15), pp. 3618–3626. doi: 10.1038/sj.emboj.7601249.

Yoshikawa, S., Shinzawa-Itoh, K. and Tsukihara, T. (1998) 'Crystal structure of bovine heart cytochrome c oxidase at 2.8 A resolution.', *Journal of bioenergetics and biomembranes*, 30(1), pp. 7–14. doi: https://doi.org/10.1023/A:1020595108560.

Youle, R. J., Pickles, S. and Vigi, P. (2018) 'Review Mitophagy and Quality Control Mechanisms in Mitochondrial Maintenance'. doi: 10.1016/j.cub.2018.01.004.

Young, M. J. *et al.* (2007) 'The evolutionary history of mitochondrial porins', *BMC Evolutionary Biology*, 7. doi: 10.1186/1471-2148-7-31.

Yun, J. *et al.* (2014) 'MUL1 acts in parallel to the PINK1/parkin pathway in regulating mitofusin and compensates for loss of PINK1/parkin', *eLife*, 2014(3), pp. 1–26. doi: 10.7554/eLife.01958.001.

Yusoff, A. A. M. *et al.* (2015) 'Understanding Mitochondrial DNA in Brain Tumorigenesis', *Molecular Considerations and Evolving Surgical Management Issues in the Treatment of Patients with a Brain Tumor*, (January 2015). doi: 10.5772/58965.

Zamponi, N. *et al.* (2018) 'Mitochondrial network complexity emerges from fission/fusion dynamics', *Scientific Reports*. Springer US, 8(1), pp. 1–10. doi: 10.1038/s41598-017-18351-5.

Zara, V., Conte, L. and Trumpower, B. L. (2007) 'Identification and characterization of cytochrome bc1 subcomplexes in mitochondria from yeast with single and double deletions of genes encoding cytochrome bc1 subunits', *FEBS Journal*, 274(17), pp. 4526–4539. doi: 10.1111/j.1742-4658.2007.05982.x.

Zara, V., Conte, L. and Trumpower, B. L. (2009a) 'Biogenesis of the yeast

cytochrome bc1 complex', *Biochimica et Biophysica Acta - Molecular Cell Research*. Elsevier B.V., 1793(1), pp. 89–96. doi: 10.1016/j.bbamcr.2008.04.011.

Zara, V., Conte, L. and Trumpower, B. L. (2009b) 'Evidence that the assembly of the yeast cytochrome bc1 complex involves the formation of a large core structure in the inner mitochondrial membrane', *FEBS Journal*, 276(7), pp. 1900–1914. doi: 10.1111/j.1742-4658.2009.06916.x.

Zhao, X. *et al.* (2011) 'Phosphoproteome Analysis of Functional Mitochondria Isolated from Resting Human Muscle Reveals Extensive Phosphorylation of Inner Membrane Protein Complexes and Enzymes', *Molecular & Cellular Proteomics*, 10(1), p. M110.000299. doi: 10.1074/mcp.M110.000299.

Zhou, A. *et al.* (2015) 'Structure and conformational states of the bovine mitochondrial ATP synthase by cryo-EM', *eLife*, 4(OCTOBER2015), pp. 1–15. doi: 10.7554/eLife.10180.

Zhu, J., Vinothkumar, K. R. and Hirst, J. (2016) 'Structure of mammalian respiratory complex i', *Nature*. Nature Publishing Group, 536(7616), pp. 354–358. doi: 10.1038/nature19095.

Zhu, J., Vinothkumar, K. R. and Hirst, J. (2017) 'Structure of mammalian respiratory complex I Jiapeng', *Nature*, 536(7616), pp. 354–358. doi: 10.1038/nature19095.Structure.

Zhu, Z. *et al.* (1998) 'SURF1, encoding a factor involved in the biogenesis of cytochrome c oxidase, is mutated in Leigh syndrome', *Nature Genetics*, 20(4), pp. 337–343. doi: 10.1038/3804.

Zischka, H. and Einer, C. (2018) 'Mitochondrial copper homeostasis and its derailment in Wilson disease', *International Journal of Biochemistry and Cell Biology*. Elsevier, 102(June), pp. 71–75. doi: 10.1016/j.biocel.2018.07.001.

Zöller, E., Todd Alexander, R. and Herrmann, J. M. (2018) 'Proteasomal degradation competes with Mia40-mediated import into mitochondria', *BMC Biology*. BMC Biology, 16(1), pp. 1–3. doi: 10.1186/s12915-018-0537-0.

Zurita Rendón, O. *et al.* (2014) 'The arginine methyltransferase NDUFAF7 is essential for complex I assembly and early vertebrate embryogenesis', *Human*

molecular genetics, 23(19), pp. 5159–5170. doi: 10.1093/hmg/ddu239.

Zurita Rendón, O. *et al.* (2016) 'A Mutation in the Flavin Adenine Dinucleotide-Dependent Oxidoreductase FOXRED1 Results in Cell-Type-Specific Assembly Defects in Oxidative Phosphorylation Complexes I and II', *Molecular and Cellular Biology*, 36(16), pp. 2132–2140. doi: 10.1128/MCB.00066-16.

Zurita Rendón, O. and Shoubridge, E. A. (2012) 'Early complex I assembly defects result in rapid turnover of the ND1 subunit', *Human Molecular Genetics*, 21(17), pp. 3815–3824. doi: 10.1093/hmg/dds209.